Technische Universität München
Fakultät für Maschinenwesen

Determining Fundamental Transport Parameters of Hydrogen Isotopes in Tungsten

Georg Holzner, M. Sc.

Vollständiger Abdruck der von der Fakultät Maschinenwesen der Technischen Universität München zur Erlangung des akademischen Grades eines

Doktor-Ingenieurs
(Dr.-Ing.)

genehmigten Dissertation.

Vorsitzender:	Prof. Dr. Peter Mayr
Prüfende/-r der Dissertation:	1. Prof. Dr. Rudolf Neu
	2. Prof. Dr. Christian Linsmeier

Die Dissertation wurde am 14.04.2020 bei der Technischen Universität München eingereicht und durch die Fakultät für Maschinenwesen am 28.06.2020 angenommen.

Technische Universität München
Fakultät für Maschinenwesen

Max-Planck-Institut für Plasmaphysik

Determining Fundamental Transport Parameters of Hydrogen Isotopes in Tungsten

Georg Holzner

Thesis zur Erlangung des akademischen Grades eines

Doktor-Ingenieurs
(Dr.-Ing.)

Abstract

The objective of this thesis was to determine the diffusion and solubility coefficients of protium and deuterium in tungsten. In the recent past major discrepancies evolved between modelling results and widely used and recommended values for protium derived from former experiments. In addition, no reliable experimental values for deuterium exist. The goal of this thesis was, therefore, to conduct measurements for these two isotopes. Accordingly, a gas loading apparatus was designed, built and commissioned in order to execute gas loading and subsequent degassing experiments with protium and deuterium on tungsten. The temperature for loading and degassing was varied between 1200 and 2600 K, gas loading pressure between 6 and 500 mbar and ramping rates between 0.2 and 30 K/s.

The newly established apparatus uses inductive heating with frequencies between 20 and 100 kHz and an estimated penetration depth of ~ 1.5 mm at 60 kHz. Specimens are placed inside a double-walled and water cooled quartz-glass tube. The sample temperature is measured utilising two independent methods: a type-C thermocouple directly welded to the specimen and optical single-wavelength pyrometry. The mounting of the specimen is realised by a tungsten shaft with a separable connection, dimensioned for temperatures up to 3200 K with a coefficient of safety of 6.1. Two geometries for the specimens and two different material grades were used in the experiments: one single-crystalline and one poly-crystalline tungsten specimen of same geometry (⌀15 mm, length 48 mm) and one bigger specimen (⌀30 mm, length 54 mm) of poly-crystalline tungsten. All specimens were high temperature conditioned at 2400 or 2600 K for 20 hours, alternately in hydrogen atmosphere (500 mbar) and vacuum to remove impurities, coarsen the grain structure and stabilise the microstructure before performing the particular measurement campaign. Hydrogen management needed extended efforts concerning safe handling, inertisation and avoiding inflammable conditions.

A series of measurements, also with a hollow cylindrical sample, were carried out to investigate, validate and quantify physical laws such as Sieverts' law or Fick's law, possible influence of traps, coating on the inner glass wall, or background-level.

A diffusion model was developed, based on the diffusion equation in 3-D cylindrical geometry to assess diffusion and solubility coefficients. The model presumes initially constant hydrogen concentration during the gas loading phase once thermodynamic equilibrium is reached. Degassing was assumed to be diffusion limited, yielding Dirichlet boundary conditions. The diffusion code fitted the measured degassing from the specimens at constant temperature and single-exponential signal decay. It simultaneously fitted the four variables which define diffusivity and solubility: the activation energy for diffusion and solubility E_A and E_S and the pre-exponential factors D_0 and S_0, respectively. An analytic solution of the diffusion equation (reduced diffusion model) was used for the assessment of the small specimens, taking advantage of their favourable geometry (length $\gg$ radius) and, hence, the term for longitudinal concentration could be neglected. In contrast, a numerical solution (full diffusion model) was required for the big specimen.

Experiments with the small specimens showed equal results for the single- and poly-crystalline sample for degassing behaviour with sufficiently fast ramps ≥ 15 K/s to constant temperatures

$\geq 1600\,\mathrm{K}$ for protium and deuterium.

Experiments with the big specimen showed excellent reproducibility for measurement cycles with equally performed loading and degassing routines throughout the whole experimental campaign.

Both, the reduced and full diffusion model combined with experiment, yielded converging results for diffusivities of protium and deuterium in tungsten. The recommended values for protium are determined to $\mathrm{E_A^H} = 0.280^{+0.02}_{-0.01}\,\mathrm{eV}$, $\mathrm{D_0^H} = 2.02^{+0.14}_{-0.11}{\cdot}10^{-7}\,\mathrm{m^2/s}$ and for deuterium to $\mathrm{E_A^D} = 0.265^{+0.02}_{-0.01}\,\mathrm{eV}$, $\mathrm{D_0^D} = 1.50^{+0.09}_{-0.05}{\cdot}10^{-7}\,\mathrm{m^2/s}$. These results deviate substantially from the widely used and recommended values for protium, being $\mathrm{E_A^H} = 0.39\,\mathrm{eV}$ and $\mathrm{D_0^H} = 4.1 \cdot 10^{-7}\mathrm{m/s^2}$. The derived values agree reasonably well with density functional theory (DFT) calculations. The parameters for solubility of protium in tungsten were derived to $\mathrm{E_S^H} = 1.13^{+0.04}_{-0.02}\,\mathrm{eV}$ and $\mathrm{S_0^H} = 8.61^{+0.99}_{-0.53}{\cdot}10^{-5}\,\left(\frac{\mathrm{H}}{\mathrm{W}}\right)\mathrm{Pa}^{-\frac{1}{2}}$, which are very similar to those derived for deuterium: $\mathrm{E_S^D} = 1.14^{+0.04}_{-0.02}\,\mathrm{eV}$ and $\mathrm{S_0^D} = 8.60^{+0.97}_{-0.59}{\cdot}10^{-5}\,\left(\frac{\mathrm{D}}{\mathrm{W}}\right)\mathrm{Pa}^{-\frac{1}{2}}$. The derived overall solubility is similar at temperatures of about 1000 K as compared to the solubility derived from the Frauenfelder values, being $\mathrm{E_A^{S:\,FF}} = 1.04{\pm}0.17\,\mathrm{eV}$ and $\mathrm{S_0^{H:\,FF}} = 2.82^{+2.73}_{-1.26}{\cdot}10^{-5}\,\left(\frac{\mathrm{H}}{\mathrm{W}}\right)\mathrm{Pa}^{-\frac{1}{2}}$. At temperatures lower than 1000 K the derived solubility is lower if compared to Frauenfelder and higher at higher temperatures. The solute energies $\mathrm{E_S}$ derived from this work are noticeably higher, but still within the error bars stated by Frauenfelder.

Kurzfassung

Ziel dieser Doktorarbeit war die Bestimmung der Löslichkeits- und Diffusionskoeffizienten von Protium und Deuterium in Wolfram. Modellierungen der letzten Jahre zeigen große Abweichungen für Protium von den bis dato empfohlenen und weitestgehend verwendeten Werten aus früheren Experimenten. Außerdem existieren keine verlässlichen Messungen für Deuterium. Ziel war es deshalb, diese Werte für diese beiden Isotope experimentell zu bestimmen. Zu diesem Zweck wurde eine Gasbeladungsapparatur geplant, errichtet und in Betrieb gesetzt um mit dieser Wolframprüflinge mit jeweils einem dieser Isotopen zu beladen und anschließend wieder zu entgasen. Die Temperatur für das Beladen und Entgasen wurde zwischen 1200 und 2600 K, der Gasdruck zwischen 6 und 500 mbar und die Rampgeschwindigkeiten zwischen 0,2 und 30 K/s variiert.

Die neue Maschine nutzt induktive Heizung mit Frequenzen zwischen 20 und 100 kHz, die errechnete Eindringtiefe bei 60 kHz beträgt circa 1,5 mm. Die Prüflinge werden in einem doppelwandigem und wassergekühltem Quartzglaskolben positioniert. Die Temperatur der Prüflinge wird gleichzeitig durch zwei Methoden bestimmt: ein Typ-C Thermoelement und optischer Pyrometrie bei einer Wellenlänge von 1,27 μm. Die Aufhängung der Prüflinge ist durch einen Wolframschaft mit einer trennbaren Verbindung realisiert, welche auf eine Maximaltemperatur von 3200 K und einen Sicherheitsfaktor von 6,1 ausgelegt ist. Es wurden zwei Geometrien von Prüflingen mit zwei verschiedenen Mikrostrukturen verwendet: ein Einkristall und ein Polykristall mit derselben, kleineren Geometrie (⌀15 mm, Länge 48 mm), und ein größerer Polykristall (⌀30 mm, Länge 54 mm). Alle Prüflinge wurden vor den jeweiligen Messkampagnen bei 2400 bzw. 2600 K für 20 Stunden abwechselnd in Wasserstoffatmosphäre (500 mbar) und Vakuum geglüht, um Verunreinigungen zu enfernen, die Körner zu vergrößern und die Mikrostruktur zu stabilisieren. Für die sichere Handhabung des Wasserstoffs an der Apparatur wurden zusätzliche Maßnahmen getroffen um entflammbare Zustände zu vermeiden und zusätzlichen Schutz im Schadensfall zu gewährleisten.

Vorversuche für die Validierung, auch mithilfe eines hohlzylinderischen Prüflings, wurden unternommen um physikalische Gesetze wie Sieverts' oder Fick's Gesetz, den möglichen Einfluss von Haftstellen, die Beschichtung der inneren Glaswand oder die Höhe des Wasserstoffhintergrunds zu quantifizieren.

Ein Diffusionsmodell, basierend auf der Diffusionsgleichung in 3-dimensionaler Zylindergeometrie, wurde entwickelt um die Diffusions- und Löslichkeitskoeffizienten aus den Experimenten zu bestimmen. Eine Annahme dieses Modells ist eine anfänglich konstante Wasserstoffkonzentration am Ende der Gasbeladungsphase nach Erreichen des thermodynamischen Gleichgewichts. Es wurden Dirichlet Randbedingungen und diffusionslimitiertes Entgasen angenommen.

Der Diffusionscode beruht auf der Anpassung des gemessenen Signals vom Prüfling bei konstanter Temperatur und einfach exponentiellem Abfalls des Signals. Die vier Variablen, welche die Diffusion und Löslichkeit beschreiben, werden simultan für einen Datensatz von mehreren Messungen angepasst: die Aktivierungs-, bzw. Löslichkeitsenergie E_A und E_S sowie die Vorfaktoren D_0 und S_0. Eine analytische Lösung der Diffusionsgleichung wurde für die Auswertung

der Messungen an den kleinen Prüflingen verwendet, da wegen ihrer vorteilhaften Geometrie (Länge $\gg$ Radius) die Konzentration in longitudinaler Richtung der Zylinder vernachlässigt werden konnte. Der große Prüfling hingegen benötigte eine numerische Lösung.

Die Experimente an den kleinen Prüflingen ergaben die gleichen Resultate für Ein- und Polykristall für das Ausgasverhalten bei ausreichend schnellen Temperaturrampen von $\geq 15\,\mathrm{K/s}$ zu konstanten Temperaturen $\geq 1600\,\mathrm{K}$ für Protium und Deuterium.

Die Experimente zeigten exzellente Reproduzierbarkeit von Messzyklen am großen Prüfling bei identisch ausgeführten Gasbeladungs- und Entladungsroutinen während der gesamten Messkampagne.

Das reduzierte als auch das vollumfängliche Diffusionsmodell lieferten konvergierende Resultate für die Diffusion von Protium und Deuterium in Wolfram. Die empfohlenen Werte sind für Protium $\mathrm{E_A^H} = 0{,}280^{+0{,}02}_{-0{,}01}\,\mathrm{eV}$, $\mathrm{D_0^H} = 2{,}02^{+0{,}14}_{-0{,}11}{\cdot}10^{-7}\,\mathrm{m^2/s}$ und für Deuterium $\mathrm{E_A^D} = 0{,}265^{+0{,}02}_{-0{,}01}\,\mathrm{eV}$, $\mathrm{D_0^D} = 1{,}50^{+0{,}09}_{-0{,}05}{\cdot}10^{-7}\,\mathrm{m^2/s}$. Diese Ergebnisse weichen beträchtlich von den weitgehend verwendeten und empfohlenen Werten von $\mathrm{E_A^H} = 0,39\,\mathrm{eV}$ und $\mathrm{D_0^H} = 4,1 \cdot 10^{-7}\mathrm{m/s^2}$ für Protium ab. Die hier gemessenen Werte stimmen besser mit Dichtefunktionaltheorie(DFT)-Berechnungen überein. Die gemessenen Löslichkeiten für Protium und Deuterium in Wolfram liegen ununterscheidbar beiinander: $\mathrm{E_S^H} = 1{,}13^{+0{,}04}_{-0{,}02}\,\mathrm{eV}$ und $\mathrm{S_0^H} = 8{,}61^{+0{,}99}_{-0{,}53}{\cdot}10^{-5}\,\left(\frac{\mathrm{H}}{\mathrm{W}}\right)\mathrm{Pa}^{-\frac{1}{2}}$, bzw. $\mathrm{E_S^D} = 1{,}14^{+0{,}04}_{-0{,}02}\,\mathrm{eV}$ und $\mathrm{S_0^D} = 8{,}60^{+0{,}97}_{-0{,}59}{\cdot}10^{-5}\,\left(\frac{\mathrm{D}}{\mathrm{W}}\right)\mathrm{Pa}^{-\frac{1}{2}}$. Die gemessene Löslichkeit bei 1000 K ist vergleichbar mit der von Frauenfelder gemessenen ($\mathrm{E_A^{S:\,FF}} = 1{,}04{\pm}0,17\,\mathrm{eV}$ und $\mathrm{S_0^{H:\,FF}} = 2{,}82^{+2{,}73}_{-1{,}26}{\cdot}10^{-5}\,\left(\frac{\mathrm{H}}{\mathrm{W}}\right)\mathrm{Pa}^{-\frac{1}{2}}$), unter 1000 K ist sie niedriger, darüber ist sie höher. Die in dieser Arbeit gemessenen Löslichkeitsenergien $\mathrm{E_S}$ sind innerhalb der Fehlerbalken höher als die von ihm angegebene.

Contents

Motivation 1

1. Theoretical background 3
1.1. Hydrogen in tungsten . . . 3
1.1.1. Solubility . . . 3
1.1.2. Diffusion . . . 4
1.2. Present data base . . . 5
1.3. How Frauenfelder analysed his measurements . . . 8
1.4. Diffusion model . . . 9
1.4.1. Diffusion . . . 10
1.4.2. Reduced diffusion model: fitting degassing gradient . . . 11
1.4.3. Cooling cycle . . . 12

2. Experimental Methods 15
2.1. Experimental set-up . . . 15
2.2. Experimental procedure . . . 18
2.3. Specimens: size, kind and high temperature treatment . . . 20
2.3.1. Small specimens: ∅ 15 mm poly- and single crystalline . . . 21
2.3.1.1. Single-crystalline sample . . . 21
2.3.1.2. Poly-crystalline sample . . . 22
2.3.2. Big specimen: ∅ 30 mm poly-crystalline . . . 23
2.4. Measuring gas species with a Quadrupole Mass Spectrometer (QMS) . . . 25
2.5. Experimental device . . . 25
2.5.1. Inductive heating . . . 28
2.5.2. Penetration depth . . . 28
2.5.3. Electromagnetic shielding . . . 29
2.5.4. Temperature measurement and control . . . 29
2.5.4.1. Measuring temperature . . . 29
2.5.4.2. Parallel usage of thermocouple and pyrometer . . . 31
2.5.5. Glass vessel . . . 32
2.5.5.1. Heat management . . . 32
2.5.5.2. Mechanical design . . . 36
2.5.5.3. Chemical cleaning . . . 36
2.5.5.4. Influence of coated inner glass wall . . . 37
2.5.6. Mounting the specimen . . . 40
2.5.6.1. Design . . . 40
2.5.6.2. Analysis . . . 41
2.5.6.3. Crash absorber . . . 43
2.5.7. Safety measures - what if? . . . 43
2.5.7.1. Water circuits . . . 43

2.5.7.2. Temperature surveillance . . . 44
2.5.7.3. Glass tube enclosure . . . 44
2.5.8. Hydrogen management . . . 44
2.5.9. The last frontier: outer shielding . . . 46

3. Experimental validation **49**
3.1. Quantifying uncertainties . . . 49
3.1.1. Reproducibility of experiments . . . 49
3.1.2. Temperature measurement differences . . . 51
3.1.2.1. Dynamic phase: ramp-up and cool-down . . . 51
3.1.2.2. Static phase at nominally constant temperature . . . 53
3.1.3. Background signals . . . 55
3.1.3.1. Estimation of background flux . . . 58
3.1.3.2. Discussion . . . 58
3.2. Guidelines for consistent measurements . . . 60
3.3. Defining the fitting window for the diffusion model . . . 61
3.4. Maximum-likelihood evaluation with the full diffusion model . . . 62
3.5. Forward modelling . . . 64
3.6. Pre-peak(s) during temperature ramp-up phase . . . 65

4. Applicability of diffusion model **69**
4.1. High temperature conditioning of specimens . . . 69
4.2. Inventory: interstitial solubility . . . 71
4.2.1. Thermodynamic equilibrium . . . 71
4.2.2. Correlation of gas pressure and dissolved hydrogen: Sieverts' law . . . 74
4.3. Applicability of solute diffusion . . . 75
4.3.1. Inventory-based scaling . . . 75
4.3.2. Different loading pressures . . . 77
4.3.3. Different loading temperatures . . . 78
4.4. Poly- and single-crystalline sample ($\varnothing\,15\,\mathrm{mm}$) . . . 80
4.4.1. Identical measured diffusivity . . . 80
4.4.2. Deviations in solubility at temperatures $\leq 2000\,\mathrm{K}$ . . . 81

5. Diffusion and solubility coefficients **83**
5.1. Reduced diffusion model . . . 83
5.2. Full diffusion model . . . 87
5.2.1. Selection of measurement cycles for final evaluation . . . 87
5.2.2. Excluded measurement cycles . . . 88
5.3. Bayesian statistics & Markov-Chain-Monte-Carlo (MCMC) sampling . . . 90
5.3.1. Results . . . 93
5.3.1.1. Solubility . . . 93
5.3.1.2. Diffusivity . . . 95
5.3.1.3. Results with total uncertainties σ_{total} . . . 95
5.3.2. Arrhenius plot of H and D diffusivities . . . 96
5.3.3. Comparison of protium and deuterium . . . 98

5.4. Synopsis . . . 101
5.4.1. Diffusivity . . . 101
5.4.1.1. Comparison of obtained results . . . 101
5.4.1.2. Comparison with Frauenfelder's results . . . 103
5.4.2. Solubility . . . 105

6. Summary **107**

Bibliography **111**

A. Appendix **117**
A.1. Glass tube: stress calculations . . . 117
A.2. Technical drawings . . . 122
A.3. Operation of gas loading apparatus "ROST" . . . 128
A.3.1. Vacuum and gas feed system . . . 128
A.3.1.1. Changing gas bottle . . . 128
A.3.1.2. Procedure for glass or specimen exchange . . . 130
A.3.1.3. Standard loading and degassing sequence . . . 132

Acknowledgements **136**

Motivation

Live is too precious to be left to chance.

(Deus X. 'Mac' Machina in:
The 13½ Lives of Captain Bluebear -
Walter Moers)

Nuclear fusion is a promising method for the next-generation source of electricity. Fusing deuterium and tritium nuclei into helium and neutrons ($^2\mathrm{H} + {}^3\mathrm{H} \longrightarrow {}^4\mathrm{He}(3.5\ \mathrm{MeV}) + {}^0\mathrm{n}(14.1\ \mathrm{MeV})$) in a magnetic confinement device exhibit the most investigated, and yet most promising method towards the development of an operating nuclear fusion power plant. The most-advanced devices of them are tokamaks (besides the currently less developed but also promising stellarators), in which a plasma is confined by axially symmetric magnetic coils in a vacuum vessel and heated to high temperature to provide sufficiently high kinetic energy (several keV) to enable nuclear fusion by overcoming electrostatic repulsion (Coloumb barrier) of the nuclei [1].

ITER, the international thermonuclear experimental fusion reactor that is currently being built in Cadarache, France, shall give evidence that a substantial power production can be achieved in a pulsed operation of 400 s. A successor device shall demonstrate an electrical net power production in combination with a closed fuel cycle, the demonstration nuclear fusion reactor (DEMO). It shall achieve pulse durations of more then two hours or even steady-state operation [2].

The operation of the plasma faces many challenges and so does the vessel itself which encloses the plasma. The plasma-facing components (PFCs) encounter technical issues which arise from heat and particle loads from the plasma and from embrittlement by neutrons. The PFCs in ITER are expected to receive particle fluxes in the range of 10^{19} - 10^{24} particles/m^2s of deuterium, tritium and other impurities like helium. In ITER the divertor, which can be seen as exhaust for helium that is product of the nuclear reaction in the plasma, will need to withstand steady-state heat loads of up to $10\,\mathrm{MW/m^2}$, not mentioning transients. This results in stringent constraints for the material choice for the PFCs. Tungsten is considered to be the most promising plasma-facing material (PFM). It exhibits a high sputtering threshold ($\mathrm{E_{th}} \sim 200\,\mathrm{eV}$ for deuterium), high melting temperature (3695 K, the highest among all metals), high thermal conductivity, low vapour pressure, low solubility of hydrogen isotopes, and comparably low long-term activation caused by neutron irradiation. ITER will use a full tungsten divertor, DEMO is planned to use PFCs of tungsten at the divertor and use EUROFER steel with a roughly 2 mm thin tungsten layer at the plasma-facing side as first-wall material [2].

Apart from the issues for the PFCs like persistence against abrasion or heat fluxes that are already mentioned, tritium transport through the PFC from the inside of the vessel to the rear side is a major issue [3]. Especially the necessary high pulse durations planned for forthcoming fusion power plants exhibit time frames (combined with elevated temperatures of the PFCs, especially the divertor) in which diffusion or transport of tritium is highly enhanced. Tritium is radioactive, hence harmful to humans, and moreover precious because it needs to be breeded

in the reactor itself. Diffusion and trapping through or by PFMs can lead to losses to the coolant and intolerable in-vessel inventories. [4]

Therefore, several diffusion-trapping transport codes are used to predict the transport of hydrogen isotopes, i.e., the loss of tritium, such as TMAP7 [5], TESSIM [6], or MHIMS [7].

Those transport codes firstly, and most prominently, use the diffusion coefficients of protium ("regular hydrogen" with one proton in the nuclei and mass = 1 amu), because solute diffusion is the governing mechanism for transport through tungsten. The fundamental transport parameters for solute diffusion are quantitatively described by the diffusion coefficients.

The transport of hydrogen in tungsten has been addressed by a number of studies, both experimentally and computationally, with partly deviating results for the activation energy [8, 9, 10, 11, 12, 13, 14, 15, 16]. A lack of experimentally derived and reliable data concerning the diffusivity of protium in tungsten led to the recommendation in a review by Causey et al. in 2001 [16] to use the diffusion coefficients derived by Frauenfelder [8]: $E_A = 0.39 \pm 0.09\,\mathrm{eV}$. Density functional theory (DFT) calculations derive divergent values of $E_A = 0.20\,\mathrm{eV}$ [12], $E_A = 0.21\,\mathrm{eV}$ [10], or $E_A = 0.25\,\mathrm{eV}$ [17], respectively. Considering those deviations from the recommended experimentally derived values, the reasonable suspicion emerges that the transport codes are potentially (and consistently) fed with unrealistic values for their most basic input parameter for solute transport of protium.

Another concern is the mass-dependent extrapolation for the diffusivity of the heavier hydrogen isotopes deuterium and tritium from the data for protium. Harmonic theory predicts a mass-dependent extrapolation factor for the pre-exponential factor of $D_0^D \propto \sqrt{m_H}/\sqrt{m_D} = \frac{1}{1.41}$, where m is the atomic mass of the isotope (protium and deuterium). The extrapolation from spurious values for the diffusivity would yield values for transport of deuterium and tritium that significantly deviate from reality. Additionally, there are several metal-hydrogen combinations known where the mass-dependenct extrapolation for hydrogen isotopes shows major deviations [18, p. 326].

To assess new experimental data, a new gas loading apparatus for measuring the diffusivity of protium and deuterium in tungsten was designed, built and commissioned. Gas loading and degassing of different samples manufactured with different material grades and with different geometries enabled the evaluation applying to two different methods: a reduced diffusion model, which uses the same method as Frauenfelder, and by a full diffusion model code that fully assesses diffusivity and, in contrary to Frauenfelder, also solubility.

1. Theoretical background

I've got science for any occasion
Postulating theorems formulating equations [...]
Droppin' science like Galileo dropped the orange

(Beastie Boys in:
Sound of Science - Paul's Boutique)

This chapter covers the topics of solubility and theory of diffusion for hydrogen in tungsten. Then results of experiment and modelling for hydrogen in tungsten are compared. A mathematical description of the gas loading experiments by Frauenfelder [8], i.e., their derivation, is shown. A diffusion model is described which allows deriving the solubility and diffusivity from gas loading and degassing measurements.

1.1. Hydrogen in tungsten

This thesis treats hydrogen in tungsten, in measurements the isotopes protium and deuterium are used. In the following "hydrogen" refers to all three isotopes:

- Protium: ^{1}H (H)
- Deuterium: ^{2}H (D)
- Tritium: ^{3}H (T)

Otherwise the isotope that is referred to is explicitly addressed.

Protium is the most common hydrogen isotope which has a nucleus that consists of one proton. Deuterium consists of one proton and one neutron - naturally 150 ppm of the existing hydrogen on earth is deuterium. Tritium's nuclei consists of one proton and two neutrons. It was artificially produced first in 1934 [19]. With a radioactive half time of about 12.3 years [20] it rarely exists on earth and is produced in the stratosphere from nuclear reactions caused by cosmic rays [21].

This thesis' investigations cover the two non-radioactive isotopes of hydrogen: protium and deuterium. Safety reasons (e.g., lack of a hot-cell) exclude the use of tritium.

1.1.1. Solubility

The equilibrium concentration, c_e, of hydrogen for low concentrations in the bulk of a body in gaseous atmospheres at temperature T depends on the partial pressure p_e of the hydrogen gas that surrounds the body. Sieverts' law describes this dependence as follows [22]:

$$\mathrm{c_e} = (\mathrm{S p_e})^{\frac{1}{2}} \tag{1.1}$$

At a given temperature, S $\left[\frac{\text{atoms}}{\text{m}^3\text{Pa}^{\frac{1}{2}}}\right]$ is the solubility of hydrogen, i.e., the number of atoms in solution per volume in the host material (tungsten) at a certain partial pressure of the surrounding gas (hydrogen). In general, this law depends on the material only and not on surface conditions. Equation 1.1 holds under equilibrium conditions. This implies that the sample has to be maintained sufficiently long at a constant temperature such that the time-dependent process of filling the bulk (the duration which depends on temperature and transport parameters) has ceased and that the net atom flux between gas phase and sample is zero on average.

The square-root dependence arises from the fact that one H_2 molecule dissociates into two atoms while it dissolves into the material. For example, for He in W the exponent is 1.

The solubility exhibits an Arrhenius-like dependence:

$$\text{S} = \text{S}_0 \exp\left(-\frac{\text{E}_\text{S}}{\text{k}_\text{B}\text{T}}\right) \tag{1.2}$$

where S_0 denotes the pre-exponential factor and E_S the heat of solution. E_S ranges from roughly -1 to $+1$ eV for metals. The algebraic sign of E_S indicates if the absorption of the gas species is exothermic or endothermic: Endothermic absorption for positive heat of solution $\text{E}_\text{S} > 0$ such as tungsten, iron, platinum, chromium or copper; exothermic absorption for negative heat of solution $\text{E}_\text{S} < 0$ such as yttrium, titanium, vanadium or tantalum [23].

The equilibrium concentration of hydrogen in tungsten can only be described by Sieverts' law at sufficiently low hydrogen partial pressure - in the range where hydrogen can be described as an ideal gas. Furthermore, the heat of solution, E_S, is independent of the solute hydrogen concentration in tungsten, because it can be assumed that the dissolved hydrogen atoms in the lattice do not influence each other and, hence, cause no additional dependence[1]. Actually, the measured hydrogen concentrations do not exceed about 10^{-4} H/W which is sufficiently low to agree with the mentioned assumption. Tungsten consists of a bcc lattice, ion-channelling experiments show that hydrogen is held in the tetrahedral interstitial sites if in solution [24].

1.1.2. Diffusion

Diffusion describes the transport process of a system that tries to equalise concentration gradients. Classical, i.e., chemical, diffusion is a process that is driven by a difference in concentration of a foreign particle species in a host material - in this case hydrogen in tungsten.

A quantitative description for the diffusive flux J $\left[\frac{\text{atoms}}{\text{m}^2\text{s}}\right]$ is given by Fick's first law (in one dimension) [25, 26, 27]:

$$\text{J} = -\text{D}\frac{\delta \text{c}}{\delta \text{x}} \tag{1.3}$$

J describes the number of particles of one species that flow through a standardised area (m^2) in x-direction per time (s). $\frac{\delta c}{\delta x}$ is the concentration gradient in the lattice. Fick's first law hence is dependent on position and time:

$$\text{J}(\text{x}, \text{t}) = -\text{D}\nabla \text{c}(\text{x}, \text{t}) \tag{1.4}$$

Here $\text{c}(\text{x}, \text{t})$ represents the local concentration of solute hydrogen. $\text{D}(\text{x}, \text{t})$ $\left[\frac{\text{m}^2}{\text{s}}\right]$ is a propor-

[1] This is shown to be the case in experimental investigations in this work, see chapter 4.2.

tional factor: the material-dependent diffusion coefficient of hydrogen in the metal. Equation 1.3 shows that the diffusion coefficient must be known for a comprehensive description of the diffusive behavior of the foreign species in the host metal. Hence, the experimental determination of the various diffusion coefficients, in that case of the various hydrogen isotopes in tungsten, is of great importance in order to predict the diffusive behavior [27].

The diffusion coefficient itself exhibits an Arrhenius-like dependence on temperature:

$$\mathrm{D} = \mathrm{D_0} \exp\left(-\frac{\mathrm{E_A}}{\mathrm{k_B T}}\right) \tag{1.5}$$

$\mathrm{D_0}\left[\frac{\mathrm{m}^2}{\mathrm{s}}\right]$ is the pre-exponential factor. $\mathrm{E_A}$[eV] is the activation energy necessary to overcome the migration barrier of the solute sites. In the classical diffusion description, $\mathrm{E_A}$ needs to be provided by the intrinsic energy of the host metal, i.e., the lattice, to jump from one interstitial site to another and is often given in electron volts.

Using the continuity equation:

$$\frac{\partial \mathrm{c}}{\partial \mathrm{t}} = -\frac{\partial \mathrm{J}}{\partial \mathrm{x}} \tag{1.6}$$

from Fick's first law (equation 1.3), for a constant diffusion coefficient for the one-dimensional case the following equation can be derived:

$$\frac{\delta \mathrm{c(x,t)}}{\delta \mathrm{t}} = \mathrm{D}\frac{\delta^2 \mathrm{c(x,t)}}{\delta \mathrm{x}^2} = \mathrm{D}\Delta \mathrm{c(x,t)} \tag{1.7}$$

This is also known as Fick's second law, the diffusion equation [25, 28]. The left side of equation 1.7 represents the change of concentration with time at a certain position.

1.2. Present data base

A series of computational approaches utilising either Density Functional Theory (DFT) or Molecular Dynamics (MD) simulations disagree with the most used diffusion coefficients experimentally derived by Frauenfelder [8]:

$$\mathrm{D} = 4.1\,^{+5}_{-2} \cdot 10^{-7}\,\frac{\mathrm{m}^2}{\mathrm{s}} \cdot \exp\left(\frac{-0.39 \pm 0.09\,\mathrm{eV}}{\mathrm{k_B\,T}}\right) \tag{1.8}$$

Figure 1.1 shows the diffusivity of Protium (H) in tungsten plotted as a function of 1/T in an Arrhenius-like plot. The measurements of Frauenfelder are plotted as red squares, the derived value for the activation barrier is 0.39 eV. Recent results from DFT simulations question this value, Heinola's result from 2010 for example yields an activation barrier of 0.21 eV [10] (or, if changing assumptions of vibrational states of the lattice: 0.25 eV [17]). If Frauenfelder's two data points for the two lowest temperatures are ignored, this would lead to a value of 0.25 eV which comes closer to the suggested values derived from DFT simulations. Measurements below roughly 1400 K are presumably influenced by trapping or surface effects - this would explain other experimental investigations for example from Zakharov [9] from 1973 which also show the trend of lower diffusivity at temperatures lower than 1400 K. The difference of Frauenfelder's measured activation energy of 0.39 eV compared with a fit that ignores the last two measurement points leads to discrepancies in diffusivity by one order of magnitude at lower temperatures.

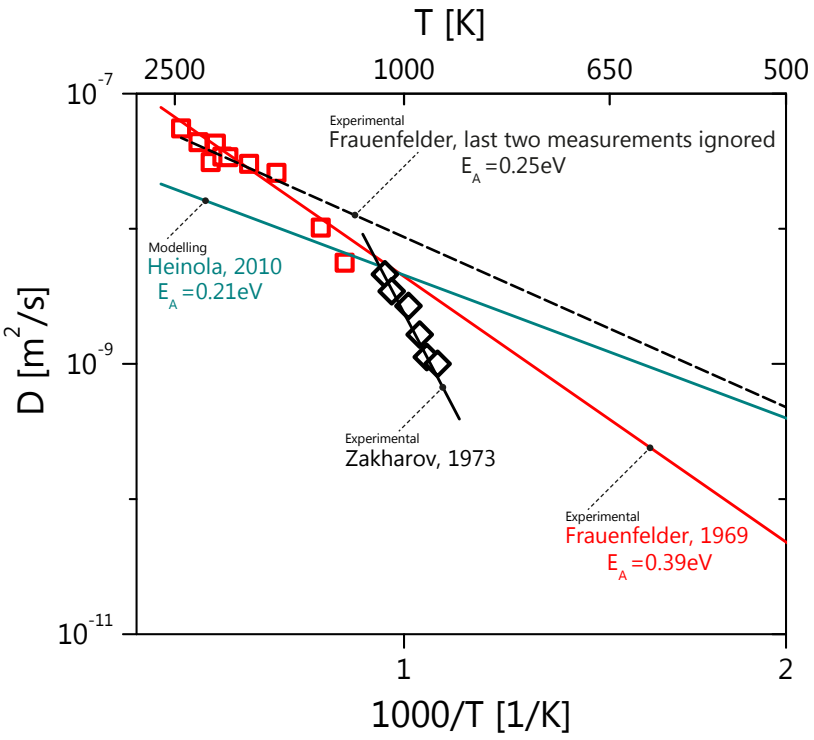

Figure 1.1.: Diffusivity of protium (H) in tungsten plotted as a function 1/T in an Arrhenius-like plot. The plot shows experimental values from Frauenfelder [8] and Zakharov [9] compared to one exemplary DFT-simulation from Heinola [10]. Ignoring Frauenfelder's last two measurements on the low temperature side, which are possibly influenced by trapping or other effects, shows better agreement of activation energies derived from DFT simulation.

The measured data suggests that the temperature of about 1400 K exhibits the threshold to distorted degassing or increased trapping.

Potential diagram of hydrogen in tungsten

Figure 1.2 shows a schematic potential diagram of protium in the tungsten lattice. As the solution of hydrogen in tungsten is endothermic, energy is needed for its uptake into the lattice. Molecular hydrogen is dissociatively adsorbed at the surface before it can penetrate into the lattice. The energy required for dissociation and uptake of hydrogen is defined by the binding energy Q_c and E_{sb}. In the present study, the tungsten samples are gas loaded in hydrogen atmosphere and heated until in thermodynamic equilibrium. The gas loading is done at constant temperature and the dwell times are extended such, that the hydrogen inventory does not rise, i.e., thermodynamic equilibrium is reached.

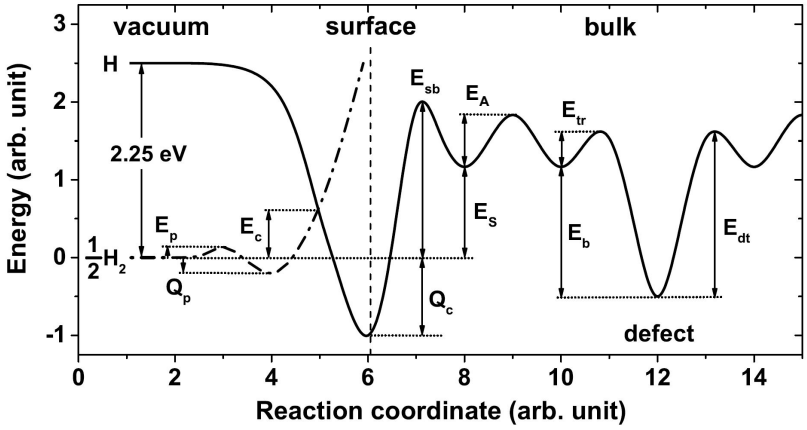

Figure 1.2.: Schematic potential diagram for protium in tungsten based on [29].

When hydrogen has entered the lattice, its migration is thermally activated. Hence, higher temperatures of the lattice lead to faster migration. When diffusing in the solute, i.e., migrating from one interstitial site to another, the activation barrier E_A needs to be overcome. Hydrogen can be trapped in defects, such as vacancies, dislocations, impurities or grain boundaries, which can significantly decelerate migration compared to solute diffusion. If the temperature is high enough, the energy provided from the lattice enables the migrating hydrogen to almost instantly being detrapped from such a defect with detrapping energy E_{dt}. At higher temperatures more and more atoms overcome the activation energy for the solute E_S, hence more interstitial sites can be occupied. This is when the migration is no longer dominated by traps but by the interstitial sites in the lattice. Such a transition to a solute diffusion dominated migration regime is believed to occur at around 1400 K, which could be represented by the kink in diffusivities in figure 1.1. As hydrogen reaches the surface, it is being adsorbed at the surface and being degassed by recombining with another hydrogen atom. Recombination of hydrogen is assumed to be not the rate-determining step for degassing of hydrogen.

1.3. How Frauenfelder analysed his measurements

The degassing from the cylindrical tungsten sample is done at one fixed temperature in order to derive the the diffusivity for that specific temperature. From these measured diffusivities at various temperatures the parameters of the diffusion coefficients, E_A and D_0, are derived by fitting.

Frauenfelder [8] measured the partial pressure p of H_2 while degassing a sample of volume V, R is the pumping speed at constant temperature:

$$pR = -V\frac{dc}{dt} \quad ;(\text{Temperature} = \text{const.}) \tag{1.9}$$

At a given, constant temperature, the partial H_2 pressure p[bar] times pumping speed R[$\frac{m^3}{s}$] exhibits a flow. Partial pressure multiplied with pumping speed (pR, the left side of equation 1.9) gives a flux of particles: $\left[\frac{\text{bar}\cdot\text{m}^3}{\text{s}}\right] = \left[\frac{\text{particles}}{\text{s}}\right] = J$.

The measured flux J $\left[\frac{\text{particles}}{\text{s}}\right]$ equals the change of concentration in the sample, i.e., the number of atoms that are degassed from the sample per time.

By reformulating Fick's second law (see equation 1.7), one gets:

$$\nabla^2 c - \frac{1}{D}\frac{\partial c}{\partial t} = 0 \tag{1.10}$$

The sample of Frauenfelder had the shape of a cylinder with length $\gg$ radius. This allows to ignore the change of concentration in longitudinal direction, hence equation 1.10 can be described in cylindrical coordinates only depending on the radial direction:

$$\frac{\partial c(r,t)}{\partial t} - D\left(\frac{\partial^2 c}{\partial r^2} + \frac{1}{r}\frac{\partial c}{\partial r}\right) \tag{1.11}$$

Exploiting the cylindrical geometry of the sample and after averaging over the radius the solution of the diffusion equation can be written as [30]:

$$c = c(t) = c_e \sum_{\nu=1}^{\infty}\left(\frac{4}{\xi_\nu^2}\right)\exp\left(-\frac{4\xi_\nu^2}{d^2}Dt\right) \tag{1.12}$$

Here d is the sample diameter, D is the diffusion coefficient and ξ_ν are the roots of Bessel functions of order zero. The first roots of Bessel functions are [30]:

$$\xi_1 = 2.4048;\ \xi_2 = 5.5201;\ \xi_3 = 8.6537 \tag{1.13}$$

For times $t > d^2/100D$ only the first term needs to be considered since the series is rapidly decaying [30]:

$$c = c_e\frac{4}{\xi_1^2}\exp\left(-\frac{4\xi_1^2}{d^2}Dt\right) \tag{1.14}$$

From equation 1.13 the time-derivative of the concentration is given as:

$$\frac{dc}{dt} = c_e\left(\frac{4}{\xi_1^2}\right)\cdot\left(-\frac{4\xi_1^2}{d^2}D\right)\exp\left(-\frac{4\xi_1^2}{d^2}Dt\right) \tag{1.15}$$

$$\frac{dc}{dt} = c_e \left(-\frac{16}{d^2}D\right) \exp\left(-\frac{4\xi_1^2}{d^2}Dt\right) \tag{1.16}$$

Recalling equation 1.9 $\left(pR = -V\frac{dc}{dt}\right)$ yields at T = constant:

$$pR = -V \cdot c_e \left(-\frac{16}{d^2}D\right) \exp\left(-\frac{4\xi_1^2}{d^2}Dt\right) \tag{1.17}$$

Replacing c_e by Sieverts' law $\left(c_e = Sp_e^{\frac{1}{2}}\right)$ yields:

$$pR = \frac{16VSp_e^{\frac{1}{2}}}{d^2}D \cdot \exp\left(-\frac{4\xi_1^2}{d^2}Dt\right) \tag{1.18}$$

Plotting equation 1.18 in an Arrhenius like plot, i.e., logarithmic scale, allows to determine the diffusivity from the slope of the measured particle fluxes for different degassing temperatures:

$$\log(pR) \propto -\frac{4\xi_1^2}{d^2}Dt \quad ;(\text{Temperature} = \text{const.}) \tag{1.19}$$

Frauenfelder derived the solubility from the total amount of hydrogen that is measured while degassing and the known volume (and density) of the sample. He assumed that the loss of hydrogen is negligible during the cool-down phase of gas loading.

1.4. Diffusion model

In the following the diffusion model of this thesis is outlined. The mathematical description of hydrogen in a cylindrical specimen is based on the diffusion-dependent concentration profile. In the conducted experiments two geometries are used: a "big" specimen with ∅30 mm, length of 54 mm and "small" specimens with ∅15 mm, length of 48 mm.

The geometry of the small specimens (length ≫ radius) allows the same reduction of the model, as used by Frauenfelder as described before in chapter 1.3. This analysis requires less computational effort and is denominated as reduced diffusion model. The geometry of the big specimen does not allow the same reduction to a 1d-model as the small specimens and requires a full-3-dimensional approach, see the following chapter 1.4.1. The descriptor function is found in equation 1.25. This model is denominated as full diffusion model. Two small specimens were used in experiments: a poly- and a single-crystalline sample. This allows: Firstly, to check if the variation of the tungsten grade has an influence on the measured diffusion coefficients. Secondly, to verify if the method of decay fitting of degassing is applicable and yields the same results as a full diffusion model. The big specimen is of poly-crystalline grade. It is used to analyse diffusivity and also solubility by means of the full diffusion model and to compare the results from the reduced diffusion model (decay fitting) on the small specimens.

In the following parts are taken from a publication within the frame of this Ph.D. project and is to be found in [4]. The model was developed by Udo von Toussaint.

1.4.1. Diffusion

Our modelling of H/D diffusion in tungsten is based on the diffusion equation in 3-D cylindrical geometry under the assumption of an initially constant hydrogen isotope concentration in the cylinder after gas loading when the hydrogen concentration in the specimen reached equilibrium. This equilibrated H concentration describes the state of the sample before the cool-down phase (phase 2 at almost 2000 s in figure 2.3). We assume diffusion limited degassing [31], i.e., that the surface concentration is zero during hydrogen release, thus yielding Dirichlet boundary conditions. In full generality, a coupled system of equations for the temperature field in the cylinder $T(\vec{r},t)$ and the concentration profile $c(\vec{r},D(T(\vec{r},t)),t)$ needs to be solved, since the diffusion depends on temperature. However, due to the high thermal conductivity of tungsten (increasing from 126 W/(K·m) above 2300 K [32] to 174 W/(K·m) [33] at room temperature) and the moderate upper limit of the cooling rates of the cylinder (at most 35 K/s, see fig. 2.3) the temperature profile in the cylinder is almost flat. Also the reduction of the thermal conductivity by the applied magnetic field is negligible at temperatures above room temperature [33]. Simulations show that the largest temperature differences in a loading-degassing cycle between the peak temperature in the core of the cylinder and at the outer radius are of $O(1\mathrm{K})$ for a cylinder loaded at 2000 K. In the following we thus use a time-dependent but spatially constant temperature profile $T = T(t)$, where the time-dependent temperature values are taken from the thermocouple measurements.

The cylindrical coordinate system allows to express the time-dependent concentration $c(r,z)$ of hydrogen in a cylinder with radius $a\,(r:0\leq r<a)$ and length $2L\,(z:-L<z<L)$ as product of one-dimensional functions in each coordinate (see, e.g., [34], chapter 8.4, Eq.5)

$$c(r,z\mid t,a,L)=c_0\psi(z\mid t,L)\,\chi(r\mid t,a) \tag{1.20}$$

where $\psi(z)$ expresses the hydrogen concentration along the cylinder axis, whereas $\chi(r)$ expresses it in radial direction.

For diffusion-limited boundary conditions $\psi(z)$ and $\chi(r)$ are given by

$$\psi(z\mid t,L)=\frac{4}{\pi}\sum_{n=0}^{\infty}\frac{(-1)^n}{(2n+1)}\exp\left[-(2n+1)^2\frac{\pi^2}{4L^2}D(T)\,t\right]\cos\left(\frac{(2n+1)\,\pi z}{2L}\right) \tag{1.21}$$

and

$$\chi(r\mid t,a)=\frac{2}{a}\sum_{m=1}^{\infty}\exp\left[-\alpha_m^2D(T)\,t\right]\frac{J_0(r\alpha_m)}{\alpha_mJ_1(a\alpha_m)}. \tag{1.22}$$

In the two previous equations $D(T)$ denotes the hydrogen isotope diffusion and $J_0(x)$ is the Bessel function of order zero of the first kind. Similarly $J_1(x)$ is the Bessel function of the first kind of order one. The parameters α_m are the consecutive positive roots of $J_0(\alpha_m a)=0$, ie. $\alpha_1=(\xi_1/a),\alpha_2=(\xi_2/a),\ldots$ with $\xi_1\approx 2.4048$, $\xi_2\approx 5.5201,\ldots$.

The expression can be reduced by using the recurrence property of the Bessel functions

$$\int_0^a \mathrm{d}r\,r^{n+1}J_n(\beta r)=\frac{1}{\beta}a^{n+1}J_{n+1}(a\beta),\ n>-1 \tag{1.23}$$

to average over the radius to get

$$\langle \chi(r \mid t,a)\rangle = \frac{1}{\pi a^2}\int_0^a \mathrm{d}r\, 2\pi r\, \chi(r \mid t,a) = \frac{4}{a^2}\sum_{m=1}^{\infty}\frac{1}{\alpha_m^2}\exp\left(-\alpha_m^2 D(T)\, t\right). \tag{1.24}$$

The total amount of hydrogen as function of time for constant temperature can be calculated by inserting equation 1.24 in equation 1.20, followed by integration over the cylinder length

$$\begin{aligned}\mathrm{M}(t) =& c_0 \int_{-L}^{L} \mathrm{d}z\, \pi a^2 \langle \chi(r \mid t,a)\rangle\, \psi(z \mid t,L) \qquad (1.25)\\ =& c_0 \frac{64\mathrm{L}}{\pi}\left(\sum_{m=1}^{\infty}\frac{1}{\alpha_m^2}\exp\left(-\alpha_m^2 D(T)\, t\right)\right)\left(\sum_{n=0}^{\infty}\frac{1}{(2n+1)}\exp\left[-(2n+1)^2\frac{\pi^2}{4L^2}D(T)\, t\right]\right).\end{aligned}$$

The displayed mathematical description of the hydrogen amount in equation 1.25 is the fundament for both specimen-sizes: in a reduced form for the small specimens (and which is described in the following chapter 1.4.2) and in its full-3-dimensional form for the big specimen as shown in equation 1.25.

For the numerical modelling the previous equations are discretised in time to take into account the varying temperature. The time-step is chosen such that the temperature change within 1 time-step is always smaller than 0.01 Kelvin and otherwise a time-step of 1 s is used. Tests with even smaller time-steps did not show any impact on the results.

1.4.2. Reduced diffusion model: fitting degassing gradient

In the limit of long times $\left(t > a^2/(100 \cdot D(T))\right)$ and for the present dimensions of the small specimens the term $\langle \chi(r \mid t,a)\rangle$ for the radial concentration in equation 1.25 dominates the decay of $\mathrm{M}(t)$. During the degassing the radial concentration profile turns from a concentration profile with higher order contributions of the Bessel functions ($m > 1$), i.e., with sharp features at the sample boundaries into a smooth concentration profile (with only the $m = 1$ term - the fundamental mode - being relevant). The degassing data of the experiments reported here support this assumption, i.e., at constant temperature the degassing signal display for longer times a single-exponential decay.

The leading degassing term (i.e., the time derivative of Eq. 1.25) for long times and constant temperature is thus given by

$$\dot{M}(t) \propto \exp(-\gamma t) \propto c_0 \exp\left(-\alpha_1^2 D(T)\, t\right) = c_0 \exp\left(-4\xi_1^2 D(T)\, t/d^2\right), \tag{1.26}$$

where the last expression has been written such that it corresponds with the equation used by Frauenfelder (cf. [8], Eq. 4), see chapter 1.3, equation 1.15. For the subsequent analysis an Arrhenius-like dependence of the pre-exponential factor on the temperature is assumed, according to the diffusion equation 1.5 with activation energy E_A for the diffusion and a pre-factor D_0.

The degassing exhibits initially a faster signal decay (i.e., exhibit an "overshoot", see figure 2.3 at the end of the temperature ramp at the degassing sequence) once the temperatures have reached their plateau values compared with the single-exponential decay later on. This is due to the presence of higher order terms ($n > 0, m > 1$) contributing to the concentration profile. However, these contributions decay faster with time than the fundamental mode ($m = 1$), cf.

Eqs. 1.21 and 1.22, and do not affect the decay at later times.

1.4.3. Cooling cycle

Because the samples unavoidably loose hydrogen in the cooling phase after gas loading the total hydrogen content in the sample is a priori not known. The modelling approach as shown in section 1.4.1 was used to calculate the loss during the cool-down phase until the start of the degassing cycle. After sufficiently long loading time, see chapter 4.2, the initial concentration profile is almost constant throughout the cylinder and can be assumed to be in thermodynamic equilibrium, i.e., the concentration of dissolved hydrogen is a function of the sample temperature and hydrogen gas pressure only. The moment the heating is stopped the cylinder cools down. Initially the heat loss is dominated by radiation losses, at later stages by convective losses to the surrounding hydrogen gas. In Figure 1.3 calculated time traces of

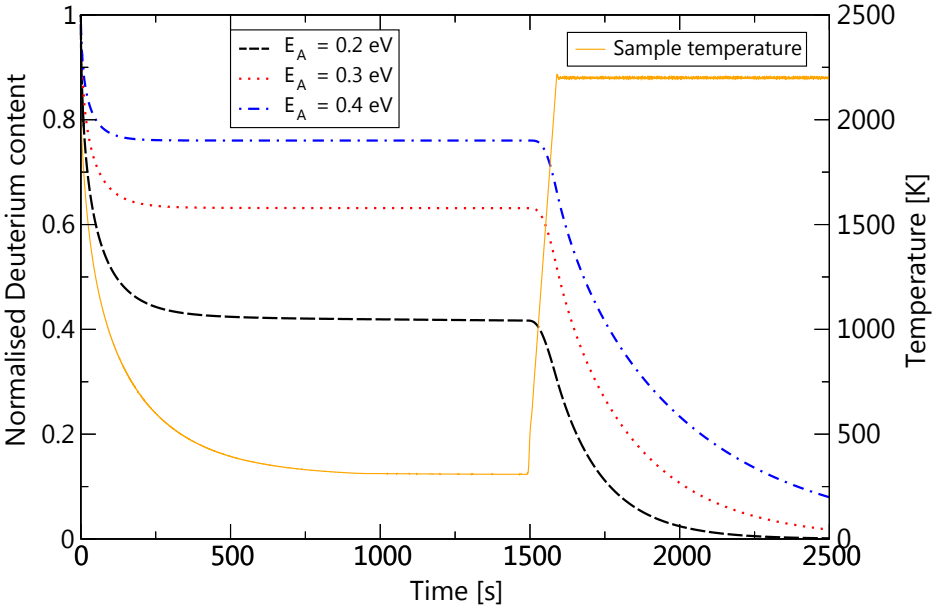

Figure 1.3.: The amount of hydrogen retained in the small tungsten specimen while the cool-down phase at the end of the gas loading sequence. The higher the activation energy is expected, the lower the loss of deuterium is during cool-down.

the cylinder temperature and the corresponding retained amount of hydrogen (normalised to the initial amount) are displayed for three different diffusion activation energies. The loading temperature was 2200 K at 500 mbar pressure.

The amount of deuterium retained in the small tungsten cylinder (dimensions: ∅15 mm; length: 48 mm) calculated as function of time for three different diffusion activation energies of 0.2 eV, 0.3 eV and 0.4 eV and a common pre-factor of $4.1{\cdot}10^{-7}\mathrm{m}^2/\mathrm{s}$ (the pre-exponential factor measured by Frauenfelder) is shown. The measured sample temperature during the cool-down is indicated on the right hand-side. The largest loss during the cooling of the sample in hydrogen atmosphere occurs immediately after switching off the heating. The retained amounts after the sample has reached room temperature are roughly 78%, 65% and 45% for assumed diffusion activation energies of 0.4 eV, 0.3 eV and 0.2 eV, respectively.

Initially the hydrogen loss is fast due to the high diffusivity at temperatures well above 750 K and the hydrogen depletion dominantly from the outer parts of the cylinder. At later times when the concentration goes towards zero, the hydrogen loss is significantly lower because close to the cylinder surfaces the hydrogen concentration is almost zero, hence here also the gradient of hydrogen concentration is very small. In addition, the hydrogen transport is slowed down by the decreasing temperature and becomes negligible below 450 K. Experiments show that the loss from the specimen at room temperature is not measurable within the uncertainty limits for equally executed experiments where only the dwell time (i.e., pumping time) after loading was varied from about 15 min to one week.

The hydrogen concentration becomes non-uniform during the cooling. The normalised initial hydrogen concentration profile of the cylinder as well as the profiles immediately before the degassing sequence (t= 1500 s) along the radial and vertical directions are presented in figure 1.4. The pre-factor is set to the Frauenfelder values of $4.1{\cdot}10^{-7}\mathrm{m}^2/\mathrm{s}$ and an activation energy of 0.41 eV. The left panel shows the longitudinal concentration profile of the specimen after loading and cool down.

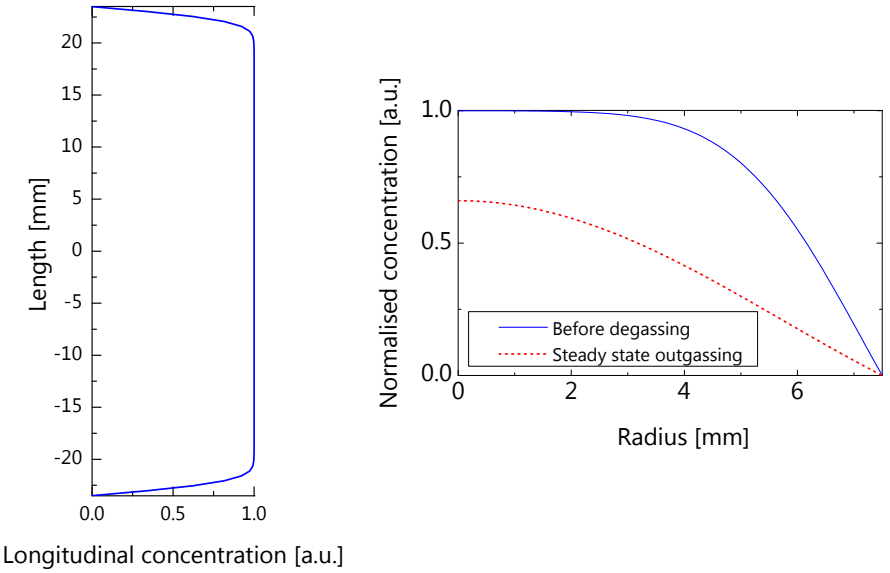

Figure 1.4.: Left panel: Longitudinal concentration profile of the specimen at radius r = 0 after gas loading and cool down. Right panel: Radial concentration after cool-down is shown as solid line - the dotted line exemplarily shows the hydrogen concentration profile at steady state degassing conditions in the sample when the temperature is already constant and the decay is single-exponential.

The radial concentration is shown on the right-hand side panel where the solid line shows the concentration profile after cool down and before degassing. The dotted line exemplarily shows the hydrogen concentration profile at steady state degassing conditions in the sample when the temperature already has reached the constant plateau. The concentration profile during the degassing proceeds from the non-sinusoidal profile (i.e., higher harmonics in the Bessel function, $m > 1$, see equation 1.5) before degassing towards a smooth profile where the fundamental mode dominates - this can also be seen in the degassing signal when an (non-single-exponential) “overshoot” appears and then decays towards a single-exponential

decay (visible as linear decay in the log-plot), see for example figure 2.3 at t $\simeq$ 3500 s when temperature just reached its plateau. From the difference in the shapes the presence of higher order terms ($m > 1$) at the onset of the degassing-sequence can be concluded.

2. Experimental Methods

Everything went great right up to the explosion.

(Marc Watney in: The Martian from Andy Weir)

This chapter covers the design and assembly (the commissioning is described in chapter 3) of a new gas loading apparatus which is named "Radiofrequency Oven for Solubility Test" (ROST), to analyse diffusivity and solubility in tungsten. At first, the experimental arrangement is described, followed by the experimental procedure. Then the specimens are described, including the intention behind their geometry and the chosen grade/microstructure. Then follows the description of the heating method, temperature measurements, the design of the quartz glass tube which houses the specimen(s), the mounting of the specimen(s) and the safety measures that also cover measures which arise from the handling of hydrogen. The chapter closes with the description of the quadrupole mass spectrometer (QMS) which is used for measuring the released hydrogen.

2.1. Experimental set-up

Figure 2.1 shows an image of the experimental set-up and figure 2.2 a sketch of the gas loading device ROST. On the right hand side of figure 2.1 ROST can be seen. The middle and left of the picture shows the ultra-high vacuum (UHV) device TESS, the Thermal Effusion Spectroscopy System, which is connected to ROST via a UHV steel pipe. The vacuum of ROST can be disconnected from the vacuum system of TESS by a full-metal valve. The Quadrupole Mass Spectrometer (QMS) used to measure the released gases is located in the TESS device. The 'blue box' on the left hand side of the picture is the tubular furnace used for thermal desorption measurements in TESS. This oven is not used for the experiments reported here. A detailed description of TESS can be found in [35].

The vacuum system of ROST is mounted in the bottom part. The heart of ROST, the quartz glass tube and the inductive heater is in the image hidden behind the steel panels. These steel panels serve as protection and as a shield for the RF radiation during inductive heating. A circular opening in the lower third of the steel panel allows to see the specimen during heating. In the actually shown image (Figure 2.1) the specimen is heated to about 2000 K and is the source of the visible light. In the upper part of ROST a buffer vessel (black barrel) for the vacuum system is mounted. The function of this buffer vessel is described further below. On the upper left part of ROST the rectangular tubes of the gas ventilation system, which is used to remove hydrogen in case of leaks, is visible.

A schematic representation of the main components of ROST is presented in figure 2.2. The blue-coloured part in figure 2.2 displays the double-walled quartz glass vacuum tube. Inside this quartz tube the tungsten specimen is mounted. The specimen hangs on a tungsten shaft that is connected to the top flange at the upper end of the quartz glass tube.

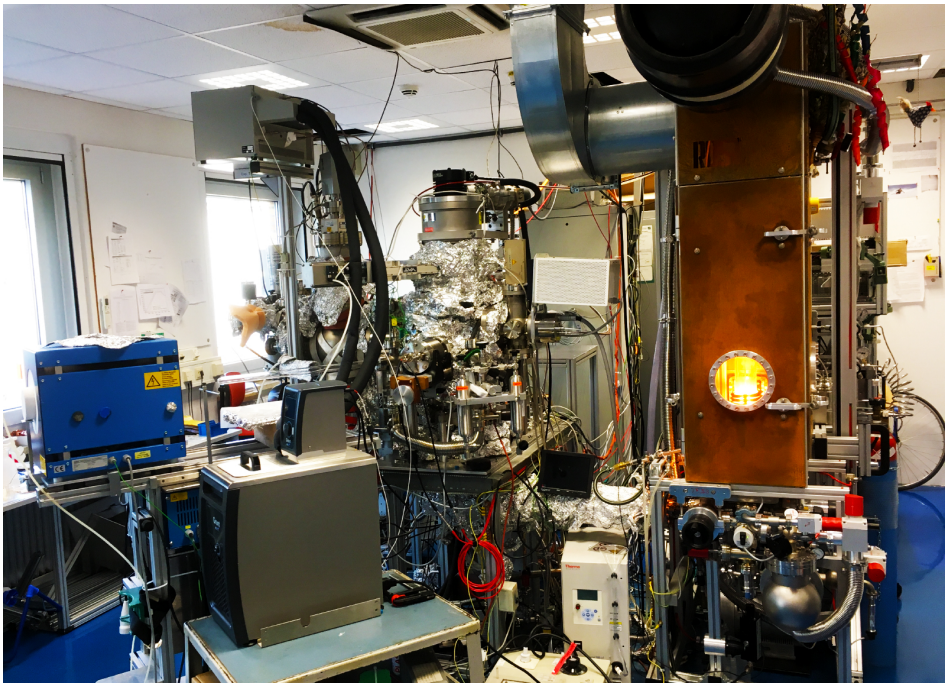

Figure 2.1.: Experimental arrangement: on the right side the gas loading apparatus "ROST" is shown. A connection to thermal effusion spectroscopy setup TESS (left side) is established to use its QMS for degassing measurements.

Because of the two geometries of the specimens, two different quartz glass tubes of different sizes are used. A smaller one with a CF-16 flange on top for the small specimens, and a bigger one with a CF-40 flange on top for the big specimen. The outer diameter of the outer glass tube is $\varnothing_o = 48\,\mathrm{mm}$ for the small quartz glass tube and $\varnothing_o = 70\,\mathrm{mm}$ for the big one. The technical drawings of those two quartz glass tubes can be found in appendix A.2. They qualitatively look the same, i.e., exhibit the same features, and can be described as functionally equal in figure 2.2.

A steel flange mounted on top of the glass tube holds the shaft for specimen mounting and a thermocouple feed-through for temperature measurement. An UHV compatible quartz-glass - steel adapter flange connects the quartz glass tube with an UHV steel flange. A copper induction coil is placed around the glass tube with which the specimen is inductively heated. 40 kW nominal output power allows fast ramps and, in principle, temperatures up to the melting temperature of the tungsten specimens.

The vacuum pump system of ROST consists of a turbo pump and a scroll pump, including a buffer vessel and inertisation system for hydrogen pumping. The gas supply system includes gas feed lines with flow controllers which are used to fill the main vacuum vessel with hydrogen for gas loading. The gas feed line also includes a liquid nitrogen (LN) trap, through which the piping is led to purify the hydrogen. The glass tube is double-walled at the middle part for efficient cooling by sending water through an in- and outlet at the glass tube towards a heat exchanger. The water cooling effectively decreases the temperature of the inner glass wall of the quartz glass tube, such that the influence of outgassing from the inner wall during measurement is kept to a minimum. The quartz glass tube is mounted via another quartz-glass - steel adapter flange at the lower end to the vacuum system. The vacuum system comprises a

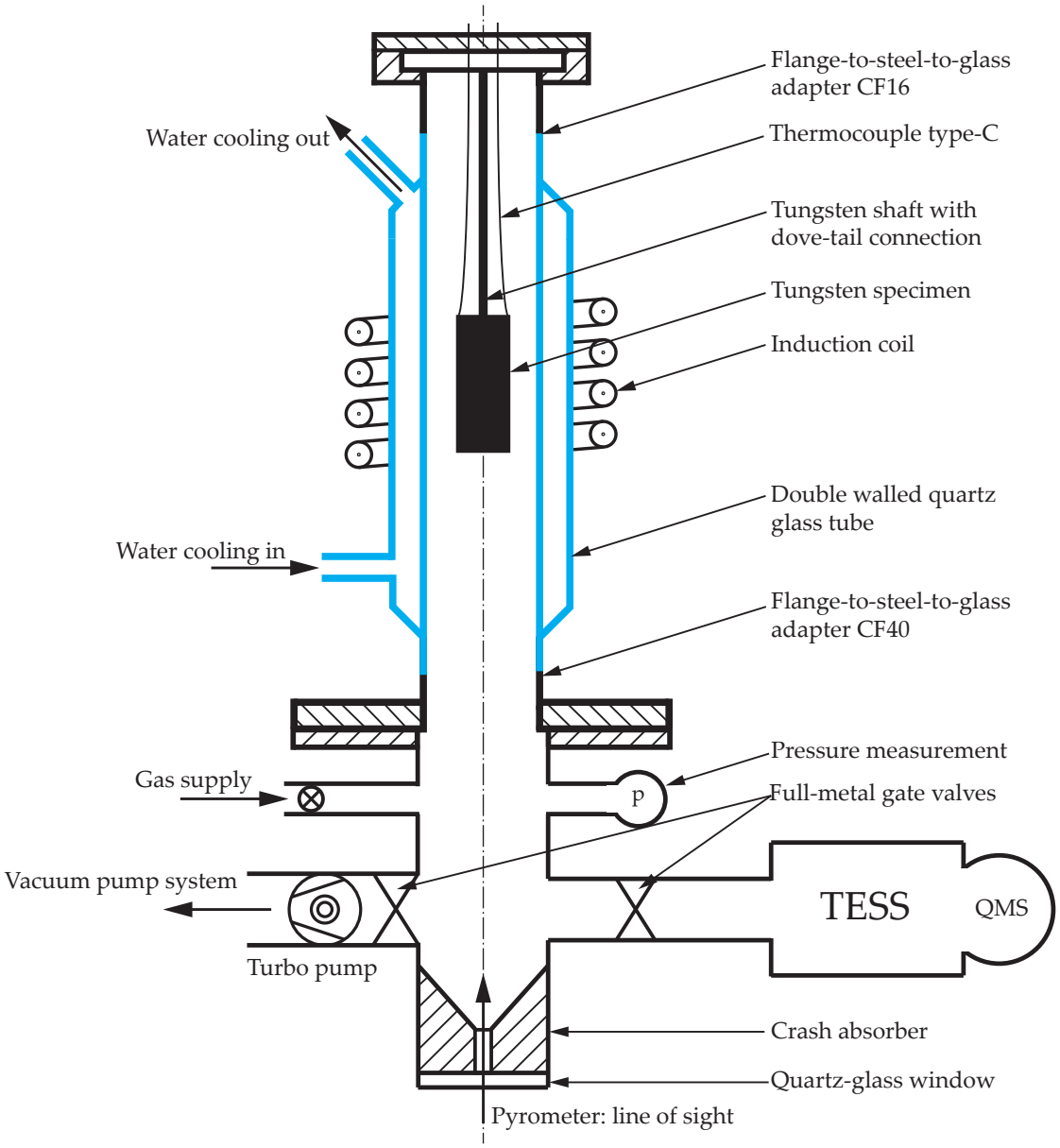

Figure 2.2.: Sketch showing the different parts of the experimental set-up. The specimen is placed in a quartz glass tube, which is surrounded by an induction coil for heating. The double-walled glass tube allows water cooling, to keep temperatures at the inner walls low. The main vacuum vessel is placed underneath the glass tube. This is where the gas is supplied. The vessel is connected to the Thermal Effusion Spectroscopy Setup (TESS), which houses the quadrupole mass spectrometer (QMS) by an UHV steel pipe (the connection to TESS is shown only very schematically). A pyrometer delivers a second temperature measurement at $T > 1273$ K. Full-metal gate valves are installed to separate the main vacuum vessel from the QMS and the turbo pump for pressurising the vessel up to 500 mbar during to gas loading.

port for gas supply. When the specimen is gas loaded, the main vacuum vessel is disconnected from the turbo pump and from TESS with full-metal gate valves. Full-metal valves are required because vacuum valves which use synthetic elastomers at the sealing surfaces cannot be used in these experiments. Elastomers usually absorb significant amounts of hydrogen and would release it on time scales of weeks into the vacuum chamber when being in UHV conditions. This would cause an unacceptably large hydrogen background in the following hydrogen release measurements.

To measure the pressure a capacitance gauge (1 - 1100 mbar) and an ionisation gauge ($5 \cdot 10^{-9} - 1$ mbar) are installed in the main vacuum chamber of ROST. Finally, at the bottom of the main vacuum chamber a quartz-glass window from Vacom is mounted. Through this window the temperature of the tungsten specimen can be measured in direct line of sight with a pyrometer (Sensortherm, Metis M313). Such temperature measurement is not possible from the top due to space reasons and from the sides due to absorption by the cooling water. The window at the bottom is secured by a crash absorber to protect it from a falling down specimen in case the mounting fails.

2.2. Experimental procedure

In the following the experimental procedure is described, which is basically identical for all three used specimens. A specimen is first loaded with hydrogen at a given temperature, then the specimen is cooled down and the hydrogen is pumped away. When the hydrogen background is low enough the specimen is again heated to a predifined temperature and the released hydrogen gas is quantitatively measured.

Figure 2.3 shows a typical measurement cycle on one of the small specimens. The left y-axis shows the temperature of the specimen (blue, solid line). The right y-axis shows the released amount of hydrogen in atoms/s.

Prior to starting the experiment the main vacuum vessel is evacuated down to at least $5 \cdot 10^{-8}$ mbar. Then the pumping is stopped and the turbo pump is disconnected from the main vacuum vessel. Afterwards the main vacuum vessel is filled with gas using the LN trap to purify the hydrogen. The temperature of the gas is hereby cooled down to 77 K and causes impurities such as H_2O or CO_2 to freeze onto the inner wall of the gas feed line. The applied filling pressures range from 6 to 500 mbar. The following gas loading sequence is the first part of the measurement cycle. First, the temperature of the specimen is at room temperature. Then it is heated to the desired loading temperature, in this case 2000 K. At this temperature hydrogen dissolves in the bulk of the specimen. The specimen is held at this temperature until thermodynamic equilibrium is reached ("dwell time", which in this case is derived to be 30 min, see chapter 4.2.1). Then the heating is switched off, the sample is cooling down. The cool down rate from 2000 K is initially dominated by radiative cooling and about 35 K/s. Later the cooling is no longer radiative but gas cooling/convection dominated and the cool down rates become smaller.

The cool down rate is sufficiently fast to trap a significant amount of the hydrogen initially dissolved in the sample. Nevertheless, some of the dissolved hydrogen is able to escape the specimen during cool down which results in a decay of hydrogen concentration to a lower level than the one previously reached at equilibrium for the loading temperature, see chapter 1.4.3.

This undesired outgassing cannot be measured because the QMS in the neighbouring TESS chamber can only be operated for pressures lower than $5 \cdot 10^{-6}$ mbar. When the specimen has

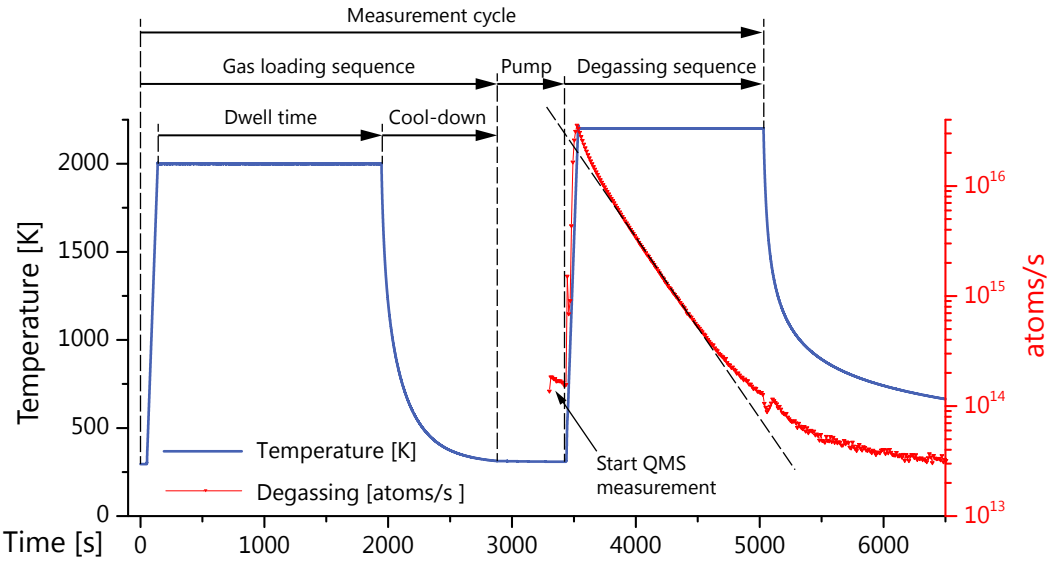

Figure 2.3.: Measurement principle and denotations. Every measurement cycle consists of a gas loading sequence, where the sample is gas loaded with hydrogen at the loading temperature, followed by a cool-down and the pumping of the vessel. Then the sample is heated to a predefined temperature and the released hydrogen is quantitatively measured. The dashed line fitted to the hydrogen release signal indicates the 'single-exponential decay phase' (for details see text).

reached 373 K (100 °C) the vessel is pumped to about $1 \cdot 10^{-7}$ mbar, this marks the pumping phase. The pumping takes about 15 minutes. Then the valve to the TESS chamber is opened.

The measured hydrogen signal is shown as red line. The corresponding axis is on the right-hand side (logarithmic scale). At roughly 3250 s, the QMS measurement starts and the decay of the background can be seen. The degassing sequence starts when the temperature is ramped up. Ramping rates usually vary between 5 and 20 K/s. The specimen temperature is ramped up to a constant temperature and the hydrogen in the specimen is mobilised and released. During the temperature ramp-up phase the hydrogen signal exhibits a small pre-peak before it finally rises to its main peak. This can be seen in most of the measurements. After the temperature has reached a constant level the hydrogen atom flux decays as a consequence of the reduction of the hydrogen concentration gradient at the surface. At the beginning of the decay the degassing signal shows an initially faster decay, i.e., a non-single-exponential decay compared with the single-exponential decay later on (which appears linear in the logarithmic scaling and is indicated in figure 2.3 by the dashed black line fitted to the hydrogen degassing signal). This initially faster decay is due to the higher order terms of the Bessel function ($n > 0, m > 1$) contributing to the concentration profile (see chapter 1.4.2 and chapter 1.4.3, figure 1.4). The constant decay (single-exponential decay) is observed until it gets influenced by the background towards the end of the degassing sequence. The heating is shut off at roughly 5000 s. Shortly after heating shut-off, a dip with a subsequent rise before the overall signal decay is observed - this dip can be seen consistently after every measurement at degassing temperatures equal to or higher than 1600 K. This could stem from a temporary getter process of the specimen itself and is further discussed in chapter 3.1.3.2. [4]

The QMS signal (counts per second) is converted to an atom flux by using a calibrated gas

leak bottle at the end of every measurement.

The inventory is defined as the amount of atoms, released from the sample which are measured during the degassing sequence, i.e., from the moment when temperature is ramped up until the heating is switched off at the end of the degassing sequence. For this time frame the calibrated mass 4 signal for deuterium or the calibrated mass 2 signal for protium is integrated. Additionally the mass 3 signals are attributed to HD molecules and are added to the inventory. At the end, the integrated background (experimentally estimated for protium and deuterium, see chapter 3.1.3) is subtracted.

2.3. Specimens: size, kind and high temperature treatment

In principle, any shape for a specimen would be good for gas loading experiments that has a favourable volume to surface ratio. Because of the chosen heating method of inductive heating (see chapter 2.5.1), an axially symmetric shape is most favourable.

Three different tungsten specimens are used - a set of two small specimens (a poly- and a single-crystalline sample) with 15 mm diameter (⌀) and a length of 48 mm. The big specimen (a poly-crystalline sample) with ⌀ 30 mm and a length of 54 mm.

The small samples are chosen mainly because of the following two reasons: Firstly, the comparison of a single- and a poly-crystalline tungsten sample with the same geometry. The single-crystalline sample could be delivered up to a diameter of 15 mm, hence, this was also chosen for the diameter of the poly-crystalline sample. Secondly, those samples shall be assessed by the reduced diffusion model for which decay fitting is sufficient to derive the diffusion coefficients. Hence, the length to radius ratio of $length \gg radius$ needs to be fulfilled so that the change of concentration in the longitudinal direction can be neglected (which is the case for the chosen values).

The big sample is evaluated by a full diffusion model code that is developed for this study - which takes the full diffusion model into account, i.e., the concentration in dependence of location and time in all dimensions. Hence, the prerequisite of $length \gg radius$ does not need to be applied for the big specimen. If the same length-to-radius ratio should have been applied also to the big specimen, it would have had to be at least 96 mm long. Such a big specimen would exhibit a high safety concern, because the quartz glass tube vessel would need to be much larger, during leads to higher volumes of hydrogen while gas loading. Also another version of the mounting shaft would had been necessary, being able to bear the higher weight. Also the inductive heating would not be possible over the whole length of the sample, leading to non-negligible temperature gradients in the sample. For these reasons and because the full diffusion model is available, the length of the big specimen is chosen such that it is still easy to handle, i.e., so that the amount of hydrogen can still be manageable, the same mounting shaft can be used as for the small specimens, and that the inductive coil fully encloses the cylindrical sample.
The evaluations of the small samples by the reduced diffusion model code offers the opportunity, to compare the results, firstly, with the full diffusion model, and secondly, with the Frauenfelder values for protium diffusivity. The big specimen yields a more favourable signal-to-noise ratio, longer fitting times at constant decay, and a lower fraction of degassed hydrogen during the cool-down phase at gas loading (compared with the small samples). This offers the additional opportunity to quantify the solubility.

On all specimens the dove-tail groove for mounting is cut on one of the end caps of the

cylindrical samples by electric-discharge machining, see chapter 2.5.6. This leaves a residue of copper and zinc on the surface, therefore the specimens are all treated in 20% nitric acid HNO_3 to remove this residue. Afterwards the samples, apart from the small poly-crystalline sample, are electro-polished before being high temperature conditioned, see chapter 4.1.

2.3.1. Small specimens: ∅ 15 mm poly- and single crystalline

Both small specimens are firstly described concerning their as-received conditions and in the following concerning their conditions after the measurement campaign.

After they had undergone the measurement campaign, a microstructural investigation is undertaken with the two small (∅15 mm) samples. They are grinded and polished perpendicular to their rotational axis. Then they are investigated in a Scanning Electron Microscope (SEM) and by Electron Backscatter Diffraction (EBSD). The poly-crystalline sample was cut from a longer bar that was delivered from the manufacturer. For this specimen also cross-sections of the material before it underwent the experimental cycles were investigated. This is not the case for the single-crystalline sample because there was only a single sample with a restricted length delivered and, therefore, not cut for microstructural investigations prior to its experimental campaign.

2.3.1.1. Single-crystalline sample

Conditions as-received

The tungsten single-crystalline sample is delivered from MaTecK GmbH. The manufacturer states a 110 orientation perpendicular to the rotational axis with an accuracy better than 2°. Concerning impurities the manufacturer states the amounts of foreign elements as follows: C $<$ 3 ppm, H $<$ 1 ppm, O = 9 ppm, N $<$ 5 ppm, Cu = 1.6 ppm, Fe = 1.8 ppm, Ni $<$ 1 ppm, Pb = 0.3 ppm, Si = 0.3 ppm and Ga, Hf and Ta are below the detection limit. It came unpolished with a length of about 51 mm and a varying diameter of roughly ∅ 16±0.2 mm.

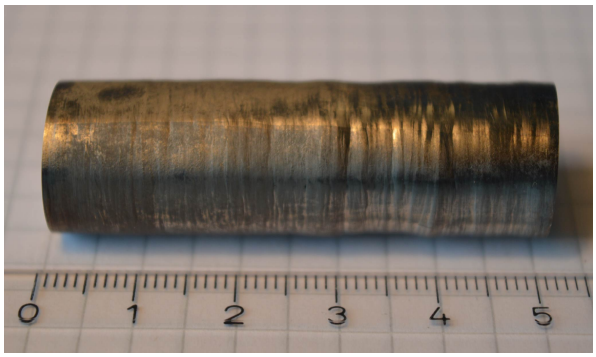

Figure 2.4.: As-received condition of the single-crystalline sample. The corrugations of distorted <110> planes that are perpendicular to the end-caps of the cylindrical sample can be seen.

The single-crystalline sample is shown in the as-received state in figure 2.4. The sides of the cylindrical sample show corrugations from light distortion of the <110> planes that grew while drawing the single-crystalline sample out of liquid solution. The diameter of the

delivered sample was around 16 mm, it is machined down to ∅15 mm before the dove-tail groove is cut into one of the end caps for mounting.

Conditions after measurement campaign

Figure 2.5 shows two SEM pictures (2.5a and b) and an EBSD picture (2.5c) of the single-crystalline specimen.

Figure 2.5a) shows a secondary electron signal in 250×-magnification. Over distances of many millimetres there is no grain boundary to be found. Figure 2.5b) shows a backscatter electron (BSE) signal in 1000×-magnification of the only change in this contrast that could be detected over the whole sample. Figure 2.5c) shows the same area as in 2.5b) (of BSE contrast change) in EBSD. The EBSD detector in the used SEM states a sensitivity for indicating the crystal orientation differences of $\geq 1°$, but indicates no grain orientation change in the same area. Hence, the angular misorientation of the two regions with different BSE contrast shown in figure 2.5b) must be lower than 1°.

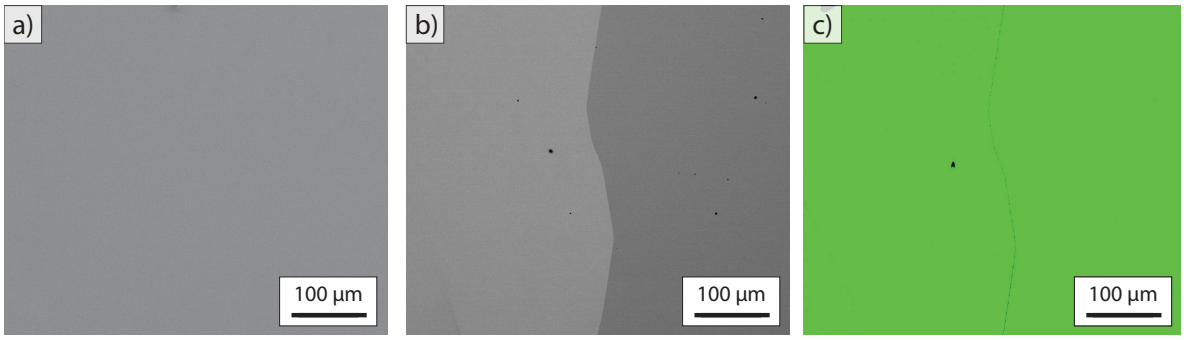

Figure 2.5.: Micrographs of the single-crystalline specimen in 250x in magnification. Image c) on the very right shows an EBSD the identical area as in b). According to the absence of EBSD contrast the angular orientation deviation of the two regions must be $< 1°$.

2.3.1.2. Poly-crystalline sample

Conditions as-received

The poly-crystalline sample was delivered from Louis Renner GmbH in form of a longer bar (800 mm). It was sintered under pressure at over 3000 °C under hydrogen atmosphere. Its nominal density was given to be around 19.2 $\frac{g}{cm^3}$. It was custom made for this purpose, because tungsten which is sintered under hydrogen atmosphere at this high temperatures, should exhibit minimal impurities like carbon (which is reduced in the hydrogen atmosphere) in comparison with metallurgically manufactured tungsten[1]. The sample with size ∅15 mm, 48 mm long was cut from this bar.

The state of the poly-crystalline sample before (by using a sample from the same raw material delivered) the measurement campaign was investigated on a slice cut from the delivered bar. This control sample is shown in the upper image of figure 2.6.

[1] Although impurities should be minimal, this sample exhibited quite an amount of voids in the centre.

Image i.0) shows the a cross-section of the specimen in a light microscope, the diameter is 15 mm. The grain size across the whole diameter of the specimen is around 1 - 5 μm. Images i.1) and i.2) show the outer area of the specimen, randomly exhibiting few voids at the grain boundaries with diameters less roughly between 0.5 and 1 μm. In the centre of the sample the grain size does not change, but the number of voids is significantly higher than in the outer area towards the cylindrical surface, see images i.3) and i.4). The overview picture already indicates that this higher void density can be recognised by eye if the surface is polished. The voids in the centre exhibit sizes of roughly 1 μm.

Micrographs: comparison before- and after measurement campaign

The state of the poly-crystalline sample after the measurement campaign is shown in the lower part of figure 2.6. Figure a.0) shows an overview picture of a cross-section at the lower end of the sample. The centre of the specimen is missing, because before the sample was analysed with the SEM the 0.5 mm thick outer area was cut from the specimen to generate a thin-walled hollow sample from the same specimen which was used for background measurement described in section 3.1.3. The technical procedure for extracting this thin-walled tube from the specimen was drilling a borehole in advance of electric-discharge machining (EDM). The straight cut at the top of the specimen was produced during EDM. The outer area of the cross-section shown in figure 2.6a.0) exhibits grains of some millimetres in diameter - as it would be expected for the high temperature conditioning (to temperatures $\leq$ 2800 K) which the specimen was undergoing (see also chapter 4.1). Image a.1) shows a section of the inner area of the specimen which exhibits much smaller grains than the outer area, ranging roughly from sizes of 50 to 100 μm. Also here voids can be seen. The further in the centre of the cross-section, i.e., the centre of the specimen, the more voids appear. Figure a.2) shows the transition zone from big grains in the outer area (lower right side of figure) towards smaller grains in the inner area. This transition zone begins at roughly 1.3 - 2.2 mm away from the outer surface (after EDM).

Contrary to expectation that the poly-crystalline sample should exhibit an almost "single-crystalline analogue" microstructure, it still shows small grains and voids towards the centre. This probably stems from the high density of voids that the specimen exhibits in its initial state, which pinned grain boundaries and hereby hindered excessive grain growth in the central area.

2.3.2. Big specimen: ⌀ 30 mm poly-crystalline

The big specimen with ⌀ 30.01 mm was purchased from Plansee GmbH, Austria. The length of the specimen is 54 mm. The impurities as given from Plansee are distinguished into "guaranteed" and "typical" values:

Typcial: W 99.97%; impurities: Al 1 μg/g, Cr 3 μg/g, Cu 1 μg/g, Fe 8 μg/g, K 1 μg/g, Mo 12 μg/g, Ni 2 μg/g, Si 1 μg/g, C 6 μg/g, H -, N 1 μg/g, O 2 μg/g, Cd 1 μg/g, Hg -, Pb 1 μg/g.

Guaranteed: W 99.97%; impurities: Al 15 μg/g, Cr 20 μg/g, Cu 10 μg/g, Fe 30 μg/g, K 10 μg/g, Mo 100 μg/g, Ni 20 μg/g, Si 20 μg/g, C 30 μg/g, H 5 μg/g, N 5 μg/g, O 20 μg/g, Cd 5 μg/g, Hg 1 μg/g, Pb 5 μg/g.

The big specimen is still in usage, hence no micrographs are available.

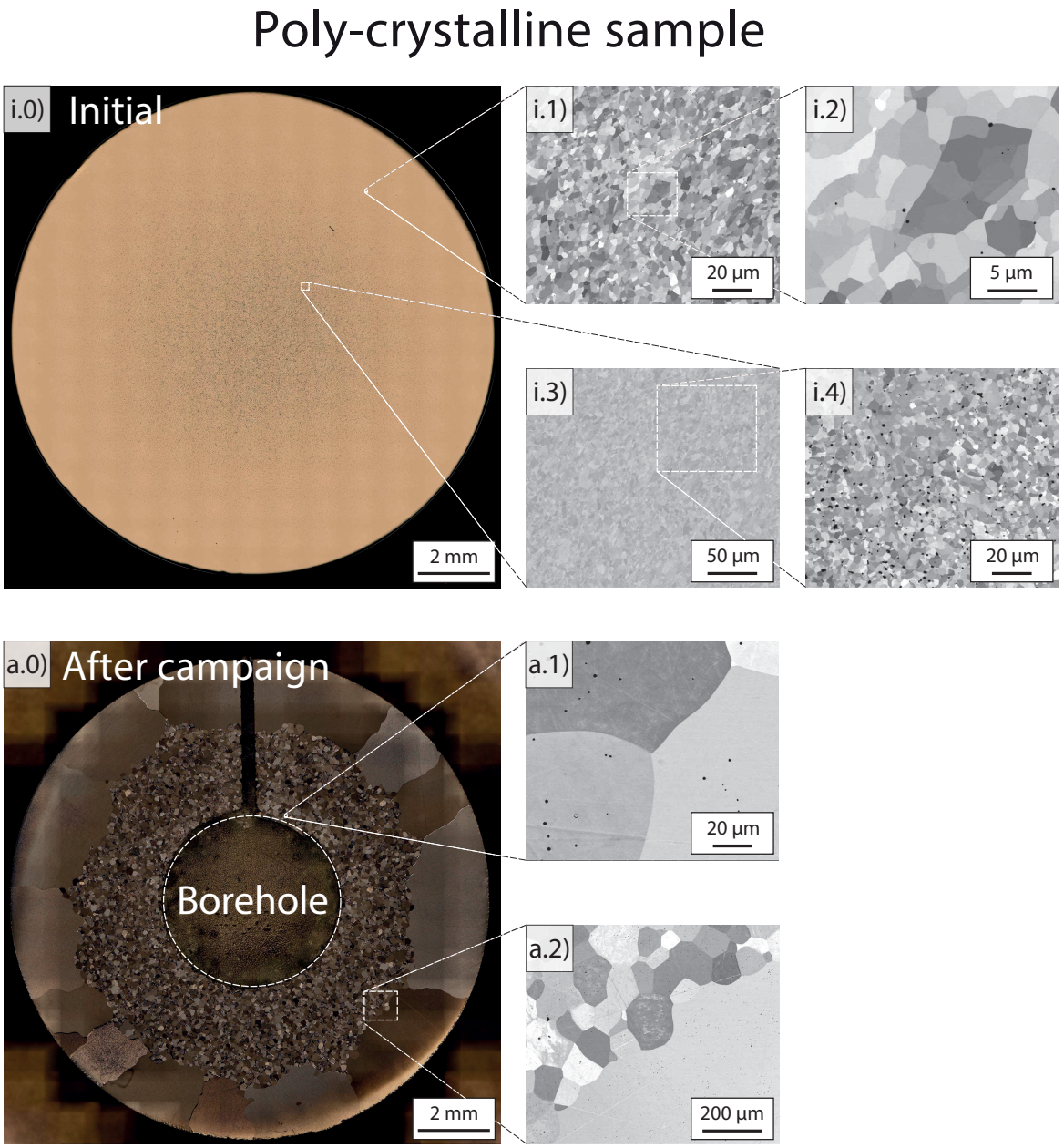

Figure 2.6.: Micrographs of the small, poly-crystalline sample before and after the measurement campaign, in which temperatures $\leq 2800\,\mathrm{K}$ were reached. The initial state of the as-received specimen (a control sample from the same raw material as the actual specimen) is shown at the upper images (i.0) to i.4)). Before the measurement campaign the specimen has grain sizes of around 1 - 5 μm and voids of roughly 1 μm. The lower images (a.0) - a.2)) show the specimen after the campaign (the core is missing because of experimental reasons, see text). The outer area shows large grains of up to $2 \times 5\,\mathrm{mm}$, in a radial distance of roughly 1.3 - 2.2 mm away from the outer surface. Towards the centre the grain size is about 50 to 100 μm. There are still voids to be seen, increasing towards the centre.

2.4. Measuring gas species with a Quadrupole Mass Spectrometer (QMS)

ROST is connected to the main chamber of the TESS setup with a ⌀ 100 mm tube of 700 mm length and a CF40 full-metal gate valve (at the side of ROST) to separate both vessels. TESS is a stainless steel chamber that allows to heat samples in ultra high vacuum by either electron bombardment or infrared radiation. A basic description of TESS is given in [35]. In all experiments reported here, the desorbed gases are detected with a high-end Pfeiffer/Inficon DMM 422 quadrupole mass spectrometer (QMS) located in the TESS main chamber. The QMS is equipped with a discrete secondary electron multiplier (SEM) that is operated in single ion counting mode. This ensures superior long term stability, avoids background noise, guarantees a dynamic range of six orders of magnitude and allows to apply Poisson statistics for determining the accuracy of the measurement. Long term stability is tested by performing a calibration after each loading degassing cycle. The multiplier voltage is adjusted to make sure the SEM operates always in the Geiger-Müller range. In cases, were the signal intensities are about to reach the maximum count rate of 10^6 counts per second, the emission current of the ionizing tungsten filament in the cross beam ionizer of the QMS is reduced. Typical emission currents range from 0.01 - 0.10 mA. Absolute calibration of D_2 desorption was performed by a D_2 calibration gas bottle with calibrated leak rates for deuterium and protium of $1.2234 \cdot 10^{14}$ D_2 molecules/sec and $1.4415 \cdot 10^{14}$ H_2 molecules/sec [Laco Technologies, Utah, USA]. The calibration factor for HD was experimentally determined by flowing either D_2 or HD gas through an orifice of known size from a calibrated volume into the QMS vessel. Based on the pressure recording of a spinning rotor gauge the calibration factor in measured QMS counts per molecule for HD was 66 % of the one derived for D_2. Contribution of HD on the total D desorption was between 0.2% (big specimen) and 12% (small specimens) and was considered in the estimation of the total hydrogen inventory. The maximal measured deviation of the calibration factor was 13% (ranging from July 2018 until September 2019). It is representing the ageing of the detector. However, the change of the calibration factor by up to 13% does not add to the experimental uncertainty, because the acutal factor was determined for each individual measurement.

The accuracy for the absolute amount of D, or H, respectively, is hence determined by the stated accuracy of the leak valve of 4.6% for D and 3.8% for H for the measurements shown in the following. The QMS was operated in the so-called multiple ion detection mode were the following mass channels were recorded m/z = 1, 2, 3, 4, 12, 14, 16, 17, 18, 19, 20, 28, 32, 40, and 44. Release was dominated by mass channel 4 for deuterium and mass channel 2 for protium. Mass channel 28 showed a clear signal at temperature ramp-up and elevated temperature of the specimen. It could not unambiguously be clarified if this signal stems from CO or N_2 molecules.

2.5. Experimental device

This section will mainly cover the "physical" setup. The apparatus is designed by firstly formulating the problem: gas loading and degassing of a tungsten specimen at temperatures up to 2800 K. Then the solution is derived, finally coming to a system/apparatus that is built as following the recommendations by Lindemann for methodical development of technical devices [36].

The requirements of the experimental apparatus are:

- Firstly, the ability of the containment which houses the specimen to effectively absorb and exhaust radiative power from the specimens with temperatures up to 2800 K
- Secondly, the ability to provide ultra-high vacuum conditions, i.e., vacuum better than $5 \cdot 10^{-9}$ mbar as well as allowing pressures of hydrogen up to 0.5 bar
- Thirdly, good temperature control and the implementation of an external induction coil for heating in combination with a contacted temperature measurement plus pyrometry for temperatures higher than $T > 2550$ K

The structural support system must fulfil various requirements, namely:

- Ability to adjust the vertical axis of the glass tube to fit into the inductive coil
- Fast and easy ability to exchange the glass tube
- Shielding of the glass tube to assure shatter protection in case of fatal glass rupture and additionally prevent electromagnetic leaking (of the electromagnetic radiation from the induction coil)
- Easy access to vacuum valves
- Fast and easy switching between gas loading and vacuum/degassing mode

The requirement to easily exchange the glass tube results in some mechanical measures: Firstly, the induction coil must be vertically movable to allow the dismounting of the glass tube in case it needs to be exchanged or cleaned. Cleaning is necessary after the high temperature conditioning (chapter 4.1) of the specimen, because evaporating surface impurities deposit on the inner glass wall and need to be removed before executing the measurements. This is realised in a vertical movement system that allows the coil and the connected induction head to be moved by about 1100 mm vertically. Since, the induction head weighs around 40 kg, there are counter weights placed inside the vertical poles. This enables almost weight-free movement of the induction head with induction coil which enables an easy mounting or dismounting of the glass tube.

Secondly, the system needs to be able to compensate a certain degree of crookedness of the glass tube. The quartz glass tubes are manufactured by hand in a turning bed where the quartz glass parts/tubes need to be heated over 1000°C while "welding" the different parts together - this results in good mechanical properties but the evenness is rather insufficient in terms of engineering standards. Hence, the quartz glass tube together with the whole main vacuum vessel is screwed onto a plate, that allows alignment in relation to the vertical movement of the inductive travel head via four M16-screw-threads. By this the whole main vacuum vessel can be adjusted in relation to the travel of the inductive coil/induction head. Figure 2.7 shows the

By the vertical movability of the inductive coil and the induction head together with connectors to the water cooling system the glass tube is easily and quickly exchangeable.

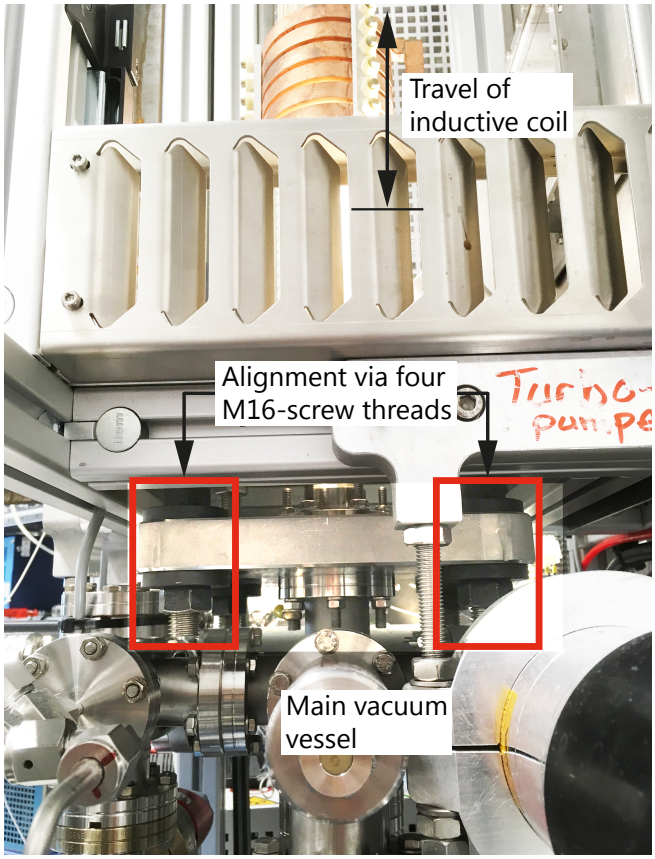

Figure 2.7.: Alignment of glass tube to travel of inductive coil. The glass tube, covered by the inductive coil at the top in the image, is mounted together with the whole main vacuum vessel to an aluminium plate in the middle. This plate is mounted via four M16-screws to the support frame on which the travel system of the inductive coil head with the coil itself is mounted to. Via the four M16-screw-washers, the glass tube is aligned to the travel of the inductive coil. The system allows the correlating movement of the main vacuum vessel by flexible CF-bellows to TESS and the pre-vacuum and hydrogen-inertisation system.

2.5.1. Inductive heating

The heating method of choice is inductive heating - firstly, because the material that shall be heated is tungsten, a metal that is conductive. Hence, a heating method like inductive heating that relies on currents can be applied. Secondly, inductive heating is efficient and contactless, so the heating actuator can be placed outside the vacuum vessel, no direct connections to the specimen for heating need to be established.

The setup consists of a generator that was purchased from Trumpf Hüttinger in Freiburg, Germany: TruHeat MF5040. The device has a nominal output power of 40 kW and an output frequency of 20 - 100 kHz. The output frequency can be adjusted by changing capacities in the device; also the maximum output power can be changed by adjusting the impedance of the device. The whole heating device consists of two main parts, the power supply and the resonant circuit, both of them are water cooled, including an internal water cooling of the copper wirings of the inductive coil.

According to the outer diameter of the two different quartz glass tubes (for the small and big specimens), there are two inductive coils: A small inductive coil with inner diameter of $\varnothing_i = 50\,\text{mm}$ for the small glass tube with outer diameter of $\varnothing_o = 48\,\text{mm}$ (leaving a tight 1 mm space between coil and glass tube) and a big one with $\varnothing_i = 75\,\text{mm}$ for the big quartz glass tube of $\varnothing_o = 70\,\text{mm}$ (exhibiting 2.5 mm headroom between coil and glass).

2.5.2. Penetration depth

The penetration depth of the electromagnetic wave in the specimen can be calculated using the formula (from [37], page 98):

$$\delta = \sqrt{\frac{2\,\rho}{\mu\,\omega}} \tag{2.1}$$

with δ : penetration depth
ρ : electric resistivity of tungsten at 2000 K: $5.3 \cdot 10^{-8} \Omega m$ [38]
μ : magnetic permeability: $\mu_0\,\mu_r$
permeability constant of air: $\mu_0 = 4\,\pi\,10^{-7}\,\frac{N}{A^2}$;
relative permeability of tungsten: $\mu_r = 1.000068$ [39]
ω : angular frequency of electromagnetic wave ($2\pi f$)
f : frequency of electromagnetic wave, automatically adjusted by minimizing the reflective loss at the inductive coil

$$f_{big\ specimen} = 40\,kHz \tag{2.2}$$

$$f_{small\ specimen} = 60\,kHz \tag{2.3}$$

The penetration depth δ is calculated for the small specimen to 1.19 mm and for the big specimen to about 1.45 mm. This is enough to effectively heat the specimens. Hence, the specimens are heated homogeneously around the radius of the specimen, causing a negligible temperature gradient while heating.

2.5.3. Electromagnetic shielding

The coil, although forming a relatively enclosed electro-magnetic field to heat the specimen, also sends electromagnetic waves to the surrounding which could disturb electrical devices or the quadrupole mass spectrometer. The smallest gap in the housing roughly needs to be smaller than the wave length of the emitted wave of the coil. The generator is able to radiate in a radio frequency range of 20 - 100 kHz:

$$\lambda_{rf} = \frac{c}{f} \tag{2.4}$$

with	λ_{rf}	:	emitted wave length	[m]
	c	:	velocity of light	$[3 \cdot 10^8\,\mathrm{m/s}]$
	f	:	frequency	[Hz]

$$\lambda_{rf} = 3 - 15 \cdot 10^3 m \tag{2.5}$$

The wave length emitted by the inductive coil is between 3 and 15 km - this makes the whole system relatively easy to shield, in contrast to systems that work with emitters in the GHz range like mobile phones for example. Hence, the structural support system itself should be able to shield the lab from noise from the inductive coil. The metal plates that also act as shatter protection and fully enclose the glass tube and the inductive coil (see chapter 2.5.9) exhibit an even better electromagnetic shielding of the whole apparatus, so it should not affect other systems in the laboratory.

2.5.4. Temperature measurement and control

2.5.4.1. Measuring temperature

Temperatures need to be measured in the support systems of the experiment and most of all for the tungsten specimen itself temperature must be precisely known. Generally, temperatures can be measured contact based and non-contact based, i.e., with thermocouples and by using pyrometry. Pyrometry is the preferred method to measure temperatures, but their measurement range is limited: here a pyrometer is used that can measure temperatures from 1000 to 3000°C. Therefore, for room temperature up to at least 1000°C a directly contacted thermocouple is used.

Thermocouple

While he was studying the thermal effects on galvanic arrangements, Thomas Johann Seebeck (1770 - 1831) found that two semicircular joined pieces of two different metals induced a magnetic disturbance [40]. He found that electrically connected different metal combinations' magnetic field strengths increase with higher temperatures. He called this "thermomagnetism". This effect was studied more extensively later on and is called "thermoelectric effect": Combinations of dissimiliar metals cause a net current because of the net difference between their thermoelectric properties [41]. The Seebeck coefficient describes the thermoelectric conversion of a temperature difference at the measuring spot (hot junction) in dependence of the electric potential [42, 43].

There are several standard material combinations that are commercially available and that are standardised. Regularly used thermoelement-pairings are made from nickel-chromium or

platinum-rhodium. Table 2.1 displays the used thermocouple combinations. The type-K are rather cheap and standard thermocouples that are used to monitor the temperature of the support systems of the experiment, for example to check the cooling water temperature or flanges of the experimental set-up. Type-C thermocouples are used to measure the temperature of the tungsten specimen because this type is among all standardised versions the one that can be used at highest temperatures.

Table 2.1.: Thermocouple combinations that are used. The types are internationally standardised by standard EN 60584.

material pair	type	temperature range
NiCr-Ni	K	73 to 1523 K (-200 to 1250 °C)
WRe3-WRe25	C	273 to 2573 K (0 to 2300 °C)

with NiCr : nickel-chromium alloy with 50 atomic percent chromium
WRe3 : tungsten-rhenium alloy with 3 atomic percent rhenium
WRe25 : tungsten-rhenium alloy with 25 atomic percent rhenium

For both sizes of specimens, small and big, a thermocouple diameter of 250 μm is the best compromise between being still able to be bend and being rigid enough for the handling during laser welding. Both thermocouple wires are directly welded to the specimen, oppositely to each other. So the source of thermoelectric voltage is indeed the volume of the specimen itself between the two wires.

The connection of the wires to the specimen though is rather challenging - regular welding techniques such as spot welding do not work well because especially the wire with lower rhenium content tends to get embrittled quite easily if parameters are not well chosen. Laser welding is the technique of choice - the parameters were set such that the welding spot does not melt the whole wire. Therefore, extensive embrittlement is prevented and the whole connection remains flexible to some extend. This makes the whole installation able to withstand several mounting processes.

Low pass filter for thermocouple

The thermocouple voltage, induced by the change of temperature, i.e., thermoelectric voltage, ranges from 0.000 mV at 0°C to 37.015 mV at 2300°C. In order to avoid rf-disturbance from the inductive coil an RC low-pass filter was added to the measurement circuit:

$$f_g = \frac{1}{2\pi RC} \tag{2.6}$$

The internal resistance of the input channels of the controller is given by the manufacturer to be higher than 10 kΩ. A 22 μF standard capacitor is used. This results in a cut-off frequency of:

$$f_g = 0.72\,Hz \tag{2.7}$$

This means that the input from the thermocouple is smoothed so that all changes in the thermoelectric voltage from the thermocouple that are (roughly) higher than 0.7 Hz are filtered

out. Experiments show that the measurement still reacts fast enough for the temperature control and the interferences from the inductive coil are completely filtered out.

Optical pyrometry

Another method to measure temperature of an object is optical pyrometry. It utilises the spectral radiated emission of an incandescent body which is dependent on its temperature T. The temperature of the body determines the intensity and the maximum of the emission spectrum [44]. The Stefan-Boltzmann formula describes the total radiated power P of an ideal blackbody. A blackbody is a hypothetical body that completely absorbs all incoming radiation of any wave length and intensity. As the ability for absorption is maximally high, the emissivity in parallel also reaches its maximum. A blackbody radiates with the specific intensity per area according to the Stefan-Boltzmann law (with σ being the Boltzmann constant):

$$P = \sigma A T^4 \tag{2.8}$$

Most materials radiate only a fraction described by the Stefan-Boltzmann formula. The emissivity, ϵ, reflects this property which is dependent on the material, surface conditions, surface colour and wave length of the emitted radiation. A is the surface of the radiating body:

$$P = \epsilon \sigma A T^4 \tag{2.9}$$

For the temperature measurements a single wavelength pyrometer from the manufacturer Sensortherm is used. The device measures at the wavelength 1.27 μm where the emissivity of tungsten remains constant over temperature. Due to the constant emissivity the pyrometer measurement is independent of temperature at least between $1600 < \mathrm{T} < 2800$ K [45].

Therefore, the pyrometer requires only one free parameter to be provided by the operator: the emissivity of the tungsten specimen. The emissivity was determined experimentally: the specimen was heated to 2000 K (1727°C) with the thermocouple as input for the controller - then the emissivity was chosen such that the pyrometer reading is equal to the thermocouple reading. The emissivity is stable after the specimen is conditioned (holding for 20 hours at 2400 K, iteratively in hydrogen and vacuum, also see chapter 2.3) and varied between 0.28 and 0.30 for the three specimens that are used. The pyrometer is placed directly underneath the specimen/main vacuum vessel at line of sight to the bottom of the cylindrical specimen through a quartz glass window (see figure 2.2).

2.5.4.2. Parallel usage of thermocouple and pyrometer

The pyrometer is the only method to measure temperatures higher than 2573 K. Below this temperatures it provides a second, independent measurement in the temperature range from 1273 K to 3273 K in parallel to the type-C thermocouple measurement that reaches up to 2573 K.

For temperatures above 2573 K the pyrometer serves as input reference for the temperature controller. The specimens were heated up to a temperature of 2800 K in explorative experiments to test the ability of the apparatus.

For measurement cycles temperatures of up to 2600 K are reached, but this high temperature is used only very rarely. Furthermore, the temperature of 2600 K appeared not to be practical

for frequent measurements because the evaporation of tungsten already reaches values that cause rapid coating of the inner glass wall. Hence, temperatures above 2400 K are avoided, see chapter 2.5.5.4. Therefore, for most experiments the type-C thermocouple reading is used for temperature control while the pyrometer serves as monitoring measurement for checking, e.g., of temperature drifts, see chapter 3.1.2.

2.5.5. Glass vessel

The tungsten specimen must be mounted in a container that is able to carry the specimens' weight, enable temperature measurement and be able to deal with the high radiative power from the specimen when it is heated to temperatures as high as 2800 K. The most stringent requirement for the material of the main container is transparency for the electromagnetic wave in the range of 20 - 100 kHz that is used to heat the specimen from the inductive coil. Not many materials fulfil this prerequisite: steel, aluminium and other metals are not applicable, because they are not transparent to the RF radiation. Glass and ceramics fulfil this property. Ceramics such as Al_2O_3 are relatively hard to be joined to steel connections and expensive. Moreover, they are non-transparent in the visible range, which makes experiments unhandy. Furthermore, it is impossible to transmit the radiative power spectrum from the specimens and, therefore, would cause heating of the walls. Hence, quartz glass is the material of choice for this application. Glass is transparent for the RF emitted by the inductive coil. It has high transparency for the emitted radiation of the specimen at high temperatures thus adsorption of radiation power and with it heating is relatively low.

The used quartz glass is Infrasil from Heraeus. At the upper and lower end of the glass vessel a flange-to-steel-to-glass adapter is installed. The upper end has a steel flange installed which connects the tungsten shaft and the specimen with the glass vessel. The lower end also needs a glass-steel connection, so that the glass vessel can be mounted to the main vacuum vessel which mainly consists of stainless steel.

2.5.5.1. Heat management

Here follows a short assessment for the heat management of the glass tube. As reference case the les favourable case of the big specimen is assessed (in the big glass tube). Because of the higher surface area it emits more radiative power than the small specimens.

With the emissivity of the used tungsten specimens of $\epsilon = 0.28$ - 0.30, the emitted radiative power of the big specimen at 2400 K with a cylindrical geometry of diameter of 30 mm and a height of 54 mm is calculated by applying equation 2.9:

$$P_{\epsilon=0.3}^{2400\,K} = 3.670\,kW \tag{2.10}$$

Figure 2.8 displays the transmission coefficient from the used Infrasil quartz glass from Heraeus with a wall thickness of 2 mm of the inner tube in comparison with a blackbody radiator at 2400 K. The spectrum is normalised to 100%. The emitted radiative spectrum is displayed as dotted blue line, the solid blue line shows the scaled spectrum behind the inner glass wall. The emitted radiative spectrum is multiplied with the normalised transmission of the first glass wall. This spectrum is then subtracted from the incoming spectrum, which estimateds the total absorption from the first wall to 6%. This results in an absorbed power of 220 W in the glass:

$$P_{1st\ glass\ wall}^{2400\,K} = 220\,W \tag{2.11}$$

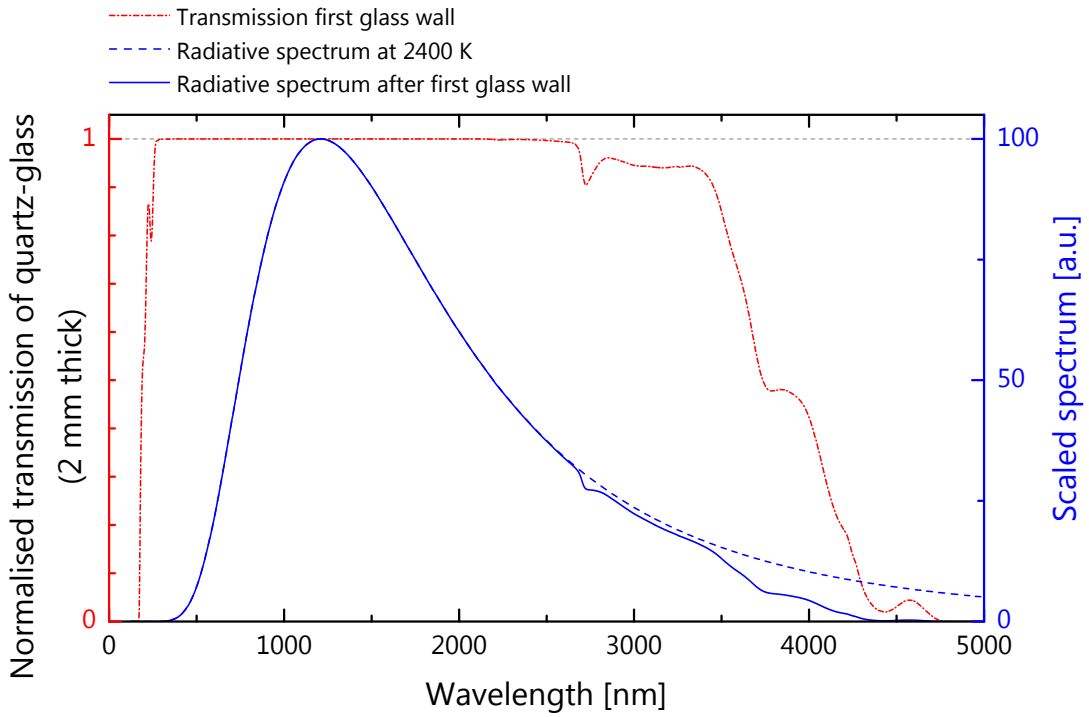

Figure 2.8.: Absorption of the radiative spectrum from the big specimen at 2400 K of the 2 mm thick inner glass of the big quartz glass tube (Infrasil quartz glass). The absorbed power from the inner glass wall is estimated to 220 W.

There is not only the glass tubes' walls that absorb some of the emitted power but also the roughly 4 mm thick water column of the cooling water. Figure 2.9 shows the absorption coefficient of water for wavelengths between 200 nm and 300 μm as measured by Querry et al. [46]. This absorption spectrum is again normalised, converted into a transmission spectrum and multiplied with the scaled spectrum that is left after the first glass wall (figure 2.10). A substantial part of the incoming spectral power is absorbed by the water column, especially the higher wavelenghts. From the power that is left after the inner glass wall the absorbed radiative power by the water column is calculated to 31%. This is evaluated by multiplying the radiative spectrum after the first glass wall with the normalised transmission spectrum of the water column in the double-walled part of the glass tube. Subsequently this is subtracted from the incoming radiative spectrum:

$$P^{2400\,K}_{water\ column} = \left(P^{2400\,K}_{\epsilon=0.3} - P^{2400\,K}_{1st\ glass\ wall}\right) \cdot 0.31 = 1070\,W \tag{2.12}$$

So the first glass wall plus the water column should in total absorb:

$$P^{absorbed\ 2400\,K}_{big\ glass\ tube} = P^{2400\,K}_{1st\ glass\ wall} + P^{2400\,K}_{water\ column} \tag{2.13}$$

$$P^{absorbed\ 2400\,K}_{big\ glass\ tube} = 1290\,W \tag{2.14}$$

The cooling water flow in the glass tube is 2 l/min, which corresponds to 0.033 kg/s. Water has a specific heat capacity of $c_{water} = 4.190\,kJ \cdot kg^{-1} \cdot K^{-1}$. For simplicity it is assumed that the cooling water absorbs all of the power that is absorbed by the glass tube. So, the

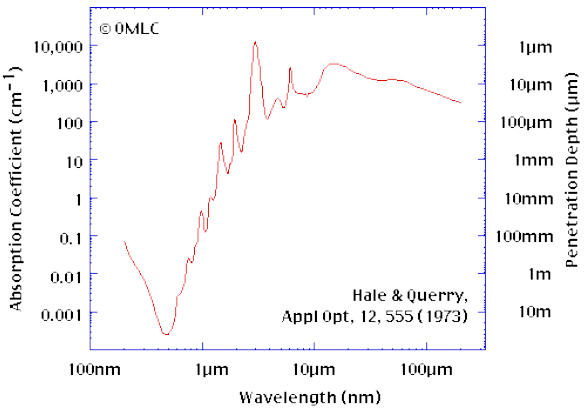

Figure 2.9.: Spectral absorption of water, data from [46], taken from the webpage: https://omlc.org/spectra/water/gif/wieliczka89.gif

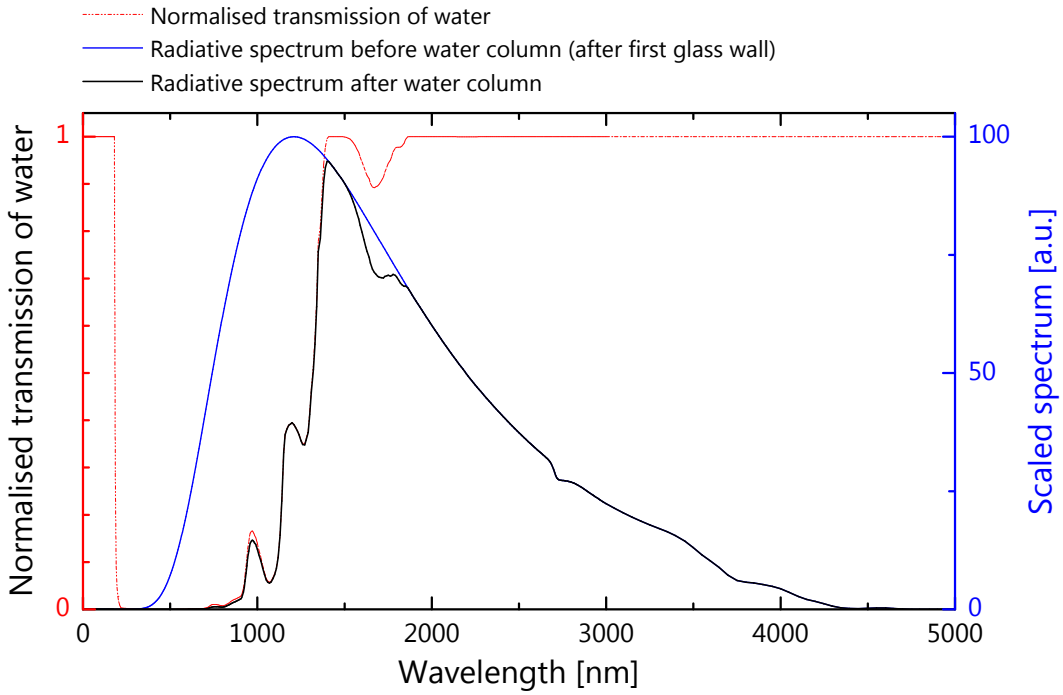

Figure 2.10.: Spectral absorption of the water column from the water cooling. All spectra are scaled to the highest spectral power density. The normalised transmission of the 4 mm thick water column is shown on the left y-axis. The transmission is shown as red line. The incoming spectrum, which has already passed the first glass wall, is shown in blue. The radiative spectrum after the water column is shown in black. The power absorbed by the water is calculated to 31% of the incoming radiative spectrum.

temperature rise of the cooling water is calculated to:

$$\Delta T^{2400\,K}_{water,\,calculated} = \frac{P^{absorbed\ 2400\,K}_{big\ glass\ tube}}{\Delta m_{water} \cdot c_{water}} \left(= \left[\frac{\frac{J}{s}}{\frac{kg}{s} \cdot \frac{J}{kg \cdot K}} \right] = [K] \right) \tag{2.15}$$

$$\Delta T^{2400\,K}_{water,\,calculated} = 9.24\,K \tag{2.16}$$

To check this estimated power absorption a type-K thermocouple was integrated into the outlet of the cooling water, at a distance of around 30 cm from the outlet of the glass tube. The outer glass tube as well absorbs parts of the radiative spectrum, the temperature rise is comparable to the inner glass tube and rather small. Hence, the small temperature rise of the cooling water has a very small influence on the temperature of the inner glass wall and is neglected. The temperature of the cooling water under the same conditions as shown above is 24.4°C. This is a temperature rise of 8.4 K, compared to the water temperature before the specimen is heated to 2400 K:

$$\Delta T^{2400\,K}_{water,\,measured} = T_{water\ initial} - T^{2400\,K}_{water\ measured} = 8.4\,K \tag{2.17}$$

The estimated temperature rise of the cooling water from radiation in equation 2.16 fits quite good to the measured temperature at those conditions described above.

For the degassing measurements it would be nice to have at least a rough idea about the temperature at the inner glass wall during experiment. A heat conduction calculation is used to estimate the maximum temperature of the inner glass wall. It assumes that all of the power is absorbed at the surface of the inner glass wall, see figure 2.11. This is, of course, a simplification, because the power from radiation is not only absorbed at the surface but distributed over the whole glass thickness. However, this simplified calculation yields an estimate of the upper limit of temperatures at the inner glass wall ($T_{vacuum\ side}$):

$$P^{2400\,K}_{1st\ glass\ wall} = -\frac{\lambda_{SiO_2}}{s} \cdot A \cdot (T_{water} - T_{vacuum\ side}) \tag{2.18}$$

$$T_{vacuum\ side} = T_{water} + \frac{P^{2400\,K}_{1st\ glass\ wall} \cdot s}{\lambda_{SiO_2} \cdot A} = 24.4°C + 33°C = 57.4°C \tag{2.19}$$

with	ΔT_{water}	:	$\Delta T^{2400\,K}_{water\ measured}$	8.4 K
	λ_{SiO_2}	:	heat conduction of quartz glass:	1.36 $\frac{W}{m \cdot K}$ [47]
	s	:	thickness of inner glass:	$2{\cdot}10^{-3}$ m
	A	:	glass surface at vacuum side: (with ∅58 mm and height of big specimen 54 mm)	$9.839{\cdot}10^{-3}\,m^2$

$P^{2400\,K}_{1st\ glass\ wall}$ is the absorbed power from the inner glass wall, $T_{vacuum\ side}$ is its temperature, This ansatz uses the surface A of the inner glass wall directly opposite to the specimen, which is a "worst-case" estimate because it assumes that the power is absorbed by the surface only and not evenly distributed in the volume of the inner glass wall.

This maximum estimated temperature of roughly 58° C of the inner glass wall at the vacuum side is uncritical for the stability of the glass. It also matches good to the observed effect of a varying water temperature on the desorption signal (see chapter 2.5.5.4).

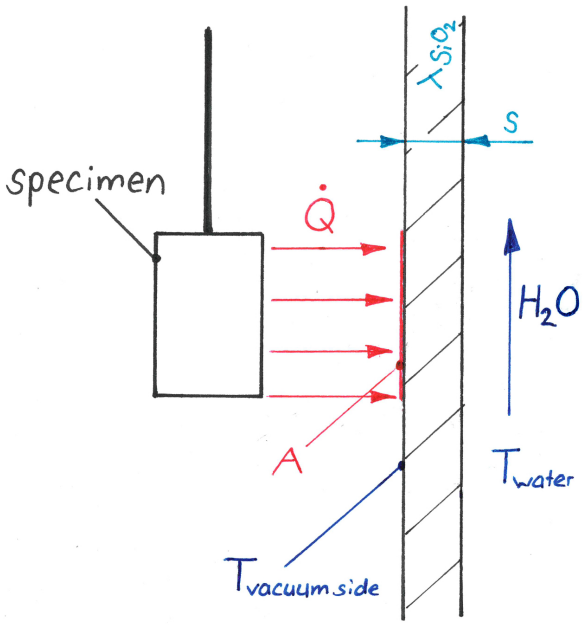

Figure 2.11.: Estimation of upper limit temperature at inner glass wall by using a heat conduction calculation. A sketch visualises the parameters for the temperature calculation of the inner glass wall that faces the specimen.

2.5.5.2. Mechanical design

The mechanical design, i.e., stress considerations for vacuum and gas loading, are considered for the glass tubes. The stress calculations for the areas of double-walled quartz glass and the flange-to-steel-to-glass connectors are done for the small glass tube. The calculated stresses are not critical and are so small, that an easy size-to-stress estimation for the big glass tube is sufficient. The in-detail calculations for the stress calculations are to be found in the appendix A.1. The single-walled flange-to-steel-to-glass connectors of the glass tube are the most delicate parts. They are fragile to tensile stresses, hence, the maximum gas loading pressure is chosen to be 500 mbar to reach lower pressure in the glass tube in comparison to ambient pressure of roughly 960 mbar. The maximum induced compressive stress is calculated to 1.2 N/mm^2 in the lower flange-to-steel-to-glass connector, which is about an estimated 2 orders of magnitude lower than the ultimate compressive stress. Compared to the residual stresses in the flange-to-steel-to-glass connectors[2], the induced stresses by vacuum and 500 mbar gas pressure are negligible small.

2.5.5.3. Chemical cleaning

The inner wall of the glass tube can get coated due to evaporation from the specimen, especially when a new specimen is high temperature conditioned. This is done to clean the specimens from impurities and to recrystallise them to decrease the number of grains (and, hence, the grain boundaries) in the material. This is done at 2600 K with the small specimens (and 2400 K

[2]Those connectors consist of roughly 5 different glass grades that shall evenly distribute the stresses induced from the differing thermal expansion gradients of steel ($11.5 \cdot 10^{-6}\,K^{-1}$) and SiO_2 ($0.54 \cdot 10^{-6}\,K^{-1}$).

with the big specimen) for 20 h in hydrogen atmosphere or vacuum (see chapter 4.1). This leads to an extensive coating on the inner glass wall, see figure 2.12. The black coating could stem from carbon, the silvery, shiny coating is at the position where one type-C thermocouple wire is and, hence, possibly is rhenium.

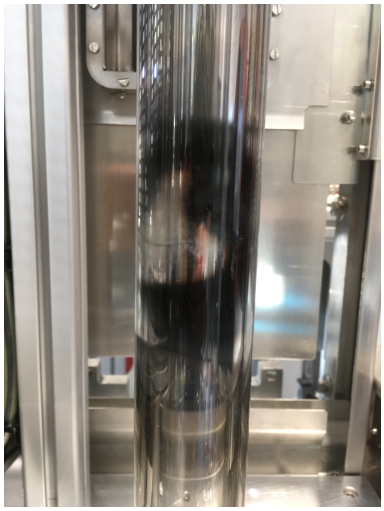

Figure 2.12.: Coated inner glass wall after high temperature conditioning. The black coating could stem from carbon impurities from the specimen, the silvery, shiny part probably stems from rhenium from the type-C thermocouple alloy.

This coating is removed by a chemical treatment of the glass tube. The glass tube is demounted and one of the CF-flanges is closed with a flange and a rubber sealing. Then the quartz glass tube is filled for cleaning with the following chemicals in the outlined sequence:

- H_2O_2 30% for about 4 h
- HNO_3 20% for about 7 h

The times for the chemical treatment are derived empirically. H_2O_2 cleans the glass from carbon and also from heavier elements such as tungsten or rhenium, HNO_3 takes care of lighter elements such as carbon or copper. If the treatment is not sufficient to clean the glass, the above stated procedures can be iteratively repeated - if there are still deposits, also $NaHSO_4$ can be used to clean the glass manually. This needs to be carried out with caution, because $NaHSO_4$ also reacts with steel, i.e., the upper and lower glass-steel flange of the glass tube. Therefore, $NaHSO_4$ shall only be used on tissues that are wetted with a few drops and then slightly rubbed over the coated inner glass wall for example with a glass stick. After that the glass tube needs to be iteratively washed out with deionized water to make sure that the flange-to-glass-to-steel connectors are not affected.

2.5.5.4. Influence of coated inner glass wall

A coating which is to be seen in figure 2.12 will absorb almost all of the radiative power from the specimen because spectral absorption increases. Hence, the main influence are increased temperatures. When completely coated, all of the radiation is absorbed by the inner glass wall.

The temperature of the cooling water was not measured in such a case, but the temperature of the inner glass wall can be estimated by equation 2.19. Assuming the same radiative power from the specimen at 2400 K (see equation 2.10: 3.67 kW), this would be fully absorbed by the inner glass wall. The temperature rise caused by the radiative power alone (the right part of equation 2.19) would be 550°C. Assuming a cooling water temperature between 30 and 100°C (the water was never boiling), this leads to temperatures of the inner glass wall between 580 and 650°C, which would cause highly increased ad- and desorption of hydrogen of the inner wall and disturb the measurements. For such an intransparent coating as shown in figure 2.12 it is mandatory to clean the glass tube before proceeding with the measurements. But the coating process in experiment is gradually, causing the temperature of the inner wall to rise and enhance secondary desorption that could influence the measurements. The higher the temperature of the specimen, the higher the vapour pressure of tungsten. The evaporation rate of tungsten is displayed in figure 2.13.

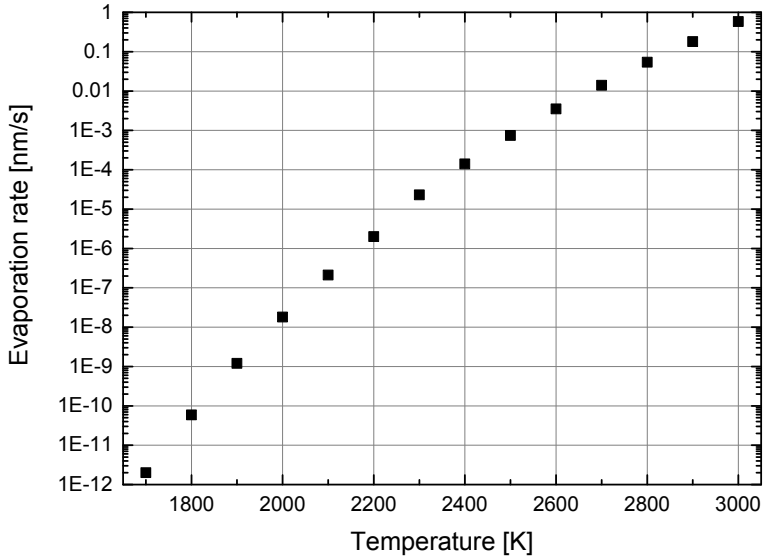

Figure 2.13.: Evaporation of tungsten as a function of the temperature [48].

The evaporation rate grows exponentially with temperature, at 2500 K in 15 min 1 nm gets evaporated from the specimen. At around 3050 K it would already be 1 μm per 15 min. Such a coating can be a problem for the cooling of the quartz glass tube if the inner glass wall is no longer transparent for the radiative spectrum from the specimen and absorbs the radiative power from the specimen completely. A coating can also cause higher secondary degassing signals from the inner glass wall and distort the degassing signal from the specimen.

Figure 2.14 shows a degassing signal from a measurement cycle when the inner glass wall is heavily coated and after the quartz glass tube got chemically cleaned. The left y-axis shows the degassing signal in deuterium atoms/s at logarithmic scale, the right y-axis shows temperature of the specimens. Loading conditions for both measurement cycles are 2000 K for 30 min in 500 mbar deuterium. Degassing is done with a temperature ramp of 2.5 K/s up to 2000 K, then the temperature is kept constant. The degassing sequences are horizontally shifted so that their temperature ramps match. The black signal stems from a measurement with coated inner glass wall, the red signal from the measurement in a clean glass tube after chemical cleaning. Both signals rise when the temperature is ramped up, exhibiting the pre-peak(s), then rise

to the main peak. After the temperature reached 2000 K, the signal decays. The signal in the environment with the coated inner glass wall shows a shifted decay and exhibits wiggles, noticeable already at a signal height of about $5{\cdot}10^{15}$ D-atoms/s. The wiggles get increasingly better visible, the lower the signal height is. Also the signal from the degassing sequence in the clean quartz glass tube shows wiggles, but the influence is to be noticed only for a signal height of about $1{\cdot}10^{14}$ D-atoms/s, which is more than one order of magnitude lower than for the coated wall.

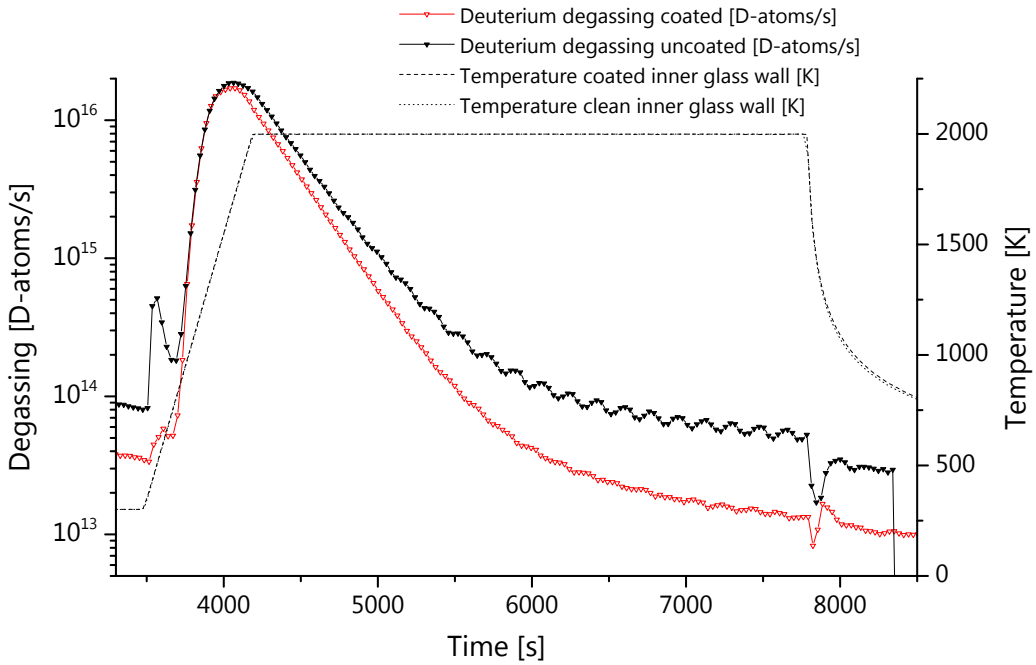

Figure 2.14.: Degassing signal from measurement cycles executed in coated and uncoated quartz glass tube. The oscillating signal from the coated glass tube correlates to the oscillation of the cooling water temperature.

The coating clearly seems to increase the background, also the inventory is higher in the coated glass. The measured deuterium inventory with the coated glass is 24.5% higher than in the clean glass.

During the above mentioned measurements the temperature measurement of the cooling water was not yet installed. It turned out that the oscillation of cooling water temperature stems from the temperature controller of the cooling water circuit which is set to 20°C. The actuator for temperature control is a valve at the secondary water cooling circuit (roughly 12°C-spring water). The valve uses an on- and off-function that is not very well adjusted, hence causing the water temperature to oscillate around the setpoint with a hysteresis of 3°C. One oscillation in 3 min is to be observed.

In contrast to a non-oscillating cooling water temperature, an oscillating cooling water temperature causes an oscillation of the degassing signal if the coating on the inner wall reached intolerable levels. If this oscillations already can be noticed at relatively high fluxes of about $\geq$ 1 - $2{\cdot}10^{15}$ atoms/s, measurements can be considered as invalid. Signs of a oscillating cooling water temperature in the QMS signals are therefore an indicator for a high influence of the inner glass wall on the measurement.

The reason for this enhanced dependence of the degassing on the inner wall seems to be, firstly, the coating itself that seems to enhance the hydrogen inventory of the inner glass wall during gas loading, and then, secondly, the increased radiative absorption of the radiative spectrum from the inner glass wall. This would cause increased temperature on the walls, which enhances desorption during degassing.

2.5.6. Mounting the specimen

In the following, the mounting of the specimen is described. The specimen is placed in the middle of the glass tube. In contrast to former gas loading experiments [8], the design was changed to an "upside-down" layout, where the main vacuum vessel is situated under the specimen and not above. This increases the intrinsic safety, because in case of a failure of the mounting, the specimen would not destroy the glass containment. The specimen is held by a shaft connected to the upper flange-to-steel-to-glass connector on the top of the glass tube. The increased stress on the glass tube is calculated to less than $0.2\,\mathrm{N/mm^2}$ which is negligible.

2.5.6.1. Design

The design of the shaft is one critical element for this setup. The shaft which holds the specimens has to withstand temperatures up to 2800 K and then still has to bear the load. The shaft also shall exhibit a low hydrogen uptake, so that the influence on the degassing signal from the specimen is as low as possible.

Only few materials are not critical at those temperatures. Steel drops out because it already would melt at these temperatures. A few ceramics such as Al_2O_3 would be suitable, in terms of temperatures, but have severe drawbacks in terms of machinability or material costs. Also the behaviour of ceramics at high temperatures concerning uptake and chemistry with hydrogen is not clear. The same also happens to be the case for tungsten alloys; they might be able to bear the temperatures but the uptake of hydrogen could be puzzling.
Hence, the material of choice for the shaft is tungsten - it is machinable at tolerable time, costs and effort; also material costs are acceptable. So there's only the kind of connection to the specimen to be decided - welding could be a possible solution, but has the drawback that after welding it is not easy to de-mount/de-connect from the specimen. A simple and easy solution for mounting and demounting is a dove tail connection - which is the chosen technique for this connection. Figure 2.15 shows a picture of the small poly-crystalline specimen with the mounting shaft in the quartz glass tube at the left panel. The specimen has a dove-tail groove at the upper end, where the shaft glides in and connects. The thermocouple wires welded to specimen can be noticed beside the groove. The right picture shows a CAD-model of both mounting shaft and small specimen. The dove-tail shape at the end of the shaft glides into the dove-tail groove for mounting. Mounting and demounting by this method is easy, also after extended measurement campaigns the connection could always be easily disconnected.

Figure 2.16 shows parts of the technical drawings of both parts, the groove from a side view in the specimen on the left side, the right side shows the axially symmetric dove-tail of the mounting shaft. When the shaft glides into the connection at the specimen, the connecting of both parts is established via line-contact. This reduces the contact surface (in comparison to "surface-to-surface" contact) of both parts and, thereby, also reduces thermal conduction from the specimen to the shaft.

The diameter of the shaft is $\varnothing\,5\,\mathrm{mm}$, the minimal diameter at the mounting shaft is $\varnothing\,3.5\,\mathrm{mm}$

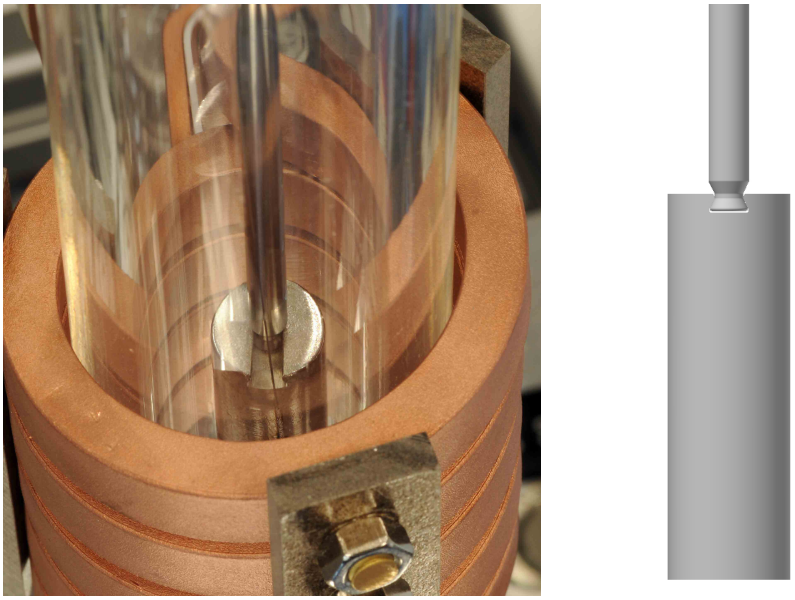

Figure 2.15.: The mounting system of the specimen is shown on the left by a picture a small specimen within the glass tube, connected to the mounting shaft by a dove-tail connection. The type-C thermocouples can be seen at the side of the dove-tail groove. The inductive coil is placed around the glass tube. The right picture shows a CAD model of the specimen with the mounting shaft, elucidating the dove-tail connection.

and represents the minimal load bearing diameter for which the safety margin is calculated in the following section 2.5.6.2. The technical drawings of the mounting system can be found in appendix A.2. Those drawings include the dove tail groove for the specimens, the mounting shaft and additionally the upper mounting connection. The upper mounting is realised by a mounting ring which connects the upper end of the mounting shaft to the upper steel flange and also enables the feed-through of two pairs of thermocouple wires.

2.5.6.2. Analysis

The load bearing diameter at the dove tail at the lower end is $\varnothing 3.5\,\mathrm{mm}$. This is also the area where high temperatures cause the degradation of the tensile strength of the tungsten shaft. The range of ductile-to-brittle transition temperature (DBTT) for tungsten is found to be between 100 - 800°C - [39, 49], which highly depends on the microstructure. Experiments cover temperatures above 1200 K only, therefore, the shaft behaves ductile in any case and is not prone to failure. This is especially desirable because 1100 K is the minimal ignition temperature for a mixture of hydrogen with air. Possible embrittlement is a problem only when temperatures are below the DBTT, i.e., when not being in operation and ignition of hydrogen mixture with air due to failure of the glass is not an issue. During experiment there is no occasion where the connection could be broken by harsh bouncing or bending. This could only happen when the shaft together with the specimen is manually mounted or de-mounted when the quartz glass tube is opened for service, which is not a safety issue.

The safety margin of the dove tail connection at the specimen is calculated for the highest

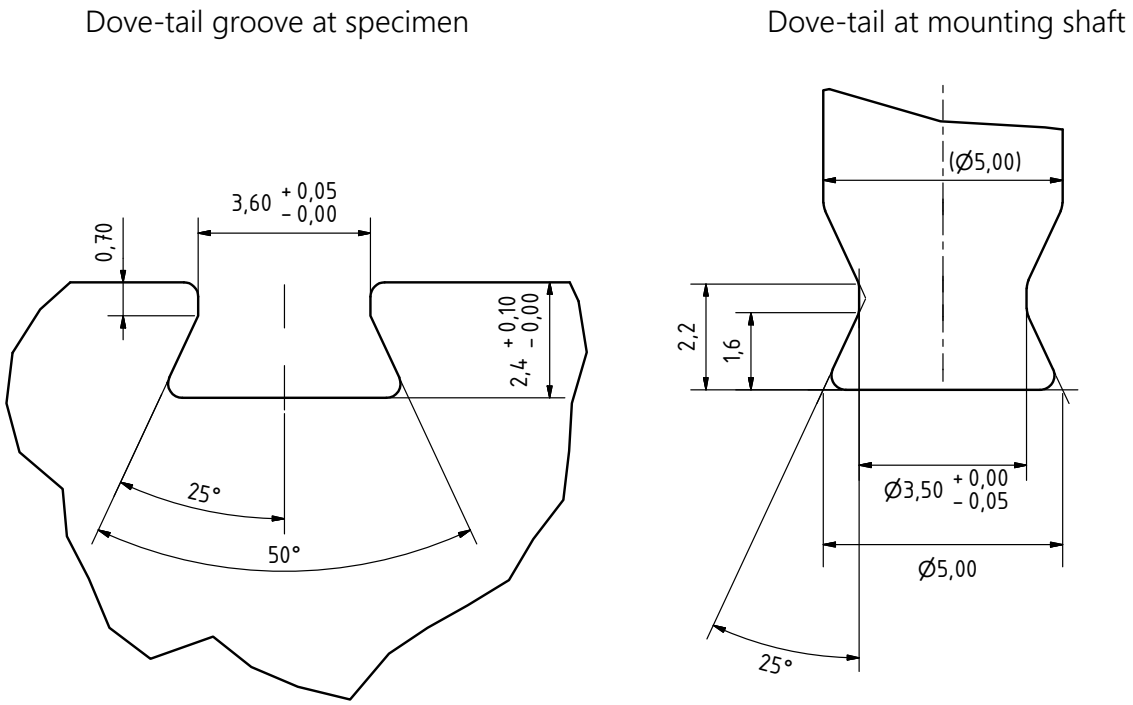

Figure 2.16.: Parts of the technical drawings of the dove-tail connection at the specimen and the mounting shaft.

temperatures that are expected in experiment. Those firstly were assumed to reach about 3000 K. It turned out that for experiments 2600 K is sufficiently high. The highest practicable temperature of 2800 K is reached for exploratory measurements to test the capability of the device. The worst case for strength is taken as baseline scenario. Therefore, data from testing temperatures as high as 3183 K are used as yield strength for the shaft. [50]. The derived yield strength from in this paper is assumed to be the minimum possible value. At 3183 K it was found to be 675 psi, which equals:

$$\sigma_{YS,T=3183\,K}^{tungsten} = 4.6\,\frac{N}{mm^2} \tag{2.20}$$

The test specimen in the case of Schmidt and Ogden was a drawn tungsten sheet with thickness of 1.01 mm, which was probably recrystallised at this high test temperature and hence can serve as valid reference.

The big specimen with a weight of 724 g exhibits the highest load, this leads to a tensile stress in the smallest diameter of the tungsten shaft of:

$$\sigma_{\varnothing\,30\,mm}^{big\ specimen} = \frac{mg}{A} = 0.75\,\frac{N}{mm^2} \tag{2.21}$$

This leads to a safety margin of:

$$\text{safety margin} = \frac{\sigma_{YS,T=3183\,K}^{tungsten}}{\sigma_{\varnothing\,30\,mm}^{big\ specimen}} = 6.1 \tag{2.22}$$

Since the safety factor of 6.1 is sufficiently high, it is very unlikely that the dove tail connection of the shaft fails at experimental operation. Especially because the shaft will very likely behave ductile at temperatures higher than 1073 K ($\sim$800° C) [39], which are below temperatures that are regularly used in the present experimental campaigns (T$\leq$1200 K).

2.5.6.3. Crash absorber

Although the safety factor is high enough, additional measures are taken to prevent damage if the specimen falls down. Most of the times the device on not in operation. Then, the temperature is 300 K and the tungsten shaft probably behaves brittle. Right underneath the specimen there is a quartz glass window to provide a line of sight for the pyrometer (see chapter 2.5.4.1). Furthermore, sometimes there are specimens placed inside the glass tube without using the shaft with the dove tail connection: for example, for background measurements a hollow cylindrical tungsten specimen is used (see chapter 3.1.3). For this case it is practicable to mount the hollow specimen only by using type-C thermocouples with $\varnothing$ 500 μm. They are directly laser welded to this hollow cylinder and are additionally used as mounting. If the weld does not bear the weight at higher temperatures such as 2000 K (and the laser welding of this thermocouples can be very delicate), the sample would drop and could break the quartz glass window. If the glass window breaks during a gas loading sequence, i.e., if the glass tube is filled with hydrogen gas, a hydrogen-oxygen gas mixture can form. The hot tungsten specimen could provide the ignition source to ignite a fire or in the worst case an explosion. To protect the glass window also a crash absorber cup was placed at the lower end of the main vacuum vessel in front of the quartz glass window. It is made of Titanium-Zirconium-Molybdenum alloy (TZM). This crash absorber cup has a bore hole with $\varnothing$ 10 mm along its rotational axis to still enable direct line of sight for the pyrometer. The hole is small enough in diameter to stop all kind of specimens that were used throughout the experiments[3].

2.5.7. Safety measures - what if?

The following section summarises the safety measures that are undertaken to prevent damage from the device. These measures incorporate a wide range of approaches: passive ones that prevent malfunctions before they can occur or active measures that either detect malfunctions and/or prevent from damage. The measures described in the following are sorted such that they mention categories/things that are either checking the machine status or in such a way that they describe a possible malheur. The inductive furnace has several possibilities to integrate custom made interlocks, such as water flow sensors or door switches. If one of them detects a malfunction of the system, the power to the inductive coil is switched off and the heating is stopped. Some of the following measures are based on this interlock principle.

2.5.7.1. Water circuits

To prevent such an incident from happening, a water leak surveillance unit is installed. Core of this are water sensors that are placed around and under the device ROST. They already register a very small water level at the ground. If that is the case, electro-magnetic valves at the entrance of the water circuits cut all of the four lines dry and also cut the power to the inductive coil - in case this is happening while an experiment is under way.

[3] Actually there was one occasion when this crash absorber cup was needed - it worked flawless.

2.5.7.2. Temperature surveillance

The inductive furnace mainly has one malfunctional pattern if talking about daily experimental usage: too high temperature and overheating because of issues with the cooling.

There are several water flow sensors in the system for the different water circuits that cool the subsystems of the device. All water circuits are also under temperature surveillance concerning temperature increase in the subsystems between inlet and outlet. If one of the subsystems exhibits an abnormal temperature increase above the defined limits, the power to the inductive coil is shut off. Abnormal temperature increase can happen mostly if the cooling power of the water circuit is not high enough to keep the temperature of the water circuit constant.

Also the minimal water flow is checked at the subsystems of the heating device, in order to assure enough cooling power. The water flow can drop either if there are bottlenecks in the water piping or if there is too much air in the system so that the pressure cannot be maintained any more. A minimal water pressure of 4 bar is enough to supply the requested water flow.

2.5.7.3. Glass tube enclosure

The glass tube vessel constitutes the most delicate part of the whole apparatus, mainly because glass is a brittle material and hence the glass tube can easily break if no countermeasures are undertaken. Because this part is filled with hydrogen during the gas loading phase of a specimen this can possibly be ignited if air ingress and an ignition source are available[4]. This is why the measures to secure this part of the apparatus is of highest importance.

The easiest and most efficient method to protect the glass tube from unintended breaking is to prevent it from external shear and tension stresses by mounting it upright to the main vacuum vessel. Glass is very delicate with the above mentioned stresses, placing it upright will (nominally) induce only compressive stress into the different glasses the whole glass tube consists of. The part that must be taken most care of is the lower flange-to-steel-to-glass connector.

A second measure to prevent the glass tube from braking is to encase it with a metal structure. This encasing also serves as shatter protection if the glass breaks. The casing is designed such that it can withstand a oxyhydrogen explosion, see section 2.5.9. The encasing can be opened at three different doors at the side, each of them can be locked by a key lock. There is also an interlocked switch at each of the doors which switches off the inductive coil, if a door is opened. This prevents, firstly, someone to unintentionally physically touching or bumping into the glass tube and, secondly, the interlock assures that no one can touch the inductive coil when being in operation.

2.5.8. Hydrogen management

Hydrogen is used in the device to gas load the specimen. Safety measures are needed so that no explosive mixture with air and its oxygen is produced during operation. The critical phase is the gas loading sequence, when the vessel is filled with hydrogen up to a pressure of 0.5 bar, the degassing phase is uncritical. The handling/manual of the device for executing

[4] The specimen itself is an ignition source, so the prerequisites for enlightenment are fulfilled in case the glass tube breaks.

experiments is outlined separately in appendix A.3. Here the principles behind the handling are outlined.

Hydrogen itself is not dangerous. However, in presence of oxygen from air and an ignition source it can be ignited and burn, or explode, depending on the composition. Hydrogen has a lower and a higher explosion limit in a mixture with air [51].

The lower explosion limit (LEL) is:

$$LEL = 4.0\,mol\,\%\,\mathrm{H_2} \tag{2.23}$$

The upper explosion limit (UEL) is:

$$UEL = 95.2\,mol\,\%\,\mathrm{H_2} \tag{2.24}$$

All mixtures of hydrogen and oxygen within this lower and upper explosion limit can possibly explode - as the denotations indicate - but there is one more essential ingredient necessary for an explosion: an ignition source. This can be hot surfaces, flames, mechanically generated sparks, electrical devices, static electricity or lightning strike. This means that the hot specimen itself exhibits a permanent ignition source while operating in hydrogen. At pressures $<$50 mbar the lower explosion limit is reached. Below this pressure, a hydrogen-oxygen mixture cannot be ignited, independently of mixture and if an ignition source is present.

To reassure that air ingress is hindered while operating the device, the device must be safely sealed. The main vacuum vessel is full-metal sealed (copper sealing) and when not in operation the pressure is usually better than $5{\cdot}10^{-9}$ mbar. Air ingress is very unlikely in the metal part of the main vacuum vessel. The most common malfunctional case for industrial devices that handle hydrogen is the case of a "small leak" and therefore, needs to be discussed. The industrial measures against hydrogen ignition because of a small leak (and an accidental ignition source) are usually to operate the device or piping in overpressure against atmosphere, because this is the easiest way to assure hydrogen handling being robust against small leaks. However, industrial facilities tend to be much bigger than ROST, with the focus on long maintenance intervals. In case of a small leak the hydrogen escapes from the vessel to the surrounding air, so that the partial pressure of this gas mixture is below the LEL of 4.0 mol % H_2. This is not feasible for ROST, because the glass tube vessel is prone to tension stresses induced by overpressure which could cause catastrophic failure rather than a small leak. Hence, it is operated at pressures lower than atmospheric pressure.

Figure 2.17 shows a simplified diagram of the pumps, pipes and valves that exhibit only the vacuum pumping system of ROST. A full sketch that also includes the gas supply system is shown in figure A.7 in appendix A.3.1.3 where also the procedure for the operator is described. The buffer vessel plus the connection pipes to the scroll pump have a combined volume of around 50 l. They are situated between scroll and turbo pump. After the gas loading phase of the specimen, when the main vacuum vessel is filled with 0.5 bar hydrogen, the hydrogen needs to be pumped. The turbo pump is disconnected from the vacuum system because it can only be operated in pressures better than roughly $1{\cdot}10^{-2}$ mbar (the pumped vessel in front) and roughly 1 mbar (the pre-vacuum system in the rear). Therefore the turbo pump was disconnected from the main vacuum chamber before the gas loading by having the valves full-metal valve VVMS2 and corner valve VKFeckTP closed.

To not form an explosive mixture with air, the roughly 0.5 bar·l hydrogen is expanded via the bypass, i.e., the full-metal corner valve VVMeck1 and VelKF1 into the previously evacuated

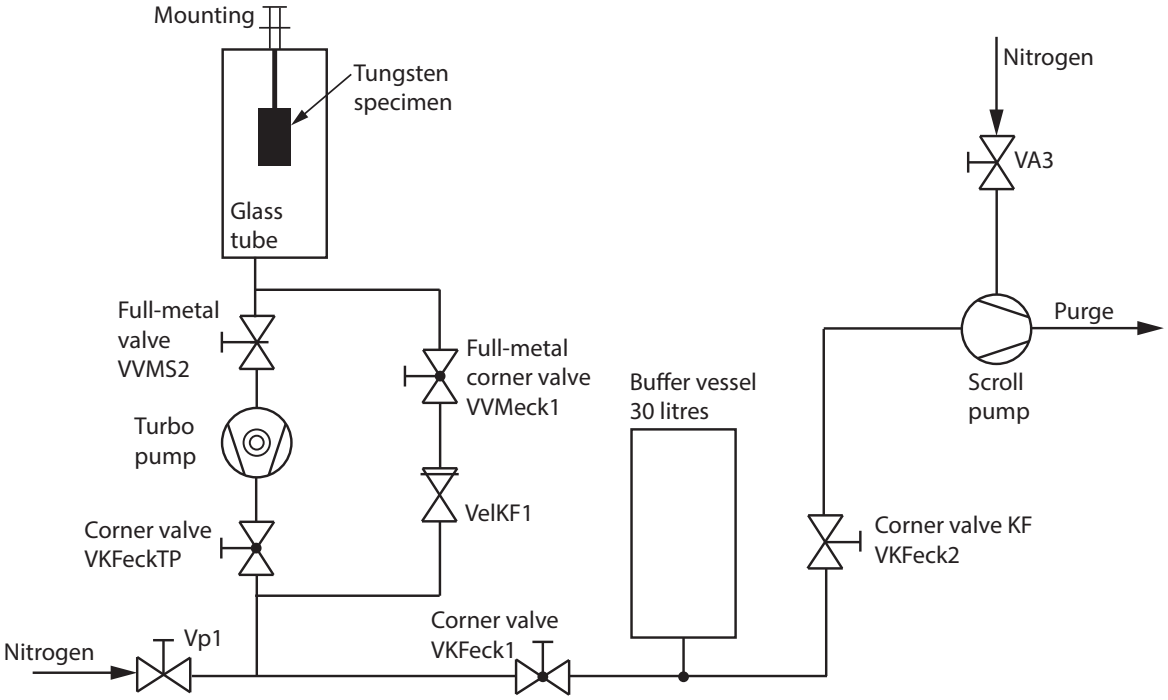

Figure 2.17.: Reduced diagram of the vacuum system.

buffer vessel (the combined volume of the main vacuum vessel with the small glass tube is about 1.07 l, with the big glass tube about 1.4 l). The valve VKFeck1 are open, VKFeck2 is closed. After the expansion of the hydrogen into both vessels, the main vacuum vessel and the expansion vessel are at 12 mbar if the small glass tube vessel is used, or 18 mbar in case of the big glass tube vessel. This is well below the lower explosion limit of 50 mbar of hydrogen. Afterwards the main vacuum vessel is disconnected by closing the full-metal corner valve VVMeck1. Then the buffer system is filled with nitrogen up to 0.8 bar by opening the valve Vp1 (nitrogen feed). This is done in order to inertise the hydrogen, so that the mixture is per se not explosive. If this would not be done the pumped hydrogen would agglomerate at pressures well above the lower explosion limit of 50 mbar at the scroll pump while pumping. Then Vp1 is closed and the buffer system is pumped to around $1{\cdot}10^{-2}$ mbar by, firstly, having the scroll pump in continuous mode and opening the valve VA3 to supply nitrogen ballast gas to the scroll pump, and, secondly, opening the corner valve VKFeck2. Then the bypass is shortly opened with the full-metal corner valve VVMeck1 to pump the main vacuum vessel down to around 1 mbar which is an acceptable pressure that the turbo pump can be connected to pump the vessel. The full-metal corner valve VVMeck1 is closed after a short waiting time of roughly 2 -3 seconds. Then the backside of the turbo pump is connected to the pre-vacuum system by opening the corner valve VKFeckTP, then the full-metal valve VVMS2 is opened to pump the main vacuum vessel to UHV conditions prior to perform the degassing sequence.

2.5.9. The last frontier: outer shielding

Additionally to the measures outlined above that shall prevent air ingress and forming of explosive mixture, an outer shielding is erected to provide protection if the glass tube suffers from catastrophic failure. The main vacuum vessel which is filled with up to 0.5 bar hydrogen

for loading of the specimen has a volume of 1.4 l with the big glass tube. This was measured by expanding hydrogen from the main vacuum vessel into the buffer system and calculating the volumes by using the pressure readings in the concerning vacuum vessels. To set the dimensions of the encasing, the maximum possible energy that can be provided in case the hydrogen forms a perfect 1:2 mixture with oxygen (which leads to the maximum detonation energy) is calculated. The released energy per mole, $\Delta_r H^0$ for the oxyhydrogen reaction is:

$$\Delta_r H^0 = -571.6 \, \frac{kJ}{mol}. \tag{2.25}$$

For the 0.029 mol hydrogen which equals the 0.5 bar hydrogen molecules in 1.4 l volume this results in a maximum inherited energy in an oxyhydrogen reaction/explosion:

$$\Delta_r H^0 = -571.6 \frac{kJ}{mol} \cdot 0.029 \, mol = -16.6 \, kJ \tag{2.26}$$

For comparison, this corresponds to the energy of 0.38 g petrol.

A report of the Bundesanstalt für Materialforschung und -prüfung concerning explosion behaviour of hydrogen (and -mixtures) [51] states a maximum explosion pressure rise gradient of

$$\frac{p_{ex}}{p_a} = 4.92 \tag{2.27}$$

after igniting a hydrogen-oxygen mixture of 93.5 mol % H_2 and 6.5 mol % O_2 at 5 bar pressure at the beginning. This exhibits the most comparable mixture if considering air entrance to the hydrogen filled vessel. From this follows a maximum explosion pressure of:

$$p_{ex} = 4.92 \cdot 0.5 \, bar = 2.46 \, bar \tag{2.28}$$

The net explosion pressure in atmosphere with pressure of $p_{atm} = 0.95$ bar is:

$$p_{ex,net} = p_{ex} - p_{atm} = 1.5 \, bar \tag{2.29}$$

This pressure equals 0.15 N/mm^2 (15 kg/m^2) which the 3 mm thick steel encasing and joining elements such as the screws can withstand easily. This low net explosion pressure allows to use plexi-glass windows of 4 mm thickness at the encasing.

So the encasing shall resist an unintended explosion of the filled glas vessel even if it would be a completely sealed encasing, which means if there were no opening where the expanding gas could expand. To additionally mitigate the possible consequences of an explosion, there is a relief area installed to avoid a complete sealing and lower the explosion pressure. The relief area is realised at the top of the apparatus by an exhaust with ⌀250 mm and a fan installed that constantly purges the area around the glass tube out of the laboratory into the atmosphere. This would additionally remove hydrogen released from potential small leaks and hinder flooding of the laboratory. However, small leaks are very unlikely because directly before loading a specimen the main vacuum vessel was at UHV-conditions, as mentioned before. Also, in the considered case of a braking glass tube vessel and an explosion the expanding gas would purge through this exhaust and, therefore, the consequences of an explosion to the laboratory and the operator should be low.

3. Experimental validation

> Wann immer einen die Dinge erschreckten,
> sei es eine gute Idee, sie zu messen.
>
> *(Daniel Kehlmann -*
> *Die Vermessung der Welt)*

This chapter treats prerequisites for experimental operation, that need to be arranged and known before valid measurement cycles can be undertaken. It covers inaccuracies, correlated to the reproducibility of equally executed measurement cycles, temperature measurement and background signals. The chapter is ending with a developed recipe for consistent measurements and their combination with the diffusion model outlined in chapter 1.4.

3.1. Quantifying uncertainties

This section treats the reproducibility of measurement cycles along a campaign, and, secondly, the uncertainty of the type-C thermocouple temperature reading in correlation to the pyrometer reading.

3.1.1. Reproducibility of experiments

The reproducibility of measurements is tested by conducting experiments that exhibit equal loading conditions (concerning gas pressure, loading temperature and dwell time) and equal degassing parameters (temperature ramp, plateau temperature). These are executed at the beginning, in the middle, and at the end of the campaign with the big specimen.

Figure 3.1a) shows three measurements with gas loading at 2000 K for 60 min in 500 mbar deuterium. Degassing is done at 2200 K for 120 min, with a temperature ramp of 20 K/s. Measurement "fk740" is executed at the beginning of the campaign with the big specimen. "fk741" is executed five weeks after "fk740" in the middle of the campaign when more than 30 measurement cycles (i.e., about half of all with the big specimen) were already done. In both cases the LN trap is used when filling the vacuum vessel with deuterium prior to gas loading. "fk742" is measured one month after "fk741" at the end of the campaign when the big specimen underwent 62 measurement cycles. This measurement cycle did not use the LN trap.

All three measurements are shifted horizontally in figure 3.1a) so that their temperature reading match. fk740 and fk741 show almost the same background level of $2{\cdot}10^{14}$ D-atoms/s when the temperature is ramped up, whereas the background level for fk742 is less than half of this ($8{\cdot}10^{13}$ D-atoms/s). In figure 3.1a) the three degassing signals match so well that they are hardly to distinguish: after the ramp-up phase the peak height shows a very similar value. The non-single-exponential decays at the beginning of constant temperature are alike. Also the single-exponential decay from all three measurements, which is the area of fitting for the

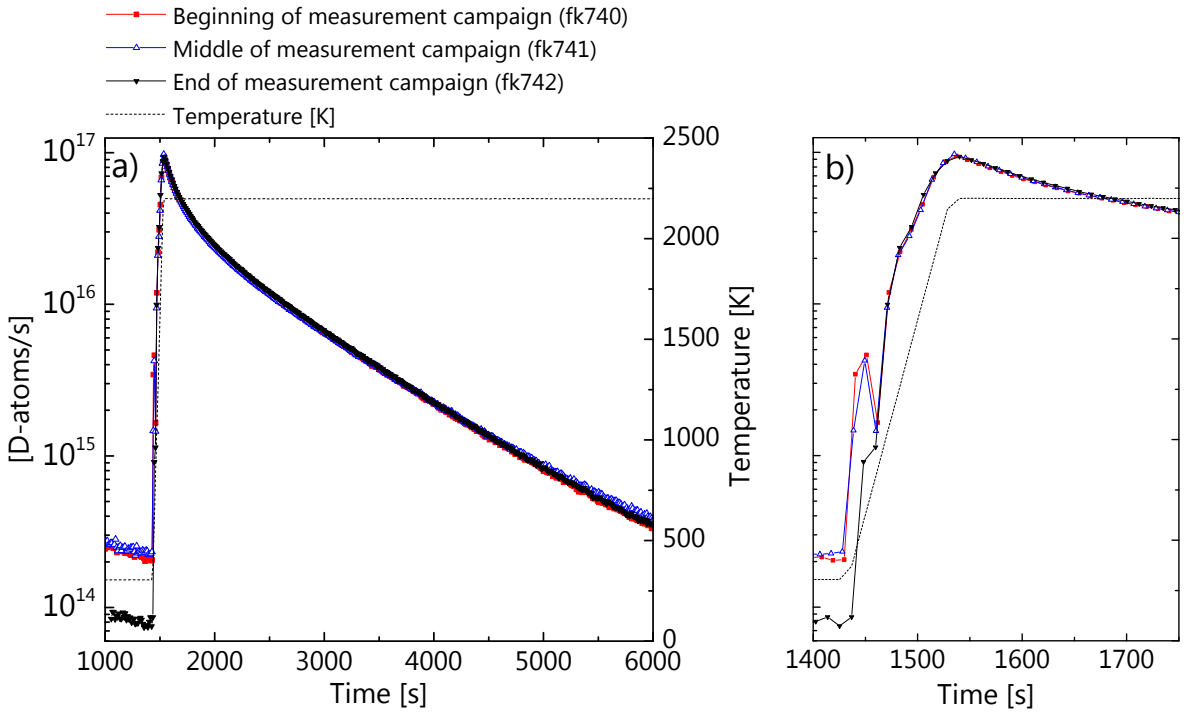

Figure 3.1.: Three different measurement cycles are shown, using the same loading and degassing conditions: loading at 500 mbar deuterium at 2000 K for 60 min, outgassing with 20 K/s to 2200 K for 120 min. Three experiments are showing the beginning of the campaign and one from the middle. They both used the liquid nitrogen trap prior to gas loading. The third measurement cycle is from the end of the campaign with 62 measurement cycles in total, the LN trap was not used. a) shows the complete cycle, b) zooms in for the ramp-up phase with identical y-axis for the D-flux and temperature as in a).

diffusion model later on (2500 s < t < 4300 s), is in excellent agreement[1]. Figure 3.1b) shows the ramp-up area in more detail. fk742 does not exhibit the usual pre-peak(s) (as discussed in the following in chapter 3.6) but nevertheless, afterwards follows exactly the same degassing behaviour of the other two measurements. The usage of the LN trap obviously plays no role in the release when having reached constant temperature.

Measurement cycles that exhibit the same loading conditions and equally executed temperature control for degassing are very reproducible and stable over time. This concludes the measurements being independent of:

- Ageing or degradation of the QMS-detector
- Usage of liquid nitrogen (LN) trap prior to filling the glass tube for gas loading
- Background flux at the beginning of the measurement
- Ageing effects of the specimen throughout the campaign

The reproducibility of the degassing is based on the repetitive accuracy of the temperature measurement and control. This relates to the relative reproducibility, i.e., that the temperature reading of repeated ramp and hold experiments show negligible deviations to each other. Hence, the high reproducibility of the degassing proofs that also the reproducibility of the temperature measurement is very high. However, the absolute accuracy of the temperature measurement cannot be proven by this and is estimated in the following section 3.1.2.

3.1.2. Temperature measurement differences

In most of the experiments, the sample temperatures did not exceed 2400 K. Hence, most of the times the input value for the temperature controller was the thermocouple. The reading of the pyrometer gives a second temperature reading above 1273 K (see chapter 2.5.4.1). By this the discrepancy of both readings can be used to estimate uncertainties in temperature measurement and contribute to error bars for the results of diffusion and solubility.
This evaluation of uncertainties in temperature is done for:
Firstly, dynamic conditions at ramp-up and cool-down, where these discrepancies are dependent on temperature gradient at ramp-up and cool-down phase at the end of gas loading. Moderate ramps of 1 K/s and fast ramps of 30 K/s as well as heating switch-off is evaluated to estimate the maximum range of deviations.
Secondly, static conditions at constant temperature, as this is important for the degassing sequences.

All experiments concerning temperature measurement discrepancy, both in dynamic and static phase, are tested with the small poly-crystalline sample.

3.1.2.1. Dynamic phase: ramp-up and cool-down

Temperature ramp-up and ramp-down: moderate ramping rates (1 K/s)

The temperature is ramped-up at a rate of 1 K/s to 2523 K and held for a dwell time of 300 s, then ramped-down again with a rate of 1 K/s. The temperature discrepancy is zero at the

[1] The fitting window is described at the end of this chapter in section 3.3 when all uncertainties and prerequisites have been defined.

beginning of the measurement range of the pyrometer. This evaluation is done in vacuum because the accuracy of the temperature while ramp-up is mainly important for the degassing measurements. For gas loading the temperature ramps are not of particular importance, because the thermodynamic equilibrium is determined by the dwell time at the gas loading temperature (see chapter 4.2.1).
The left panel in figure 3.2 shows the type-C thermocouple reading minus the pyrometer reading as function of the type-C thermocouple reading. The nominal accuracy of the type-C thermocouple (±1% of the temperature in °C) is shown as red dotted line.

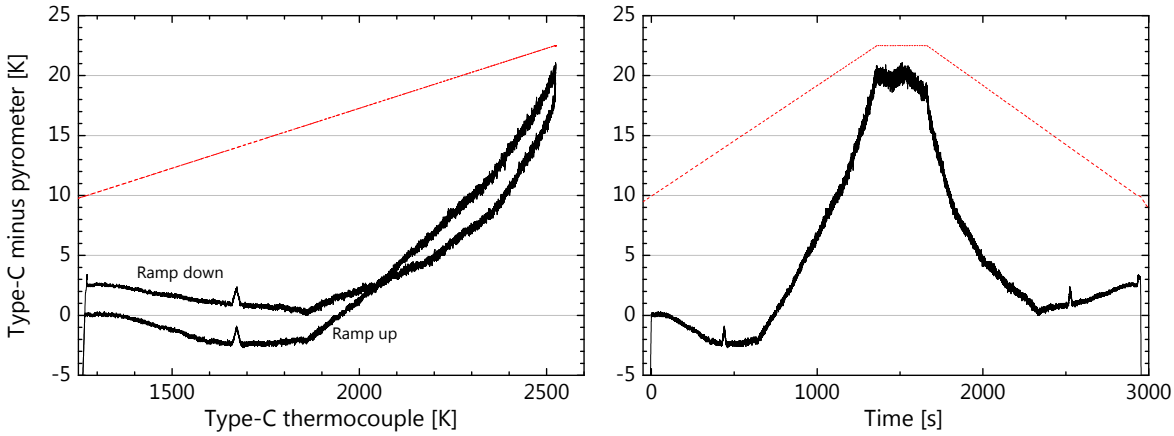

Figure 3.2.: Difference of the type-C thermocouple and the pyrometer reading. A temperature ramp-up and ramp-down of 1 K/s to 2523 K with a dwell time of 300 s can be seen. The maximum deviation of both readings is about 20 K and does not exceed the nominal accuracy of the type-C thermocouple of ±1%, which is shown as red dotted line.

The measurement range of the pyrometer begins at 1273 K (1000°). The hysteresis shows only a marginal difference of the readings for ramp-up and ramp-down. At about 1623 K (1350°C) in both temperature traces a small "spike" in positive temperature direction of less than 2 K can be observed. At this kind of plot this spike is always to be seen at the same temperature. The origin of this spike is unknown, possibly the temperature measurement is influenced by internal adjustments of the inductive furnace. It seems plausible that this is a systematic artefact from the furnace rather than a "real" physical effect. The right panel in figure 3.2 shows the deviation of the two readings in dependence of time. The maximum deviation of roughly 20 K is at the plateau temperature of 2532 K. The total discrepancy over the whole ramp is within the nominal accuracy of the type-C thermocouple At the plateau temperature of 2532 K this is ±22.5 K (as the accuracy is defined with 1% difference from the temperature reading in °C).

Dynamic phase with fast temperature ramp-up (30 K/s) and shut-off heating at plateau temperature

The deviation of the temperature readings is also measured in vacuum for a rather fast ramp-up of 30 K/s - which is by 10 K/s more than the fastest ramp utilised for quantitative measurements of 20 K/s. When reaching the final temperature of 2523 K the temperature is held

for 45 s, then the heating is switched off. The same procedure is undertaken in 500 mbar deuterium. The deviation is comparable or smaller, hence only the vacuum case is shown.

Figure 3.3 shows the hysteresis of the difference of type-C thermocouple and pyrometer reading at the left panel. As before, the difference is shifted so that it is zero at the beginning of the measurement range of the pyrometer.

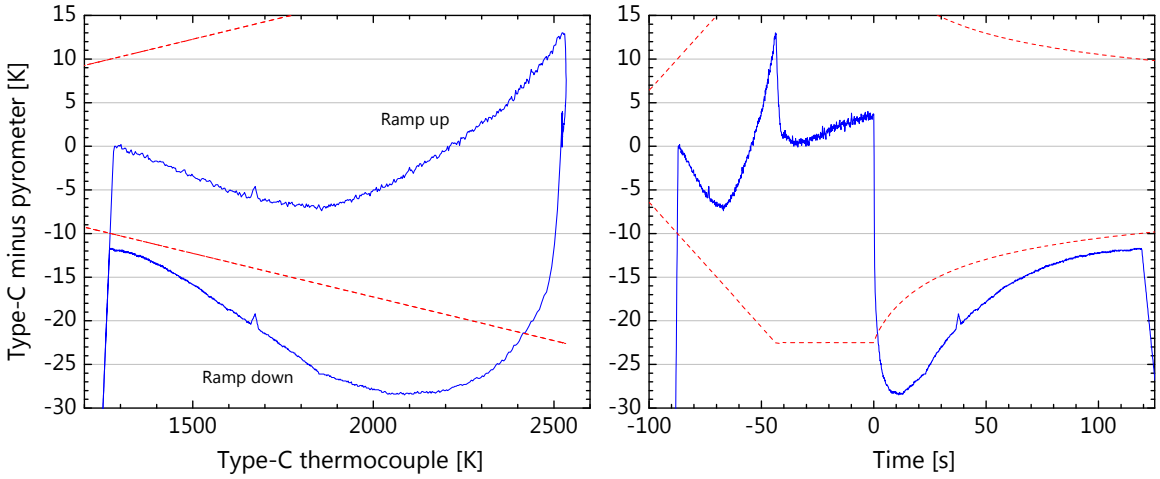

Figure 3.3.: 30K/s ramp and following shut-off of the heating in vacuum. The nominal accuracy of the type-C thermocouple (±1% of the temperature in °C) is plotted as red-dotted lines.

The deviation becomes negative at the beginning, then becoming positive at about 2200 K. It reaches about +13 K when temperature is just reaching the plateau temperature. The right panel in figure 3.3 (deviation plotted over time) shows that when temperature has reached its plateau at about -45 s, the deviation goes down sharply and reaches +3 K. At 0 s the heating is switched off. The deviation rises sharply to a negative value of nearly 30 K, the thermocouple reading shows a higher value than the pyrometer. Shortly after the heating is switched off the deviation exceeds the nominal accuracy of the thermocouple until the end of the measurement range of the pyrometer. The maximum deviation at 2050 K while cool-down is about 1.6%.

The temperature reading at the cool-down phase is especially relevant at the gas loading of every measurement cycle. When the diffusion model is applied at each measurement, it does a forward calculation to estimate the amount of hydrogen which is left in the specimen when the degassing phase begins. The hereby exhibited enhanced uncertainty in temperature readings are taken into account in this concern - especially the analysed solubility is affected.

The difference of both readings increases with higher temperature gradients, e.g., the deviation at the beginning of the cool-down phase is at its maximum when the gradients are still high (see figure 3.3). The deviation gets less when the gradient gets smaller. This indicates a higher inertia of the type-C thermocouple reading in comparison with the pyrometer.

3.1.2.2. Static phase at nominally constant temperature

This section treats a temperature drift of the thermocouple compared to the pyrometer and is observed in hydrogen (protium as well as deuterium) atmosphere mainly. In vacuum a smaller drift is to be observed, about one third of the drift in hydrogen. This drift in vacuum

stays within the ±1% nominal accuracy of the type-C thermocouple. The drift in hydrogen atmosphere seems of another nature than the one described in chapter 3.1.2.1 and hence is treated in a separate subsection.

The left panel in figure 3.4 shows a temperature ramp and hold to 2400 K in 500 mbar deuterium. The ramp is executed at 20 K/s, the type-C thermocouple is the input parameter for the temperature controller. When reaching final temperature, the plot shows a constant temperature reading of the type-C thermocouple and a drift of the pyrometer reading downwards in temperature. The observed drift endures roughly 500 s after reaching the temperature plateau. The relative output power qualitatively follows the trend of the pyrometer temperature reading.

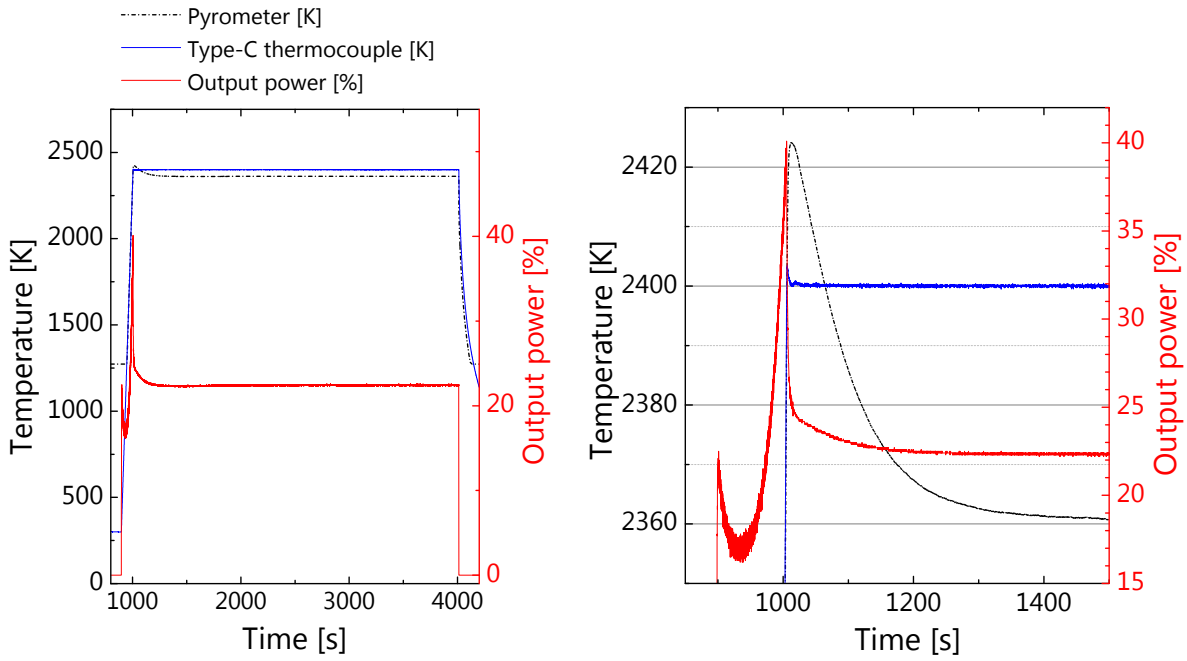

Figure 3.4.: Temperature drift of pyrometer in comparison to type-C thermocouple reading in 500 mbar deuterium atmosphere. Total observed drift is 63 K.

Figure 3.4 in the right panel shows a zoom of the transit of the temperature ramp toward the plateau. The beginning of the temperature ramp at about 900 s shows an overshoot of power input in the beginning with a subsequent drop to follow the ramp. At about 1000 s, the type-C thermocouple reading reaches the temperature plateau of 2400 K and then stays constant. The power input decreases sharply accordingly at the beginning of the temperature plateau, but it also decreases further until about 1300 K although the temperature reading of the type-C thermocouple stays constant. The temperature reading from the pyrometer decreases accordingly to the power input and stays constant at 1500 s. The drift of the pyrometer reading is about 63 K (from 2424 K down to 2361 K). This drift is observed in all gas loading sequences and is consistent with a drift of input power. The long-term deviation of the pyrometer temperature reading is 1.8%. Hence, the uncertainty concerning the temperature (which is input for the diffusion model) is extended by this value in negative direction, i.e., towards lower temperatures.

Discussion

There are two scenarios plausible that could cause such a temperature drift of the pyrometer reading: Either temperature is really changing and the reading from the thermocouple is wrong - or the emissivity of the specimen is decreasing in hydrogen atmosphere.

If we assume th type-C thermocouple output is drifting to higher values at nominally constant temperature of the sample, the controller would compensate it by lowering the power. However, as the temperature drift is consistently observed and always the same, the reason cannot be an ageing of the type-C thermocouple. It is therefore unlikely that the temperature really changes.

The other scenario is that not the temperature is changing, but the emissivity of the tungsten specimen. This would explain that type-C thermocouple reading stays constant. The pyrometer would show lower temperature because of lower emissivity. The requested power output for heating drops, because decreasing emissivity of the specimen means that it radiates less power at the same temperature.

By comparing the drop in power with the according change in emissivity (by utilising equation 2.9 and correlating the pyrometer reading to change of emissivity) this yields a change of emissivity of 0.03 from 0.31 to 0.28 within 570 s. The decreased required input power by the induction furnace exactly correlates with the assumed decrease of emissivity. If the emissivity really changes, the time scale of the drift of some hundred seconds would suggest that the reason could be the reduction of tungsten on the hot surface, e.g., in interaction with elements from the inner glass wall, that changes the emissivity, but the proof could not be given within this thesis' work.

3.1.3. Background signals

All measurements with protium and deuterium exhibit a background-flux measured with the QMS that stems from surface desorption at the inner walls of the apparatus. For example, increased radiation from the specimens at high temperatures causes increased temperature of the inner glass wall and hence increased desorption from the inner glass wall[2]. This influence of secondary signals distorts the degassing signals from the specimens, especially at low signal-intensities (e.g., low hydrogen inventory measured from one of the small specimens). Hence, the diffusion model needs an estimate for the background level for the measurements. This background is estimated in the following.

A thin hollow cylindrical sample is used to estimate the background level during degassing measurements. A hollow specimen of tungsten with an outer diameter of ∅15 mm, a wall thickness of 0.5 mm and a height of 48 mm is used. This sample is gas loaded and degassed. Because of the small wall thickness, almost no hydrogen is held in solute in the bulk. In comparison to the bulk sample the measured inventory is by 3.7%. The sample, mounted within the glass tube, is shown in figure 3.5. It is mounted directly with the two type-C thermocouple wires (∅0.5 mm) that are manually laser-welded to the inner surface of the hollow specimen. The inductive coil can be seen around the glass tube.

Figure 3.6 shows a full measurement cycle with gas loading and degassing of the hollow sample in the small glass tube. This is compared to the same measurement cycle that is done with the single-crystalline specimen of similar size. The gas loading for both specimens is

[2]Naturally the protium background is higher compared to deuterium background, because of its naturally higher abundance in air.

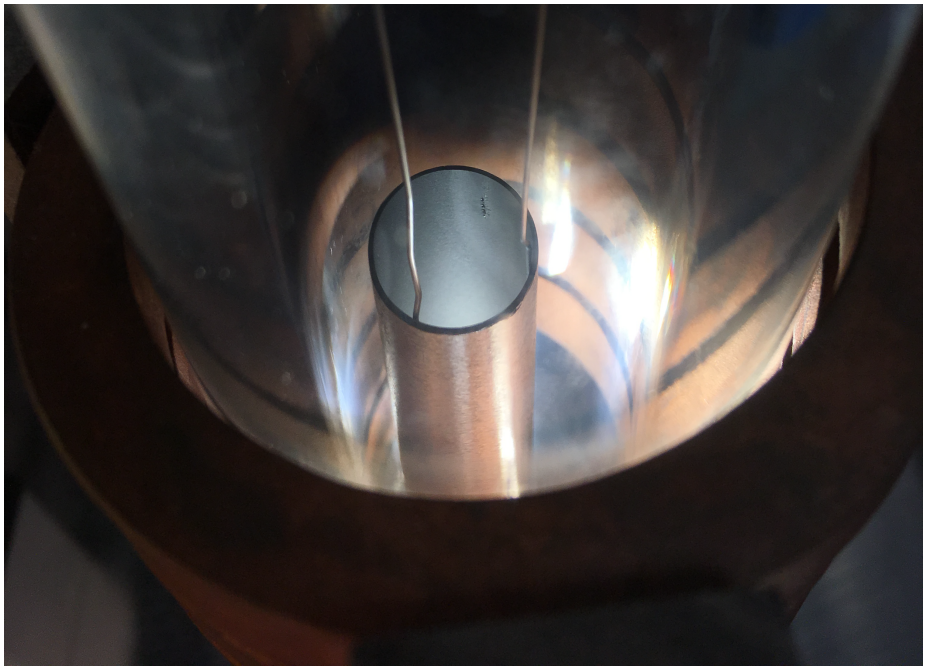

Figure 3.5.: A picture of the hollow sample, already mounted in the glass tube. The sample has an outer diameter of ∅15 mm, a wall thickness of 0.5 mm and a height of 48 mm. It is mounted directly with the two type-C thermocouple wires (∅0.5 mm) that are manually laser-welded to the inner surface.

done at 2000 K for 30 min in 500 mbar deuterium, using the LN trap. Both measurements are started at the same background level of roughly $5.5{\cdot}10^{13}$ D-atoms/s. The sample temperature is ramped up with 1 K/s to a temperature of 2000 K and held constant. The spectra are horizontally shifted so that their temperature ramps match each other - the shut off of the heating differs in time.

Figure 3.6 shows the flux of atoms (left scale), the temperature of the specimens (right scale), in addition the temperature of the cooling water of the glass tube from the hollow sample measurement (very right scale). This temperature is measured in the water pipe at the outlet of the glass tube, i.e., after the area where the specimen is heated.

At the beginning of the temperature ramp the signal of the (bulk) single-crystalline specimen rises sharply to roughly $2{\cdot}10^{14}$ D-atoms/s. The signal seems to show a shoulder before decaying to roughly $1{\cdot}10^{14}$ D-atoms/s. Then the signal rises to the main peak, which is during the temperature ramp-up because the ramp is sufficiently slow. Then the signal decays and shows a faster decay when temperature reached its plateau of 2000 K. Towards the end of the temperature plateau, beginning at fluxes of about $3{\cdot}10^{14}$ atoms/s (i.e., already background level) small oscillations of the signal can be seen. When the heating is switched off, the signal from the single-crystalline specimen shows a "dip" before it decays further. The signal from the hollow sample also rises sharply at the beginning of the temperature ramp-up until it reaches a peak flux of about $3.5{\cdot}10^{14}$ D-atoms/s. After the first peak the signal from the hollow sample also exhibits a sharp drop. At roughly 750 K the signal rises again to a peak before it sharply drops again to roughly background-flux before the beginning of the measurement. The signal from the hollow sample then rises slowly while the temperature ramp continues,

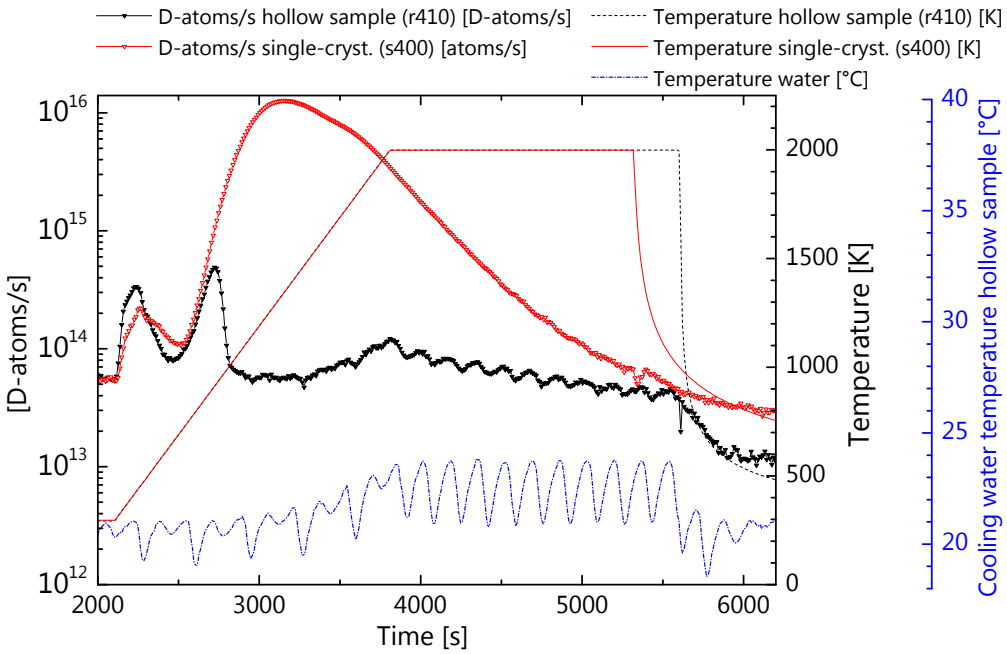

Figure 3.6.: The single crystalline specimen in comparison with a background measurement (by utilising a hollow thin cylinder). Loading and degassing was executed equally: loading at 2000 K for 30 min in 500 mbar deuterium, degassing with a 1 K/s ramp to 2000 K. The hollow sample shows two peaks at the ramp-up phase (presumably from the surface and the bulk) and a strong correlation of measured deuterium flux to the cooling water temperature.

exhibiting irregular small dips. When the temperature reaches the constant plateau of 2000 K, the overall signal decays, exhibiting regular "wiggles". They coincide with the temperature variation of the cooling water. When the heating is turned off and the temperature decreases, the measurement of the hollow sample exhibits a very short dip (measured by only one mass scan at mass 4 from the QMS). Then the signal decays with decreasing temperature.

When the plateau temperature of the hollow specimen is reached, the temperature of the cooling water (hollow sample measurement) is oscillating roughly within the range of 20.8°C to 23.8°C (3°C magnitude). This oscillation is allowed intentionally to signal the high influence of background-flux from the inner glass wall and is described in chapter 2.5.5.4.

3.1.3.1. Estimation of background flux

The wiggling deuterium signal from the hollow sample that rises slowly after the two sharp main peaks do not stem from the hollow sample itself - it is gone after the second peak that exhibits the bulk inventory. The first peak presumably stems from surface effects, see next section 3.1.3.2. The conclusion can be drawn that the background-flux mainly stems from increased degassing of the inner glass wall (or the glass sub-surface) from the increased temperature caused by the radiation of the specimen. Hence the outer surface of the hollow sample is roughly the same as the surface from the small specimens, the background for those bulk samples should be in the same range. The large influence of the cooling water temperature oscillation suggests that the temperature of the inner glass wall is not much higher than the cooling water temperature (see also chapter 2.5.5.1).

The background-level varies between $1{\cdot}10^{14}$ atoms/s at the beginning of constant temperature and about $2{\cdot}10^{13}$ atoms/s at the end of the degassing phase.

The background-level for the big glass tube ranges at the same levels. Therefore, the following levels are taken as background in the evaluation of the exponential decay:

- Protium (H): $5{\cdot}10^{13}$ atoms/s.
- Deuterium (D): $2{\cdot}10^{13}$ atoms/s.

The full diffusion model which is used to analyse diffusion and solubility coefficients, integrates the background-level as part of the input. These background-levels are assumed to be constant. The application of the estimated (and assumed to be constant) background-levels shows that this assumption is convenient and delivers reasonable outcomes.

3.1.3.2. Discussion

Presumable surface peaks

The first peak during the temperature ramp around 500 K that was visible for the hollow sample seems to correlate with a surface monolayer of deuterium atoms. The hollow sample with a calculated surface of $4.5{\cdot}10^{-3}$ m^2 (inner and outer surface of the hollow cylindrical specimen) would exhibit a monolayer of deuterium of $4.5{\cdot}10^{16}$ D-atoms[3]. The measured amount of deuterium from this peak from the hollow sample is $4.48{\cdot}10^{16}$ D-atoms (integrated D-flux signal from $2105\,\text{s} < t < 2478\,\text{s}$, the measured background flux of $5.5{\cdot}10^{13}$ D-atoms/s which

[3] By assuming an equivalent of D-atoms in comparison to the measured monolayer of H-atoms on tungsten of $1{\cdot}10^{19}$ H-atoms/m^2 by Tamm & Schmidt [52].

leads to an integrated background of $2.05{\cdot}10^{16}$ D-atoms is already subtracted).
The single-crystalline specimen has a surface of $2.615{\cdot}10^{-3}\,\mathrm{m}^2$, which results in an estimated amount of $2.62{\cdot}10^{16}$ D-atoms if a monolayer of deuterium is assumed. The integrated amount of the signal within the same range as for the hollow sample gives $3.41{\cdot}10^{16}$ D-atoms (also subtracting the correlating background).
The comparison of the calculated amount of deuterium and the measured amount of deuterium from the hollow sample shows excellent agreement. The calculated amount for the single-crystalline specimen is about $\frac{1}{4}$ less than the measured amount of deuterium. This "missing" fraction could stem from the tungsten mounting shaft, or the peak is simply too much smeared out so that the total measured amount deviates.
These observations lead to the conclusion that the pre-peak(s) presumably stem from the specimens' surface, because of: Firstly, the good agreement of measured deuterium from the first peak with an estimated monolayer of deuterium on the surface. Secondly, deuterium desorption from the hollow sample and the single-crystalline specimen starts at the same temperature which is in line with the same activation energy for desorption of both specimens' surfaces.

The second peak in the spectrum from the hollow sample measurement probably stems from the bulk of the thin-walled sample. The 0.5 mm thin wall can only hold a fraction of the solute deuterium in the bulk after the cool-down phase of the gas loading.

Dip at the end of the measurement

Figure 3.6 shows the degassing signal of the single-crystalline specimen. At the end of the temperature plateau the heating is switched off and a "dip" can be seen: the signal goes down instantly when the temperature goes down, then rises again (although the temperature is still decreasing), to about the level before, and then decays slowly. This dip is characteristic for most of the measurements of all specimens. The dip only appears for degassing measurements with temperatures $\geq 1600\,\mathrm{K}$. At temperatures below this it not observed.

The amount of deuterium "missing" in the dip of this measurement of the single-crystalline specimen is $7.3{\cdot}10^{14}$ D-atoms. This does not correlate with an estimated monolayer at the specimens' surface or the surrounding glass wall of the glass tube. The amount that is missing in the sharp dip from the measurement of the hollow sample cannot be estimated because it is only covered by one scanning cycle at mass 4 of the QMS.

A possible mechanism could be a temporary getter process of the specimen itself. As the temperature steeply decreases when the heating is shut off, the outgassing from the specimen also goes down sharply. Additionally, as long as the specimen exhibits temperatures above $\sim$1300 K it still re-getters parts of the hydrogen that is still in the glass and impacts on the surface of the specimen from the present background in the vacuum vessel. This background is increased before by radiative power from the specimen, warming also other parts and surfaces of the main vacuum vessel, i.e., inner glass wall, the mounting shaft, upper steel flange of the quartz glass tube. This could lead to an overall larger drop below background level until the specimen reached 1300 K. Therefore the dip would be a lot smaller in the measurement with the hollow sample, because it cools down much faster below 1300 K. The threshold temperature of 1300 K is estimated from the experiment, i.e., the extension of the dip in the signal from the small poly-crystalline sample. The dip ends at about 1300 K. At lower temperatures both samples stop desorbing additional hydrogen. The signal rises back up to the slowly decaying background level of the vacuum vessel.

3.2. Guidelines for consistent measurements

After quantifying the uncertainties concerning temperature measurement or background-flux, a few qualitative guidelines are defined and which shall be used in the quantitative assessment (qualitative measures that yield reliable quantitative results). All measurement cycles that are used for the data set as input for the diffusion model[4] fulfil the following recipes:

- Temperature ramps shall be as fast as possible
  - They help to raise the signal height, i.e. the main amount of dissolved hydrogen can be used for identifying and fitting the single-exponential decay at degassing rates when they are still sufficiently high. This yields a high signal-to-noise ratio which increases the fitting area and keeps possible background effects low.
  - They yield a relatively high overshoot of the non-single-exponential decay where the higher modes in the specimen decay towards the single-exponential decay, see figure 1.4 in chapter 1.4.3. Hence the settling towards single-exponential decay can be observed in the signal (and need not to be assumed). This helps identifying the beginning of the fitting window and yields reliable outcomes.
  - They lead to a fast rush through the temperature region of signals that cannot clearly be denoted, e.g., presumably surface effects.
  - Possible trapping or surface effects at estimated temperatures $\leq 1600\,\mathrm{K}$ are acting at a small time window at the rise of the degassing signal, which is not used for fitting.
  - Generally, the faster the ramp to the fitting region at constant temperature is, the less time there is that the sample can change by surface effects.
- High loading temperatures
  - They lead to high signals, similar to fast temperature ramps. Loading temperature needs to be varied to derive the solubility. But the higher the loading temperature is, the less influence presumably background effects have.
  - Temperatures higher than roughly 1600 K help to eradicate trapping effects. Even if traps are present, the higher the temperature, the less populated they are and hence hydrogen populates the solute only (this is also observed in experiment, see chapter 4.4.2 and 5.2.2).

These guidelines help to execute measurement cycles that are stable against varying crystalline structure of the specimens, background flux, trapping effects (for both at loading and degassing) and presumable surface effects.

Fast temperature ramps are in contrast to deliberate operation of the QMS, i.e., to the measurement range of the QMS. Temperature ramps that are too fast and result in count rates higher than roughly 10^6 counts/scan substantially age the detector and can significantly shorten its service time, making a soon opening of TESS necessary for replacement (cf. chapter 2.4). Hence, using fast ramps is delicate and always a trade-off function between altering the QMS detector and getting high signal rates.

[4] There are two data sets for each of the modelling methods, reduced and full diffusion model. One data set with measurements cycles with protium, one with deuterium.

3.3. Defining the fitting window for the diffusion model

To derive diffusivity and solubility the experimental data is evaluated by the diffusion model. It fits a pre-defined range of the experimentally measured degassing decay and adjusts the four variables E_A, D_0, E_S, and S_0 in order to get the best fit for a data set of measurement cycles. For this a fitting window is defined that can be applied for both the big specimen and the small specimens (single- and poly crystalline).

The upper end of the fitting window is chosen to be the beginning of single-exponential decay at constant temperature, i.e., when the concentration profile in the specimen is dominated by the fundamental mode ($m = 1$), see chapter 1.4.3 and figure 1.4.

The lower end of the fitting window is estimated by an estimation of the influence of the background on the gradient of the decay.

The height of the background-level for protium and deuterium is estimated in chapter 3.1.3.1 and is also part of the input for the diffusion model code.

Figure 3.7 shows a degassing measurement of the big specimen that was loaded at 2400 K for 50 min in 500 mbar deuterium. The degassing is done at 2200 K with a ramp of 20 K/s. The originally measured signal is shown, and exemplarily the signal after subtraction of various backgrounds, ranging from $1{\cdot}10^{13}$ atoms/s to $1{\cdot}10^{14}$ atoms/s. The background as input for the diffusion model is estimated to $2{\cdot}10^{13}$ atoms/s for deuterium and to $5{\cdot}10^{13}$ atoms/s) for protium in chapter 3.1.3.1.

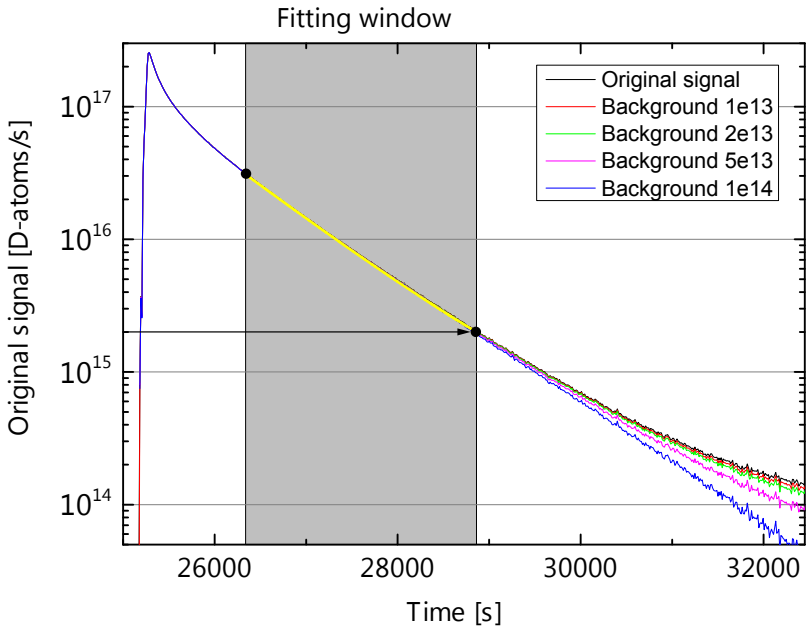

Figure 3.7.: A degassing measurement of the big specimen which is loaded at 2400 K for 50 min in 500 mbar deuterium atmosphere. Degassing is done with a 20 K/s ramp to 2200 K. The influence of various background-levels to the main signal is shown. The maximum shown background of $1{\cdot}10^{14}$ atoms/s (five times higher than the experimentally measured background) starts to have a significant influence on the single-exponential decay at a flux lower than $2{\cdot}10^{15}$ atoms/s. This value is chosen as lower value for the fitting window of the diffusion model.

All signals are hard to be distinguished from each other, until they reach a flux level of about $2{\cdot}10^{15}$ atoms/s, hence the level of $2{\cdot}10^{15}$ atoms/s is chosen as lower end of the decay fitting window.

Accordingly, the fitting window for the diffusion model is defined firstly, by the beginning of single-exponential decay at constant temperature and after the overshoot, and secondly, when the signal reaches a flux of $2{\cdot}10^{15}$ atoms/s.

3.4. Maximum-likelihood evaluation with the full diffusion model

The experimental data is handed over to the full diffusion model code as a set of 7 different measurement cycles for the big specimen with protium, or 9 measurement cycles with deuterium, respectively. Each exhibit a different loading and degassing sequence. The set of measurement cycles for both isotopes is shown in figure 5.4 in chapter 5.2. The degassing signal in the form atoms/s is converted from the QMS-raw signal (counts/s) to a flux of hydrogen (H oder D) atoms, by making use of the calibration method (see chapter 2.4). The temperature reading is included in the data set with time steps of 0.1 s. The temperature reading that is handed over to the diffusion model code begins already at the moment when the cool-down phase sets in at the end of the gas loading sequence.

Additionally, the loading temperature and gas pressure of the designated measurement cycle are fed to the full diffusion model code. The background is also included in the model, as mentioned above. Furthermore the geometry, i.e., radius and height of the cylindrical specimen is provided as an input for each measurement cycle. Finally, for every measurement cycle the fitting window is chosen manually by applying the methods described in the previous section 3.3.

The full diffusion model uses a maximum-likelihood evaluation of the measured data within the fitting window. Figure 3.8 shows the fitting window of a measurement cycle with protium with the big specimen. The temperature has already reached the plateau and the decay of degassing behaves single-exponential, hence appears almost linear in the logarithmic plot. This measurement is part of a data set of 7 measurement cycles for protium which are simultaneously analysed by the full diffusion model code. Gas loading is done at 2000 K for 60 min, degassing is done with 15 K/s to 1800 K. The number of degassed protium atoms per second is shown on the left y-axis in logarithmic scaling together with the best fit. The comparison of the amount of hydrogen from the measurement is also part of the model. χ^2 is shown at the right axis of figure 3.8. χ^2 is a measure for deviation of the fit from the experimentally measured degassing signal [53, 54, 55]:

$$\chi^2 = \sum_{j=1}^{m} \frac{(N_j - n_j)^2}{(\sqrt{N_j} + 0.01 \cdot N_j)^2} \tag{3.1}$$

where N_j[counts] is the value of a measured degassing signal within one time step and n_j is the modelled degassing signal, derived from the diffusion model code at the same time step. The numerator presents the squared difference of model and measured degassing signal. The denominator presents the squared estimated statistical uncertainties. They concern, firstly, the counting statistics $\sqrt{N_j}$ of the QMS and, secondly, the relative statistical uncertainties of the measured degassing signal which are estimated to be 1%: $0.01 \cdot N_j$. The 1% statistical

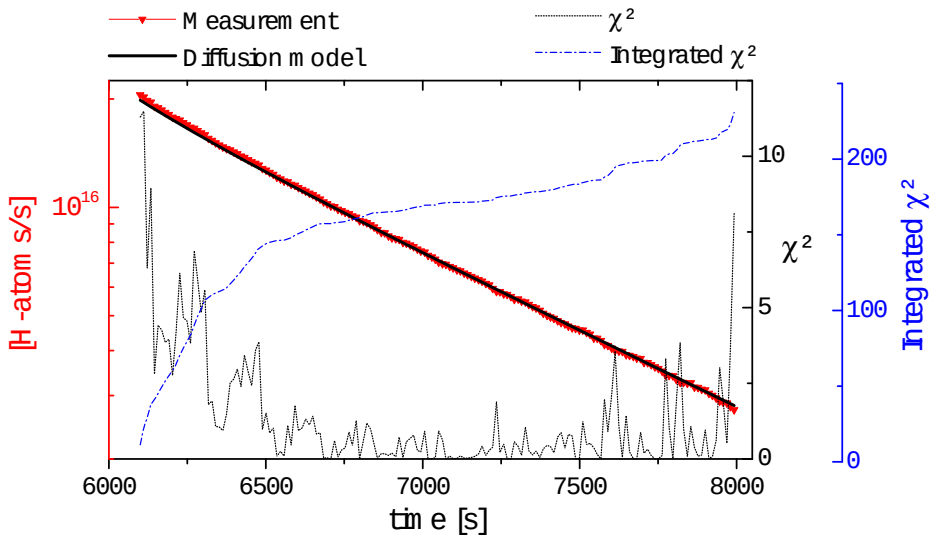

Figure 3.8.: Measured hydrogen desorption (protium fk110) and the result for the best fit from the full diffusion model is shown in the fitting window of single-exponential decay of the degassing. Loading conditions are 2000 K for 60 min in 500 mbar protium, degassing is done with 15 K/s to 1800 K. The best fit is shown as solid black line. χ^2 is shown as dotted black line, it represents the deviation of the model from the measured data and is a relative measure for the quality of the fit. The integrated χ^2 is shown as dashed blue line at the very right y-axis.

uncertainty represents possible uncertainties in wall effects of the inner glass wall, e.g., by increasing coating of the glass, or drifts of the QMS detector that are measured during the calibration after every measurement and that are measured to be smaller than 1%.

In the example of figure 3.8 the χ^2 value is smallest in the middle area of the fit. The integrated χ^2 value in this case rises slight over 200. The code simultaneously adjusts the 4 variables, E_A, D_0, E_S, and S_0, for all 7 measurement cycles in parallel so that the "goodness of fit", the χ^2 value, for all fits is minimal. The full diffusion model code for protium and deuterium uses the χ^2 value for fitting. To obtain an independent quantity to compare the goodness of fit for different measurement cycles, it is advantageous to normalise χ^2 to the number of measurements. This yields the average goodness of fit $\hat{\chi}^2$ for a run of the full diffusion model code for each data set.The normalised, dimensionless $\hat{\chi}^2$ is defined by:

$$\hat{\chi}^2 = \frac{\chi^2}{\sum_{n=1}^{N} t_n \cdot \nu_n} \tag{3.2}$$

$\hat{\chi}^2$ depends on the accumulated duration of the fitting windows t_n for each data set n. ν_n denotes the measurements per second and is calculated by the inverse of the duration of one mass scan from the QMS (which is the same for both, mass 2 and mass 4):

$$\nu = \nu_n = \frac{1}{10.67\,s} \tag{3.3}$$

This yields:

$$\hat{\chi}^2 = \frac{\chi^2}{\nu \sum_{n=1}^{N} t_n} \tag{3.4}$$

$\hat{\chi}^2$ should be around 1 [56]. If $\hat{\chi}^2$ yields a value much bigger than 1, the uncertainties are underestimated. If $\hat{\chi}^2$ yields values much smaller than 1, the uncertainties are overestimated.

3.5. Forward modelling

The forward modelling shows, if the full diffusion model is able to describe also the degassing outside the fitting window at earlier times. When fitting the single-exponential decay of degassing within the fitting window of a measurement cycle, the full diffusion model code derives the values of the four variables E_A, D_0, E_S, and S_0 that describe solubility and diffusivity. With the evaluated variables, the presumed degassing profile before the fitting window can be modelled by applying the prerequisites from the diffusion model.

The measured temperature trace of the specimen before the fitting window (beginning when heating is switched off at the end of the gas loading sequence) is used to derive the solubility and diffusivity to forward-calculate the degassing.

Figure 3.9 shows the degassing sequence of a measurement cycle (fk850), together with diffusion model within the fitting window (yellow line). Also the forward modelling of the full diffusion model before the fitting window is shown as red line. The loading conditions

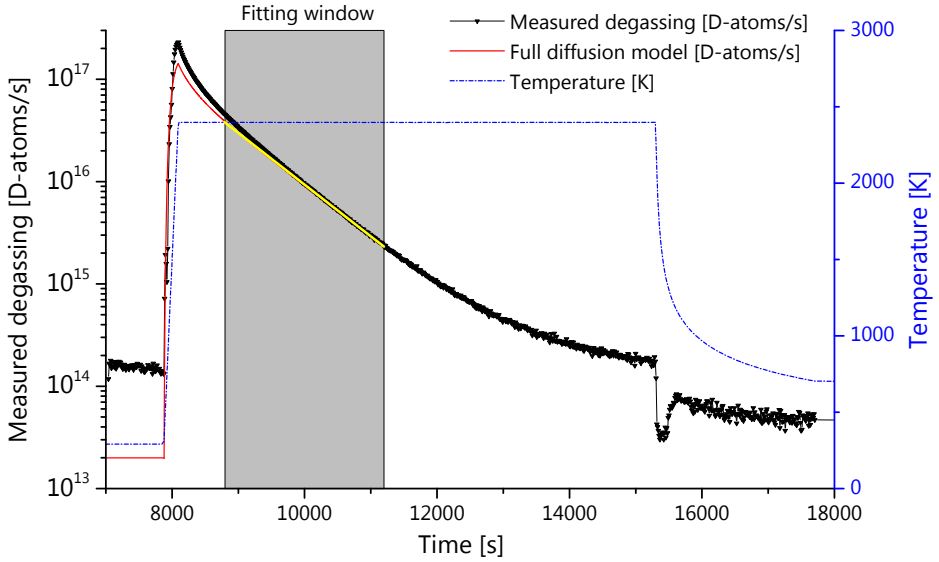

Figure 3.9.: Deviation of forward modelling from the measured degassing signal. Gas loading is done at 2400 K for 50 min in 500 mbar deuterium. Degassing is executed with a 20 K/s temperature ramp to 2400 K. Although the fit is sufficiently good within the fitting window, the modelling yields a lower degassing rate at the signal overshoot. This seems to stem from non-diffusive transport phenomena that act before the single-exponential decay, i.e., presumed temporary oxide layer on the specimen or effects from the inner glass wall. Nevertheless, these effects seem to vanish before the fitting window and hence do not influence the evaluation.

are 2400 K for 50 min in 500 mbar deuterium atmosphere; the degassing is done with 10 K/s to a temperature plateau of 2400 K. The degassing signal rises when temperature is ramped up, exhibiting the presumed surface spike. At the end of the temperature ramp the usual overshoot/non-exponential decay can be seen, then becoming single-exponential. This is where the fitting window is applied and for which the four variables are adjusted to fit the measured profile. Towards the end of the degassing sequence the signal decreases close to the background. When the heating is shut off, it shows the characteristic dip, see chapter 3.1.3.2.

The fitting window for the diffusion model in this measurement is set to 8800 s $<$ t $<$ 11200 s, according to the procedure for decay fitting, see chapter 3.3. The graph also includes the forward modelling of the diffusion model, i.e., t $<$ 8800 s, the background is added to the graph because the modelled degassing signal is given out background-subtracted. The diffusion model qualitatively describes the degassing behaviour like the measured degassing signal. It shows a non-single-exponential overshoot when temperature reached the plateau. The model however underestimates the measured degassing signal which reaches a peak higher than predicted from the diffusion model. The peak height from the diffusion model is about 3/5 compared to the measured peak height. This trend of the modelling in comparison with the measurement is qualitatively the same throughout all fitting-measurement combinations for protium as well as for deuterium.

The diffusion model per se describes transport based on Fick's equations for diffusive transport, in dependency of the concentration gradient and temperature in 3-dimensional geometry, see chapter 1.4. It assumes that transport is depending on the bulk properties only, whereas it ignores the surface of the inner glass wall or surface effects on the specimen, such as presumed temporary oxide layers, cf. the following in chapter 3.6. Such non-diffusive effects which are not described by the diffusion model, seem to appear at the temperature ramp-up phase and shortly after when the temperature reaches the constant level and the degassing signal overshoots, i.e., decays non-single-exponentially. This is the area, which the diffusion model cannot describe by utilising its assumptions of diffusive transport. However, after this area when the fitting window begins, the diffusion model matches the experimental observations. It is not known, which effects exactly cause the difference of model and measurements, but those effects seem to vanish before the area of single-exponential decay, which is chosen for the fitting window.

3.6. Pre-peak(s) during temperature ramp-up phase

As mentioned before, pre-peaks are regularly observed at the temperature ramp-up phase. Regularly in this case means, that the pre-peaks can be triggered by the usage of the LN trap in the gas feed line while filling the vacuum vessel with hydrogen, prior to gas loading.

Figure 3.10 shows two nominally identical measurement cycles: the gas loading is done for both at 2400 K for 50 min in 500 mbar deuterium. The only difference is that in measurement fk890 the LN trap in the gas feed line was not used. Measurement fk891 was executed directly after measurement fk890 on the same day, but not using the LN trap. The temperature is ramped up with 3 K/s. This rather slow temperature ramp is chosen, so that the deuterium flux can be sufficiently resolved. The background of the water signal at mass 18 (not shown) at measurement fk891 (with LN trap) is roughly half of the background of fk890 (without LN trap), as it is to be expected.

At about 4300 s the temperature ramp is started. The deuterium flux at measurement

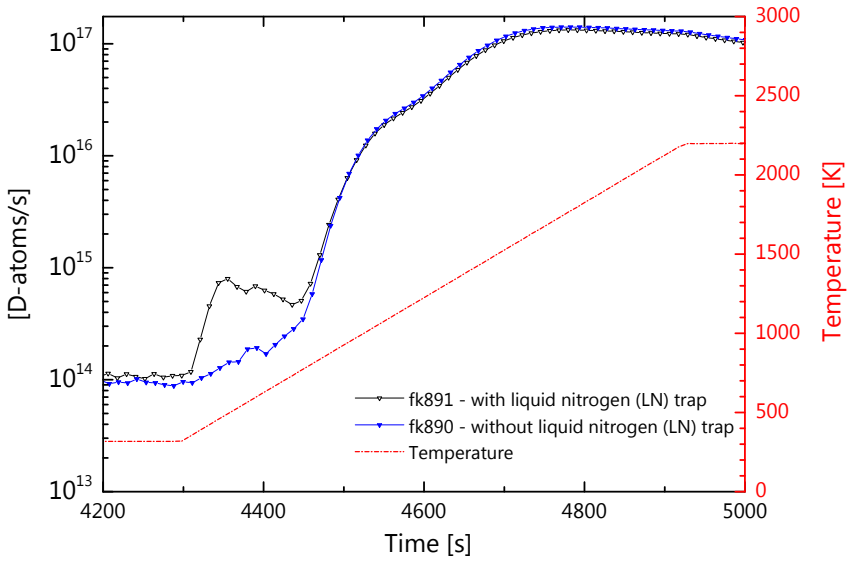

Figure 3.10.: Comparison of two equally executed measurement cycles, except for that measurement cycle fk891 used the LN trap prior to gas loading, whereas fk890 did not. The loading temperature is 2400 K for 50 min in 500 mbar deuterium. Degassing is done with a 3 K/s ramp to resolve the pre-peaks, the plateau temperature is 2200 K. The usage of the LN trap seems to trigger the appearance of pre-peaks in the degassing signal when ramping up temperature.

fk891 (with LN trap) rises right at the moment when temperature is ramped up. The signal rises to almost $1{\cdot}10^{15}$ D-atoms/s and then exhibits a double peak until it decreases until the temperature reaches about 750 K. Then the signal rises to the main peak and a shoulder can be seen before the peak during the temperature ramp up phase.

Measurement fk890 (without LN trap) exhibits no sharp rise in the deuterium signal when temperature is ramped up. It rises comparably slower than in measurement fk890 and does not show the first of the pre-peaks. A small peak appears shortly before 4400 s, the same that seem to appear in fk891 with higher magnitude. The signal from measurement fk890 rises sharply when reaching around 750 K. Then the signal follows the same evolution as in fk891, including the main peak, just that the signal is slightly higher.

When the temperature reaches its plateau at 2200 K both deuterium signals decay in the same way.

Figure 3.11 shows the whole degassing cycle of both measurements. Both deuterium signals are in very good agreement after the pre peak of fk891 during the temperature ramp up phase. Especially during the decay after having reached constant temperature both signals are almost not to distinguishable. This means that this pre-peaks, i.e., the usage of LN trap prior to gas loading the sample is of no relevance concerning the method of fitting the deuterium flux decay with the diffusion model, also of the pre-peaks. In summary, no correlation of the usage of the LN trap and the inventory of hydrogen could be found.

The origin of this pre-peaks could not be fully resolved within this thesis. As discussed in chapter 3.1.3, they seem to stem from the surface, i.e., correlate with surface effects. It could be that surface oxides form on the specimen and their thickness correlate with the amount of water background in the vacuum vessel. When ramping up the temperature, the formation

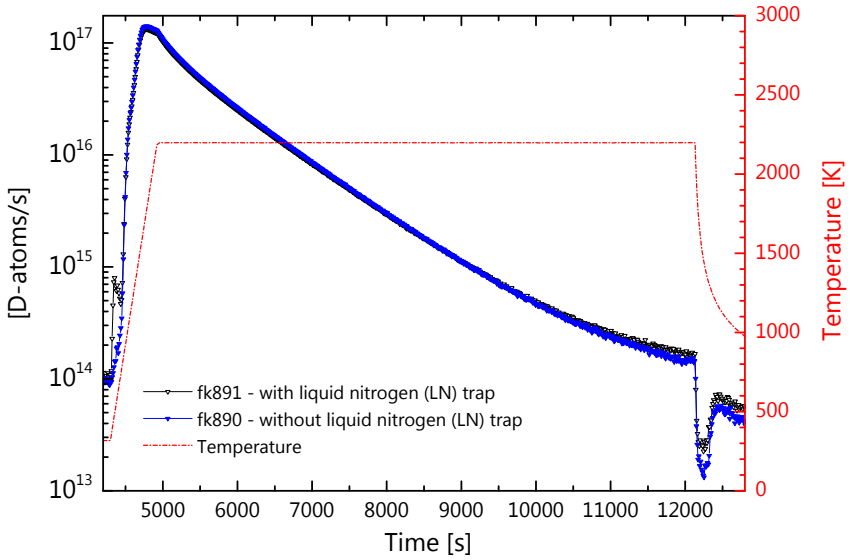

Figure 3.11.: Deuterium degassing signal for the measurement cycles with (fk891) and without (fk890) using the LN trap. Although the degassing signal at temperature ramp up phase is influenced by the usage of the LN trap, it does not seem to have an influence on the rest of the degassing signal, especially not on the single-exponential decay.

of oxides is enhanced by higher oxidation rates from water, exhibiting a temporary surface barrier. Up to a temperature of 1600 K the oxide formation rate dominates, above the oxide sublimates, according to [39].

This could also be the reason why measurement cycles with slow ramping rates during the degassing sequence yield different results from fast-ramped measurements. The slow ramps could cause an increased thickness of the oxide layer so that it is present during most of the degassing phase and hamper the measurements by establishing a surface barrier. This would yield non-Dirichlet boundary conditions (i.e., non-zero concentration of deuterium at or right below the surface) which cannot be described by the diffusion model in the present state.

4. Applicability of diffusion model

> The difficulty comes from
> our lack of confidence.
>
> *(Lucius Annaeus Seneca - Letters from a Stoic)*

This chapter covers the first part of the results, beginning with measures that establish static microstructural conditions in the specimens and, hence, reproducibility throughout their measurement campaigns. In the following, the applicability of the solute diffusion model ("tracer diffusion") for gas loading and degassing is evaluated.

4.1. High temperature conditioning of specimens

Prior to using the specimens for their measurement campaigns, they are high temperature conditioned. This mainly is done to remove impurities from the specimens, such as carbon and oxygen. The holding temperature for the big specimen is 2400 K, for the small, single- and poly-crystalline samples it is 2600 K, the duration of cycling at the respective temperatures is 20 h for each specimen. The heating is done sequentially in 500 mbar deuterium atmosphere and in vacuum, repeating five times the cycle of 2 h in deuterium and then 2 h in vacuum. This high temperature conditioning is done with each of the three specimens, before using them in their measurement campaign.

The high temperature conditioning causes massive grain coarsening and annealing of lattice defects because of the extended holding time at this high temperature. It is believed that it results in quasi-static microstructure conditions for the following measurements at temperatures that are lower than or equal to the chosen temperatures for this conditioning. The long holding at high temperature in hydrogen will also cause at least partial removal of impurities from the specimens. Common tungsten impurities such as oxygen or carbon can diffuse to the surface, react with the ambient hydrogen and desorb. The preparation process was started in hydrogen atmosphere and not in vacuum to hinder the formation of tungsten-carbides on the surface of the specimen because those would be hard to get rid off afterwards even in hydrogen atmosphere and at high temperatures. (Parts of this paragraph are taken from [4])

Figure 4.1 shows two deuterium release spectra of the big specimen before and after the high temperature conditioning. The loading conditions were identical: 180 min at 1600 K in 500 mbar deuterium. The LN trap was used when filling the vessel with deuterium. Degassing was performed applying the same procedure for both measurements, with 20 K/s to 1600 K and holding for 3 h. 1600 K for both loading and degassing temperature was chosen for this experiment such that the microstructure of the specimen was not yet massively changed, prior to the high-temperature conditioning.

The plot shows the temporal behaviour of the degassing of both measurement cycles. The horizontal time scales are aligned so that their temperature traces match each other. The left y-axis shows degassed deuterium atoms per second, the two right y-axes show the cooling

water temperature from the glass tube vessel (outlet). The right scales are vertically shifted for better visibility. The temperature of the cooling water is oscillating due to the controller settings of the cooling water chiller, see chapter 2.5.5.4.
Both deuterium degassing signals rise in parallel but peak at different heights. Before the high temperature conditioning, the signal from the degassing sequence exhibits a higher peak and a higher overall signal. As a consequence the measured inventory of deuterium is larger by a factor of 1.4.

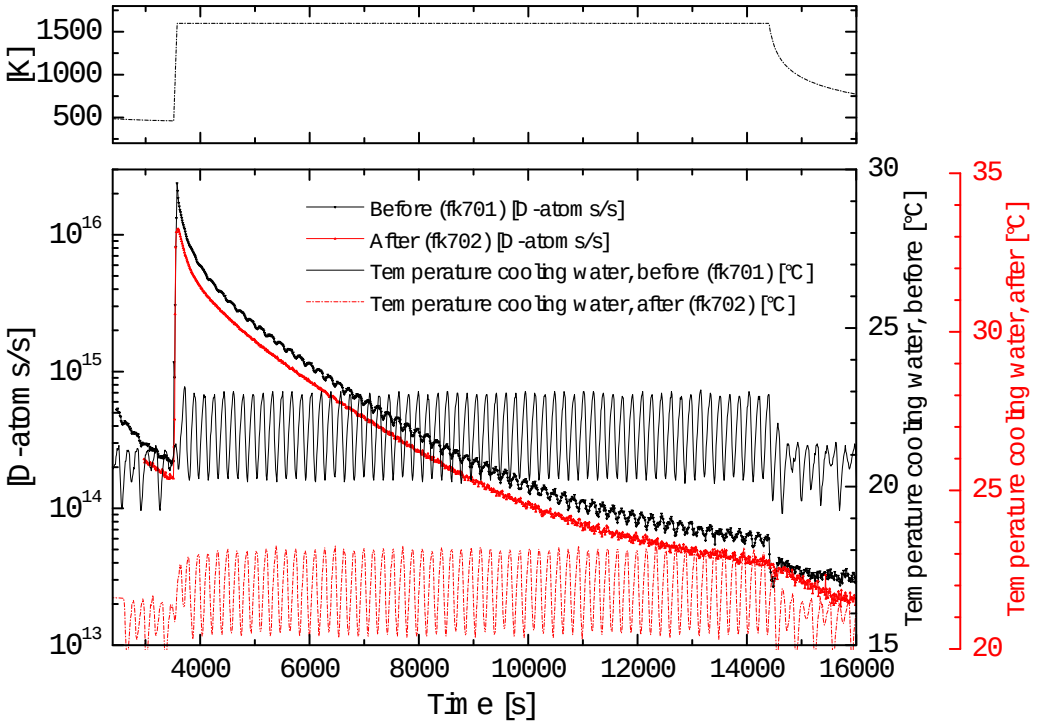

Figure 4.1.: Influence of the high temperature conditioning (2400 K for 20 h sequentially in 500 mbar deuterium and vacuum) on the degassing spectra. The degassing spectra from the big specimen before and after the high temperature conditioning are shown. Loading is done prior to both degassing sequences at 1600 K for 3 h in deuterium. Degassing is done with 20 K/s to 1600 K. The temperature of the specimen is shown in the upper panel.

When the temperature of the specimen(s) is constant, both signals decay in parallel. The measurement prior to the high temperature conditioning (black line) is highly influenced by the oscillating temperature of the cooling water. Already before the temperature is ramped up during the pumping phase, the deuterium signal shows wiggles that coincide with the oscillating water temperature. After the temperature of the specimen reached the holding temperature of 1600 K, the decay of the degassing signal is oscillating in parallel to the oscillating water temperature. This is visible already at relatively high D fluxes of roughly 5 - $7 \cdot 10^{15}$ D-atoms/s. The degassing signal oscillates until the end of the temperature plateau (3 h).

The equally executed degassing sequence subsequently to the high temperature conditioning (red line) shows only a very weak dependence on the oscillating water temperature. First oscil-

lations can be seen at D fluxes lower than $7{\cdot}10^{14}$ D-atoms/s, getting more visible as the signal decays, but remain much lower than for the specimen before high temperature conditioning.

The oscillations in the degassing flux prior to the high temperature conditioning indicate a high dependence of the degassing flux on the temperature and state of the inner glass wall. The glass tube was clean before the high temperature conditioning, but it seems that it was coated during the gas loading sequence of the first measurement cycle by evaporation of impurities from the specimen such as carbon or hydrocarbon, although the specimen was electro-polished before the gas loading. This potential coating seems to have a high influence on the degassing signal, already before the specimen is heated to 1600 K. But, the higher inventory seems not to stem from the glass tube, because the deuterium degassing signal of both measurements decay in parallel. It is very unlikely that an additional, or separate, inventory from the glass tube shows a similar decay as the inventory from the specimen. Hence, the high temperature conditioning seems to cause decreased trap density, however it is unknown of which type these traps were before.

After the high temperature conditioning and prior to the second experiment shown in figure 4.1, the glass tube was chemically cleaned as described in section 2.5.5.3. This seems to decrease the dependence of the deuterium degassing signal on the inner glass wall temperature drastically. There was no need to clean the glass tube again during the measurement campaigns, apart from the measurement explorations to temperatures of 2800 K with the small poly-crystalline specimen during the commissioning of ROST to test its capabilities. This led to increased coating and again to a high dependence of the degassing signal on the oscillating cooling water temperature as described in section 2.5.5.4.

4.2. Inventory: interstitial solubility

This section describes preliminary experiments necessary to define the measurement procedure and boundary conditions for the gas loading experiment. This includes deriving the required dwell times for gas loading of both specimen geometries for various temperatures and to check if the experiments are in agreement with Sieverts' law. Especially Sieverts' law is a strong indicator, whether the measured dissolved deuterium atoms at the test temperature of 2000 K stem from interstitial inventory only, i.e., trapping or surface effects are negligible at this temperature.

At a certain temperature, the concentration, c, of a gas in a metal is dependent on, firstly, the partial pressure, p, of the surrounding gas in thermodynamic equilibrium and, secondly, of the temperature dependent solubility, $S(T)$. $S(T)$ is highly dependent on the metal-gas combination. For di-atomic gases in a metal Sieverts' law is given as [22]:

$$S(T) = \frac{c^2}{p} \;\Rightarrow\; c = \sqrt{S(T)\,p} \tag{4.1}$$

4.2.1. Thermodynamic equilibrium

First, the dwell times necessary in deuterium atmosphere to reach thermodynamic equilibrium are examined for both specimen sizes. This is done by executing dwell-time-dependent gas loading cycles with subsequent degassing. For the small specimens only the poly-crystalline specimen was investigated because it exhibits the same size as the single-crystalline specimen.

The gas loading sequences are done for both geometries in 500 mbar deuterium atmosphere and at 2000 K.

The subsequent degassing sequences are executed with 20 K/s to 2000 K for both geometries. The dwell time for gas loading is varied, up to 60 min for the small, and 120 min for the big specimen.

Figure 4.2 shows the dependence of dissolved deuterium in the big specimen on dwell time of the gas loading phase. The measured amount of deuterium rises for dwell times of 10, 15, and 60 min. A 120 min dwell time shows no further increase in inventory in comparison with 60 min within the measurement accuracy. It seems that for the big specimen at 2000 K thermodynamic equilibrium during gas loading is reached at a minimum dwell time of 60 min. In additional experiments it was checked that the dwell time for thermodynamic equilibrium is independent of gas pressure during gas loading.

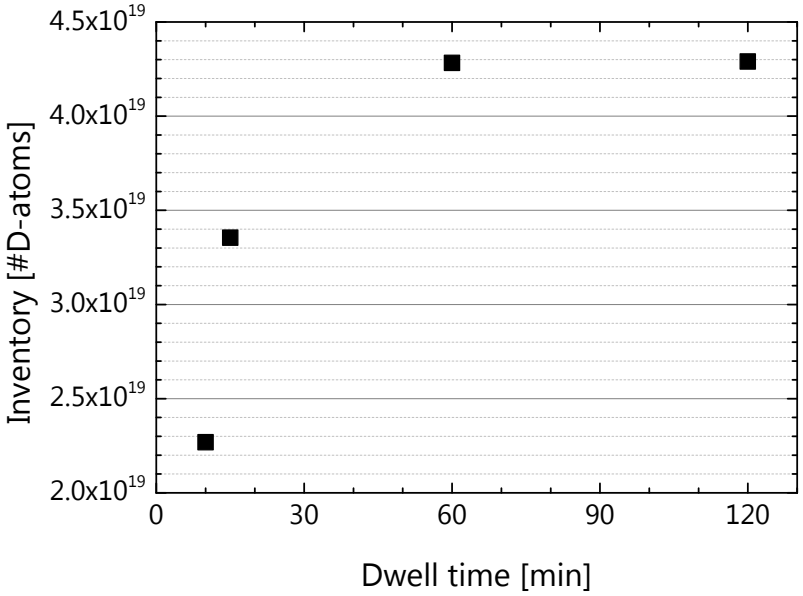

Figure 4.2.: The deuterium inventory in the big specimen is measured for different dwell times during gas loading. The deuterium inventory is measured with a subsequent degassing cycle, ramping up to 2000 K with 20 K/s and holding for 120 min. The loading temperature and pressure was kept constant for all gas loading sequences at 2000 K and 500 mbar deuterium pressure. The dwell time for gas loading was varied from 10 to 120 min.

The experimentally determined minimal dwell time at 2000 K is used as scaling factor to derive the dwell times for other temperatures. At first, the diffusivity at 2000 K is estimated by applying Frauenfelder's diffusion coefficients [8] to the diffusion formula:

$$\mathrm{D}_{\mathrm{FF}}^{2000\,\mathrm{K}} = 4.1 \cdot 10^{-7}\,\frac{\mathrm{m}^2}{\mathrm{s}} \cdot \exp\left(\frac{-0.39\,\mathrm{eV}}{\mathrm{k_B} \cdot 2000\,\mathrm{K}}\right) = 4.3 \cdot 10^{-8}\frac{\mathrm{m}^2}{\mathrm{s}} \tag{4.2}$$

The dwell times were derived before the diffusivities could be derived, hence, Frauenfelder's values were used. But, instead of protium (whose values are used in the estimated diffusivity in equation 4.2), deuterium is used for deriving the dwell time at 2000 K, whose diffusivity is expected to be smaller. Harmonic theory expects the pre-exponential factor of deuterium to

be smaller by a factor of $\sqrt{2}$ than for protium. Therefore, using the Frauenfelder values for protium to extrapolate the necessary dwell times for deuterium, this will yield longer dwell times than necessary and safely thermodynamic equilibrium will be reached.

This lower-limit estimate for diffusivity at 2000 K is now used together with the experimentally derived dwell time as a scaling factor:

$$D_{FF}^{2000\,K} \cdot t_{dwell\ measured}^{2000\,K} = 4.3 \cdot 10^{-8} \frac{m^2}{s} \cdot 60\,min \tag{4.3}$$

The dwell time for the big specimen (⌀ 30 mm) at 1800 K is estimated by:

$$D_{FF}^{1800\,K} = 4.1 \cdot 10^{-7}\,\frac{m^2}{s} \cdot \exp\left(\frac{-0.39\,eV}{k_B \cdot 1800\,K}\right) = 3.3 \cdot 10^{-8} \frac{m^2}{s} \tag{4.4}$$

$$t_{dwell\ estimated}^{1800\,K} = \frac{D_{FF}^{2000\,K}}{D_{FF}^{1800\,K}} \cdot 60\,min = 77\,min \tag{4.5}$$

This dwell time scaling, i.e., estimation for diffusivity from a single tested temperature to other temperatures for a three dimensional body like the used cylindrical samples is valid, because the experimentally derived dwell time at 2000 K already includes the dependence on the geometric dimensions for the object of extrapolation.

The same procedure to determine the necessary dwell time until thermodynamic equilibrium is reached is done with the small sample. Table 4.1 shows the experimentally applied loading times as well as the estimated loading times for the big specimen and the small specimens. The experimentally determined, minimal dwell times for thermodynamic equilibrium at 2000 K are marked as figures in bold. For gas loading temperatures lower than 2000 K some additional

Table 4.1.: Dwell times for the small and big specimens (⌀15 mm and ⌀30 mm) for gas loading at various temperatures. The experimentally applied dwell times are shown in the left two columns. The estimated dwell times are derived by extrapolating from the experimentally derived dwell times for both specimen geometries at 2000 K, which are marked as bold figures. This is done by applying Frauenfelder's [8] values for diffusivity to scale the dwell times measured at 2000 K to the other temperatures.

	dwell time			
	applied		estimated	
Loading temp. [K]	⌀15 mm [min]	⌀30 mm [min]	⌀15 mm [min]	⌀30 mm [min]
1300	480	-	101	203
1400	360	480	79	158
1500	240	-	64	128
1600	90	180	53	106
1800	60	90	39	77
2000	**30**	**60**	**30**	**60**
2200	25	55	24	49
2400	20	50	21	41
2600	20	-	18	36

time to those estimated dwell times is added, to compensate for uncertainties like surface effects or increasing/relevant trapping. Their influence is expected to be higher at lower temperatures, therefore the extra time which is added to the estimated dwell times is substantially increased at lower temperatures. Also Frauenfelder's dwell times are considered here, which were up to 400 min at 1120 K (and a diameter of his sample of ∅31.7 mm).

Additionally, the experimentally applied dwell time was cross-checked for the small, polycrystalline sample at 1800 K by doubling the dwell time. The measured inventory yields the same results within measurement accuracy. The same loading times are also applied for experiments using protium. Since the diffusivity of protium is assumed to be higher than for deuterium, it can be assumed that thermodynamic equilibrium is reached faster than for deuterium.

Side remark

When the dwell time series for gas loading of the big specimen at 2000 K was performed, it turned out that even for the same dwell time the inventory of deuterium atoms constantly increased from one gas loading sequence to another (at the same gas loading temperature and gas pressure).

The measurement series for finding the dwell times for gas loading were undertaken right after the high temperature conditioning of the specimen (see chapter 2.5.5.3). In the aftermath of the high temperature conditioning the glass tube was chemically cleaned and during this procedure the specimen was exposed to air (but not treated chemically or in any other way). For the high temperature conditioning the specimen was heated to 2400 K. This was by then the highest specimen temperature in the corresponding measurement campaign. Then, after the exposure to air, the dwell times were determined by heating to 2000 K for each test cycle (it was not re-heated to 2400 K beforehand). After heating the specimen again to 2400 K for 30 min the conditions were stable and the dwell times could be derived. The reason for this unstable conditions remains unknown, potentially surface effects could had been the reason.

4.2.2. Correlation of gas pressure and dissolved hydrogen: Sieverts' law

In order to confirm Sieverts' law, the big specimen is gas loaded in deuterium at 2000 K for 60 min at different gas pressures. Figure 4.3 shows the measured inventory of deuterium atoms as a function of the deuterium pressure during gas loading. The pressure is varied starting from 6 mbar being the lowest loading pressure, leading to a desorption signal that still can be distinguished clearly from the background signal. Measurements are conducted at 6, 20, 100, and 500 mbar. The integrated signals, i.e. total number of measured deuterium atoms, are shown as black squares on double logarithmic scales. In addition a linear fit to this data is shown as black line. The fit in the plot shows a slope of 0.52±0.05. This quite accurately reproduces Sieverts' law that predicts a square-root, i.e., a 0.5 (#D/p) behaviour.

This agreement of the gas loading experiments at 2000 K over 2 orders of magnitude of pressure with Sieverts' law verifies that trapping at defects or surface effects for these temperatures is of no relevance for the solubility, i.e., do not contribute to the measured inventory. The measured, dissolved number of atoms is varied by one order of magnitude. More precisely the measured number of D-atoms in the 500 mbar gas loading is of a factor 9.7 higher than in the 6 mbar gas loading case. The anticipated ratio according to Sieverts' law is $\sqrt{\frac{500\,mbar}{6\,mbar}} = 9.1$. If traps would be populated at the gas loading temperature of 2000 K, the fraction of trapped deuterium compared with solute deuterium should change with variation of pressure. In other

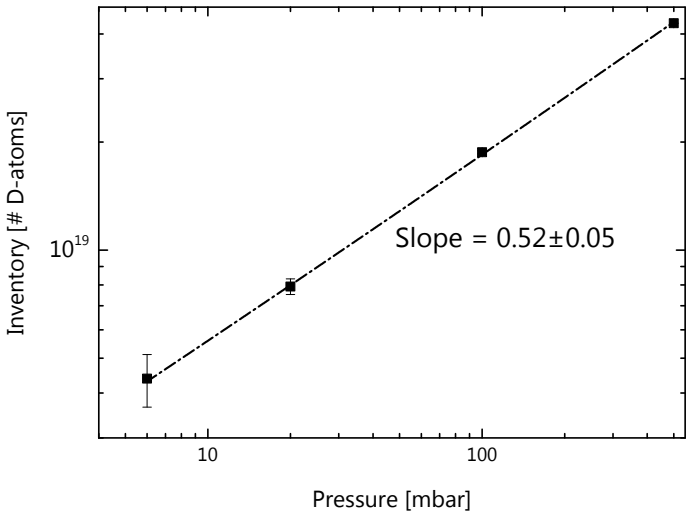

Figure 4.3.: The double-logarithmic plot shows the measured deuterium inventory as a function of pressure. The fit shows a slope of 0.52 ± 0.05 #D/p, which exhibits good agreement with Sieverts' law that predicts a square-root dependence.

words, the number of deuterium atoms in solute from 500 to 6 mbar decreases by more a factor of 9, but the number of deuterium atoms in traps, if they were populated, should not change. That would lead to a change in the fraction of deuterium in traps to deuterium in solute. As a consequence, the measured number of atoms at lower pressures would in that case be higher than anticipated from Sieverts' law.

So, from the actually very good correlation of the data with Sieverts' law as documented in figure 4.3, it can be concluded that at 2000 K traps are essentially unpopulated and that the measured hydrogen inventory is only determined by interstitial solubility.

4.3. Applicability of solute diffusion

This section investigates whether the governing migration mechanism is due to solute diffusion and is not influenced by trapping effects. Measurements with influence from higher detrapping energies than the activation barrier E_A would falsify the results. Also surface effects shall play no role, which could act as surface barrier (see chapter 3.6). Further, Fick's law of diffusion, which is the foundation of this evaluation (see chapter 1.4) would not be applicable if interactions would exist between, and among, diffusing hydrogen atoms.

Pressure variation during the gas loading sequence is used to produce varying amounts of dissolved deuterium. In the previous chapter only the inventory was evaluated, now the degassing behaviour is analysed: if the retained deuterium atoms interact or are influenced by trapping effects, a varying concentration of deuterium in the specimen should yield different degassing behaviours.

4.3.1. Inventory-based scaling

The two measurements at 100 and 500 mbar deuterium pressure which are part of the pressure variation sequence presented in section 4.2.2 are used to be compared with respect to their

degassing behaviour. To facilitate a direct comparison of the degassing curves the data are scaled with respect to their deuterium inventory:

$$\frac{\#\mathrm{D}-\mathrm{atoms}\ 500\,\mathrm{mbar\ loading}}{\#\mathrm{D}-\mathrm{atoms}\ 100\,\mathrm{mbar\ loading}} = \frac{4.28\cdot 10^{19}}{1.87\cdot 10^{19}} = 2.29. \tag{4.6}$$

This value fits very well to the prediction of Sieverts' law which yields $\sqrt{\frac{500\,mbar}{100\,mbar}} = 2.24$.

Figure 4.4 shows the scaled degassing of the 100 mbar loading sequence scaled with the factor from equation 4.6 in comparison with the unchanged degassing signal from the 500 mbar loading.

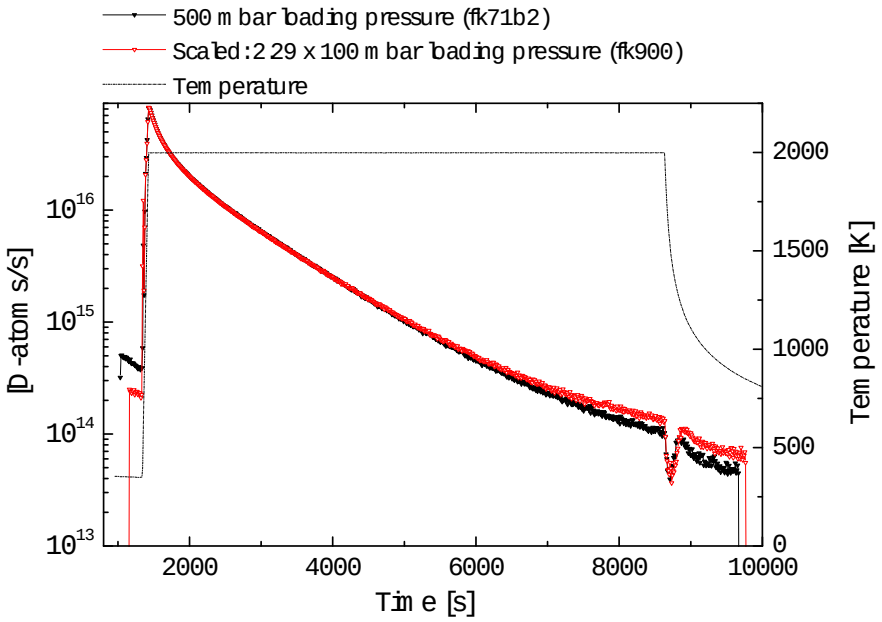

Figure 4.4.: Comparison of two degassing sequences with the big specimen after gas loading at 100 and 500 mbar deuterium pressure, 2000 K and 60 min dwell time. Degassing is done with 20 K/s to a 2000 K plateau. The 100 mbar loading pressure signal is multiplied by a scaling factor of 2.29.

The spectra are horizontally shifted so that their temperature readings match. The background before the temperature ramp-up varies, but this is of no influence on the deuterium degassing spectra. Both signals rise when the temperature is ramped up. They exhibit the same peak height, also the overshoot/non-single-exponential decay shows very good agreement. Both signals match each other when their decay becomes single-exponential afterwards, i.e., when the decay appears linear in the logarithmic plot. At the end of the temperature plateau both signals get influenced by the background. The scaled signal from the 100 mbar-loading exhibits a higher background signal at the end shortly before the heating is turned off, which stems from lower signal-to-noise ratio according to the lower amount of deuterium from lower loading pressure. Both signals show the usual dip when the heating is turned off.

If the migration mechanism at this temperature of 2000 K is dependent on the filling level of deuterium (i.e., if the deuterium atoms influence each other in the lattice), the change of filling level would yield a change in degassing behaviour. If traps at the lower loading pressure

play a role, the hypothetically higher fraction of deuterium in traps would be depopulated slower. The decay gradient of the deuterium degassing signal would yield a smaller value and result in lower diffusivity.

The excellent comparability of the signals from different loading pressures is a strong hint that the migration is not influenced by mutual interaction of the diffusing deuterium atoms. Further, no influence of trapping effects can be observed at 2000 K. Hence solute diffusion via interstitial sites is with high probability the governing transport mechanism at this temperature, despite the fact that the examined (big) specimen is of poly-crystalline microstructure.

4.3.2. Different loading pressures

Figure 4.5 shows the comparison of the degassing sequence of the priorly described four pressure variations in a logarithmic scaled plot. The degassing is done with 20 K/s to 2000 K plateau temperature. The signals are adjusted in time that their (identical) temperature readings match. The lower the loading pressure, the longer the pumping time prior to degassing is chosen to reach a reasonable background flux before starting the measurement. All four signals rise simultaneously when the temperature ramp is started. The peak heights vary according to loading pressure. When the temperature reaches 2000 K after the ramp, the

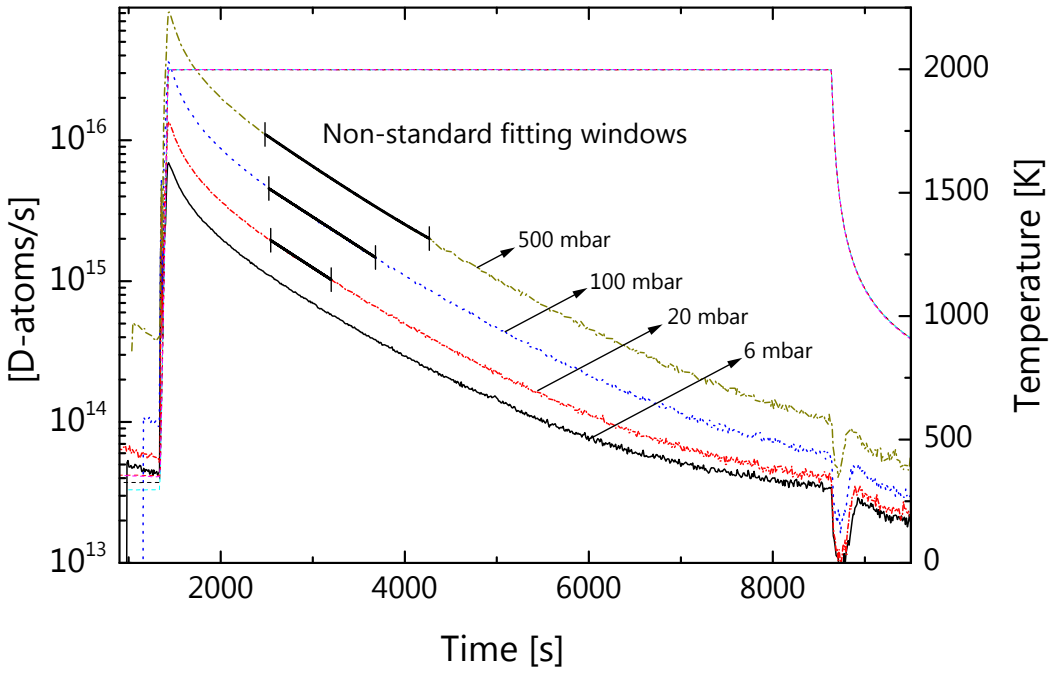

Figure 4.5.: Degassing measurements with the big specimen for four different gas loading pressures: 6, 20, 100, and 500 mbar. Gas loading temperature is 2000 K for 60 min. Degassing is executed equally: 20 K/s to 2000 K plateau for 120 min. All four degassing signals show the same qualitative evolution: they start at the same temperature and peak when temperature reaches its plateau. The three highest signals decay with a comparable single-exponential gradient.

decay of all four signals develop from non-single-exponential at the beginning, to a single-exponential decay (whereas the decay of the lowest signal is already strongly influenced by

background). At the end of the temperature plateau all four measurements exhibit the dip in signal and then decay towards the background.

In contrary to the fitting procedure described in chapter 3.3, as an exception the fitting window for the three measurements from the lower loading pressures is enhanced to lower fluxes than $2{\cdot}10^{15}$ atoms/s. The fitting window is enhanced to lower deuterium fluxes as long as they appear linear in the logarithmic plot. None of the measurement cycles with the 6, 20, or 100 mbar gas loading sequences are used for quantitative assessment by means of the diffusion model later on.

Figure 4.5 shows the fitting windows for the three highest signals. The degassing signal from the 6 mbar gas loading sequence is not further evaluated because the signal runs into background basically right after the non-single-exponential overshoot.

The examined decay gradients of the three highest signals (500, 100, and 20 mbar) vary only by 0.8%. This observation supports the assumption that solute diffusion is the governing migration mechanism, in line with the previous section 4.3.1. Especially, corresponding to Fick's description of solute diffusion that is used for the diffusion model applied to derive diffusion and solubility (as described in chapter 1.4), varying hydrogen inventories do not influence the evaluation.

4.3.3. Different loading temperatures

Parts of the following sequence are also described in a publication that was produced in the course of this thesis [4]. Figure 4.6 shows a series of deuterium degassing signals for the single-crystalline sample. The plateau temperature is the same for all three degassing cycles: 2200 K. The ramps are 15 or 20 K/s.

For the three presented spectra, the loading temperatures are varied. The leftmost signal was loaded at 2200 K, the signal in the middle at 2000 K and the rightmost at 1800 K. It can be seen that the total amount of deuterium increases with increasing gas loading temperature. Nevertheless, the decay constant of the signal at later times for the three loading conditions is identical.

For ease of comparison and clarity in figure 4.6 all degassing signals have been shifted horizontally (along the time-axis) such that the spectra are aligned with respect to the effusion flux of $2 \cdot 10^{15}$ D-atoms/s.

Although the loading temperature is varied such that the integral amount of deuterium differs by a factor of about 3.5 from the 2200 K loading in comparison with the 1800 K loading, the single-exponential decays yield the same gradient. Also the variation of temperature ramps between 15 or 20 K/s does not seem to play a role.

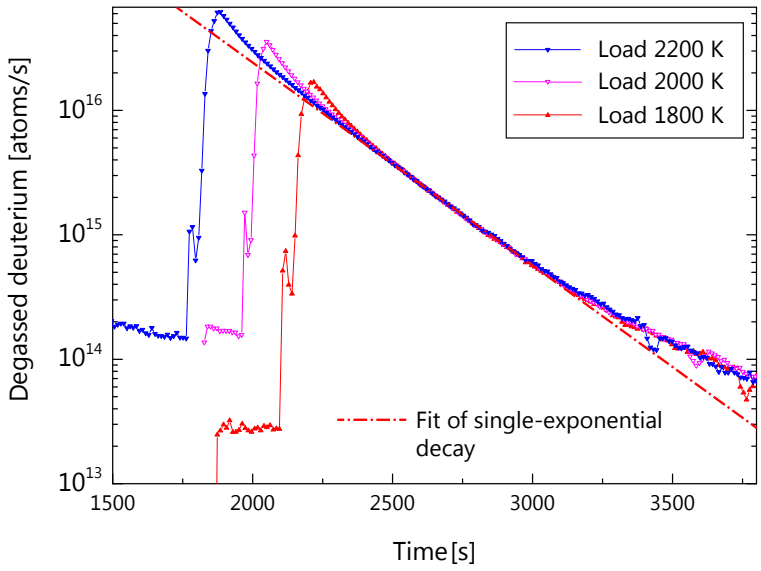

Figure 4.6.: Comparability of different loading conditions: Deuterium degassing spectra for deuterium gas loaded single-crystalline sample. The spectra show three different sample loading temperatures, from left to right: 2200 K, 2000 K, 1800 K at 500 mbar. A temperature ramp of 15 (the leftmost spectrum) or 20 K/s up to 2200 K was used, then keeping the sample at this temperature plateau until the signal approaches the background level (spectra have been horizontally shifted for clarity). For all plateau temperatures the exponential decay of the deuterium signal is fitted using the maximum-likelihood ($\hat{\chi}^2$) fitting method as described in section 3.4.

4.4. Poly- and single-crystalline sample (∅ 15 mm)

Finally, it is checked if poly- and single-crystalline sample yield the same degassing behaviour at the testing temperatures.

4.4.1. Identical measured diffusivity

(Parts of the following section are to be found in a paper that was published within this thesis project [4].) Figure 4.7 exemplarily shows the degassing sequences of the single- and poly-crystalline sample that are loaded equally at 500 mbar deuterium at 2000 K and degassed at 2000 K with a 20 K/s ramp.

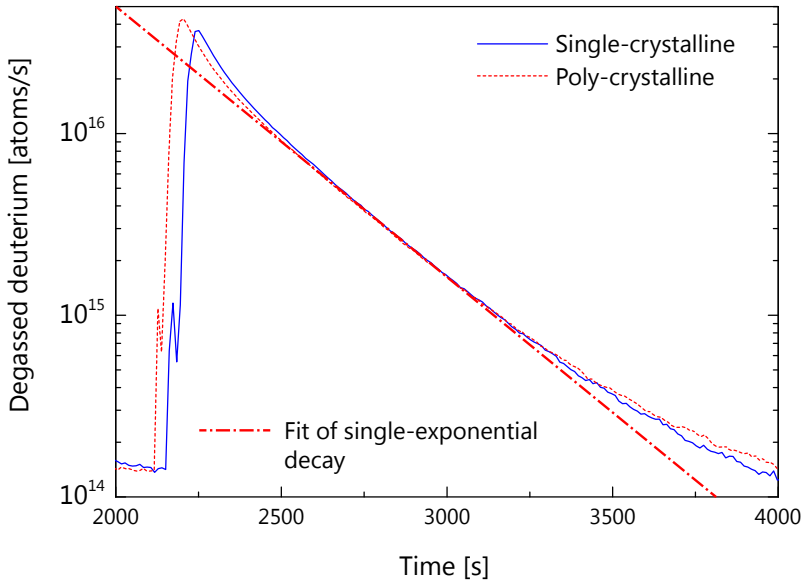

Figure 4.7.: Spectra from a single- and a poly-crystalline specimen. The gas loading conditions are identical: 2000 K for 30 min in 500 mbar deuterium atmosphere. The degassing conditions are a 20 K/s ramp up to a 2000 K plateau. The spectrum of the single-crystalline specimen is shifted to match the exponential decay of the poly-crystalline sample. Although at the beginning of the ramp the deuterium atom degassing signals differ, both samples can be fitted with the same single-exponential fit after the temperature has reached the higher modes decayed.

The two signals are shifted relative to each other to emphasize the common exponential decay constant. The signals vary at the temperature ramp up phase, but after the non-single-exponential decay both signals eventually decay single-exponentially at the same slope until both signals are affected by the background.

The derived decay constant for the single-crystalline specimen and the poly-crystalline specimen is identical within the measurement accuracy. Degassing sequences of poly- and single-crystalline specimen are compared to each other at temperatures ranging from 1600 to 2400 K. Although the poly-crystalline specimen exhibits many grain boundaries in the centre in comparison to the single-crystalline specimen (see chapter 2.3), their degassing yields identical

results for the reduced diffusion model, i.e., the fit of single-exponential decay at degassing temperatures $\geq 1600\,\mathrm{K}$.

This largely excludes a potential influence from different trap concentrations or grain boundaries [57]. Also the influence of surface effects that could act as surface barrier for the degassing hydrogen, are widely excluded at these temperatures. Ramps slower than roughly $10\,\mathrm{K/s}$ yield a very short single-exponential decay due to the longer times at the temperature ramp-up phase and non-single-exponential overshoot. They deviate from the guidelines that yield coherent measurements (see section 3.2). Hence, measurements with slower ramping rates than $15\,\mathrm{K/s}$ are not used for evaluation.

4.4.2. Deviations in solubility at temperatures $\leq 2000\,\mathrm{K}$

Figure 4.8 shows the measured inventory for different gas loading temperatures in the small specimens. The corresponding dwell times of gas loading are stated in table 4.1. The measured deuterium inventory is shown for both the poly- and single-crystalline sample. Only measurement cycles are considered, in which the degassing temperature was higher or equal than $1800\,\mathrm{K}$, because the background-to-signal ratio at lower temperatures gets increasingly unfavourable and causes higher uncertainties in comparison to the desorption signal. The uncertainties for equally executed measurement cycles are lower than the scatter of the measured inventories of the individual measurement cycles at the same loading temperatures. Especially for the loading temperature of $2000\,\mathrm{K}$ the scatter is bigger, this loading temperature was used as baseline temperature to compare the behaviour at different degassing temperatures. This deviation seems to stem from the estimation of background (see section 3.1.3), which causes a higher scatter as the degassing temperatures are lower, and, hence, yield a longer degassing time in combination with lower overall signal heights. Nevertheless, the plot shows a deviation trend of the integrated deuterium from the single-crystalline sample to lower values than from the poly-crystalline sample at the loading temperatures of 1500, 1600, 1800 and $2000\,\mathrm{K}$.

This effect seems to be significant - the average over 15 loading cycles at $2000\,\mathrm{K}$ with the poly-crystalline sample against 10 loading cycles at $2000\,\mathrm{K}$ with the single-crystalline sample shows that the single-crystalline sample retains 4.2% less deuterium. The number of executed loading cycles for both specimens is 3 or less for the loading temperatures of 1800, 1600 and $1500\,\mathrm{K}$. Nevertheless the trend is consistent and shows 11 - 17% less deuterium in the single-crystalline sample; the comparison at loading temperature of $2200\,\mathrm{K}$ (2 measurements with the poly- and 1 with the single-crystalline sample) shows 4.3% less deuterium in the single-crystalline sample.

The uncertainties from counting statistics yield values in the sub per mill range of the measured inventory and can be neglected. The uncertainties are assumed to be dominated by the estimation of the background flux (evaluated by measurements: $2{\cdot}10^{13}\,\mathrm{D\text{-}atoms/s}$ for deuterium, see chapter 3.1.3.1) throughout the measurement cycles. The uncertainties for the background flux are estimated to $\pm\frac{1}{3}\cdot 2{\cdot}10^{13}\,\mathrm{D\text{-}atoms/s}$. Those relatively small uncertainties for the inventory are validated by equally performed measurement cycles. Nevertheless, the measured inventories vary when the degassing sequences are varied by changing the degassing temperature and holding time, which can be seen in the scatter for individual measurement cycles with the same loading temperature of $2000\,\mathrm{K}$. Also Frauenfelder's measurement cycles with the same gas loading sequences but varying degassing temperatures exhibit a comparable scatter for the inventory [8, p. 390].

The single-crystalline sample has 1% less mass than the poly-crystalline sample. Further-

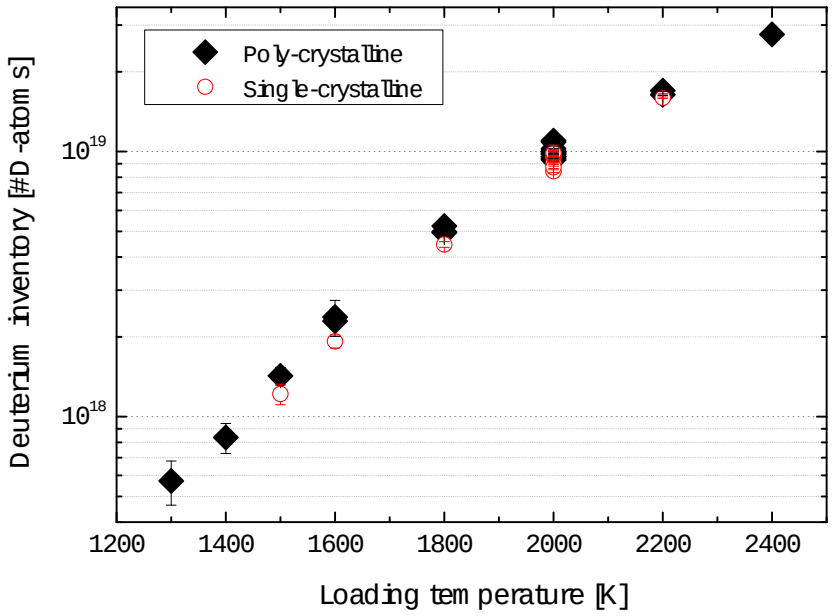

Figure 4.8.: Measured deuterium inventory in single- and poly-crystalline sample in dependency of the loading temperature. The pressure is in all cases 500 mbar. At and below gas loading temperatures of 2000 K the inventory of the single-crystalline sample noticeably deviates from the inventory of the poly-crystalline sample towards lower values.

more, the single-crystalline sample is about 65 μm less in diameter - but neither the weight nor deviation in diameter (tested with the full diffusion model) can explain the difference in measured deuterium inventory in solute at the different temperatures.

The origin of this effect could be the microstructure of the poly-crystalline sample which very probably offers additional trapping sites in comparison with the single-crystalline sample, for example grain boundaries, carbon impurities or the voids in the centre of the sample (see chapter 2.3 for micrographs). They can be populated additionally to the solute sites during the loading phase.

Although the inventory of poly- and single-crystalline sample varies, the degassing behaviour, i.e., single-exponential decay at constant temperature higher than 1600 K does not show any variations (see section 4.4.1). This means that both samples can be used in terms of the diffusivity with the reduced diffusion model.

5. Diffusion and solubility coefficients

> I get obsessed by little nerdy things in my corner that no one else is interested in.
>
> *(Björk Guðmundsdóttir)*

In this chapter the results of the reduced diffusion model on the two small cylindrical samples and the results of the full diffusion model on the big cylindrical sample are presented. The synopsis sums up the findings from this work, compares the results from the reduced and the full diffusion model. Finally it compares them with published data.

The coefficients of diffusivity, E_A and D_0, and of solubility, E_S and S_0, respectively, are strongly correlated. This is a property of the applied model and can be deduced from the mathematical descriptions of the diffusion (see equation 1.5) and solubility (see equation 1.2). In this context it gets clear that if one variable of diffusivity is changed (E_A or D_0), the other variable must change accordingly to still be able to describe the experimental data. By the similarity of the mathematical description, also E_S and S_0 will be strongly correlated.

5.1. Reduced diffusion model

The reduced version of the full diffusion model provides results for the diffusivity only, but not for the solubility. As described in chapter 1.4, this model is applied for the measurements with the small specimens only - whose main purpose is the experimental check whether or not the diffusivity measured for both the single- and poly-crystalline specimen is the same, i.e., that the diffusivity is not influenced by trapping, grain boundaries or surface effects that could act as permeation barrier. A further purpose is to test if the method used by Frauenfelder [8], i.e., the evaluation with the reduced version of the diffusion model (on cylindrical specimens with a length $\gg$ radius), is applicable and yields results for diffusivity comparable to the full diffusion model (on the big specimen). The following section is partly to be found in the publication [4].

Solubility

The determination of the solubility of hydrogen in tungsten by applying the reduced diffusion model as outlined in chapter 1.4.2 faces some challenges. The loss of hydrogen during cool-down is unknown, hence, the present experimental approach alone does not yield results for the solubility. When applying the full diffusion model code (that includes all 3 dimensions) on the small specimens as described in chapter 1.4, the solubility can be determined, but with noticeable uncertainty. This is a consequence of the lower signal-to-noise ratio (in comparison with the big specimen) and the relatively high fraction of deuterium, being desorbed as HD; roughly 10 - 12% in comparison with about 0.2 - 0.4% for the big specimen. Hence, the determination of the solubility is evaluated only with the full diffusion model on the big specimen (see chapter 5.3.1.1).

Diffusivity

In this subsection the diffusivity with the reduced diffusion model on the small specimens is evaluated. For each isotope five measurement cycles are included. The degassing temperatures are varied between 1800 K and 2600 K for protium, and between 1600 K and 2400 K for deuterium. The gas loading pressure for all measurement cycles is 500 mbar, the loading temperatures varied between 1800 and 2400 K. In contrary to the full diffusion model, the reduced version does not need the input of the solubility coefficients to yield the result for the diffusivity, hence, it evaluates only the relative decay for different degassing temperatures.

The estimated decays $\gamma(T)$ for protium and deuterium are displayed in figure 5.1 as function of the inverse outgassing temperature. Both data sets are fitted independently with an exponential function $\gamma(x) = A\exp(-E \cdot x)$ with $x = 1/\mathrm{kT}$. For the case of protium this yields as maximum-likelihood estimate $\mathrm{A_H} = 0.0212 \cdot 1/\mathrm{s}$ and an activation energy for the diffusion of $\mathrm{E_A^H} = 0.28\,\mathrm{eV}$. For the case of deuterium this yields as maximum-likelihood estimate $\mathrm{A_D} = 0.0167 \cdot 1/\mathrm{s}$ and the same activation energy for diffusion of $\mathrm{E_A^D} = 0.28\,\mathrm{eV}$.

According to equations 1.26 and 1.5 the pre-exponential factor $\mathrm{D_0^H}$ of equation 1.5 can be obtained via

$$\mathrm{D_0^H} = \left(\frac{a}{\xi_1}\right)^2 \mathrm{A_H} \tag{5.1}$$

and analogously for deuterium.

The prefactors derived from this approach are, hence, $\mathrm{D_0^H} = 2.06 \cdot 10^{-7}\,\mathrm{m^2/s}$ and $\mathrm{D_0^D} = 1.60 \cdot 10^{-7}\,\mathrm{m^2/s}$, respectively.

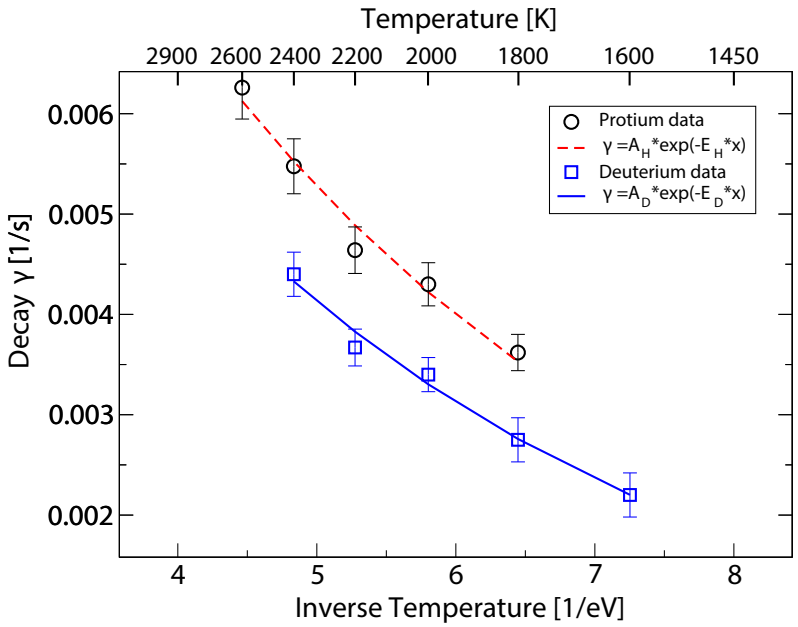

Figure 5.1.: Decay constants for protium and deuterium derived from decay fitting as outlined in chapter 1.4.2 (symbols). The pre-exponential factor of diffusivity and the activation energies for both protium and deuterium are derived by fitting the decays as function of 1/T. The fits are shown as dashed and solid lines. The faster decay for protium indicates higher diffusivity in comparison with the heavier isotope deuterium.

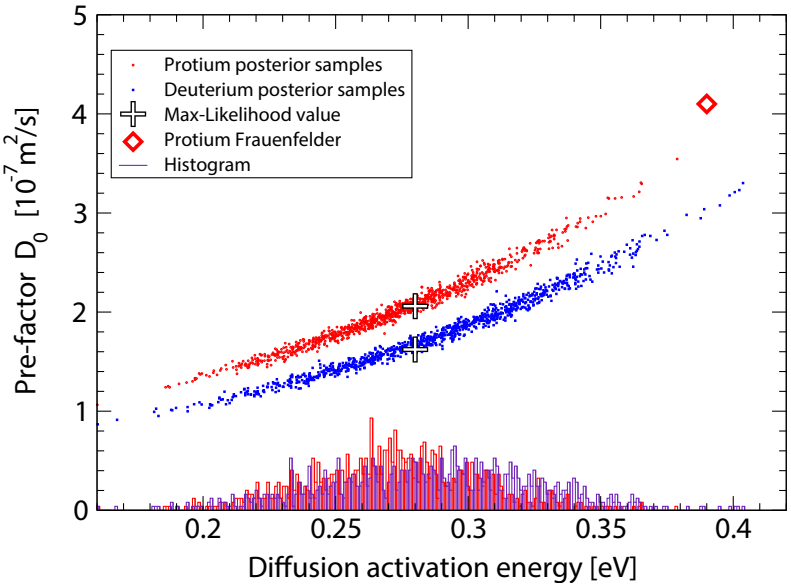

Figure 5.2.: Samples from the posterior probability distributions $p\,(\mathrm{E_A}, \mathrm{D_0} \mid \mathbf{d})$ for protium and deuterium. Also indicated is the corresponding value of Frauenfelder for hydrogen [8] and the maximum likelihood parameter values for protium and deuterium. At the bottom of the plot the (non-normalised) marginal distributions $p\,(\mathrm{E_A} \mid \mathbf{d})$ for protium and deuterium are displayed.

The standard parameter uncertainties provided by maximum-likelihood estimation schemes like Levenberg-Marquardt are derived from (the inverse of) the local Hessian matrix at the optimum [58]. It is known that these uncertainties may be misleading if the model is not linear in its parameters [59, 56]. Thus, to ensure a realistic assessment of the uncertainties, a Bayesian approach is applied [60]: Using an uniform prior probability distribution $\mathrm{p}\,(\mathrm{E_A}, \mathrm{D_0})$ for the parameters 1000 posterior samples $\{\mathrm{D_0}, \mathrm{E_A}\}_i, i = 1, \ldots, 1000$ are sampled from the posterior distributions $\mathrm{p}\,(\mathrm{D_0}, \mathrm{E_A} \mid \mathbf{d})$ ($\mathrm{p}(\mathbf{d} \mid \mathrm{E_A}, \mathrm{D_0}) \cdot \mathrm{p}(\mathrm{E_A}, \mathrm{D_0})$ being the likelihood for these two variables):

$$\mathrm{p}(\mathrm{E_A}, \mathrm{D_0} \mid \mathbf{d}) = \frac{\mathrm{p}(\mathbf{d}|\mathrm{E_A}, \mathrm{D_0}) \cdot \mathrm{p}(\mathrm{E_A}, \mathrm{D_0})}{\iint \mathrm{dE_A}\,\mathrm{dD_0} \cdot\ \mathrm{p}(\mathbf{d} \mid \mathrm{E_A}, \mathrm{D_0}) \cdot \mathrm{p}(\mathrm{E_A}, \mathrm{D_0})}, \tag{5.2}$$

using rejection sampling for both, protium and deuterium. The obtained samples are presented in figure 5.2. In addition, the maximum-likelihood parameters from figure 5.1 are indicated by crosses. Based on the marginal densities of the activation energies $p\,(\mathrm{E_A} \mid \mathbf{d})$ which are shown at the bottom of figure 5.2 an uncertainty of 0.06 eV for the diffusion activation energies is derived for protium and deuterium, i.e., $\mathrm{p}(\mathrm{E_A^H} \mid \mathbf{d})$ and $\mathrm{p}(\mathrm{E_A^D} \mid \mathbf{d})$. The marginal distribution of the activation energies for protium and deuterium are shown at the bottom of figure 5.2. The marginal distribution are calculated via $\mathrm{p}(\mathrm{E_A} \mid \mathbf{d}) = \int \mathrm{dD_0} \cdot \mathrm{p}(\mathrm{E_A}, \mathrm{D_0} \mid \mathbf{d})$ and, thus, include also the uncertainty of $\mathrm{D_0}$.

It should be pointed out that the probability distributions are asymmetric around the mean-value and thus are not Gaussian distributions. For comparison, also the parameter values of Frauenfelder for protium ($\mathrm{E_A^H} = 0.39\,\mathrm{eV}$ and $\mathrm{D_0^H} = 4.1 \cdot 10^{-7}\,\mathrm{m^2/s}$) are displayed in figure 5.2 [4]. The so-derived diffusion coefficients for protium by the reduced diffusion model applied on the small specimens (cross for the maximum-likelihood value in the red data cloud) differ

substantially from the Frauenfelder value for protium.

Figure 5.3 shows an Arrhenius plot of the derived diffusivities as a function of inverse temperature for protium and deuterium. The Frauenfelder data, for which the evaluation method outlined before was used, [8] is also plotted.

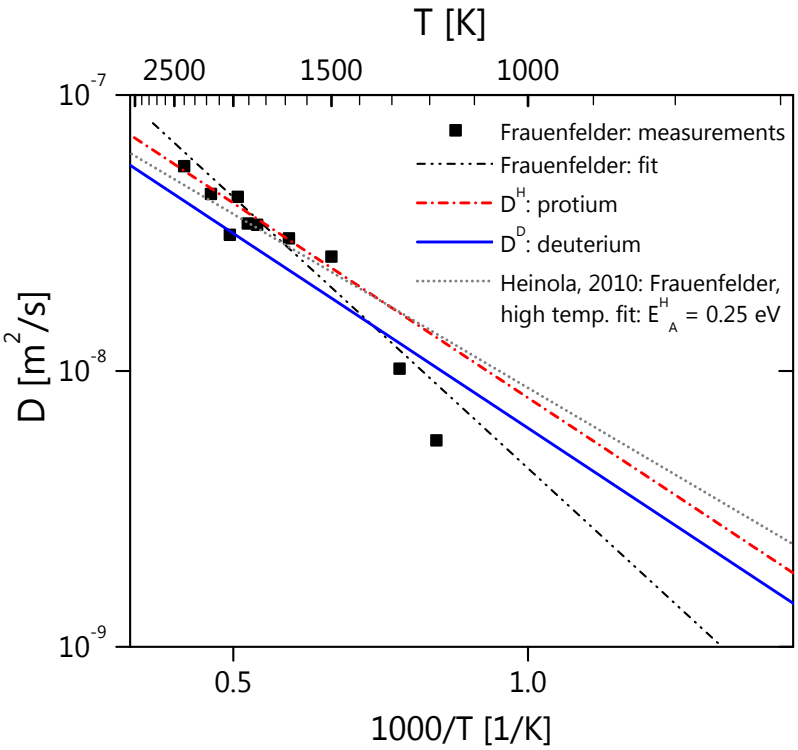

Figure 5.3.: Arrhenius plot of diffusivity versus temperature. Shown are the derived diffusivities by means of the reduced diffusion model on the small poly- and single crystalline samples. For comparison, the experimental data as well as the diffusivity for protium from Frauenfelder is shown [8] as well as a fit from Heinola [10].

It should be pointed out that although the pre-exponential factor as well as the activation energy derived here deviate substantially from the Frauenfelder values, the derived diffusivity values for protium agree very well with the measured diffusivities of the Frauenfelder data set above and equal to 1500 K. This is in line with Heinola's assumption [10] who suggests that only the high temperature degassing sequences of Frauenfelder higher than 1500 K should be used. Heinola's evaluation of Frauenfelder data above 1500 K yields a pre-exponential factor of $1.58{\cdot}10^{-7}\,\mathrm{m^2/s}$ and an activation barrier of 0.25 eV for the fit. Heinola's fit is shown in figure 5.3 as dotted grey line for comparison. It is in good agreement with the results of this work.

The pre-exponential factor ratio $q_{exp} = D_0^{D:\,red.}/D_0^{H:\,red.} = 1.27$ of protium and deuterium differs from the value which is predicted by the classical theory [23] of $\sqrt{\frac{m_D}{m_H}} = 1.41$.

5.2. Full diffusion model

The full diffusion model, which is described in chapter 1.4, is applied for sets of complete measurement cycles for the big specimen (chapter 3.4 outlines how the full diffusion model code is applied). The full diffusion model simultaneously adjusts the four variables E_A, D_0, E_S, and S_0 to data sets measured under different loading and degassing conditions. There are two data sets, one for protium and one for deuterium. Each set includes various measurement cycles of one isotope species.

5.2.1. Selection of measurement cycles for final evaluation

At first, all measurement cycles with protium are used as input for the full diffusion model code. Using the maximum-likelihood approach (see chapter 3.4), the maximum likelihood values for the four variables E_A, D_0, E_S, and S_0 for protium are simultaneously determined. In a second step, the same procedure is applied for measurement cycles with deuterium.

This first evaluation with all measurement cycles for each isotope comprises 12 for hydrogen and 13 for deuterium. A big advantage of this analysis with the full diffusion model is that all measurement cycles for one isotope are evaluated simultaneously. However, a careful comparison of the model results with the experimental data shows that the fit for some of the measurement cycles provides only a poor agreement with the data. Therefore, measurement cycles with poor agreement were rejected and not included in the final evaluation. The reasoning why individual measurement cycles were not accepted for final evaluation is discussed in the following section. To further identify "bad" measurement cycles and quantify the misfit the following procedure is applied: The normalized chi-square, $\hat{\chi}^2$, for the measurement cycles of the final analysis is computed (see section 3.4). For simplicity this will be denoted "$\hat{\chi}^2_{good}$". Then, a "bad" measurement cycle is added to the data set, and the whole set of accepted measurement cycles plus the one "bad" measurement cycle is used for analysis. This produces a new set of fit parameters. For this simulation the normalised chi-square ($\hat{\chi}^2_{bad}$) is computed and compared with $\hat{\chi}^2_{good}$. In general, for the so-identified "bad" measurement cycles it is found that $\hat{\chi}^2_{bad} \gg \hat{\chi}^2_{good}$.

The measurement matrix shown in figure 5.4 serves as orientation to show the collection of measurement cycles and which ones are used as input for the final evaluation. Protium is shown in the left and deuterium in the right panel. Measurement cycles which are used as input for the final evaluation are plotted as full symbols (squares for protium, triangles for deuterium). Measurements which are rejected and, therefore, not used for the final evaluation are shown with open symbols. The identification number of the corresponding measurement cycles is written next to the symbols as reference. The integrated measurement time from the fitting windows (definition see chapter 3.3, cf. figure 3.7) for each data set is shown in the lower right corner of each panel. The data set for final evaluation for protium contains 7 measurement cycles with a total fitting time of 13900 s (which corresponds to 1300 measured data points; one mass scan with the QMS takes 10.67 s, the time for one mass 2 and one mass 4 scan is 1 s each). The deuterium data set for final evaluation contains 9 measurement cycles with total fitting time of 17700 s (which corresponds to 1660 measured data points).

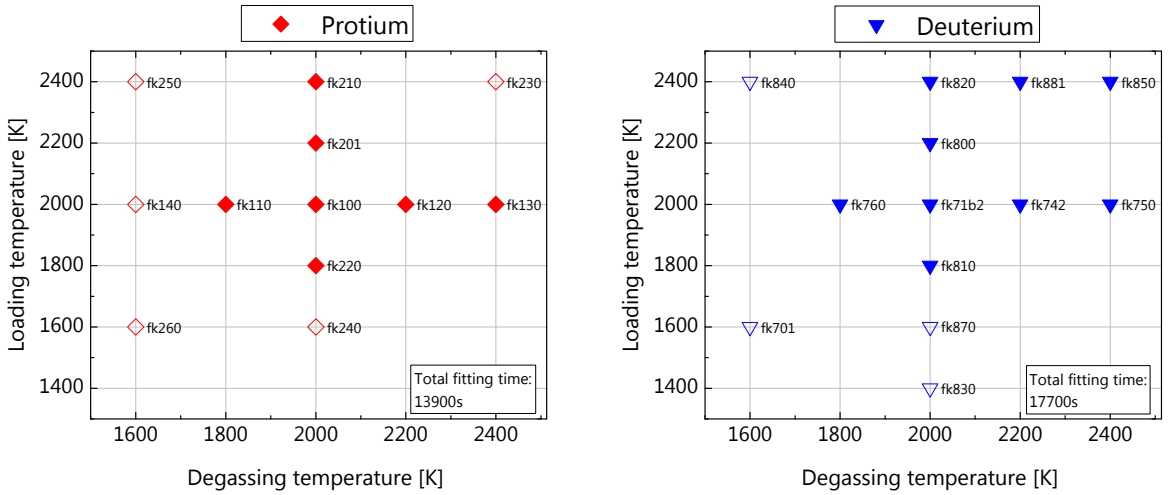

Figure 5.4.: Measurement cycles for the big specimen are shown as a function of their loading temperature (y-axis), and their degassing temperature (x-axis). For final analysis only measurements with loading and degassing temperatures higher than 1600 K are considered (for details see text). Accepted measurement cycles are displayed as full symbols, rejected ones by open symbols. In total, all 12 measurement cycles are shown for protium, and all 13 for deuterium.

5.2.2. Excluded measurement cycles

Gas loading at temperatures $\leq$ 1600 K

Measurement cycles with gas loading temperatures below or equal to 1600 K do not yield good fits. Significantly increased $\hat{\chi}^2$ values indicate that the below described measurement cycles deviate from the diffusion model. It turns out that, if these measurement cycles are part of the data set for evaluation with the full diffusion model code, the corresponding fits systematically deviate from the degassing signal, even if the outgassing temperature is 1800 K or higher. Figure 5.5 shows two measurement cycles that yield $\hat{\chi}^2_{bad} \gg \hat{\chi}^2_{good}$. The panels show measured data for protium on the left panel, and for deuterium on the right panel, within the fitting window. The dotted lines mark the best fits for these degassing sequences if these measurement cycles are part of the data set for final evaluation. The measured degassing data is shown as triangles, every triangle shows one measurement point. The two measurement cycles presented are both gas loaded at 1600 K for 3 h in 500 mbar and degassed at 2000 K with a 20 K/s ramp. They correspond to measurement cycles shown in the measurement matrix in figure 5.4 (open symbols, fk240 for protium, fk870 for deuterium).

These two measurement cycles are not used for quantitative assessment from the full diffusion model, because the fits to these measurements clearly and consistently differ in a systematic way. Both underestimate the inventory, in contrary to the other fit-measurement combinations of the data sets. In both cases, the diffusion model yields best fits for the bad measurement cycles with degassing signals that are consistently too low, i.e., a bad fit concerning the absolute "height" of the degassing signal. As a side effect, the $\hat{\chi}^2$ values increase if these measurement cycles are included. For protium, the inclusion of the bad measurement cycle yields $\hat{\chi}^2_{bad} = 2 \cdot \hat{\chi}^2_{good}$, i.e., this single measurement cycle accounts for half of the $\hat{\chi}^2$ from the model in comparison with the other 7 measurement cycles. For deuterium, the goodness

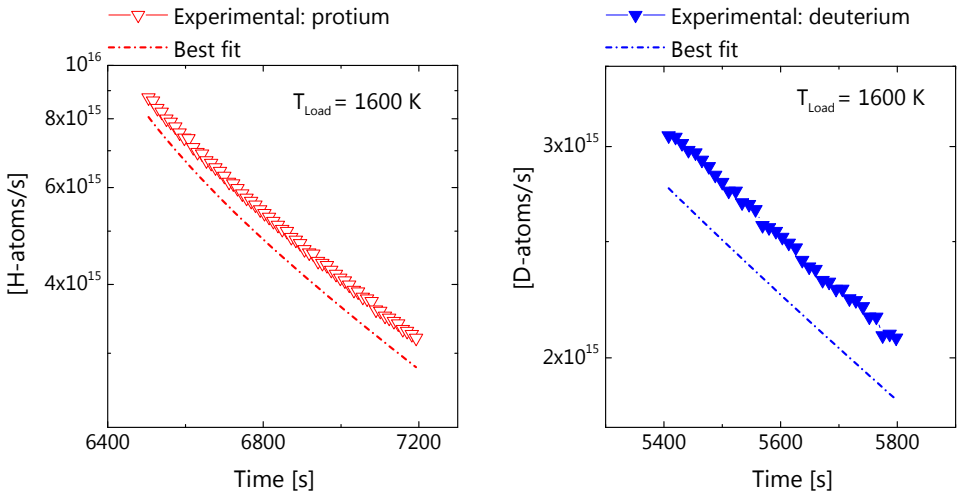

Figure 5.5.: Two degassing measurements from the big specimen with their best fits when being part of the data set used for final evaluation, plotted on a logarithmic scale. Shown is in both cases only the section of the fitting window as defined in section 3.3. The loading conditions are 1600 K at 500 mbar for 3 h. The degassing temperature for both is 2000 K. The panels show the measured degassing signal as triangles. The predicted degassing signal from the full diffusion model is shown as dash-dotted lines. The diffusivity, i.e., the slope of decay, fits quite well, whereas the absolute amount does not. The inventory in the experiments exceed the models' predictions.

of fit for the whole data set even yields $\hat{\chi}^2_{bad} = 3 \cdot \hat{\chi}^2_{good}$.

However, both rejected measurement cycles produce good matches with respect to the decay, i.e., the slope of the shown curves which determine the diffusivity at this degassing temperature of 2000 K.

These characteristic and systematic deviations indicate, that the solubility as described from the model does not apply to these measurement cycles, i.e., gas loading conditions. At temperatures below 1600 K the dissolved hydrogen in the bulk could be able to populate also an enhanced fraction of traps. That means during the gas loading phase is, in addition to the solute hydrogen, some hydrogen stored in traps. Because the full diffusion model considers only the solute hydrogen (determined by Sieverts' law, see equation 1.2) to calculate the retained amount, the predicted amount from the model is too low compared with the experiment. If the temperature in the degassing phase is equal to or higher than 1800 K, the migration mechanism is solute diffusion only and, therefore, follows the predicted relative decay, but the measured degassing level does not match the predicted absolute height because initially more hydrogen was retained in the sample.

An alternative explanation is the presence of a surface effect (e.g., tungsten-oxide layer) for temperatures up to 1600 K. A presumed surface layer could act as permeation barrier during the cool-down phase at the end of the gas loading sequence and lead to increased hydrogen inventory in the bulk. This could equally well explain the observed deviations. Some indications for such a layer have been seen in the measurements (compare section 3.6).

Degassing at temperatures $\leq 1600\,\mathrm{K}$

As it is the case for measurement cycles with gas loading temperatures at 1600 K or lower, also degassing at temperatures $\leq 1600\,\mathrm{K}$ leads to increased $\hat{\chi}^2$ values. E.g., gas loading at 2000 K and degassing at 1600 K yields a fit that shows a reasonable match of the magnitude of flux (i.e., solubility) but deviations in the decay rates (i.e., diffusivity). The measured degassing decays are slower than the model predicts. This observation is true for all analysed measurement cycles with degassing at $T \leq 1600\,\mathrm{K}$ and it is independent of the applied gas loading temperature, i.e., the absolute signal height does not seem to play a role for this effect.

The reason for this deviation of the degassing decay could be attributed to trapping effects during degassing. At temperatures lower than or equal to 1600 K, an increasing fraction of traps could be populated. Also the existence of a permeation barrier at the surface up to around 1600 K, e.g., forming tungsten-oxide, could equally explain the decreasing degassing compared with temperatures equal to and higher than 1800 K. Both effects would slow down the measured solute diffusion, described in equation 1.5 and which is the foundation of the full diffusion model that is used for the evaluation. Hence, measurement cycles with degassing sequences at or below 1600 K are excluded from the data set for final evaluation.

Ramps slower than 3 K/s

The decay constants substantially deviate if the samples are ramped up to the degassing temperature at rates of 3 K/s or slower. A measurement cycle ("fk230") with gas loading at 2400 K for 50 min and degassing at 2400 K/s with a 3 K/s temperature ramp does exhibit a bad fit concerning the decay. The measured decay is slower compared to the other measurement cycles that are part of the final evaluation. The good measurement cycles are all ramped at rates equal to or higher than 5 K/s and show no deviation as described above.

Presumable surface effects that could cause this deviation are discussed in chapter 3.6. It is suggested that at the lower ramping rate of 3 K/s the potential oxide layer(s) at the surface could grow to a larger thickness. This surface oxide could act as surface barrier for degassing of hydrogen thus reducing degassing rates. Higher ramping rates are assumed to cause a thinner or no tungsten oxide layer at constant degassing temperatures, because sublimation of tungsten oxide outweighs its formation at temperatures higher than about 1600 K. Therefore, faster ramping rates at temperatures higher than 1600 K would hinder the formation of thicker tungsten oxide layers that are not completely sublimated at the time of the fitting window. Whereas, a definite explanation of the potential reason for this cannot be given, the measurement cycle fk230 is also excluded from final evaluation, based on this strong deviation.

5.3. Bayesian statistics & Markov-Chain-Monte-Carlo (MCMC) sampling

The 4-dimensional probability density function (pdf) of the four variables E_A, D_0, E_S, and S_0 $p(E_A, D_0, E_S, S_0 \mid \mathbf{d}) = p(\boldsymbol{\Theta} \mid \mathbf{d})$ is derived from the full diffusion model code. For protium 7 measurement cycles, for deuterium 9 measurement cycles are used. The accepted data sets for the final analysis are defined in 5.2.1. According to Bayes theorem the pdf is given by

$$\mathrm{p}(\boldsymbol{\Theta} \mid \mathbf{d}) = \frac{\mathrm{p}(\mathbf{d} \mid \boldsymbol{\Theta}) \cdot \mathrm{p}(\boldsymbol{\Theta})}{\int \mathrm{d}\Theta \; \mathrm{p}(\mathbf{d} \mid \boldsymbol{\Theta}) \cdot \mathrm{p}(\boldsymbol{\Theta})} \tag{5.3}$$

where $\mathrm{p}(\mathbf{d} \mid \boldsymbol{\Theta})$ denotes the likelihood of the data $\mathbf{d}$ and $\mathrm{p}(\boldsymbol{\Theta})$ the prior probability for the parameters. The prior distribution is chosen to be constant within the hyper rectangle

$$\begin{pmatrix} 0.2 \;\leq\; \mathrm{E_A}\,[\mathrm{eV}] \;\leq\; 0.4 \\ 1 \;\leq\; \mathrm{D_0}\,[10^{-7}\mathrm{m^2/s}] \;\leq\; 10 \\ 0.65 \;\leq\; \mathrm{E_S}\,[\mathrm{eV}] \;\leq\; 1.35 \\ 1 \;\leq\; \mathrm{S_0}\,[10^{-3}\left(\frac{\mathrm{H}}{\mathrm{W}}\right)\mathrm{atm}^{-\frac{1}{2}}] \;\leq\; 30 \end{pmatrix} \text{ and } \mathrm{p}(\Theta) = 0 \text{ for parameters outside.} \tag{5.4}$$

Care was taken that the boundaries did not affect the optimisation and sampling. Using Markov-Chain-Monte-Carlo (MCMC) sampling, the parameter probability distribution is sampled. This provides additional information about the parameters compared to the best fit (χ^2 and $\hat{\chi}^2$, see chapter 3.4) value only. Since the parameter space is 4-dimensional, each sample consists of a tuple of $\mathrm{E_A}$, $\mathrm{D_0}$, $\mathrm{E_S}$, and $\mathrm{S_0}$. This 4-d probability distribution is projected into different 2-dimensional subspaces to provide a visual impression of these distributions. To avoid spurious contributions from the choice of the arbitrary starting point of the MCMC chain the first 30000 MCMC steps are discarded (burn-in phase). Then 25000 MCMC steps are performed. To reduce the correlation of the individual steps only every 50th step is retained (thinning of MCMC chain), resulting in $N_{samples} = 500$ [56]. Assuming independence of the retained samples $\boldsymbol{\Theta}_\mathrm{i} \ldots \boldsymbol{\Theta}_{\mathrm{N_{samples}}}$ they can be used to compute the moments K of the probability distributions via

$$\langle \boldsymbol{\Theta}^\mathrm{K} \rangle = \frac{1}{\mathrm{N_{samples}}} \sum_{\mathrm{i}=1}^{\mathrm{N_{samples}}} \boldsymbol{\Theta}_\mathrm{i}^\mathrm{K} \quad ; \boldsymbol{\Theta}_\mathrm{i} = \begin{pmatrix} \mathrm{E_A} \\ \mathrm{D_0} \\ \mathrm{E_S} \\ \mathrm{S_0} \end{pmatrix} \tag{5.5}$$

Thus the mean is given by $\langle \Theta^1 \rangle$ and the variance by

$$\sigma_\Theta^2 = \langle \Theta^2 \rangle - \langle \Theta^1 \rangle^2 \tag{5.6}$$

Within the uncertainty the result of the MCMC sampling and the maximum-likelihood ($\hat{\chi}^2$) approach coincide for all four variables $\mathrm{E_A}$, $\mathrm{D_0}$, $\mathrm{E_S}$, and $\mathrm{S_0}$. Therefore, the parameter set with the largest posterior value (which coincides here with the maximum-likelihood result) of the MCMC sampling is taken as final result of the four variables.

Uncertainty analyses

The uncertainties of the evaluated values for $\mathrm{E_A}$, $\mathrm{D_0}$, $\mathrm{E_S}$, and $\mathrm{S_0}$ consist of a combination of statistical and systematic uncertainties.

The value of σ_MCMC represents uncertainties, that are part of the diffusion model. They are counting statistics and other relative deviations of the flux (which are estimated to 1% of the measured flux), caused by, e.g., QMS detector drifts, enhanced coating of the inner glass wall, or variations of background flux (see chapter 3.4, equation 3.1: $\sqrt{N_j} + 0.01 \cdot N_j$). Hence, these statistical errors are reflected by the mean value of the width of the MCMC sampling

trace corresponding to the individual variable (see figure 5.6). Those uncertainties that are part of the diffusion model, i.e., MCMC sampling, have a rather low influence on the total uncertainty of the results and are indicated in table 5.2.

Other systematic uncertainties that are not part of the diffusion model stem from temperature measurement $\sigma_{temp.\,drift}$ and the calibration method, i.e., the uncertainties in the flux from the calibrated leak bottles for protium and deuterium $\sigma_{calibr.\,leak}$.
The uncertainty in temperature measurement is determined by the nominal accuracy of the thermocouple, i.e., $\pm\,1\%$ (of temperature in °C), plus the estimated extended temperature deviations/drifts at dynamic and static conditions that exceed the nominal accuracy (see chapter 3.1.2). The maximum measured drifts of $^{+1.8\%}_{-1.0\%}$ are used for testing the influence of temperature deviation on the full diffusion model.
The systematic uncertainty in the measured degassing flux of protium or deuterium atoms stems from the calibrated leak bottles for both species (as described in chapter 2.4). The uncertainty for the protium leak bottle is $\pm\,3.8\%$, in the case of deuterium this is $\pm\,4.6\%$.
Because these two systematic uncertainties are not part of the diffusion model, artificial data sets are produced from the evaluated data set (that was used for the final evaluation) such, that they are charged with these maximum uncertainties. I.e., these measurement cycles are altered such, that they exhibit the maximum estimated differences for either the temperature or the absolute degassing flux. For example, for protium all degassing signals of the measurement cycles from the data set for final evaluation are charged with $+\,3.8\%$, and the following deviation for all four variables E_A, D_0, E_S, and S_0 is derived to represent the influence of the uncertainty of the calibrated leak in positive direction. By this, for each isotope, protium and deuterium, 4 altered data sets are generated and evaluated with the full diffusion model, thus providing new solutions for the model parameters which are afflicted with the corresponding uncertainty. The difference to the nominal value is taken as uncertainty. Each altered data set exhibits one single change of each parameter.

Further uncertainties could arise from the size of the fitting window which is defined in chapter 3.3. Especially the beginning of the fitting window could vary, because the starting point was chosen manually, i.e., when the measured degassing signal appeared to become single-exponential after the overshoot. Hence, both data sets for protium and deuterium are re-analysed to assess the influence of this choice. As test, the fitting window in every measurement cycle was started 100 s earlier. The variation of the fitting window leads to virtually identical results for the four variables within the uncertainty of the full diffusion model, e.g., the same activation energy within 10^{-4} eV for both, protium and deuterium, i.e., the result was insensitive to this variation.

Hence, three uncertainties are taken into account, the uncertainties which are part of the model and are defined from the mean value of the the width of the MCMC sampling, and the systematic uncertainties from the temperature drift and calibrated leak:

$$\sigma_{\text{total}} = \sqrt{\sigma^2_{\text{MCMC}}} + \sqrt{\sigma^2_{\text{temp. drift}} + \sigma^2_{\text{calibr. leak}}} \tag{5.7}$$

σ_{total} is used for the uncertainties of the final results.

5.3.1. Results

5.3.1.1. Solubility

The results for the solubility coefficients from the MCMC sampling are shown for protium and for deuterium in figure 5.6. The posterior samples $\{\mathrm{E_S}, \mathrm{S_0}\}_\mathrm{i}$ obtained by MCMC for protium (red circles) and deuterium (blue triangles) are presented on the left panel. The y-axis marks the solute energy E_S and the x-axis the pre-factor of solubility S_0. Each panel shows $25000/500 = 500$ samples of the MCMC post sampling and reflects the shape and extent of the relevant part of the probability distribution of the parameters $\mathrm{p}(\mathrm{E_S}, \mathrm{S_0} \mid \mathbf{d})$. A strong positive correlation between the two parameters is clearly visible. Based on the extension of the MCMC probability distribution, the uncertainty from the statistical uncertainties can be derived. These are shown exemplarily in the upper and lower right panel in figure 5.6 for the pre-factor of solubility S_0^D for deuterium. The statistical uncertainty for the solute energy E_S^D is equally derived. These widths reflect the statistical uncertainty that stem from counting statistics from the QMS ($1/\sqrt{\mathrm{N_j}}$, N_j being the number of QMS counts) and the estimated relative accuracy of the QMS measurement ($1/0.01 \cdot \mathrm{N_j}$), see chapter 3.4. These statistical uncertainties are similarly derived for protium. This plot displays the higher uncertainties of the pre-factor (that also Frauenfelder described [8]). The same goodness of fit inherently yields higher uncertainties for the pre-exponential factor of solubility $\mathrm{S_0}$ than for the solute energy $\mathrm{E_S}$.

Under some technical assumptions [56], the correct choice of the statistical error and in the limit of an infinite amount of data $\hat{\chi}^2$ should converge towards 1. The observed values of $\hat{\chi}^2$ of 1.19 and 0.30 are in good agreement with that. The value of $\hat{\chi}^2_H = 1.19$ means, that the estimation of uncertainties for measurement cycles with protium is quite accurate. $\hat{\chi}^2_D = 0.30$ for deuterium concludes that the uncertainties for the deuterium measurement may be chosen too conservative. This effect could stem from the 3 orders of magnitude lower background flux for deuterium compared with protium (because of the higher natural abundance of protium in comparison to deuterium) which lowers the uncertainties in the measured degassing signal and the calibration.

The correlation of solute energy E_S and the pre-exponential factor S_0 is clearly indicated by the results of the MCMC sampling that form a tilted "line" in the plot. This means that if $\mathrm{E_S}$ is changed from the model towards higher values, also $\mathrm{S_0}$ needs to go up, to compensate for the change to still yield a good χ^2 value, i.e., a good fit to the measured data.

The maximum likelihood values are shown in figure 5.6 in the left and upper right panel for protium, and deuterium, respectively. The lower right panel shows the counting statistics of the probability distribution from MCMC sampling. The shape of the distribution does not match a Gaussian probability distribution. Hence, the value with the maximum likelihood (i.e., the best $\hat{\chi}^2$) is not necessarily to be found in the middle of the distribution. This value is also sensitive to noise in contrary to the mean values of the probability distribution which are more stable. Hence, the mean values are chosen as final parameters. Those are marked in figure 5.6.

The final parameters for the solubility, together with their total uncertainties are shown in subsection 5.3.1.3 in table 5.1.

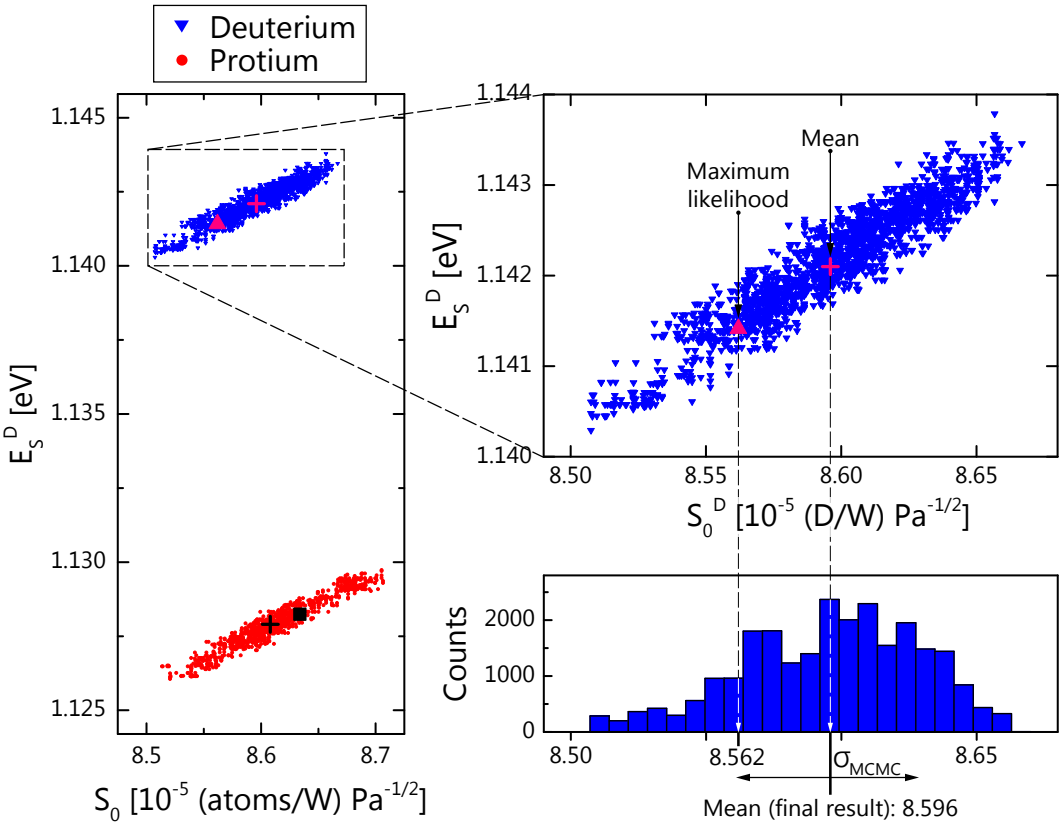

Figure 5.6.: The results for the solubility coefficients from MCMC posterior sampling. The left panel shows the posterior samples for protium (red circles) and deuterium (blue triangles), the maximum likelihood values are marked as black square (H) and pink triangle (D). The mean values are marked as black (H) or pink (D) crosses. They are chosen as final results because they are more stable. They yield for protium 1.13 eV and $8.61{\cdot}10^{-5}$ $\left(\frac{\mathrm{H}}{\mathrm{W}}\right)$ $\mathrm{Pa}^{-\frac{1}{2}}$ and for deuterium 1.14 eV and $8.60{\cdot}10^{-5}$ $\left(\frac{\mathrm{D}}{\mathrm{W}}\right)$ $\mathrm{Pa}^{-\frac{1}{2}}$. The upper right panel shows an enlarged view of the posterior samples for deuterium. The maximum likelihood value and mean value does not yield the same numbers, as exemplarily indicated for S_0^D in the lower right. The lower right panel shows the counting statistics of the MCMC posterior sampling. The distribution is asymmetric and not a Gaussian probability distribution. Hence, the maximum likelihood value (with the best $\hat{\chi}^2$) does not necessarily appear in the middle of the distribution. The mean value σ_{MCMC} marks 67% of the points.

5.3.1.2. Diffusivity

The same posterior samples from the MCMC sampling for the diffusion coefficients of protium and deuterium are shown in figure 5.7 in the upper panels. The lower panels show the counting statistics of the MCMC posterior sampling for the activation energies. All four frames of

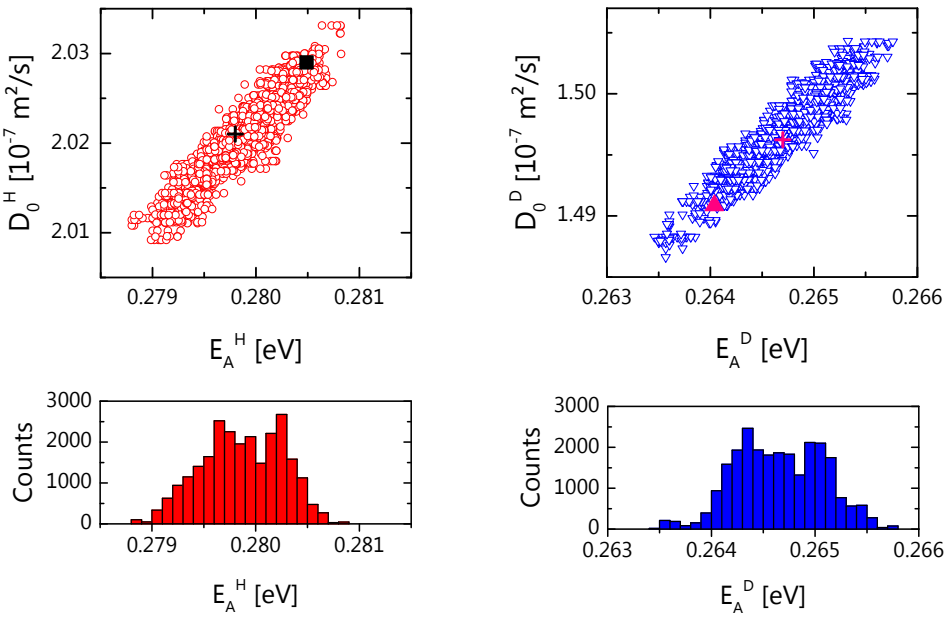

Figure 5.7.: The upper panels show the posterior samples from MCMC sampling (from the 4d-posterior distribution) for the diffusivity parameters for protium and deuterium. The maximum likelihood values, i.e., exhibit the best $\hat{\chi}^2$ value, are shown as black squared marker (H) and as pink pyramid (D). Also the mean value of the posterior sampling distributions are shown as black (H) and pink (D) crosses, these values are taken as final parameters. The lower panels show the counting statistics of the MCMC posterior sampling. The distributions are asymmetric.

protium and deuterium cover the same range of activation energy. In the E_A-D_0 plots in the upper panels, the correlation of the coefficients for diffusivity (a property of the model), manifests itself as results of the MCMC sampling which form a tilted line. As for the solubility, the uncertainties from the statistical uncertainties are higher for the pre-exponential factor for both isotopes. The uncertainties are derived from the width of the probability distributions, as shown for solubility in subsection 5.3.1.1. The maximum likelihood values, i.e., those with the best $\hat{\chi}^2$ values, are also shown in the upper panels. The lower panels show the counting statistics of the posterior sampling, both distributions are asymmetric, and, hence, are not Gaussian distributions. The mean values are taken as final parameters and are listed in the next section 5.3.1.3 in table 5.1 with their total uncertainties σ_{total}.

5.3.1.3. Results with total uncertainties σ_{total}

The final values from the full diffusion model on the big specimen, together with their total uncertainties σ_{total}, are presented in table 5.1 The uncertainties for the diffusivity coefficients are relatively small, the uncertainty towards higher values is roughly double than to

Table 5.1.: Results from the full diffusion model for the four variables E_A, D_0, E_S, and S_0 for protium and deuterium with their total uncertainties σ_{total}.

	Results from full diffusion model			
	Diffusivity		Solubility	
	E_A [eV]	D_0 [$10^{-7}\mathrm{m}^2/\mathrm{s}$]	E_S [eV]	S_0 [$10^{-5}\left(\frac{\mathrm{atoms}}{\mathrm{W}}\right)\mathrm{Pa}^{-\frac{1}{2}}$]
Protium	$0.280^{+0.02}_{-0.01}$	$2.02^{+0.14}_{-0.11}$	$1.13^{+0.04}_{-0.02}$	$8.61^{+0.99}_{-0.53}$
Deuterium	$0.265^{+0.02}_{-0.01}$	$1.50^{+0.09}_{-0.05}$	$1.14^{+0.04}_{-0.02}$	$8.60^{+0.97}_{-0.59}$

lower values. This stems from observed asymmetrical temperature drifts. The uncertainties for the solute energy is relatively small as well, also here an extended uncertainty towards higher values can be observed. The pre-exponential factor for solubility exhibits the highest uncertainties, compared with the other coefficients. This is because it is sensitive to variations of the temperature and the total measured inventory only.

5.3.2. Arrhenius plot of H and D diffusivities

The here derived diffusivities from the full diffusion model for protium and deuterium are shown in an Arrhenius plot in figure 5.8. The full diffusion model yields the results for the diffusion coefficients from the simultaneous evaluation of all measurement cycles from the final evaluation for protium or deuterium, respectively. These results are represented by the lines for protium and deuterium. To derive the individual diffusivities from the measurement cycles that are part of the data sets for final evaluation (see figure 5.4), they are evaluated one by one with the full diffusion model code. For this, both coefficients that determine the solubility are fixed to the derived values (according to section 5.3.1.1), only the coefficients for diffusivity, E_A and D_0, are left as free adjustable variables. Hence, the code determines those coefficients that best match the fitting window for this single measurement. They are shown as full, coloured symbols in figure 5.8. They also represent the accepted measurement cycles that were used for the final evaluation of the full diffusion model. These individual measurements match the lines (which represent the simultaneous final evaluation of all measurement cycles) very good.

Additionally to results of the accepted measurement cycles, also some of the not-accepted measurement cycles (according to section 5.2.2) are shown in the plot. These are related to measurement cycles with degassing sequences at temperatures of 1600 K and lower and are shown as open symbols.
From all measurements which are part of the data sets for the full diffusion model assessment, these respective diffusivities are derived and plotted in figure 5.8. Diffusivities of measurement cycles with degassing temperatures at or below 1600 K show a significantly higher deviation towards lower diffusivities. The exclusion of these measurement cycles from the final evaluation (as described in section 5.2.2), seems to be justified. The derived diffusivity for the degassing sequence with protium at 1600 K, is 8% lower than the value from the full diffusion model.

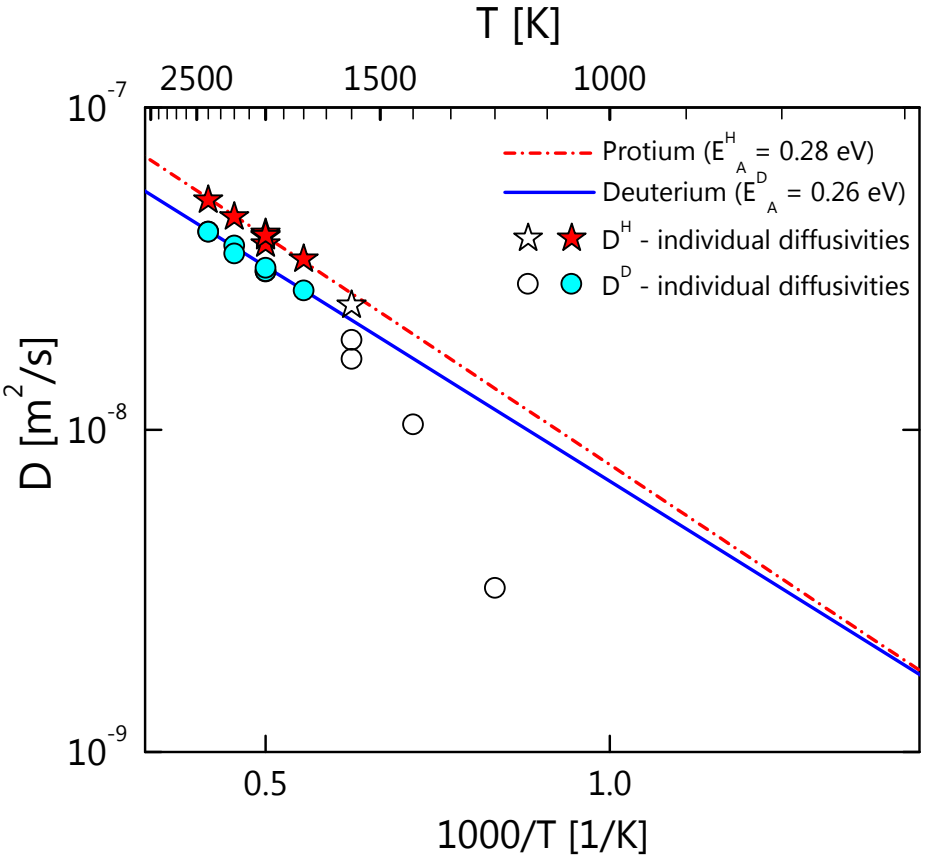

Figure 5.8.: Arrhenius plot of the diffusivities for protium and deuterium, derived by applying the full diffusion model to the measured data. The derived diffusivities from the full diffusion model on the big specimen are shown as lines for protium and deuterium. The single measurements at distinct degassing temperatures are shown as symbols. Measurements from the final evaluation are shown as solid, coloured symbols. At 2000 K for each isotope 4 measurements are shown, but yielding such similar values that they cannot be distinguished. Measurements which noticeably deviate and are not part of the quantitative assessment are shown as open symbols.

The degassing sequences for deuterium at 1600 K are lower by 13%, or 24%, respectively. The diffusivities are further decreasing as the degassing temperatures become lower. The diffusivity for deuterium at 1400 K is measured to be 38% lower than the diffusivity derived from the full diffusion model, at 1200 K it is already 72% lower.

5.3.3. Comparison of protium and deuterium

Certain questions concerning the difference of the results for the two isotopes are addressed in the following, e.g., is the solubility different? To compare protium and deuterium, different uncertainties need to be considered from case to case. As outlined above, the uncertainties stem from two different sources: Firstly, the systematic uncertainties which are derived from the uncertainties in temperature measurement and the uncertainty of the absolute degassing flux from the calibrated leak bottles. Secondly, the uncertainties which are already part of the MCMC sampling (statistical and systematic uncertainties) (see chapter 3.4). Table 5.2 shows the results for the uncertainties, sorted by their kind and isotope. The first line from each isotope (P.0, D.0), denoted with "Control sample", shows the values from a run with the full diffusion model with no differences, i.e., altering in temperature or flux.
The following lines (P.1 - P.4, D.1 - D.4) show the deviation of the result, if the temperature reading fed to the full diffusion model code is changed by +1.8% or -1.0% for all measurement cycles in the data set for final evaluation. This represents the deviation of the results that stem from the experimentally derived drift of the temperature reading (see chapter 3.1.2).
The subsequent lines (P.5 - P.8, D.5 - D.8) in the table show the results, if the fluxes of all involved measurement cycles from the data set for final evaluation are changed. This corresponds to the uncertainty of the calibrated leak bottle (for the calibrated protium leak bottle this uncertainty is stated as ±3.8%, for deuterium ±4.6%).
Altered data sets with mixed uncertainties, i.e., both taking temperature and flux into account, yield smaller uncertainties than if these corresponding uncertainties are considered separately and then summed up (by using equation 5.7) and hence not taken into account further.
The last lines for each isotope (P.9, D.9) show the uncertainties which are part of the model, represented by the σ_{MCMC}.

Uncertainties in the temperature reading have the highest overall impact on the resulting four variables, because temperature is the leading term for diffusivity as well as for solubility. But, for a comparison of the values for protium and deuterium from this work the uncertainty of the temperature can be ignored. It is a relative uncertainty, i.e., it is equal for every measurement independently of the isotope. The uncertainty of the temperature reading is only important for the absolute values of the results from the final evaluation, not for relative comparisons within this work.

Solubility

The question is, if the solubility of protium and deuterium yields different values. For this comparison, the uncertainties from the model need to be taken into account (lines P.9 and D.9 in table 5.2), because, e.g., counting statistics applies. The corresponding percentages are calculated from the control sample (lines P.0 and D.0). Also the calibrated leak uncertainties for both isotopes need to be considered (lines P.5 - P.8 and D.5 - D.8 in table 5.2), because there are two physically different calibrated leak bottles with different uncertainties for both species. The uncertainty caused from the temperature reading (lines P.1 - P.4 and D.1 - D.4)

does not need to be taken into account, because these relative deviations are the same for protium and deuterium measurements.

These relevant uncertainties summed up yield very low values for the solute energy E_S: for protium $1.13^{+0.002}_{-0.003}$ eV and for deuterium $1.14^{+0.002}_{-0.002}$ eV. This implies that, apart from temperature, E_S is not sensitive to variations of the degassing flux.
The uncertainties of the pre-exponential factor for protium yield $8.61^{+0.075}_{-0.070} \cdot 10^{-7} \left(\frac{H}{W}\right) Pa^{-\frac{1}{2}}$ and for deuterium to $8.60^{+0.073}_{-0.072} \cdot 10^{-7} \left(\frac{H}{W}\right) Pa^{-\frac{1}{2}}$. The values agree within the uncertainties. The overall uncertainties of the pre-factor of solubility S_0 are the highest from the four variables E_A, D_0, E_S, and S_0. This seems to result from the overall higher dependence of S_0 on all three uncertainties (statistical, temperature and calibrated leak bottle). S_0 shows the weakest correlation on the other three variables E_S, E_A, and D_0. Equation 1.18 in chapter 1.3 describes the dependence of the degassing signal pR (left side of equation) to solubility and diffusivity. Replacing the solubility S with the actual expression from Sievert yields:

$$pR = \frac{16\,V\,S_0 \exp\left(-\frac{E_S}{k_B T}\right) p_e^{\frac{1}{2}}}{d^2} D \cdot \exp\left(-\frac{4\xi_1^2}{d^2} Dt\right), \tag{5.8}$$

in which pR is the measured flux of atoms (p is the partial pressure and R the pumping speed). Having a closer look at the right side of the equation, it can be seen that S_0 is the only variable which shows a linear dependence on the degassing signal. E_S has a single-exponential dependence on the degassing signal, the variables for diffusivity (E_A and D_0) show various dependencies of single and multiple exponential character. This makes S_0 much more sensitive to uncertainties that concern the degassing, because even high changes of S_0 have a relatively low impact on the degassing signal in comparison to the other three variables[1].

Diffusivity

For the diffusivity, it shall be estimated if the activation energies E_A of protium and deuterium can be regarded as indistinguishable within the uncertainties. The uncertainties which need to be taken into account are the uncertainties σ_{MCMC} (lines P.9 and D.9 in table 5.2) and the uncertainties from the calibrated leak bottles (lines P.5 - P.8 and D.5 - D.8), because, as described for the solubility, each isotope uses a physically different calibrated leak bottle. As for the solubility, the temperature uncertainties do not need to be taken into account, because the relative deviations are regarded as equal for both isotopes.
For this internal comparison both regarded uncertainties yield the results with their uncertainties are analysed for protium to $0.280^{+0.003}_{-0.005}$ eV and for deuterium to $0.265^{+0.001}_{-0.001}$ eV. The results for the activation energies differ at the second decimal place, but the uncertainties for both results are very small, i.e., negligible.Because of this, no firm statement can be given if the activation energies for both isotopes are equal or not. But, this does not mean that the same activation energy E_A can be used for protium and deuterium. As a consequence of the strong correlation of activation energy and pre-exponential factor, one value cannot be changed without adjusting the other correspondingly.

As a side remark: Cross-combinations between the variables of diffusivity and solubility, i.e., E_A - E_S and D_0 and S_0 show only weak correlations. With other words, the change of activation energy does not necessarily require an adjustment of the solute energy.

[1] This also explains why D_0, also a pre-exponential factor which is sensitive to changes of the activation or solute energy, shows a weaker correlation to uncertainties of all kinds.

Table 5.2.: Deviations of the results for the four variables for protium and deuterium, caused by uncertainties. The uncertainties stem from the temperature measurement, calibration of the degassing flux of protium and from the MCMC sampling. The uncertainties for temperature and flux are derived by evaluating the altered original data sets with the full diffusion model.

		Protium			
		E_A^H [eV]	D_0^H [$10^{-7}\mathrm{m}^2/\mathrm{s}$]	E_S^H [eV]	S_0^H [$10^{-5}\left(\frac{\mathrm{H}}{\mathrm{W}}\right)\mathrm{Pa}^{-\frac{1}{2}}$]
P.0	Control sample	0.283	2.055	1.128	8.604
P.1	Temperature [K]: +1.8%	0.299	2.194	1.167	9.534
P.2	Temperature [K]: -1.0%	0.271	1.951	1.107	8.128
P.3	Deviation from control sample	$^{+0.016}_{-0.012}$	$^{+0.139}_{-0.104}$	$^{+0.039}_{-0.021}$	$^{+0.093}_{-0.048}$
P.4	Deviation from control sample	$^{+5.7\%}_{-4.3\%}$	$^{+6.8\%}_{-5.1\%}$	$^{+3.5\%}_{-1.9\%}$	$^{+10.8\%}_{-5.5\%}$
P.5	Degassing [H-atoms/s]: +3.8%	0.281	2.038	1.128	8.925
P.6	Degassing [H-atoms/s]: -3.8%	0.279	2.013	1.129	8.329
P.7	Deviation from control sample	$^{+0.002}_{-0.004}$	$^{+0.017}_{-0.042}$	$^{+0.000}_{-0.001}$	$^{+0.032}_{-0.027}$
P.8	Deviation from control sample	$^{+0.7\%}_{-1.4\%}$	$^{+0.8\%}_{-2.0\%}$	$^{+0.0\%}_{-0.1\%}$	$^{+3.7\%}_{-3.2\%}$
P.9	MCMC [%]	±0.1%	±0.2%	±0.2%	±0.5%
		Deuterium			
		E_A^D [eV]	D_0^D [$10^{-7}\mathrm{m}^2/\mathrm{s}$]	E_S^D [eV]	S_0^D [$10^{-5}\left(\frac{\mathrm{D}}{\mathrm{W}}\right)\mathrm{Pa}^{-\frac{1}{2}}$]
D.0	Control sample	0.264	1.490	1.141	8.555
D.1	Temperature [K]: +1.8%	0.280	1.581	1.180	9.446
D.2	Temperature [K]: -1.0%	0.255	1.441	1.120	8.108
D.3	Deviaton from control sample	$^{+0.016}_{-0.009}$	$^{+0.091}_{-0.049}$	$^{+0.039}_{-0.021}$	$^{+0.089}_{-0.045}$
D.4	Deviation of control sample	$^{+6.1\%}_{-3.4\%}$	$^{+6.1\%}_{-3.3\%}$	$^{+3.4\%}_{-1.8\%}$	$^{+10.4\%}_{-5.2\%}$
D.5	Degassing [D-atoms/s]: +4.6%	0.264	1.489	1.141	8.945
D.6	Degassing [D-atoms/s]: -4.6%	0.264	1.489	1.141	8.172
D.7	Deviation from control sample	$^{+0.000}_{-0.000}$	$^{+0.001}_{-0.001}$	$^{+0.000}_{-0.000}$	$^{+0.039}_{-0.038}$
D.8	Deviation from control sample	$^{+0.0\%}_{-0.0\%}$	$^{+0.0\%}_{-0.1\%}$	$^{+0.0\%}_{-0.0\%}$	$^{+4.5\%}_{-4.4\%}$
D.9	MCMC [%]	±0.2%	±0.3%	±0.2%	±0.4%

5.4. Synopsis

5.4.1. Diffusivity

The following chapter compares the results from the reduced and the full diffusion model with the values for diffusivity that are widely used until now [8, 16]. Gas loading and degassing measurements were performed by both using the small specimens and the big specimen. The gas loading pressure for these measurements was always 500 mbar for both, protium and deuterium. The small specimens (the single- and poly-crystalline) are evaluated with the reduced diffusion model, with 5 measurement cycles for protium (degassing temperature between 1800 and 2600 K) and 5 for deuterium (degassing temperature between 1600 and 2400 K). The loading temperature was varied between 1800 and 2400 K. The big specimen is evaluated with the full diffusion model. 7 measurement cycles for protium and 9 measurement cycles for deuterium were analysed. Both, the gas loading and degassing temperatures varied between 1800 and 2400 K.

5.4.1.1. Comparison of obtained results

Results from both applied methods, reduced and full diffusion model are compared in figure 5.9. The reduced diffusion model yields for activation barrier and pre-exponential factor of protium and deuterium (with their total uncertainties, i.e., σ_{total} for the full diffusion model):
$E_A^{H:\,red.} = 0.28 \pm 0.06\,eV$, $D_0^{H:\,red.} = 2.06{\cdot}10^{-7}\,m/s^2$ and
$E_A^{D:\,red.} = 0.28 \pm 0.06\,eV$, $D_0^{D:\,red.} = 1.60{\cdot}10^{-7}\,m/s^2$.
In comparison the full diffusion model yields:
$E_A^{H:\,full} = 0.280^{+0.02}_{-0.01}\,eV$, $D_0^{H:\,full} = 2.02^{+0.14}_{-0.11}{\cdot}10^{-7}\,m^2/s$ and
$E_A^{D:\,full} = 0.265^{+0.02}_{-0.01}\,eV$, $D_0^{D:\,full} = 1.50^{+0.09}_{-0.05}{\cdot}10^{-7}\,m^2/s$.

For protium the diffusivities derived from both, reduced and full diffusion model, compare very well. The corresponding lines in figure 5.9 are essentially indistinguishable. The activation barrier for protium is derived to 0.28 eV from both approaches. The pre-exponential factor only differs by the second decimal place. For deuterium the full diffusion model yields a 0.02 eV smaller value for the activation barrier than the reduced model. This leads to a slightly different slope of the model lines in figure 5.9. As mentioned before, the uncertainties do not allow to unambiguously decide if the activation barrier of protium and deuterium really differ. In any case, the model results fit very well to the data points for the evaluation of individual measurements with the full diffusion model (symbols in figure 5.9).

As mentioned above, the ratio of the pre-factors from protium and deuterium for the full diffusion model yields as anticipated about 1.4. The corresponding ratio determined from the evaluation with the reduced diffusion model yields only 1.27, while the activation energies agree within the experimental uncertainties. The reason for the deviation of the pre-factor ratio is presently unclear. Nevertheless, the prediction of different activation energies for protium and deuterium is not foreseen in harmonic theory which predicts equal activation energies for the same elements.

Given the small scatter of individual diffusivities and excellent fits to the measured data of the full diffusion model solutions, these values should be preferentially used instead of the values derived from the reduced diffusion model.

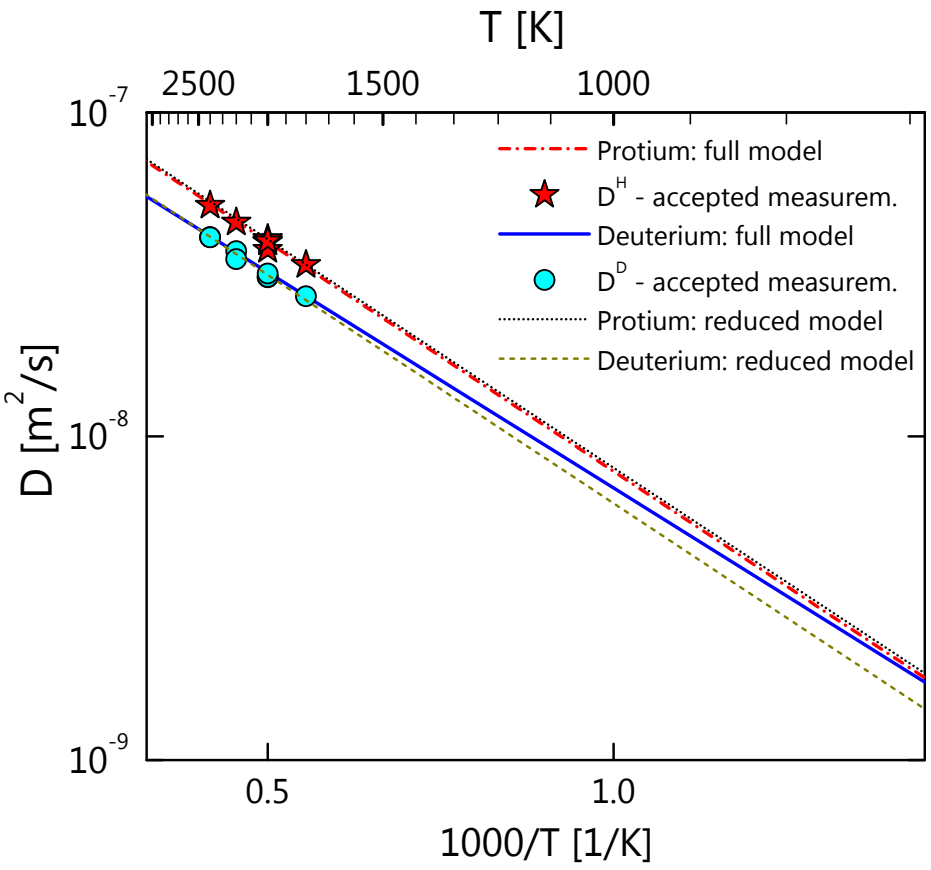

Figure 5.9.: Diffusivities for both, protium and deuterium, derived from the reduced diffusion model (with the small specimens) as well as the from the full diffusion model (with the big specimen), shown in an Arrhenius plot. The diffusivities from individual measurements (i.e., the final evaluation of measurement cycles with the big specimen and the full diffusion model) at certain degassing temperatures are marked as coloured symbols. The correlated fits are marked as lines. Please note that no individual diffusivities from certain degassing sequences (but just the the pre-exponential factor and the activation energy) can be derived from the reduced model, hence, only the correlated fits are to be seen in the graph.

5.4.1.2. Comparison with Frauenfelder's results

In this paragraph the derived diffusion coefficients will be compared to the values available which are recommended and commonly used [8].

The diffusivities evaluated with the full diffusion model with data sets measured on the big specimen are shown in an Arrhenius plot in figure 5.10. The corresponding fits are shown as lines for both hydrogen isotopes with the derived values for the diffusion coefficients (which can be found in table 5.1 in chapter 5.3.1.3). The individual diffusivities determined by single-evaluation of individual measurement cycles are shown for protium and deuterium as solid, coloured symbols. Individual diffusivities from measurements which are not accepted for evaluation are shown as open symbols. These diffusivities are compared with Frauenfelder's values

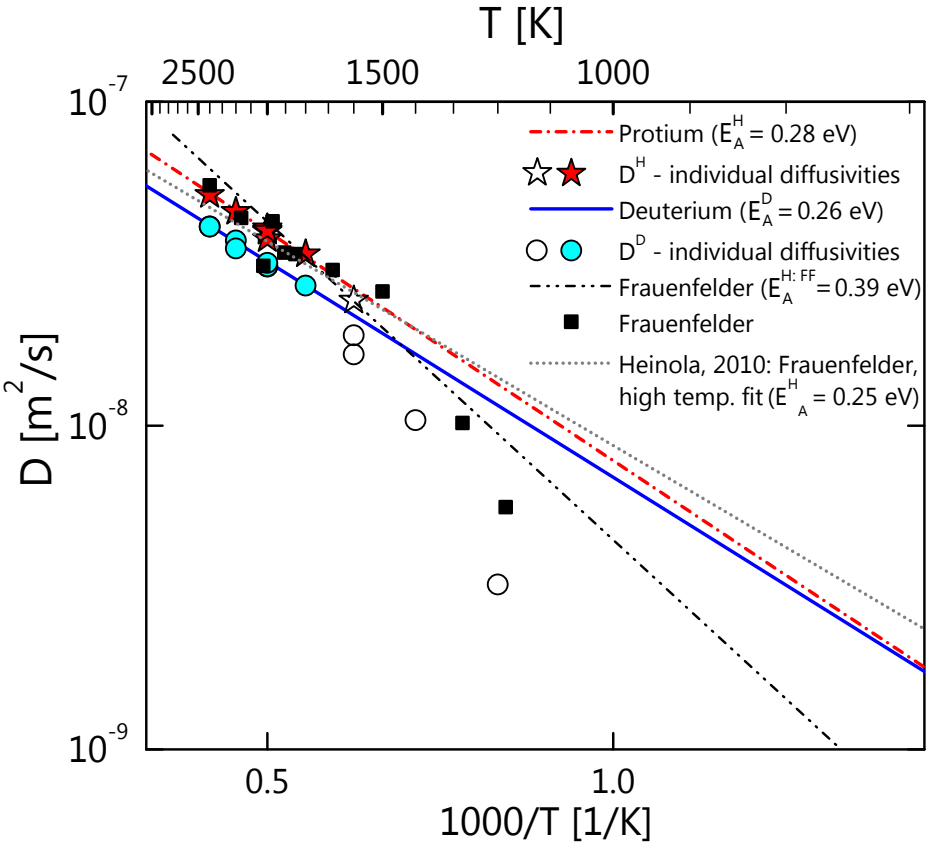

Figure 5.10.: Diffusivities for both protium and deuterium derived from the full diffusion model applied on the big specimen are shown in an Arrhenius plot, together with Frauenfelder's values [8]. The lines represent the fits to the correlated data set. The symbols represent the measured diffusivities of individual measurements at the corresponding degassing temperatures. Measurements from this study at degassing temperatures equal to or lower than 1600 K clearly deviate towards lower diffusivities. These measurements show the same trend as Frauenfelder's diffusivities on the low-temperature side.

for protium (i.e., $E_A^{H,\,FF} = 0.39\,eV$, $D_0^{H,\,FF} = 4.1{\cdot}10^{-7}\,m/s^2$)[8]. His measured individual diffusivities are shown as black symbols and the the corresponding fit for all measurements as black, dash-dotted line.

The evaluated activation energies from this study for the two hydrogen isotopes yield very similar results,but are substantially lower than the value of $E_A^{H,\,FF} = 0.39\,eV$ derived by Frauenfelder. Also the derived pre-exponential factor from this study for protium, $D_0^H = 2.02^{+0.14}_{-0.11}{\cdot}10^{-7}\,m^2/s$, is substantially lower than his derived pre-exponential factor of $D_0^{H,\,FF} = 4.1{\cdot}10^{-7}\,m^2/s$.

Despite these large discrepancies the derived values of Frauenfelder in the high temperature range, i.e., $1500\,K < T < 2400\,K$, fit exceptionally good to the diffusivities derived in this work. The only difference to the diffusivities measured by Frauenfelder in this temperature window is, that they exhibit a slightly higher scatter in comparison with this study. Frauenfelder's low-temperature measurements (degassing temperatures of 1180 and 1280 K) clearly deviate to lower diffusivities, if compared with the trend of the diffusivities measured at higher degassing temperatures. The same deviation for the individual diffusivities (of single degassing sequences) towards lower diffusivities at temperatures at or below 1600 K can be observed in this study. Figure 5.10 shows two diffusivities measured at 1200, 1400, and 1600 K for deuterium (open circles). The diffusivities at higher degassing temperatures follow a different trend[2].
Based on the results this leads to the conclusion that Frauenfelder's two measurements for diffusivity below 1400 K are influenced by an effect that hampers solute diffusion. According to Frauenfelder [8], Heinola [10] or Fernandez et al. [12], this has been assigned to trapping effects and, hence, also non-solute diffusion effects would come into play. Heinola fitted Frauenfelder's high temperature measurements, from which he derived for the pre-exponential factor $D_0^{H:\,FF,\,high\,temp.} = 5.2{\cdot}10^{-8}\,m^2/s$ and for the activation barrier $E_A^{H:\,FF,\,high\,temp.} = 0.25\,eV$. This matches better to values which he derived within the same work from DFT measurements: $D_0 = 5.2 \cdot 10^{-8}\,m^2/s$ and $E_A = 0.21\,eV$. In later work, also DFT simulations, he derived 0.25 eV for the activation barrier in which harmonic vibrations were allowed for the H atom, but not for the lattice [17]. The work from this thesis delivers a new experimentally derived data set, which can serve as additional reference.

It is mostly argued, that trapping effects must have influenced Frauenfelder's measurements up to 1500 K. It is noteworthy, that surface effects which act as permeation barrier, would equally well explain this observed effect on the degassing measurements, i.e., the measured diffusivity. The observed pre-peaks (which are described in chapter 3.6) and the degassing sequences with low temperature ramping rates (that deviate noticeably from fast-ramped ones, see chapter 5.2.2) seem to correlate with a temporary existence of a surface barrier (possibly an oxide layer) at temperatures equal or lower than 1600 K. Frauenfelder did not measure or use the degassing data from the temperature ramp up phase, Heinola does modelling of H-W bulk systems. The ansatz to exclude measurements up to 1600 K, both for gas loading and degassing temperature, seems reasonable in the light of this work, although the acting mechanism is to be debated.

No data for deuterium were provided by Frauenfelder [8]. The presented data for deuterium is, therefore, the first experimental data for diffusivity and solubility of deuterium in tungsten (to my knowledge).

The full diffusion model applied on the big specimen yields a pre-exponential factor ratio of $q_{exp} = D_0^{D:\,full}/D_0^{H:\,full} = 1.37$. This is in reasonable agreement with harmonic theory predictions of the ratio of pre-exponential factors $q_{th} = \sqrt{2}/1 = 1.41$ [23].

[2] The lower degassing temperatures lead to lower fluxes. Therefore, the diffusivities at lower temperatures are mainly measured for deuterium, to benefit from lower natural background in comparison to protium.

5.4.2. Solubility

Figure 5.11 shows the derived solubilities from the full diffusion model applied on the big specimen,
for protium: $E_S^H = 1.13^{+0.04}_{-0.02}$ eV and $S_0^H = 8.61^{+0.99}_{-0.53}{\cdot}10^{-5}$ $\left(\frac{H}{W}\right)$ $Pa^{-\frac{1}{2}}$;
for deuterium: $E_S^D = 1.14^{+0.04}_{-0.02}$ eV and $S_0^D = 8.60^{+0.97}_{-0.59}{\cdot}10^{-5}$ $\left(\frac{D}{W}\right)$ $Pa^{-\frac{1}{2}}$.
The figure also shows the solubility for protium, derived by
Frauenfelder: $E_A^{S:\,FF} = 1.04{\pm}0.17$ eV and $S_0^{H:\,FF} = 2.82^{+2.73}_{-1.26}{\cdot}10^{-5}$ $\left(\frac{H}{W}\right)$ $Pa^{-\frac{1}{2}}$ [8].

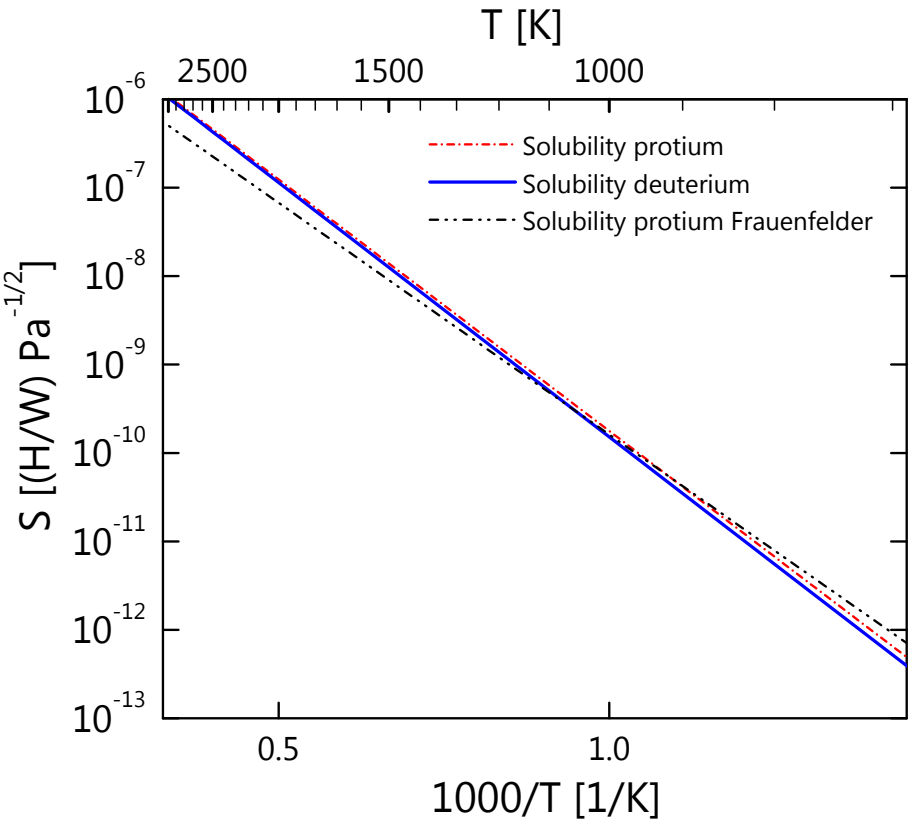

Figure 5.11.: Solubility derived from the full diffusion model applied on the big specimen compared with the solubility derived by Frauenfelder [8]. The solubility derived in this study yields identical results for protium and deuterium.

The derived overall solubility is comparable with the solubility measured by Frauenfelder at the temperature of around 1000 K, whereas the derived solubility is lower at lower temperatures than that and higher at temperatures above 1000 K. The here derived solubility is about 40% higher at a temperature of 1500 K compared to Frauenfelder, at 2000 K it yields 70% higher values. The results for E_S of protium and deuterium yield significantly higher values than the solute energy of $E_A^{S:\,FF} = 1.04{\pm}0.17$ eV as stated by Frauenfelder. The pre-exponential factors S_0 derived from this study are roughly a factor of 3 higher compared to his value of $S_0^{H:\,FF} = 2.82^{+2.73}_{-1.26}{\cdot}10^{-5}$ $\left(\frac{H}{W}\right)$ $Pa^{-\frac{1}{2}}$.

The larger values for the solute energy found in the present experiments could be explained with a different hydrogen pressure during loading. In the present study samples were loaded at 500 mbar, while they were loaded at 800 mbar in Frauenfelder's case. One could, therefore,

expect a lower surface coverage with hydrogen in the present experiments. Very recent investigations indicate that the energy barrier for hydrogen uptake depends on surface coverage: the lower the surface coverage, the higher the solute energy [61].

6. Summary

Have you not succeeded? Continue!
Have you succeeded? Continue!

(Fridtjof Nansen)

Experimental set-up

In order to resolve the puzzle about discrepancies of widely used and recommended values for protium diffusion in tungsten in comparison with recent modelling results, an experimental gas loading apparatus was designed, built and commissioned. Tungsten samples were placed in ultra-high vacuum (UHV) in a quartz glass tube to minimise hydrogen uptake and subsequent outgassing of surrounding parts. Two different quartz glass tubes for two different sizes of specimens were designed and custom-built. The combination of a glass containment and inductive heating enables contactless heating and placing the actuator outside the vacuum vessel. Furthermore, the usage of quartz glass keeps the temperature increase of the inner (glass-) wall minimal, despite relatively high radiative power from the specimens at high temperatures (3.67 kW at 2400 K). Two methods were used for temperature measurement, a type-C thermocouple and optical pyrometry. With these two independent measurements temperature control was possible from room temperature up to 2800 K. By parallel usage of thermocouple and pyrometry temperature drifts could be investigated and quantified. With the set-up temperatures beyond 2800 K are possible but lead to strong evaporation of tungsten and, hence, coating of the glass tube. For experimental investigations the maximum practicable usable temperature was chosen to be 2600 K for a hand full of measurements that were more of exploratory character. 2400 K turned out to be sufficient and feasible for frequent measurement cycles without massive coating of the inner glass wall.

The layout of the gas loading apparatus is partly similar to experiments that were formerly used for diffusivity and solubility investigations of hydrogen in tungsten [8]. However, the design was changed such that safety was substantially increased. By changing the former design to an "upside-down" version in combination with a crash absorber underneath the specimen, possible failures of the mounting do not lead to catastrophic failure of the quartz glass tube. The mounting of the specimen was implemented by a tungsten shaft in combination with a dove-tail groove connection to the specimen, with a calculated safety factor of 6.1 even at a temperature of around 3200 K. This type of connection enabled easy mounting and also demounting, even after temperature explorations up to 2800 K. The usage of tungsten as material for the mounting shaft represents an increase in safety since tungsten is ductile at the operating temperatures of the experiments. This means that the performance of the mounting shaft is best in the most critical phase when the specimen is gas loaded at temperatures of 2400 K in 500 mbar hydrogen atmosphere and failure of the mounting shaft would be worst. The usage of hydrogen for gas loading in a glass vessel at high temperatures requested particular safety measures, e.g., prevention of mechanical impacts, interlocks for heating or a ventilation system

to aspirate the area around the glass tube. Safety measures concerning hydrogen handling with an auxiliary system (i.e., gas feed and pumping) included expanding the hydrogen below the lower explosion limit and inertisation of the mixture with nitrogen before pumping. The outer shielding of the glass tube was designed such that it is able to withstand catastrophic failure of the glass tube and ignition of a possibly forming oxy-hydrogen mixture.

Results

Gas loading and degassing experiments on cylindrical samples were executed with this newly established device to evaluate diffusivity and solubility of protium and deuterium in tungsten. The gas loading pressures varied between 6 and 500 mbar, the temperatures between 1200 and 2600 K.

Two geometries of specimens were used: Firstly, two small specimens with geometry ∅ 15 mm and 48 mm length of single- and poly-crystalline grade. Secondly, a big specimen with ∅ 30 mm and 54 mm length of poly-crystalline grade.

In a combined approach the measurement data from these samples were evaluated by either a reduced or a full diffusion model.

The reduced diffusion model is similar as the analytical solution which was used by Frauenfelder [8]. It evaluates the degassing hydrogen by fitting an Arrhenius-like decay at constant temperature. The model hereby makes advantage of the geometry of the small ∅ 15 mm specimens (length $\gg$ radius) which allows to neglect the concentration change in longitudinal direction, taking into account the concentration gradient in radial direction only.

The above procedure was preformed for degassing temperatures which were varied between 1800 and 2600 K for protium and between 1600 K and 2400 K for deuterium. The gas loading pressure was 500 mbar. Plotting the hereby derived decay constants as a function of inverse degassing temperature allows to derive the diffusivity coefficients. The pre-exponential factors for protium and deuterium were derived to $D_0^H = 2.06 \cdot 10^{-7} m^2/s$ and $D_0^D = 1.60 \cdot 10^{-7} m^2/s$. The activation energy for both isotopes was derived to $E_A = 0.28 \pm 0.06$ eV, which differs substantially from the activation energy provided by Frauenfelder ($E_A^{H:\,FF} = 0.39^{+0.09}_{-0.09}$ eV) [8]. At sufficiently high temperature ramping rates ≥ 15 K/s and temperature plateaus ≥ 1600 K, the single-exponential decay of the degassing flux delivered equal results for the diffusivity for single- and poly-crystalline specimen despite their different microstructure. Trapping or surface effects do not play a role and solute diffusion seems to be the governing migration mechanism at these temperatures, both in the single- and in the poly-crystalline sample.

The full diffusion model was used to evaluate measurements of the big specimen. The measurements with the big specimen were evaluated by the full diffusion model which provides a numerical solution of the diffusion equation. It solves the diffusion limited degassing of a cylindrical specimen with a coupled system of equations for the temperature field and the concentration profile in full generality. It describes degassing at constant temperature, including the cool-down phase after the loading phase when the heating is switched off. All four variables of diffusivity and solubility (E_A, D_0, E_S and S_0) are simultaneously adjusted so that the model shows the smallest deviation from the measured decay in the hydrogen desorption at constant temperature in a least squares (χ^2) fit. The fitting window was previously defined and consistent for all 16 measurements on protium and deuterium for the final evaluation. The loading and degassing temperatures were varied within the range of 1800 K $< T <$ 2400 K for both protium and deuterium. The evaluation within the diffusion model

is done simultaneously for all measurement cycles of one isotope. The data set for protium included 7 measurement cycles, the one for deuterium 9 measurement cycles. The analysis derived the activation barriers for protium and deuterium of: $E_A^H = 0.280^{+0.02}_{-0.01}$ eV and $E_A^D = 0.265^{+0.02}_{-0.01}$ eV, respectively. The activation energies for both isotopes are not distinguishable within the error bars. These values are in agreement with the values derived from the reduced diffusion model on the small specimens, but with significantly lower uncertainties.

The pre-exponential factors were derived by the full diffusion model and are summarised in table 6.1. As can be seen the ratio of $\frac{D_0^D}{D_0^H} = 1.37$, which is in reasonable agreement with harmonic theory which predicts $q_{th} = \frac{\sqrt{m_D}}{\sqrt{m_H}} = 1.41$.

In summary, the results for diffusivity derived by the full diffusion model differ substantially from the diffusivities derived by Frauenfelder ($E_A^{H:\,FF} = 0.39^{+0.09}_{-0.09}$ eV and $D_0^{H:\,FF} = 4.1^{+5}_{-2}{\cdot}10^{-7}\,m^2/s$) [8]. The derived activation energy for protium is 28% lower, the pre-exponential factor is 50% lower. Heinola's [10] ansatz, to use only Frauenfelder's measurements above 1500 K seems reasonable, because trapping or surface effects seem to have an impact in this temperature-range. Frauenfelder's data points at the higher temperatures are in excellent agreement with the measurements from this work.

The solubilities for protium and deuterium are also given in table 6.1. The solubilities of both isotopes are identical within the error bars. The derived solute energy E_S from this study is higher than the value of 1.04 eV derived by Frauenfelder. The larger value for the solute energy found in the present experiments could be explained with a different hydrogen pressure during loading. In the present study samples were loaded at 500 mbar, while they were loaded with 800 mbar in Frauenfelder's case. One could, therefore, expect a lower surface coverage with hydrogen in the present experiments. Very recent investigations indicate that the energy barrier for deuterium uptake depends on surface coverage: the lower the surface coverage, the higher the activation barrier [61]. The overall solubility resulting from this thesis is comparable with the solubility derived by Frauenfelder.

Based on the experimental result presented in this thesis the following values for solubility and diffusivity of protium and deuterium in tungsten are recommended:

Table 6.1.: Recommended values for solubility and diffusivity of hydrogen in tungsten.

Recommended values		
	Protium (H)	Deuterium (D)
Pre-exponential factor D_0 [10^{-7}m^2/s]	$2.02^{+0.14}_{-0.11}$	$1.50^{+0.09}_{-0.05}$
Activation barrier E_A [eV]	$0.280^{+0.02}_{-0.01}$	$0.265^{+0.02}_{-0.01}$
Pre-exponential factor S_0 [$10^{-5}\left(\frac{\text{atoms}}{\text{W}}\right)\text{Pa}^{-\frac{1}{2}}$]	$8.61^{+0.99}_{-0.53}$	$8.60^{+0.97}_{-0.59}$
Solute energy E_S [eV]	$1.13^{+0.04}_{-0.02}$	$1.14^{+0.04}_{-0.02}$

Advances of full diffusion model in comparison with former approaches

Applying sophisticated experimental methods for gas loading and degassing in combination with a full diffusion model code yields advances over the decay fitting method as applied by Frauenfelder [8]:

- The ability to actively control the temperature by means of a temperature controller decreases uncertainties in temperature reading. Frauenfelder most likely was only able to control the power of the inductive furnace and regulated it manually by taking the temperature reading from a pyrometer by eye [8].
- As described in chapter 3.1.2, drifts can be observed during gas loading as well as during degassing. A directly contacted thermocouple as used in the present experiment, is regarded more reliable than pyrometry. Frauenfelder's temperature measurement relied on a pyrometer only, which is directly dependent on emissivity, which can change irreproducibly depending on the surface state.
- Applying a full diffusion model which simultaneously analyses a data set of multiple measurement cycles that vary in gas loading and degassing temperature allows for:
  - Including the influence of the experimentally measured background into the model.
  - Simultaneous fitting of the four variables E_A, D_0, E_S, and S_0 to identify and isolate differences from individual measurements, concerning solubility and diffusivity.
  - Reducing experimental uncertainties for the derived results, due to simultaneous fitting of a large data set.
  - Considering explicitly outgassing in the cool-down phase at the end of gas loading, whereas Frauenfelder had to use a specimen big enough to neglect this effect [8].

Outlook

The established apparatus Radiofrequency Oven for Solubility Test ("ROST") considerably extends the experimental abilities and capabilities at the Max-Planck-Institut für Plasmaphysik and could be used for:

- Measurements in dependence of gas loading pressure to derive the diffusivity and solubility of hydrogen or other gases in arbitrary conductive materials.
- Solubility measurements of deuterium in tungsten, varying the gas loading pressure to check for a possible dependence of solubility on surface coverage.
- Recrystallisation of tungsten in dependence of solute hydrogen fraction at elevated temperatures.
- Helium degassing due to the high temperatures that can be reached (at least 2800 K).
- Isotope exchange by sequential gas loading and degassing of protium and deuterium.
- Melt extraction of native hydrogen of conducting materials.
- High temperature quenching of metals to produce vacancies.

Bibliography

[1] F. F. Chen, "Plasma Applications," in *Introduction to Plasma Physics and Controlled Fusion* (F. F. Chen, ed.), pp. 355–411, Cham: Springer International Publishing, 2016.

[2] G. Federici, W. Biel, M. R. Gilbert, R. Kemp, N. Taylor, and R. Wenninger, "European DEMO design strategy and consequences for materials," *Nuclear Fusion*, vol. 57, p. 092002, June 2017.

[3] J. Roth and K. Schmid, "Hydrogen in tungsten as plasma-facing material," *Physica Scripta*, vol. T145, p. 014031, Dec. 2011.

[4] G. Holzner, T. Schwarz-Selinger, T. Dürbeck, and U. v. Toussaint, "Solute diffusion of hydrogen isotopes in tungsten—a gas loading experiment," *Physica Scripta*, vol. T171, p. 014034, Jan. 2020. Publisher: IOP Publishing.

[5] G. M. Wright, M. Mayer, K. Ertl, G. de Saint-Aubin, and J. Rapp, "TMAP7 simulations of deuterium trapping in pre-irradiated tungsten exposed to high-flux plasma," *Journal of Nuclear Materials*, vol. 415, pp. S636–S640, Aug. 2011.

[6] K. Schmid, U. von Toussaint, and T. Schwarz-Selinger, "Transport of hydrogen in metals with occupancy dependent trap energies," *Journal of Applied Physics*, vol. 116, p. 134901, Oct. 2014.

[7] E. A. Hodille, E. Bernard, S. Markelj, J. Mougenot, C. S. Becquart, R. Bisson, and C. Grisolia, "Estimation of the tritium retention in ITER tungsten divertor target using macroscopic rate equations simulations," *Physica Scripta*, vol. T170, p. 014033, Oct. 2017.

[8] R. Frauenfelder, "Solution and Diffusion of Hydrogen in Tungsten," *Journal of Vacuum Science & Technology*, vol. 6, pp. 388–397, May 1969.

[9] A. P. Zakharov, V. M. Sharapov, and É. I. Evko, "Hydrogen permeability of polycrystalline and monocrystalline molybdenum and tungsten," *Soviet materials science : a transl. of Fiziko-khimicheskaya mekhanika materialov / Academy of Sciences of the Ukrainian SSR*, vol. 9, pp. 149–153, Mar. 1975.

[10] K. Heinola and T. Ahlgren, "Diffusion of hydrogen in bcc tungsten studied with first principle calculations," *Journal of Applied Physics*, vol. 107, no. 11, p. 113531, 2010.

[11] T. Tanabe, "Review of hydrogen retention in tungsten," *Physica Scripta*, vol. T159, p. 014044, 2014.

[12] N. Fernandez, Y. Ferro, and D. Kato, "Hydrogen diffusion and vacancies formation in tungsten: Density Functional Theory calculations and statistical models," *Acta Materialia*, vol. 94, pp. 307–318, Aug. 2015.

[13] T. Oda, D. Zhu, and Y. Watanabe, "Kinetic Monte Carlo simulation on influence of vacancy on hydrogen diffusivity in tungsten," *Journal of Nuclear Materials*, vol. 467, pp. 439–447, Dec. 2015.

[14] T. Ahlgren and L. Bukonte, "Concentration dependent hydrogen diffusion in tungsten," *Journal of Nuclear Materials*, vol. 479, pp. 195–201, 2016.

[15] E. A. Hodille, Y. Ferro, N. Fernandez, C. S. Becquart, T. Angot, J. M. Layet, R. Bisson, and C. Grisolia, "Study of hydrogen isotopes behavior in tungsten by a multi trapping macroscopic rate equation model," *Physica Scripta*, vol. 2016, no. T167, p. 014011, 2016.

[16] R. Causey and T. Venhaus, "The use of tungsten in fusion reactors: A review of the hydrogen retention and migration properties," *Physica Scripta T*, vol. 94, pp. 9–15, 2001.

[17] K. Heinola, T. Ahlgren, K. Nordlund, and J. Keinonen, "Hydrogen interaction with point defects in tungsten," *Physical Review B*, vol. 82, Sept. 2010.

[18] Y. Fukai, "The Metal-Hydrogen System: Basic Bulk Properties," 2005. OCLC: 758337369.

[19] M. L. E. Oliphant, P. Harteck, and E. Rutherford, "Transmutation effects observed with heavy hydrogen," *Proceedings of the Royal Society of London. Series A, Containing Papers of a Mathematical and Physical Character*, vol. 144, pp. 692–703, May 1934.

[20] L. L. Lucas and M. P. Unterweger, "Comprehensive Review and Critical Evaluation of the Half-Life of Tritium," *Journal of Research of the National Institute of Standards and Technology*, vol. 105, no. 4, pp. 541–549, 2000.

[21] D. Lal and B. Peters, "Cosmic Ray Produced Radioactivity on the Earth," in *Kosmische Strahlung II / Cosmic Rays II* (K. Sitte, ed.), Handbuch der Physik / Encyclopedia of Physics, pp. 551–612, Berlin, Heidelberg: Springer, 1967.

[22] A. Sieverts, "The absorption of gases by metals," *Zeitschrift für Metallkunde*, vol. 21, pp. 37 – 46, 1929.

[23] Y. Fukai, *The Metal-Hydrogen System: Basic Bulk Properties*. Springer Science & Business Media, Feb. 2006. Google-Books-ID: CshrIxMIQaoC.

[24] S. T. Picraux and F. L. Vook, "Deuterium Lattice Location in Cr and W," *Physical Review Letters*, vol. 33, pp. 1216–1220, Nov. 1974. Publisher: American Physical Society.

[25] A. Fick, "Ueber Diffusion," *Annalen der Physik*, vol. 170, no. 1, pp. 59–86, 1855.

[26] R. J. Borg and G. J. Dienes, *An Introduction to Solid State Diffusion*. London: Academic Press, Inc., 1988.

[27] T. Heumann, *Diffusion in Metallen*, vol. 10 of *Werkstoff-Forschung und -Technik*. Berlin: Springer-Verlag, 1992.

[28] J. K. Fink, *Physical chemistry in depth*. Heidelberg [Germany] ; New York: Springer, 2009. OCLC: ocn401158494.

[29] M. Zibrov, *The Influence of Radiation, Mechanical, and Plasma-Induced Damage on Deuterium Retention in Tungsten*. PhD thesis, 2018.

[30] R. M. Barrer, *Diffusion in and Through Solids*. CUP Archive, 1941. Google-Books-ID: 7SQ9AAAAIAAJ.

[31] R. A. Causey, "Hydrogen isotope retention and recycling in fusion reactor plasma-facing components," *Journal of Nuclear Materials*, vol. 300, pp. 91–117, Feb. 2002.

[32] R. D. Allen, L. F. Glasier, and P. L. Jordan, "Spectral Emissivity, Total Emissivity, and Thermal Conductivity of Molybdenum, Tantalum, and Tungsten above 2300°K," *Journal of Applied Physics*, vol. 31, pp. 1382–1387, Aug. 1960.

[33] J. G. Hust and A. B. Lankford, "Thermal conductivity of aluminum, copper, iron, and tungsten for temperatures from 1 K to the melting point," Tech. Rep. PB-84-235878; NBSIR-84/3007, National Bureau of Standards, Boulder, CO (USA). Chemical Engineering Science Div., June 1984.

[34] H. Carslaw and J. Jaeger, *Conduction of Heat in Solids*. Oxford: Oxford University Press, 2nd revised edition ed., 2011.

[35] E. Salançon, T. Dürbeck, T. Schwarz-Selinger, F. Genoese, and W. Jacob, "Redeposition of amorphous hydrogenated carbon films during thermal decomposition," *Journal of Nuclear Materials*, vol. 376, pp. 160–168, May 2008.

[36] U. Lindemann, *Methodische Entwicklung technischer Produkte: Methoden flexibel und situationsgerecht anwenden*. VDI-Buch, Berlin Heidelberg: Springer-Verlag, 3 ed., 2009.

[37] E. J. Davies, *Conduction and Induction Heating*. IET Power Engineering Series 11, London, United Kingdom: The Institution of Engineering and Technology, 2nd ed., 2007.

[38] P. D. Desai, T. K. Chu, H. M. James, and C. Y. Ho, "Electrical Resistivity of Selected Elements," *Journal of Physical and Chemical Reference Data*, vol. 13, pp. 1069–1096, Oct. 1984. Publisher: American Institute of Physics.

[39] E. Lassner and W.-D. Schubert, "Tungsten and Tungsten Alloy Products," in *Tungsten: Properties, Chemistry, Technology of the Element, Alloys, and Chemical Compounds* (E. Lassner and W.-D. Schubert, eds.), pp. 283–305, Boston, MA: Springer US, 1999.

[40] T. J. Seebeck, "Ueber die magnetische Polarisation der Metalle und Erze durch Temperaturdifferenz," *Annalen der Physik*, vol. 82, pp. 253–286, Jan. 1826.

[41] J. Fraden, *Handbook of Modern Sensors: Physics, Designs, and Applications*. Springer Science & Business Media, 2004. Google-Books-ID: XymGRsRlvRQC.

[42] J. Martin, "Protocols for the high temperature measurement of the Seebeck coefficient in thermoelectric materials," *Measurement Science and Technology*, vol. 24, no. 8, p. 085601, 2013.

[43] K. Irrgang, *Temperaturmesspraxis mit Widerstandsthermometern und Thermoelementen*. Essen: Vulkan-Verlag GmbH, 2004.

[44] J. F. Swindells, *Precision Measurement and Calibration: Selected NBS Papers on Temperature*. U.S. Department of Commerce, National Bureau of Standards, 1968. Google-Books-ID: m7nSVol84xIC.

[45] J. C. De Vos, "A new determination of the emissivity of tungsten ribbon," *Physica*, vol. 20, pp. 690–714, Jan. 1954.

[46] M. R. Querry, P. G. Cary, and R. C. Waring, "Split-pulse laser method for measuring attenuation coefficients of transparent liquids: application to deionized filtered water in the visible region," *Applied Optics*, vol. 17, pp. 3587–3592, Nov. 1978.

[47] O. A. Sergeev, A. G. Shashkov, and A. S. Umanskii, "Thermophysical properties of quartz glass," *Journal of engineering physics*, vol. 43, pp. 1375–1383, Dec. 1982.

[48] C. B. Alcock, V. P. Itkin, and M. K. Horrigan, "Vapour Pressure Equations for the Metallic Elements: 298–2500K," *Canadian Metallurgical Quarterly*, vol. 23, pp. 309–313, July 1984. Publisher: Taylor & Francis _eprint: https://doi.org/10.1179/cmq.1984.23.3.309.

[49] J. W. Davis, V. R. Barabash, A. Makhankov, L. Plöchl, and K. T. Slattery, "Assessment of tungsten for use in the ITER plasma facing components1#AC-3013 with Sandia National Laboratories.1," *Journal of Nuclear Materials*, vol. 258-263, pp. 308–312, Oct. 1998.

[50] F. F. Schmidt and H. R. Ogden, "THE ENGINEERING PROPERTIES OF TUNGSTEN AND TUNGSTEN ALLOYS," vol. 191 of *DMIC Report*, Columbus 1, Ohio: Defense Metals Information Center, Sept. 1963.

[51] V. Schröder, "Explosionsgrenzen von Wasserstoff und Wasserstoff/Methan-Gemischen," *Bundesamt für Materialforschung und -prüfung*, vol. Forschungsbericht 253, 2003.

[52] P. W. Tamm and L. D. Schmidt, "Binding States of Hydrogen on Tungsten," *The Journal of Chemical Physics*, vol. 54, pp. 4775–4787, June 1971.

[53] K. F. Pearson, "X. On the criterion that a given system of deviations from the probable in the case of a correlated system of variables is such that it can be reasonably supposed to have arisen from random sampling," *The London, Edinburgh, and Dublin Philosophical Magazine and Journal of Science*, vol. 50, pp. 157–175, July 1900.

[54] R. A. Fisher, "On the Interpretation of χ^2 from Contingency Tables, and the Calculation of P," *Journal of the Royal Statistical Society*, vol. 85, no. 1, pp. 87–94, Jan. 1922.

[55] W. G. Cochran, "The χ^2 Test of Goodness of Fit," *The Annals of Mathematical Statistics*, vol. 23, pp. 315–345, Sept. 1952.

[56] W. v. d. Linden, V. Dose, and U. v. Toussaint, *Bayesian Probability Theory: Applications in the Physical Sciences*. Cambridge, United Kingdom: Cambridge University Press, June 2014.

[57] T. Oda, "Thermodynamic model for grain boundary effects on hydrogen solubility, diffusivity and permeability in poly-crystalline tungsten," *Fusion Engineering and Design*, vol. 112, pp. 102–116, Nov. 2016.

[58] W. H. Press, S. A. Teukolsky, W. T. Vetterling, and B. P. Flannery, *Numerical Recipes 3rd Edition: The Art of Scientific Computing*. Cambridge University Press, Sept. 2007. Google-Books-ID: 1aAOdzK3FegC.

[59] D. Sivia and J. Skilling, *Data Analysis: A Bayesian Tutorial*. OUP Oxford, June 2006. Google-Books-ID: Kxx8CwAAQBAJ.

[60] U. von Toussaint, "Bayesian inference in physics," *Reviews of Modern Physics*, vol. 83, pp. 943–999, Sept. 2011.

[61] E. A. Hodille, S. Markelj, M. Pecovnik, M. Ajmalghan, Z. A. Piazza, Y. Ferro, T. Schwarz-Selinger, and C. Grisolia, "A kinetic model for hydrogen absorption in tungsten with coverage dependent surface mechanisms," *to be published*.

[62] K.-C. Thienel, "Werkstoffe des Bauwesens - Glas," tech. rep., Institut für Werkstoffe des Bauwesens, Fakultät für Bauingenieur- und Vermessungswesen, Universität der Bundeswehr München, 2008.

A. Appendix

A.1. Glass tube: stress calculations

In the following, the design concerning mechanical properties of the small glass tube for the two small specimens is outlined, at the end an estimation also for the big glass tube is provided.

The quartz glass tube consists of four glass-parts: the two flange-to-steel-to-glass connectors at the upper (CF16) and lower (CF40) end and two SiO_2 glass tubes in the middle part that form the double-walled tube for water cooling. Table A.1 shows the values of the wall thicknesses and middle diameters (because those values are used for the pressure vessel equation).

Table A.1.: Wall thickness and middle diameter of the four parts of the glass vessel, values in [mm].

	SiO_2 double-walled vessel		glass-steel flange	
	inner tube	outer tube	CF16	CF40
s	1.8	2.5	1.1	1.4
d_m	30.2	45.5	18.2	35.0

with s : wall thickness [mm]
d_m : middle diameter [mm]

The inner glass tube has a middle diameter of $d_m = 30.2\,\text{mm}$ and thickness of $s_i = 1.8\,\text{mm}$. Two pressure regimes are to be considered: 500 mbar pressure while gas loading, from now on referred to as "gas loading case" and vacuum while measuring, from now on referred to as "vacuum case".

Glass can easily handle compressive stress. The ultimate stress-level for compression is rather high while tensile stress is more critical [62]. In the underlying case this means that vacuum conditions in the glass vessel and thus negative relative pressures (in comparison with atmospheric pressure) are less critical than positive relative pressures while gas loading. To calculate the relevant stress in the glass vessel, the "pressure vessel equation", see equation A.1, can be used to calculate the mechanical stress in an internally pressure loaded rotational symmetric body with constant radius and thin walls ($d > 10 \cdot s$). Tangential tension is the relevant stress, indicated as lower index "t".

$$\sigma_t = \frac{p \cdot d_m}{2 \cdot s} \tag{A.1}$$

with σ_t : tangential stress [N/mm^2]
p : internal pressure [N/mm^2]
d_m : middle diameter [mm]
s : wall thickness [mm]

The outer tube's stresses are dependent on the value of the atmospheric pressure and water pressure of the cooling channel. They are independent of the filling pressure in the vessel. The stresses of the flange-to-steel-to-glass connectors are dependent on the pressure in the glass tube and atmospheric pressure because they are single walled.

In the following the stresses and safety margins for the quartz glass tube are calculated. At first, the middle part with inner and outer tube are discussed, followed by the two flange-to-glass-to-steel connectors.

Inner and outer tube

The different thicknesses of the various glasses are listed in table A.1. The wall thickness at the inner tube is $s^i = 1.8\,mm$ and the middle diameter is $d_m^i = 30.2\,mm$. The outer tube has $s^i = 2.5\,mm$ and a middle diameter of $d_m^i = 45.5\,mm$.

Vacuum case:

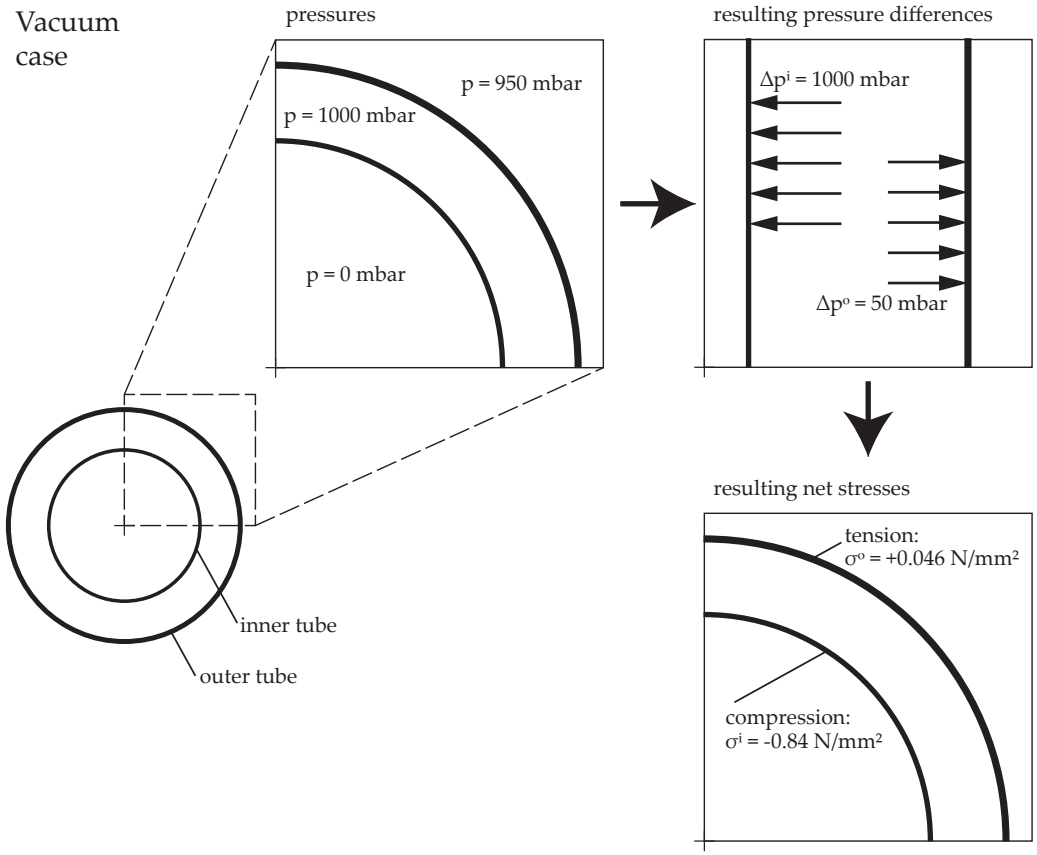

Figure A.1.: The pressure conditions in the glass tube while vacuum is applied. The inner tube experiences a pressure of 0 mbar, while the section between inner and outer tube experiences 1000 mbar water pressure. Outside the glass tube is atmospheric pressure of at least 950 mbar absolute pressure.

Figure A.1 schematically displays a cut through the glass tube and the pressure conditions. Within the inner tube vacuum is applied, the pressure there is 0 mbar. Between inner and outer tube the water flow is applied to cool the vessel. The water pressure is kept around 1000 mbar. Outside the outer tube is atmospheric pressure which is at least 950 mbar absolute pressure.

Starting with the inner tube, the net pressure is:

$$\Delta p^{i}_{vacuum} = +1000\,mbar \tag{A.2}$$

Formula A.1 applied for this value for the inner glass this leads to a stress of:

$$\sigma^{i}_{t,vacuum} = -0.84\,N/mm^2 \tag{A.3}$$

This means that the inner tube is under compressive stress which is, firstly, uncritical for glass and, secondly, far below the stated ultimate compressive strength of quartz glass of $-500\,N/mm^2$ to $-700\,N/mm^2$, according to Thienel [62].

The outer tube is exposed to a maximum pressure difference of around $|\pm 50|\,mbar$, if an absolute atmospheric pressure of $950\,mbar$ is assumed.

$$\Delta p^{o}_{vacuum} = -50\,mbar \tag{A.4}$$

$$\sigma^{o}_{t,vacuum} = +0.046\,N/mm^2 \tag{A.5}$$

This means that the outer tube is under tensile stress.

The values for ultimate tensile strength of glass vary and can generally scatter over a wide range. [62] states that quartz glass reaches ultimate tensile strength values of about $\sigma^{u}_{t} = +30\,N/mm^2$ to $+80\,N/mm^2$. This is due to the brittle nature of glass.

$$\sigma^{tensile\,max}_{t,constant} = +7\,N/mm^2 \tag{A.6}$$

is acceptable [62]. This is rather low, but the actual tensile stress in the inner glas of $\sigma^{i}_{t,gas\ \ loading} = +0.046\,N/mm^2$ The vacuum case for the inner and outer tube can be assumed as uncritical to failure.

Gas loading case:

The calculation of the resulting stresses follows the same method as the vacuum case. Gas loading pressure is 500 mbar, which cuts the resulting pressure difference for the inner glass to half in comparison with the vacuum case. This leads to compressive stress of:

$$\sigma^{i}_{t,gas\ \ loading} = -0.42\,N/mm^2 \tag{A.7}$$

The inner glass is also under compression stress during gas loading which is in general by the favourable stress state for glass. The value for the stress is again well below the ultimate compression stress for glass and, therefore, uncritical.

Flange-to-glass-to-steel connectors

The two flange-to-glass-to-steel connectors of the glass vessel are both only dependent on the inner pressure of the glass vessel and absolute atmospheric pressure.

Vacuum

The wall thickness and the middle diameter is stated in table A.1. Formula A.1 applied leads to the following stresses in the lower "CF40" and the upper "CF16" glass-steel flange:

$$\sigma_{t,vacuum}^{CF40} = -1.19\,N/mm^2 \tag{A.8}$$

$$\sigma_{t,vacuum}^{CF16} = -0.79\,N/mm^2 \tag{A.9}$$

While the vessel is under vacuum, the flange-to-glass-to-steel connectors are under tangential compressive stress which is the generally more preferable stress state.

Conditioning

$$\sigma_{t,gas\ loading}^{CF40} = -0.72\,N/mm^2 \tag{A.10}$$

$$\sigma_{t,gas\ loading}^{CF16} = -0.29\,N/mm^2 \tag{A.11}$$

This is also means uncritical compressive stress at the flange-to-glass-to-steel connectors for vacuum and the gas loading case.

Resulting stresses

Table A.2 summaries the results for the applied pressure and stress states for all four parts of the glass vessel.

Table A.2.: Net pressures and tangential stresses in the four parts of the glass vessel. The "Inner tube" is the inner quartz glass tube that form the central part of the glass vessel, between "inner tube" and "outer tube" the water flow supplies the cooling. "CF40" and "CF16" adress the two flange-to-glass-to-steel connectors at the lower (CF40) and upper (CF16) part of the vessel.

	vacuum		gas loading	
	Δp_{vacuum} [mbar]	$\sigma_{t,vacuum}$ [N/mm^2]	$\Delta p_{gas\ loading}$ [mbar]	$\sigma_{t,gas\ loading}$ [N/mm^2]
inner tube	-1000	-0.84	-500	-0.42
outer tube	+50	+0.046	+450	+0.046
CF40	-950	-1.19	-450	-0.72
CF16	-950	-0.79	-450	-0.29

with

Δp_{vacuum}	:	pressure difference at vacuum	[mbar]
$\Delta p_{gas\ loading}$	:	pressure difference at gas loading at 500 mbar	[mbar]
$\sigma_{t,\ vacuum}$	:	tangential stress at vacuum	[N/mm^2]
$\sigma_{t,\ gas\ loading}$	:	tangential stress at gas loading	[N/mm^2]

Negative values for σ_t (compressive stress) in table A.2 are generally to prefer over positive values, i.e., tensile stresses [62]. The outer tube's stress levels are independent from filling pressure as long as the filling pressure is lower than the applied cooling water pressure (which is the case here), hence do not need to be considered. The weakest part of the glass vessel is the CF40 glass-steel flange because here the highest tangential tension stresses, i.e., positive values for $\sigma_{t,gas\ loading}$ appear. Maximum pressures are restricted by this part of the glass vessel.

The quartz glasses from the double-walled core of the vessel can handle slight overpressure. If for example the water pressure is slightly above atmospheric pressure this is not desirable, but tolerable (see also table A.2) because those quartz glass tubes are relatively thick (>2 mm). The flange-to-glass-to-steel connectors are more delicate parts - the glass part consists of around five different glass rings that are welded to each other to spread the stresses that originates from the different thermal expansion coefficients of quartz glass (SiO_2: $0.54{\cdot}10^{-6}\,K^{-1}$) and steel ($11.5{\cdot}10^{-6}\,K^{-1}$). This means that there are already internal stresses in the glass-steel adapter. Also the wall thickness is rather small for both sizes (1.1 mm for the CF16- and 1.4 mm for the CF40-flange, also see table A.1). Hence, it is best that the flange-to-glass-to-steel connectors are kept at pressures below atmosphere to lower the probability for a catastrophic failure.+ For the unlikely case of a total failure of the glass tube vessel an encasing with stress relief area is installed that would keep damage from the environment.

Big glass tube

For the containment of the bigger specimen a new glass tube needed to be manufactured so that also at the upper end a CF40 glass-steel flange could be installed. The bigger glass container has an outer diameter of 70 mm instead of 48 mm. Hence, tangential stress $\propto$ diameter, this results in 30% higher values, hence still not critical.

A.2. Technical drawings

The technical drawings cover all parts, that are necessary to mount the specimen. It includes the dimensions of the dove-tail groove in the specimen and of the mounting shaft, the shaft is held in a mounting ring that sits at the upper end of the glass tube in a flange on the glass-to-steel-to-flange connector.

- Figure A.2: the dove-tail groove in the specimen
- Figure A.3: the mounting shaft
- Figure A.4: the mounting ring (stainless steel) which is placed on top of the glass tube
- Figure A.5: glass tube, version with CF16 steel-to-flange-to-glass connector on top
- Figure A.6: glass tube, version with CF40 steel-to-flange-to-glass connector on top

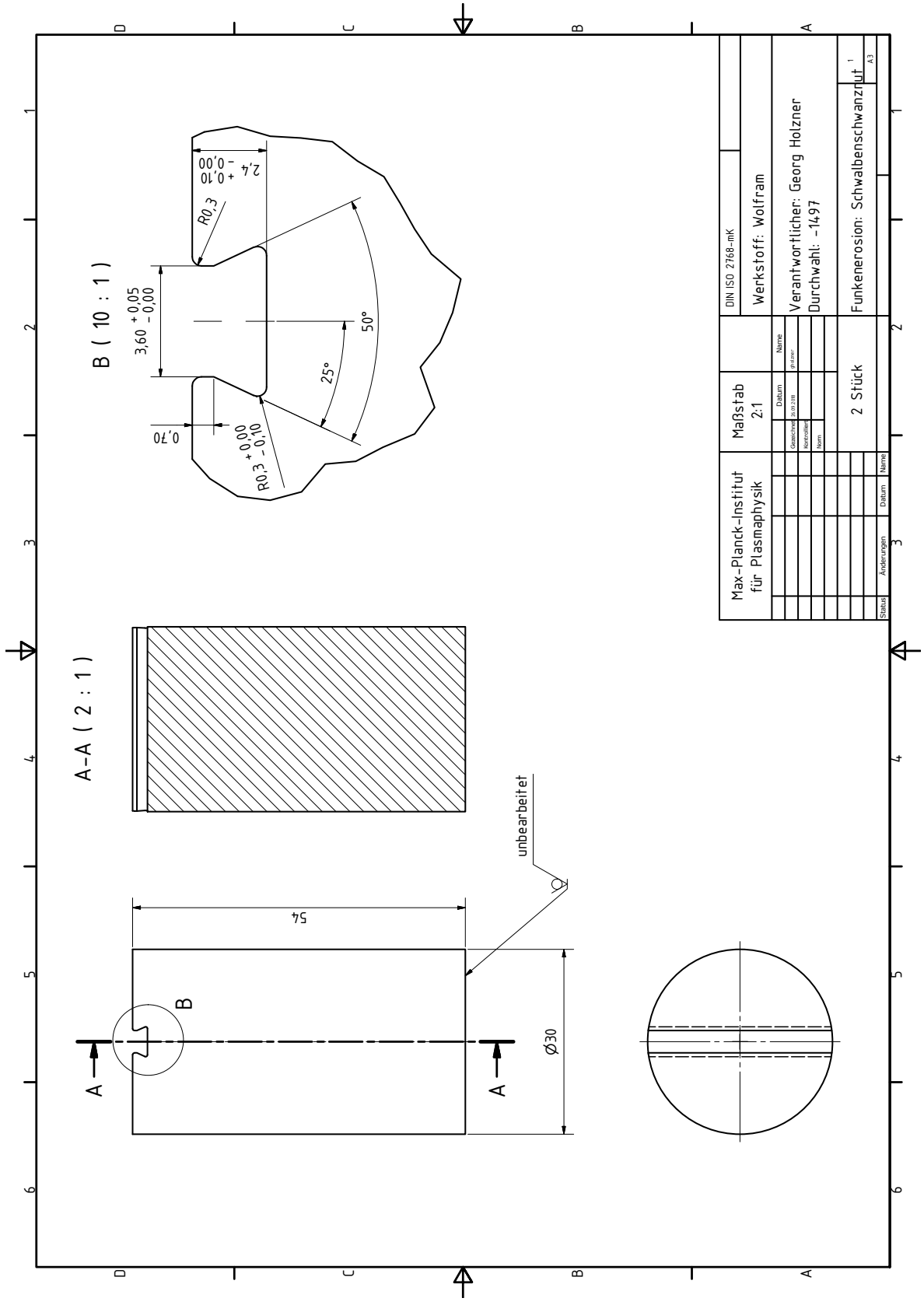

Figure A.2.: Dove-tail groove in specimen.

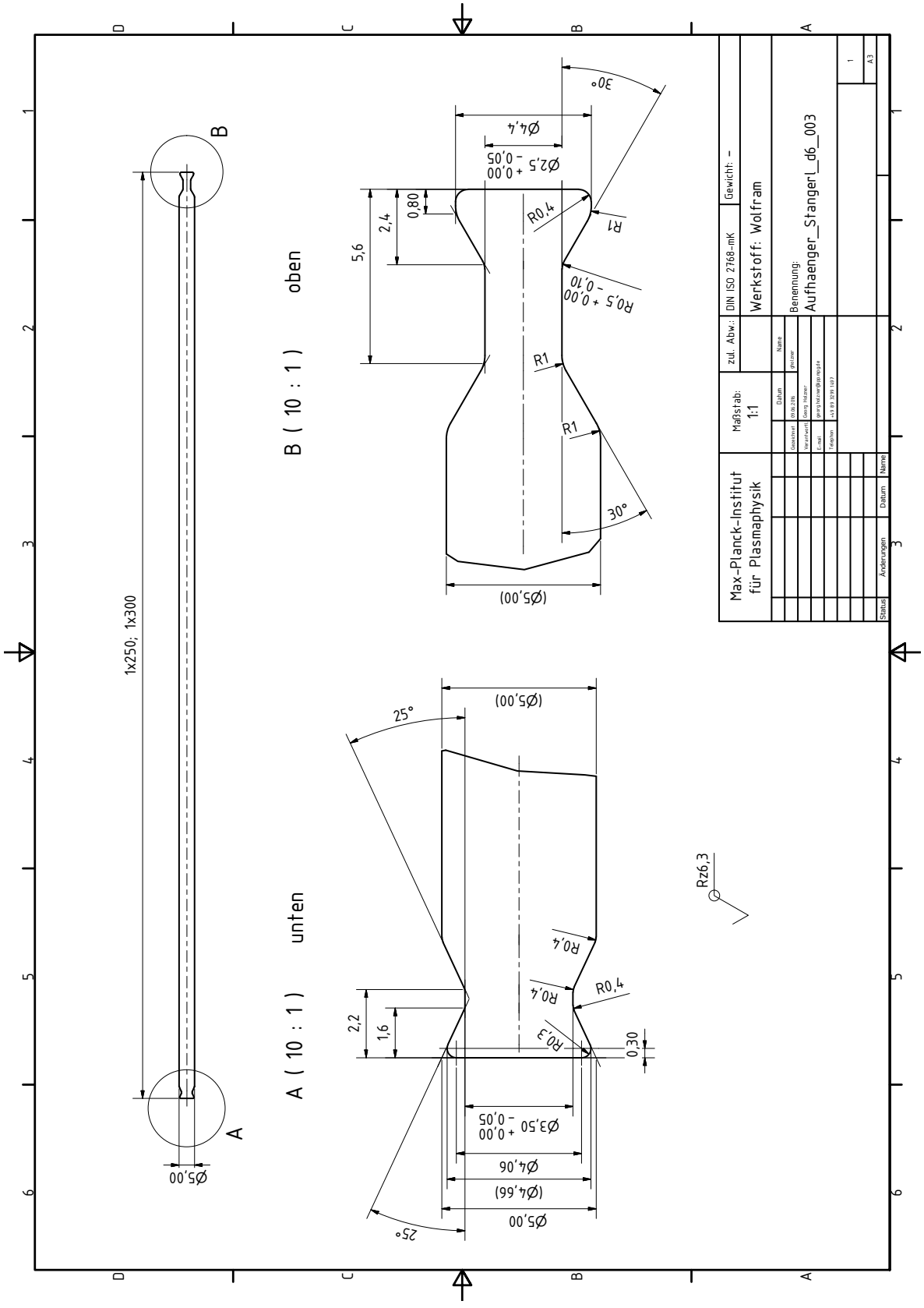

Figure A.3.: Mounting shaft for specimen with dove-tail connection.

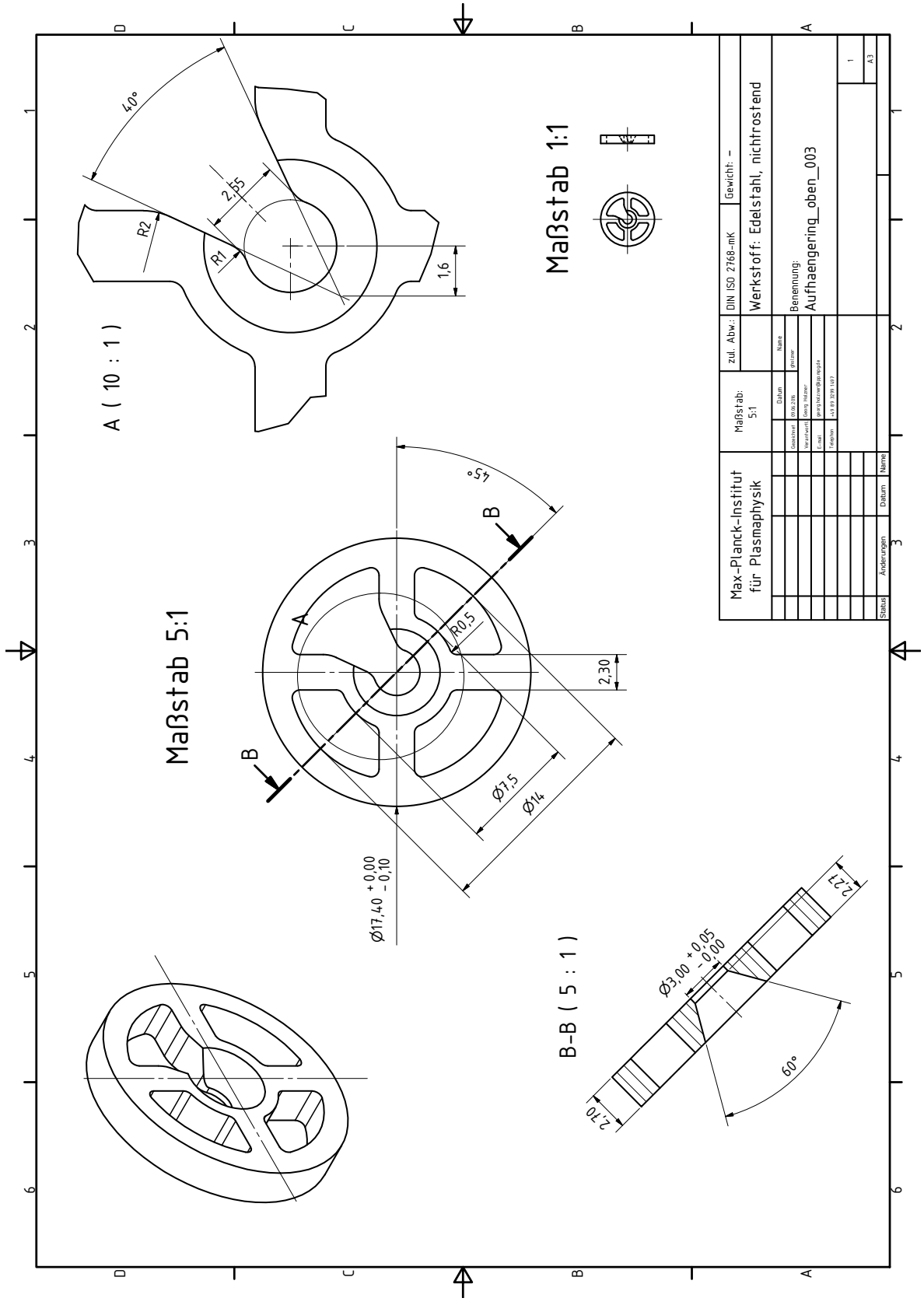

Figure A.4.: Mounting ring on top of glass tube for mounting shaft.

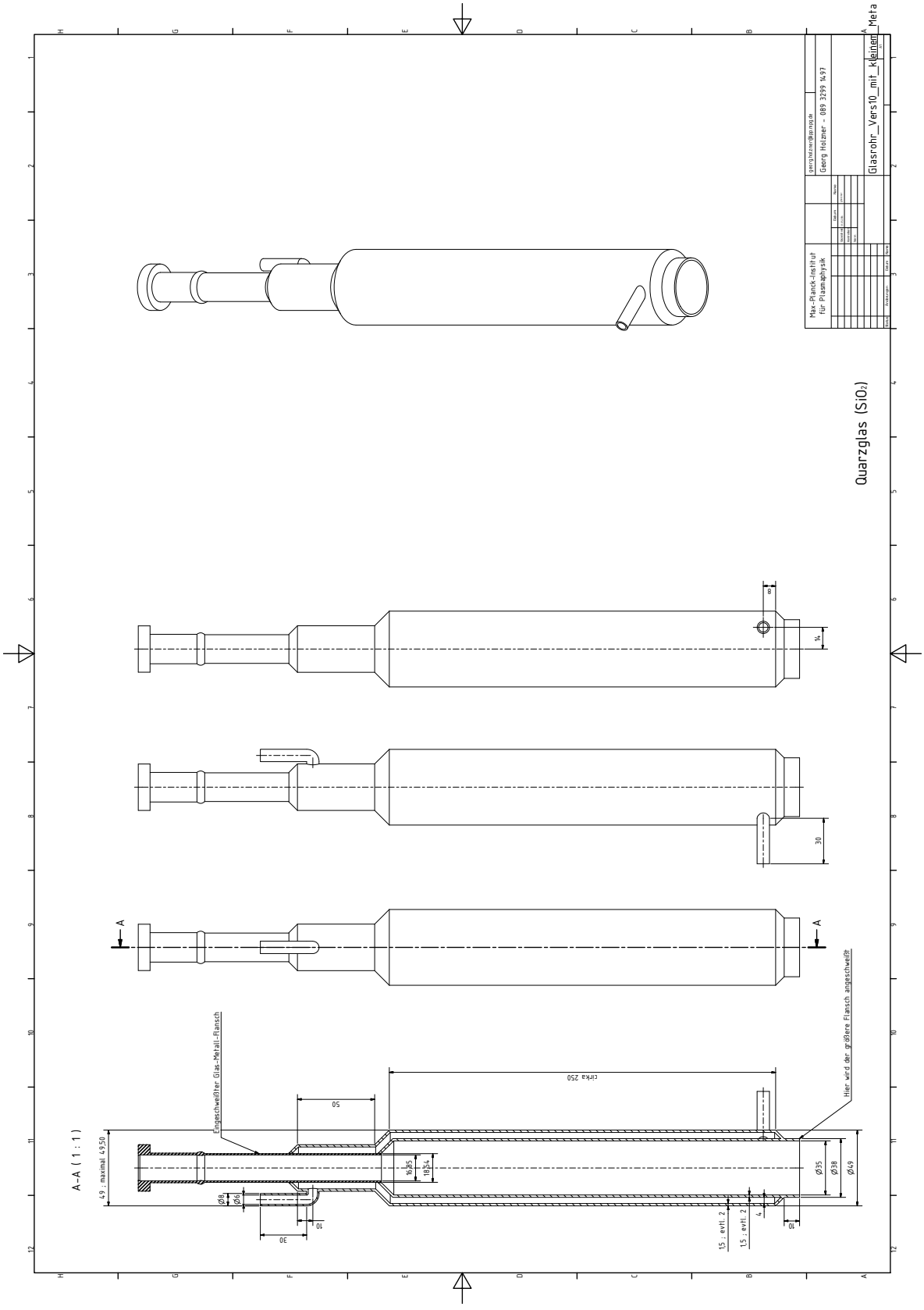

Figure A.5.: Glass tube, version with CF16 steel-to-flange-to-glass connector on top.

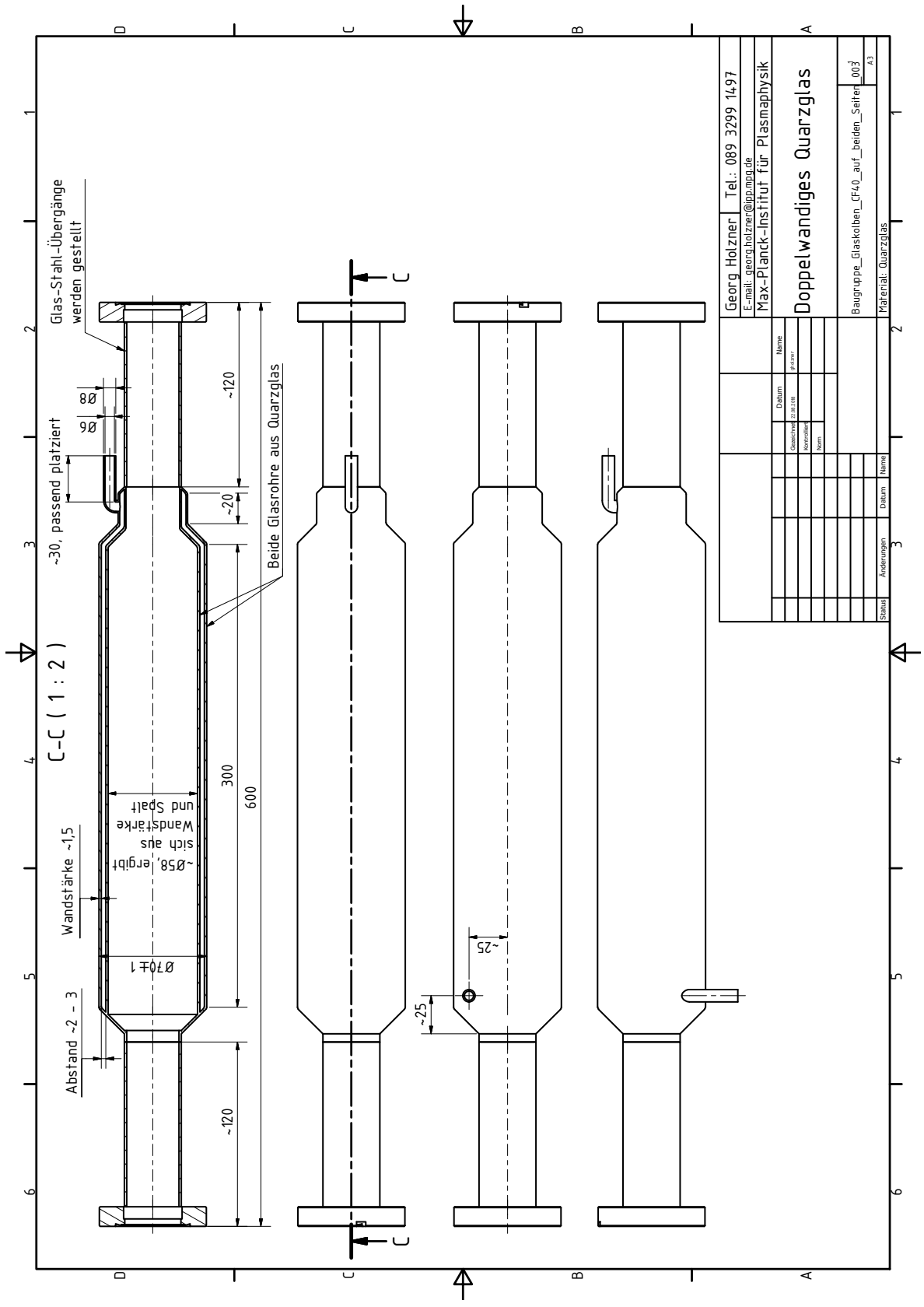

Figure A.6.: Glass tube, version with CF40 steel-to-flange-to-glass connector on top.

A.3. Operation of gas loading apparatus "ROST"

In the following a manual to operate the gas- and vacuum piping at ROST is outlined - it is specifically meant to be used by operators who are not yet familiar with the device.

A.3.1. Vacuum and gas feed system

This subsection describes the manual operation of the apparatus ROST for loading and degassing. Figure A.7 schematically shows the gas piping diagram, including valves and pressure gauges. The procedures for different operations (e.g., first gas bottle connection, gas loading of a specimen and so on) will be explained underneath by stating references to the different actuators in figure A.7.

A.3.1.1. Changing gas bottle

This is the procedure for exchanging one of the two gas bottles which are placed beside the apparatus ROST for gas loading of a specimen.

There are two plugs for (hydrogen-)gas supply. To install a new gas bottle, first the one gas bottle that shall be deconnected, for ease let assume that this is the deuterium bottle at the left pressure regulator unit (marked with "A"), must be closed (if is not so before) at its main valve that is directly on top of the gas bottle - this valve is not part of the gas piping diagram. The valve VA1 is closed. Then the scroll pump needs to be activated, which is done by turning the switch on the ground from "Rootspump-automatic" ("0") to "Rootspump permanent on" ("I"). Then the valve VA3 ("Scroll N_2") is opened to establish ballast gas flow for the scroll pump. The 2/3 directional valves are usually closed and secured by a locking mechanism that can be opened with a key. Before opening the locking mechanism the valve VKFeck2 ("Vorpumpe vor Ausgleichsgefäß"Moun) needs to be closed. [1] The key is used to open the locking mechanism. Then, by opening the 2/3 directional control valve "A" ("CH1" - which stands for "channel 1") the gas feed line to the deuterium bottle at port "A" is pumped. Open valve VA1, the closing valve at the pressure regulator unit to pump also the spiral gas feed line that connects the pressure regulator unit with the gas bottle - please be sure that the main valve directly at the gas bottle is closed! Otherwise the gas bottle is directly pumped by the scroll pump, this should be avoided. The capacitance manometer unit will display the pressure of the Pirani gauge ("3 SCRL") that is placed directly at the scroll pump: a pressure of around $5{\cdot}10^{-2}$ mbar is good enough to go on with the deconnection procedure. Close valve VA1 at the pressure regulator unit. The cap nut of the gas bottle can be opened and the securing chain of the gas bottle being released - the bottle can be exchanged.

The new gas bottle is being placed in the empty unit, then secured with the chain. The cap nut of the spiral pipe connection can be screwed to the bottle, the polymer-ring seal of the gas bottle should be clean and unharmed. After tightening the cap nut and establishing the connection to the gas bottle the main valve of the gas valve can be opened (valve VA1 at pressure regulator unit "A" still closed), the pressure measurement unit at the pressure

[1] This is also where the key is stored: to make sure someone closes this valve for opening the 2/3 directional control valve. There is only one scroll pump at the whole apparatus, so this scroll pump is both used for establishing the pre-vacuum before the turbo pump and as well to pump the gas feed system. When the 2/3 directional control valve is opened with the valve "Vorpumpe vor Ausgleichsgefäß" open the gas from the piping system enters directly the pre-vacuum part of ROST and will vent the turbo pump from behind which can possibly leads to its destruction.

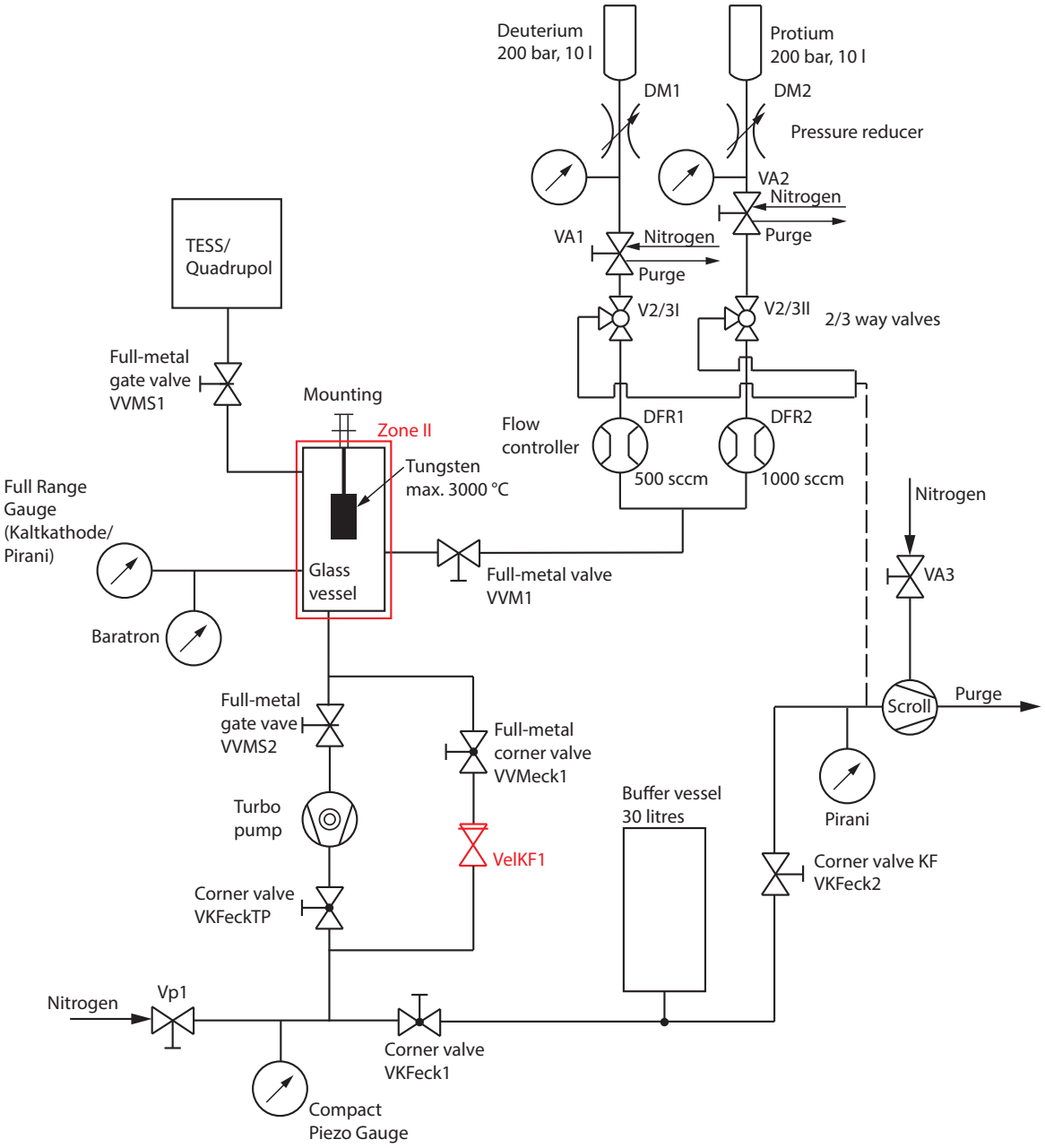

Figure A.7.: Schematic view of the ROST vacuum and gas feed system by March 2020.

regulator unit will show the bottle pressure. Before opening valve VA1 at the pressure regulator unit the pressure reducer should be closed (by turning the wheel counter-clockwise) if the former pressure level is unknown. Open valve VA1 at the pressure regulator unit and then open the pressure reducer (by turning the wheel clockwise) until a pressure of around 0.8 bar (absolute pressure) is reached. There is also a digital pressure measurement unit installed above the locking mechanism - the left one is for the gas feed channel "A" and the right one for gas feed channel "B". This unit shall show roughly -0.2 bar because it measures relative pressure (with absolute air pressure in Garching assumed to be around 0.95 bar). This pressure level is chosen such that the gas flow controller sees overpressure in comparison to the central vessel in ROST (vacuum) but lower pressure than ambient pressure. This is to avoid gas filling of the glass vessel to pressures higher than ambient pressure which would result in potentially harmful tensile stress to the glass tube, especially the glass-steel connectors.

A.3.1.2. Procedure for glass or specimen exchange

As the apparatus is in stand-by mode the central vacuum vessel is pumped - the vacuum normally is better than $5{\cdot}10^{-9}$ mbar (which is the end of the lower pressure measurement range of the full range gauge) after one day. What follows is the procedure to exchange the specimen or demount the glass vessel for cleaning, followed by re-mounting and sub-sequential pumping of the central vacuum vessel to put the apparatus into service again. The procedure would be the same if other parts of the central vacuum vessel are to be exchanged, a measurement gauge for example.

The status quo before flooding the vessel in preparation to demount the glass tube is as follows: The full-metal valve of the gas feed system VVM1 ("gas feed") is closed, the full-metal gate valve to TESS VVMS1 ("TESS") is also closed. The full-metal valve of the Bypass VVMeck1 ("Bypass") is closed. The central vacuum vessel is only connected to the internal pumping stage via the full-metal gate valve VVMS2 ("Turbo"), the valve behind the turbo pump VKFeckTP ("Ausgang Turbo") is also open. Also all other valves on the piping system to the scroll pump are open: VKFeck1 ("Vorpumpe"), VKFeck2 ("Vorpumpe vor Ausgleichsgefäß"), the nitrogen feed via the valve VA3 ("Scroll N_2) to the scroll in regular vacuum mode is shut, so are the connections to the gas feed system via the 2/3 directional control valves. The scroll pump usually is in sequential pumping mode, the switch on the ground is in "Rootspump - automatic" ("0") mode. It is activated by the capacitance manometer that measures the power from the turbo pump; if the amperage required from the turbo pump [2] reach a maximum value of 0.24 A the scroll pump is activated until the required amperage for the turbo pump reach 0.12 A [3].

In order to vent the central vacuum vessel, close the full-metal gate valve VVMS2 ("Turbopumpe") in front of the turbo pump, also close the valve behind the turbo pump VKFeckTP ("Ausgang Turbo"); the turbo pump is now running "in its own juice" with no pumping from behind, but the valves are so tight that the turbo can run in this mode for days. Also close the valve VKFeck1 ("Vorpumpe") in order to vent only the central vacuum vessel and not the whole system including the buffer vessel and the scroll pump. Now that the turbo is safe and

[2] Which is an indirect but very accurate reading of the power.

[3] The higher the pressure in the pre-vacuum system at the end of the turbo pump, the more power is required to run the turbo pump. The scroll pump could be running continuously but as the scroll pump is a dry, oil free pump its service time is quite restricted - it is best to run it iteratively as the apparatus is in stand-by mode to keep the on operation time of the scroll pump low.

the rest of the pre-vacuum system is shut, the full-metal valve VVMeck1 ("Bypass Turbo") can be opened (the electrical valve VelKF1 is always open) - now the turbo pump is bypassed. Open the first valve in the nitrogen feed system to the central vacuum vessel VA4 ("Absperr Ausgleichsgefäß N_2") at the red nitrogen feed line. When now the next valve at the nitrogen feed line is opened the central vacuum vessel will be flooded with nitrogen - if the valve is permanent open the central vacuum vessel will reach ambient pressure within 3 - 4 seconds. Please be careful while doing this, overpressure in the glass tube shall be avoided. Open the valve Vp1 ("Ausgleichsgefäß N_2") for about 1 or 2 seconds, so a feeling for the filling velocity can be developed. Now open this valve for shorter nitrogen bursts while having the pressure reading "2 FULL" at the capacitance manometer in sight, so you come near to the desired filling pressure of about 930 mbar, which is close to ambient pressure but still underneath(!). The analogue pressure gauge directly at the valve helps while filling the central vacuum vessel until about 700 mbar or so[4], then the pressure should be adjusted by looking at the pressure reading at the capacitance manometer. When having reached 930 mbar in the vessel, close valves Vp1 ("Ausgleichsgefäß N_2") and VA4 ("Absperr Ausgleichsgefäß N_2"). The valve VKFeck1 ("Vorpumpe") can be opened so that the volume before the central vacuum vessel is pumped again by the scroll pump. Shut the water cooling of the glass tube by closing the water valve with the switch at the water cooling control tableau. Best if also both hand operated water valves are also closed at the water cooling connection station at the basin. Also the copper wristband cooling unit is closed by the two valves which are above head. Now, for example, the exchange for the specimens can be undertaken by firstly deconnecting the red plug for the temperature measurement line and following opening of all 6 screws from the CF-flange at the upper end of the glass vessel. When the screws are demounted the specimen can be carefully withdrawn straight upwards by pulling the whole unit out, hands on the upper flange. Then the cooling wristband can be dismantled by loosing the 6 screws. The whole glass tube can now be loosened by opening the 6 screws at the lower end of the glass tube. Deconnect the water cooling pipes from the glass tube at the connectors. The induction coil is now be pulled into the upper position, carefully pulling the water cooling pipes through the induction coil as well. The glass tube can be withdrawn now from the apparatus and cleaned.

To re-assemble the apparatus the glass tube needs to be set onto the CF-flange, firstly pulling the water cooling pipe through the coil. The glass tube is rotated such that the lower water cooling pipe is facing towards the connector. The induction coil is to be lowered before the glass tube is tightened to the lower CF-flange to leave enough room that the water cooling pipe can fit through the induction coil. Tighten the lower 6 screws at the CF-flange - the CF-flange needs to be tightened as such that the glass tube is straight in line with the induction coil. Connect the water cooling pipes by attaching it to the connection points, fix the water pipes with cable straps to the foreseen attaching points. Then the specimen can be placed in the glass tube by sliding the whole mounting unit in from above. Carefully tighten the 6 screws for the upper CF-flange, then attach the cooling wristband with the 6 screws. The water cooling of the glass tube is re-established by activating the water cooling of the glass tube at the water cooling tableau and re-opening the hand actuated water valves above the basin. Also re-connect the temperature measurement line at the top of the glass tube. To pump the central vacuum vessel the full-metal valve VVMeck1 ("Bypass Turbo") is opened slowly, the scroll pump is to be put in continuous mode (if it not still is) by setting the scroll

[4]Because one needs to bend over the body quite a bit to see the pressure reading while having one hand on the valve.

pump to "Rootspump permanent on" ("I"). Wait until the pressure has gotten to around $1{\cdot}10^{-2}$ mbar, indicated by the full range gauge shown at the capacitance manometer at "2 FULL". Now close the bypass of the turbo pump by closing the valve VVMeck1 ("Bypass Turbo"). The rear of the turbo pump is opened by the valve VKFeckTP ("Ausgang Turbo"). After this slowly the full-metal gate valve VVMS2 ("Turbopumpe") in front of the turbo pump is opened. The central vacuum vessel is now pumped to UHV conditions and ready for operation.

A.3.1.3. Standard loading and degassing sequence

What follows is the procedure for a standard loading and degassing sequence of a specimen.

The apparatus is in stand-by condition, i.e. under vacuum, pressure better than $5{\cdot}10^{-9}$ mbar. In this condition since days, or in the few 10^{-8} mbar range if a loading and degassing cycle was executed at the same day. A vacuum better than $8{\cdot}10^{-8}$ mbar is enough as pre-condition for a gas loading and degassing sequence.

The gas piping system is pumped by closing the valve VKFeck2 ("Vorpumpe vor Ausgleichsgefäß"), then open the locking mechanism of the 2/3 directional control valves with the key. The scroll pump is activated by putting it into continuous mode (switch in "Rootspump permanent on" ("I")). The nitrogen ballast of the scroll pump is activated by opening the valve VA3 ("Scroll N_2"). Both 2/3 directional control valves are opened to pump the gas piping of both gas bottles. When the pressure at the scroll pump has lowered to about $2{\cdot}10^{-2}$ mbar liquid nitrogen is filled into the thermos flask until the flask is full. Now both 2/3 directional control valves are closed, also the locking mechanism is closed. The valve VKFeck2 ("Vorpumpe vor Ausgleichsgefäß") needs to be left closed. The scroll pump can be put into discontinuous mode by switching it into "Rootspump - automatic" ("0"). The valve VA1 or VA2 (depending on which line is in use) of the pressure regulator unit at the desired gas station is closed. If the pressure regulator at this unit was not used before, which is closed by turning the wheel counter-clockwise. Now the main valve at the gas bottle is opened once such that the spiral connector is filled with the gas at bottle pressure. The pressure gauge at the right side of the pressure regulator unit indicates the bottle pressure. The main valve of the gas bottle is closed for safety reasons - the amount of gas in the spiral pipe is enough to execute one gas filling at 500 mbar and it is better to have the gas bottle regularly closed. Now the pressure regulator is opened until the analogue pressure gauge at the left of the pressure regulator unit shows a pressure of around 0.8 bar (which is absolute pressure). The digital pressure measurement unit above the locking mechanism shall show -0.2 bar - it measures relative pressure. "This pressure is chosen such that the gas flow controller has overpressure in comparison to the central vessel in ROST (vacuum) but lower pressure than ambient pressure. This is to avoid gas filling of the glass vessel to pressures higher than ambient pressure which would result in potentially harmful tensile stress to the glass tube, especially the glass-steel connectors are delicate parts." see chapter A.3.1.1. Valve VA1 or VA2 is opened (depending if the A or B line is used), the liquid nitrogen should now boil a bit until the gas is cooled down. Now the gas piping system is filled until the gas flow controller. Gas flow controller unit 1 (for line A) or 2 (for line B) needs to be activated, depending which line is used. The all-metal gate valve VVMS2 ("Turbopumpe") in front of the turbo pump is closed. Mind the indicator markings at the valve for the closed position. Also, for safety reasons, the valve behind the turbo pump VKFeckTP (" Ausgang Turbo") is closed. The full-metal valve VVM1 ("gas feed") is opened at the end of the gas feed line at the corner of the central vacuum

vessel, a half turn counter-clockwise is enough, the indicator marking in green colour helps here. The desired gas flow controller unit (1 or 2) is adjusted to a gas flow of 50 or 100 sccm - this is assumed to be enough that the flowing gas is cooled down sufficiently in the liquid nitrogen trap and the filling itself is established in about 3 - 5 minutes. The gas flow controller is started, gas is filled into the central vacuum vessel until the vessel reaches a filling pressure of around 20 mbar under the desired filling pressure. Maximum filling pressure is recommended to be 500 mbar. Now the gas flow is stopped by switching off the gas flow at the control unit. Now a flow of 10 or 20 sccm is adjusted (the slower flow will help to end the filling at the desired pressure). The gas flow controller is started again. Wait until the desired gas pressure is reached, hit the "off"-button and close the full-metal valve VVM1 ("gas feed"). Now the valve VA1 or VA2 (depending if line A or B is used) is closed at the pressure regulator unit. The generator of the induction oven is activated by closing the relais with the green button on the generator unit. The desired temperature programme in the software is loaded into the controller and the programme started. After the end of the programme, the specimen is allowed to cool down to around 100°C (or lower, if desired). Then the gas from the central vacuum vessel is expanded into the expansion unit ("Ausgleichsgefäß") by opening the valve VVMeck1 ("Bypass Turbo") [5]. It will take about 1 - 2 seconds until the pressure of the central vacuum vessel and the expansion volume is equalised. Valve VVMeck1 ("Bypass Turbo") is opened again to add inert gas (nitrogen) to the expansion volume in order that the gas is not explosive when it is pumped by the scroll pump (pure hydrogen would be under the explosion pressure when being expanded into the expansion volume - but when being pumped without being mixed with nitrogen it would be agglomerated again at the scroll pump when being pumped). Valve VA4 ("Absperr Ausgleichsgefäß N_2") is opened. Then valve Vp1 ("Ausgleichsgefäß N_2") is opened - a hissing sound of the inflowing nitrogen can be heard - until the pressure has reached 800 mbar; the analogue pressure gauge directly at the valve will help to check the pressure, but the relevant pressure reading is to be done at the capacitance manometer at "4 INRT". The sensor is placed in the expansion volume. After having closed valves Vp1 ("Ausgleichsgefäß N_2") and VA4 ("Absperr Ausgleichsgefäß N_2") the scroll pump is to be put in continuous mode by switching it into "Rootspump permanent on" ("I"), also the nitrogen ballast is applied at the scroll pump by opening the valve VA3 ("Scroll N_2"). To pump the hydrogen-nitrogen gas mix the valve VKFeck2 ("Vorpumpe vor Ausgleichsgefäß") is opened, there will be a quite loud "whoosh"-noise while doing so, also the flexible vacuum pipe system towards the scroll pump will move a bit - don't get frightened, this is normal. After having reached a pressure of around $2{\cdot}10^{-2}$ mbar at the sensor "3 SCRL" (to be checked at the capacitance manometer) again the bypass full-metal valve VVMeck1 ("Bypass Turbo") is opened just so short to allow to equalise the left gas pressure from the central vacuum vessel to escape and establish an acceptable pressure for the turbo pump - this will lower the pressure from 10 - 20 mbar (depending if the small or big glass tube is used) to around 1 mbar. Then the valve VKFeckTP ("Ausgang Turbo") behind the turbo pump is opened and after this cautiously the full-metal gate valve in front of it is opened. The QMS at the TESS chamber can be activated now. When a pressure of $5{\cdot}10^{-7}$ mbar[6] is reached, the full-metal gate valve VVMS1 ("TESS") is opened to connect to the TESS chamber where the QMS is inherited. The full-metal gate valve VVMS2 ("Turbopumpe") is closed to pump the ROST

[5] Before it should be made sure that the valve VKFeckTP ("Ausgang Turbo") is still closed! The valve VKFeck2 ("Vorpumpe vor Ausgleichsgefäß") needs to be still closed as well.

[6] This is true for emission currents of $I_{em} < 0.1$ mA at the Inficon QMS at TESS.

apparatus exclusively via the TESS chamber. Now the desired temperature programme at the ROST-PC can be applied and the specimen can be degassed.

Acknowledgements

Ein herzliches und großes Danke an meinen Doktorvater Prof. Dr. Rudolf Neu. Für seine Einwilligung, mich mit diesem wichtigen und feinem Thema der doch sehr klassischen Festkörperphysik, oder auch "Frauenfelder reloaded", zu betrauen. Noch dazu in diesem fruchtbaren Umfeld. Ich freue mich sehr darüber, dass ich Teil dieser Gemeinschaft von wunderbaren und bereichernden Wissenschaftlern sein durfte und darf, ich habe viel dazugelernt!

Prof. Dr. Ulrich Stroth danke ich sehr für sein Einverständnis, mich in die Gruppe als Doktorand aufzunehmen. Ich empfinde es als sehr bereichernd, in diesem Bereich des Institutes arbeiten zu können.

Es freut mich, dass Prof. Dr. Christian Linsmeier seine Zusage gegeben hat sich als Zweitprüfer zur Verfügung zu stellen, merci vielmals!

Dr. Thomas Schwarz-Selinger war mir der beste Betreuer, den ich mir wünschen konnte. Der Aufbau gelang wesentlich schöner und besser, als es mir ohne ihn möglich gewesen wäre. Ich bin sehr dankbar für sein großes Vertrauen, dass ich den Aufbau des Experiments über große Strecken selbstständig und ohne viel Anleitung schaffe. Auch bei den anschließenden Experimenten ließ er mich an der langen Leine. Das war mir Ansporn und sehr erhebend. Falls ich doch nicht mehr weiter wusste oder die Dinge doch nicht so wollten wie ich mir das vorstellte, half seine Expertise als auch seine ruhige und verbindliche Art, den Dampf aus dem Kessel zu nehmen und die Dinge wieder ins rechte Lot zu rücken. Als begnadeter Experimentator hatte er die besten Ideen für effiziente, schöne und unprätentiöse Lösungen, so zum Beispiel ein Bierfass im Vakuumkreislauf als Puffer- und Inertisierungsgefäß (billig, einfach, und noch dazu sehr dekorativ). Merci vielmals Thomas, es war und ist mir eine Freude und große Bereicherung!

Dr. Udo von Toussaint muss ich immer wieder bewundern für seine Fähigkeiten in der Mathematik und dem Programmieren. Der Diffusionscode den er für mich schrieb (in Fortran!), hat ihn sicher einige Nächte gekostet. Die anschließenden Diskussionen mit mir vermutlich auch ein paar Nerven. Aus Udo sprudeln ständig und ohne Unterlass Ideen und Hypothesen für Experimentführung und Beobachtungen, was zu schnellen Lösungen führte, und noch häufiger zu Denkanstößen durch die sich mir das Thema auch von mathematischer Seite her neu erschloss. Vielen Dank Udo!

Dr. habil. Wolfgang Jacob als Leiter der Arbeitsgruppe PMI unterstützte mich wo er nur konnte und war stets mit Rat und Tat zur Stelle. Ihm danke ich vielmals für das Vertrauen in mich und dass er mir ermöglichte meine Arbeit in Übersee vorzustellen. Nicht zu knapp bin ich außerdem dankbar für seine Ideen zu meiner Doktorarbeit, danke dafür!

Dr. Klaus Schmid, für fruchtbare Gespräche über Gleichgewichtszustände von Teilchen in der Gasphase und dem Festkörper. Und für die ganzen anderen unterhaltsamen Zusammenkünfte, merci!

Thomas Dürbeck kennt jedes Vakuumbauteil, jeden Flansch und jede Pumpe beim Namen und weiß bis ins Detail, wo diese sich derzeit versteckt halten. Auf die Frage "Du Thomas, weiß Du eigentlich ob wir 'dieses oder jenes X-beliebige Vakuumbauteil irgendwo herumliegen haben?" benennt er zuverlässig deren Aufenthaltsort, bzw. -schrank. Er muss wohl nicht allzu

begeistert gewesen sein, dass sich zu anfangs sogar zwei neue Leute in seinem Labor breit und an seiner TESS zu schaffen machten. Dass ich wochenlang im Schneidersitz am Boden sitzend dieses Monstrum erschuf (um dieses dann auch noch mit seiner TESS zu verheiraten!) und noch dazu Vassily mit seinem Elektronenstoßheizer zu Beginn doch recht häufige Überschläge bei 5 kV in seiner TESS verursachte, war zugegebenermaßen nervenzehrend. Ein herzliches Danke, für all die Mithilfe beim Aufbau, Rat und Tat bei den Messungen, und dass er mir das zusätzliche Chaos nachsah, das mit mir einzog. Danke, für das angenehme Zusammenarbeiten!

Der gesamten Gruppe PMI danke ich dafür, dass sie um mich herumplanten weil ich geschätzt ein Jahr Messzeit an TESS für mich beansprucht habe.

Dr. Armin Manhard sprudelt über vor Ideen für neue Experimente und Gerätschaften. Von ihm kam die Idee, woher denn diese Oszillationen in meinem Desorptionssignal kommen könnten (nämlich vom Regler des Wasserkühlkreislaufes im Keller). Eine weitere dieser Ideen war die Anschaffung eines Laserschweißapparates. Ohne dieses Gerät wäre ich wohl heute noch dabei, die Thermoelemente an meine Prüflinge per Widerstandsschweißen anzupunkten, zu verspröden und wieder abzubrechen. Danke!

Karl-Heinz Stemmer danke ich sehr für seine Hilfe und große Expertise im Umgang mit Item-Bauteilen und seinem Sinn für schöne mechanische Lösungen. Ritter ROST wäre nie so schön und einfach zu bedienen geworden, hätte er sich nicht als Neuzugang in der mechanischen Werkstatt der Apparatur angenommen. Ein wahrer Glücksfall! Merci vielmals!

Die ASDEX-Werkstatt um Karl Eismann durfte ich allzeit nerven mit meinen Sonderwünschen. Karl, Manfred und Bernhard wurden aber trotzdem nicht müde, mir zügig unter die Arme zu greifen mit sauberen Speziallösungen für Wolframhohlzylinder und Schwalbenschwanznuten! Danke!

Dem Team um den Tandem-Beschleuniger, Michi Fußeder, Arno Weghorn und Joachim Dorner danke ich, dass sie mich so bereitwillig und herzlich bei ihnen aufgenommen haben. Wenn, vor allem zum Schluss hin, die Tage und Nächte bei mir lang wurden, sahen sie es mir bereitwillig nach dass ich mich ihn ihrem Besprechungsraum teilweise etwas über Gebühr breit machte.

An dieser Stelle werden sich manche fragen: 'Hey, dankt dieser Kerl denn nicht auch all jenen lieben Menschen, die nicht in seine wissenschaftliche Arbeit involviert waren? Die für ihn da sind, ihn liebhaben, auch wenn er grántelt, ihn wässern und füttern wenn er es selbst nicht auf die Reihe bekommt, ihn nach draußen zogen, damit er mal wieder durchgelüftet wurde nach langen Tagen in seinem Kämmerlein? Seinen Eltern, ohne die das alles gar nicht möglich gewesen wäre? Seinen Freunden, die er so sträflich vernachlässigte, wenn er sich in sein Labor verkrümelte und er sich tage-, wochen-, monatelang nicht sehen oder hören ließ?' Keine Sorge, das werde ich, aber im wirklichen Leben!